Doctorate Dissertation
博士論文

Measurements of neutrino charged-current interactions on water and hydrocarbon targets using a sub-GeV anti-neutrino beam
(サブ GeV 反ニュートリノビームを用いた
水および炭化水素標的に対する
ニュートリノ荷電カレント反応の測定)

A Dissertation Submitted for Degree of Doctor of Philosophy
December 2018
平成 30 年 12 月博士 (理学) 申請

Department of Physics, Graduate School of Science
The University of Tokyo
東京大学大学院理学系研究科物理学専攻

Naruhiro Chikuma
竹馬 匠泰

Abstract

T2K is a long-baseline neutrino oscillation experiment, using a muon neutrino beam at J-PARC and measuring it by Super-Kamiokande. T2K has successfully observed the electron-neutrino appearance and muon-neutrino disappearance, and now set a goal of the first observation of the CP violation in neutrino sector. However, it is indispensable to reduce the systematic uncertainties for the precise measurements of neutrino oscillation. Especially, poor understanding of neutrino-nucleus interactions gives rise to a large systematic uncertainty in the neutrino oscillation analysis.

In order to measure neutrino interactions with water and hydrocarbon targets, we developed a new detector, WAGASCI, in the T2K near detector hall. It allows measurements with a neutrino energy spectrum similar to Super-Kamiokande. We performed the first data taking with WAGASCI from October 2017 to May 2018.

This thesis presents measurements of neutrino charged-current interactions using the T2K anti-neutrino beam with the WAGASCI detector. The motivation of this analysis is to provide new samples to improve understanding of anti-muon-neutrino interaction dependency on nuclear targets between water and hydrocarbon. The signal is charged-current interactions with no pions and no protons in the final state (CC0π0p). It corresponds to a characteristic of charged-current quasi-elastic (CCQE), $\overline{\nu}_\mu + p \rightarrow \mu^+ + n$, which is the main signal in the T2K neutrino oscillation analysis.

The main result is the flux-integrated cross sections of CC0π0p with a muon angle less than 30 degrees on H_2O and CH:

$$\begin{aligned}
\sigma^{\overline{\nu}_\mu}_{\mathrm{H_2O}} &= \left[1.082 \pm 0.068(\mathrm{stat.})^{+0.145}_{-0.128}(\mathrm{syst.})\right] \times 10^{-39}\mathrm{cm}^2 \cdot \mathrm{nucleon}^{-1}, \\
\sigma^{\overline{\nu}_\mu}_{\mathrm{CH}} &= \left[1.096 \pm 0.054(\mathrm{stat.})^{+0.132}_{-0.117}(\mathrm{syst.})\right] \times 10^{-39}\mathrm{cm}^2 \cdot \mathrm{nucleon}^{-1}, \\
\sigma^{\overline{\nu}_\mu}_{\mathrm{H_2O}}/\sigma^{\overline{\nu}_\mu}_{\mathrm{CH}} &= 0.987 \pm 0.078(\mathrm{stat.})^{+0.093}_{-0.090}(\mathrm{syst.}),
\end{aligned}$$

where the cross sections are normalized by all nucleons in molecules of H_2O and CH. The anti-neutrino beam is predicted to have the mean energy at 0.86 GeV, and the peak energy at 0.66 GeV with 1σ spread of $^{+0.40}_{-0.25}$ GeV. This results provides the first sample to show a direct relation between water and hydrocarbon targets for neutrino interaction among the measurements using the T2K anti-neutrino beam.

Acknowledgments

Firstly, I would like to express my deepest gratitude to my supervisor,
Prof. Yokoyama, who offered his unwavering support for the five years since my master degree. While he has guided me in the whole of my research, he has given me great opportunity to explore many of my working interests. I am confident that I have gained precious experience which should be important not only in the physics region, but in my future endeavours. I have also been helped and encouraged by the other people at our laboratory in the University of Tokyo and I would like to thank all those people whom I have worked together with.

All of my work owes an important debt to the contributions from the WAGASCI and INGRID collaborators. I would certainly not have completed the detector construction and electronics development without their great support. Since I have spent most of my Ph.D. time period on work for the WAGASCI detector, I am deeply grateful to the collaborators for all of their support.

I would like to show my greatest appreciation to the T2K collaborators, especially to the people in the cross section group who shared a great amount of their knowledge which helped to lead me in the right direction for my analysis. I feel honored to have been a member of such a brilliant collaboration.

In addition, I would like to thank the Advanced Leading Graduate Course for Photon Science (ALPS) at the University of Tokyo, and the Japan Society for the Promotion of Science (JSPS) for the grant that made it possible for me to complete this study.

Finally, I would like to offer my special thanks to all of the people who have supported me for those stressful periods, especially to my family for their concerns and home cooking after those late nights working in the office.

Contents

Chapter 1

Introduction

The Standard Model of particle physics is a theory to describe the interactions and kinematics of subatomic particles. It is established based on the quantum field theory along with the gauge principles, and consists of elementary particles and antiparticles: fermions which constitute matters and gauge bosons which carry electromagnetic, weak, and strong nuclear forces. It successfully explains a wide variety of experimental results; however, there remain unexplainable issues in the universe, such as the origin of the universe and the matter-antimatter asymmetry. In the early universe an equal amount of matter and antimatter existed, but the observations suggested the universe at present is abundant in matter. One of the keys to explain the matter-antimatter asymmetry is an asymmetry in phenomena between particles and antiparticles, which is known as CP violation. CP violation has been observed in the mixing of quarks, but the CP violation in the quark sector does not provide a sufficient explanation. Hence, the observation of CP violation in the lepton sector is also awaited, and the prospective first measurement is aimed in the neutrino mixing.

Neutrino is one of the elementary particles in the Standard Model with spin 1/2 and no electric charge, and interacts only via weak force. Neutrino has three different flavors, electron-, muon-, and tau-neutrinos, and mixings between those flavors occur in the case of nonzero and nonidentical masses. The discovery of neutrino oscillation proved the framework of neutrino mixing with definite masses, and the next step is to observe the CP violation via the neutrino oscillation measurements.

Neutrino oscillation parameters have been measured in various experiments, and they aim to achieve more precise measurements of neutrino oscillation. In the future experiments with sufficient statistics, suppression of the systematic uncertainty is desired, therefore better understanding of neutrino sources, neutrino interactions, and neutrino detectors are indispensable. Especially, poor modeling of neutrino interactions currently imposes a large uncertainty. Since modern neutrino

experiments adopt various nuclear targets for neutrino detection, measurements of neutrino-nucleus interactions with various interaction modes are important.

In the Tokai-to-Kamioka (T2K) experiment, neutrinos are detected via weak charged-current interactions with water and hydrocarbon targets by using neutrino or anti-neutrino beam with sub-GeV energy. Since T2K started the operation with a neutrino beam and recently changed to anti-neutrino beam, lack of measurements with anti-neutrino beam is apparent. In order to provide new samples, various measurements have been going on by using the T2K neutrino beam, and new detectors have been built to investigate neutrino interactions. We developed a new water-target detector, WAGASCI, to perform neutrino cross section measurement which has not been achieved by previous measurements. This thesis presents the cross section measurements of neutrino charged-current interactions on water and hydrocarbon targets with the WAGASCI detector in the T2K experiment.

This thesis begins with a brief review of neutrino oscillation, including its history, theoretical framework, and recent and future measurements (Chapter 2). It is followed by theoretical understanding of neutrino interactions and standing position of this thesis among other measurements (Chapter 3). The experimental apparatus (Chapter 4) and the analysis strategy (Chapter 5) are explained before the main report of the cross section analysis (Chapters 6–8). Conclusion with the results are described at the end (Chapter 9).

Chapter 2

Neutrino oscillation

2.1 Historical introduction

2.1.1 Discovery of neutrino

Neutrinos were first proposed by Pauli in 1930[1], as neutral, light and weakly interacting fermions to explain the continuous β decay spectrum. Neutrino mass was expected to be zero, assuming the tail shape of β decay coming from a point-like interaction. The first clear direct detection of neutrinos was achieved by Reines and Cowan in 1956[2], using a fission reactor at Savannah River Plant. Using a water target enriched with $CdCl_2$ surrounded by liquid scintillator, positrons and neutrons are detected from inverse β decays:

$$\overline{\nu}_e + p \rightarrow e^+ + n. \tag{2.1}$$

In 1962, a second type of neutrino, the muon neutrino, was observed at Brookhaven National Laboratory by the AGS neutrino experiment, which was the first serious accelerator neutrino experiment[3]. Muon neutrinos were produced by decays of charged pions coming from accelerated protons striking a beryllium target, and detected via neutrino charged current interactions. The results indicated that the process with electrons in the final state:

$$\nu_\mu + N \rightarrow e^- + X \tag{2.2}$$

is forbidden, hence muon and electron neutrinos were identified as different particles. Since the τ lepton was discovered at SLAC in 1975[4], neutrinos were also expected to have another generation, the tau neutrino. In 2001, the first observation of ν_τ was finally achieved by the DONUT experiment at Fermilab[5], where ν_τ was produced via decay of charmed mesons. The next question was about the number of generation of neutrinos. It was confirmed by the Z boson resonance

in LEP[6] that there are three light neutrino species coupling to the Z boson, although it is still possible that extra heavy neutrinos or neutrinos not coupling to the Z boson might exist.

2.1.2 Discovery of neutrino oscillation

In 1968, it was reported by the Homestake experiment led by Ray Davis[7] that the measured neutrino flux from the Sun was smaller than its prediction. As the solar model, the CNO cycle, was established well, to describe the solar activity by an exothermic chain of nuclear reactions that capture protons and produce helium, photons, positrons and neutrinos. The solar neutrinos, mainly from ^{7}Be and ^{8}B, were detected by using C_2Cl_4 and estimating the amount of argon from a reaction:

$$\nu_{\mathrm{e}} + {}^{37}\mathrm{Cl} \rightarrow \mathrm{e}^{-} + {}^{37}\mathrm{Ar}. \tag{2.3}$$

There were similar reports in the 1980s, such as SAGE[8] and GALLEX[9], which were using ^{71}Ga in order to have a lower energy threshold, and to be more sensitive to solar neutrino from pp fusion. Around that time, Kamiokande also measured the solar neutrinos, using an elastic scattering on an electron:

$$\nu_e + e^{-} \rightarrow \nu_e + e^{-}. \tag{2.4}$$

All experiments above observed less neutrinos than the solar model expectation. This discrepancy between the measured number of neutrinos and expectation from the solar model was called the Solar Neutrino Problem.

In order to understand the solar neutrino problem, the idea of neutrino oscillation is provided as described in Sec. 2.2. The first observation of neutrino oscillation was achieved by Super-Kamiokande (SK) in 1998[10]. SK is a water Cherenkov detector to observe neutrinos from cosmic ray interactions in the atmosphere. Event rates of ν_e and ν_μ as a function of zenith angle, which represents the flight length in the earth and varies the neutrino oscillation probabilities, were fitted better by a model including an oscillation, $\nu_\mu \rightarrow \nu_\tau$, rather than a model with no oscillation.

Sudbury Neutrino Observatory (SNO) verified that the solar neutrino problem was solved by the neutrino oscillation in 2002[11]. Using a heavy-water Cherenkov detector, three different detections of neutrinos were performed: ν_e was detected via charged current interaction on deuterium, all types of neutrinos were detected via scattering off deuterium through neutral current, and ν_e was also detected by elastic scattering off electrons. The results showed non-zero value of $\nu_\mu + \nu_\tau$ flux, that meant a clear evidence of solar neutrino oscillations.

Neutrino oscillations were also measured by reactor experiments[12], and the results were explained by the same oscillation framework consistently to the solar

neutrino oscillation. In addition to measurements of the neutrino flux reduction, a neutrino appearance channel, $\nu_\mu \to \nu_e$, was observed in the Tokai-to-Kamika (T2K) experiment[13]. Further experiments, as described in Sec. 2.3, have been performed until now to precisely measure the neutrino oscillation parameters.

2.2 Theory of neutrino oscillation

Neutrino oscillations are described as a consequence of a mixing of neutrino flavor states. Assuming states of neutrino generated in a flavor, $|\nu_\alpha\rangle$, are different from neutrino mass eigenstates, $|\nu_i\rangle$, and those mass eigenvalues have non-zero values and not identical to each other, the neutrino flavor eigenstates are expressed as a linear combination of the mass eigenstates by using a unitary transformation:

$$|\nu_\alpha\rangle = \sum_i U^*_{\alpha \mathrm{i}} |\nu_i\rangle. \tag{2.5}$$

In the minimal neutrino mixing scheme, three mass eigenstates exist, so that the mixing is expressed by a 3×3 matrix, which is known as the Pontecorvo-Maxi-Nakagawa-Sakata (PMNS) matrix[14][15]:

$$U = \begin{pmatrix} 1 & 0 & 0 \\ 0 & c_{23} & s_{23} \\ 0 & -s_{23} & c_{23} \end{pmatrix} \begin{pmatrix} c_{13} & 0 & s_{13}e^{-i\delta} \\ 0 & 1 & 0 \\ -s_{13}e^{i\delta} & 0 & c_{13} \end{pmatrix} \begin{pmatrix} c_{12} & s_{12} & 0 \\ -s_{12} & c_{12} & 0 \\ 0 & 0 & 1 \end{pmatrix}, \tag{2.6}$$

where $c_{ij} = \cos\theta_{ij}$ and $s_{ij} = \sin\theta_{ij}$. $\delta = \delta_{\mathrm{CP}}$ is the CP-violating phase.

A propagation in time for a mass eigenstate is expressed by the Schroedinger equation:

$$i\frac{\mathrm{d}}{\mathrm{d}t}|\nu_i(t)\rangle = H|\nu_i(t)\rangle, \tag{2.7}$$

where H represents the Hamiltonian. In vacuum, the mass states are the eigenvector of the free Hamiltonian:

$$H|\nu_i(t)\rangle = E_i|\nu_i(t)\rangle, \tag{2.8}$$

hence the mass eigenstates evolve in vacuum as a plane wave:

$$|\nu_i(t)\rangle = e^{-iE_it}|\nu_i\rangle. \tag{2.9}$$

Evolutions of the flavor eigenstates in vacuum are expressed as:

$$|\nu_\alpha(t)\rangle = \sum_i U^*_{\alpha \mathrm{i}} e^{-iE_it}|\nu_i\rangle \tag{2.10}$$

$$= \sum_i \sum_\beta U^*_{\alpha \mathrm{i}} U_{\mathrm{i}\beta} e^{-iE_it}|\nu_\beta\rangle. \tag{2.11}$$

Consequently, the neutrino oscillation probability in vacuum is calculated by using the unitary transformation matrix as:

$$P(\nu_\alpha \to \nu_\beta) = |\langle \nu_\beta(t)|\nu_\alpha\rangle|^2 \tag{2.12}$$

$$= \delta_{\alpha\beta} - 4\sum_{k>j} \mathrm{Re}(U^*_{\alpha k}U_{\beta k}U_{\alpha j}U^*_{\beta j}) \sin^2\left(\frac{\Delta m^2_{kj}L}{4E}\right) + 2\sum_{k>j} \mathrm{Im}(U^*_{\alpha k}U_{\beta k}U_{\alpha j}U^*_{\beta j}) \sin\left(\frac{\Delta m^2_{kj}L}{2E}\right), \tag{2.13}$$

with differences in the squares of masses of eigenstates, $\Delta m^2_{ij} = m^2_i - m^2_j$, assuming ν_α with energy E is generated with charged current weak interaction, propagated for a distance L, and then detected as ν_β. Since neutrinos are ultrarelativistic, $E_i \simeq E + m^2_i/2E$ and $t \simeq L$ are assumed.

In the 3×3 mixing scheme, the neutrino oscillation probabilities are expressed with mixing angles in the PMNS matrix. For instance, a probability of disappearance of a muon neutrino is expressed as:

$$P(\nu_\mu \to \nu_{x(\neq\mu)}) \simeq \sin^2 2\theta_{23} \sin^2\left(\frac{1.27\ \Delta m^2_{32}[\mathrm{eV}^2]\ L[\mathrm{km}]}{E_\nu[\mathrm{GeV}]}\right), \tag{2.14}$$

where only the dominant contribution is shown. In the case of electron neutrino appearance, the leading term is expressed as:

$$P(\nu_\mu \to \nu_e) \simeq \sin^2 2\theta_{13} \sin^2\theta_{23} \sin^2\left(\frac{\Delta m^2_{31}L}{4E_\nu}\right) \tag{2.15}$$

$$= \sin^2 2\theta_{13} \sin^2\theta_{23} \sin^2\left(\frac{1.27\ \Delta m^2_{31}[\mathrm{eV}^2]\ L[\mathrm{km}]}{E_\nu[\mathrm{GeV}]}\right). \tag{2.16}$$

Whilst this term is common between $\nu_\mu \to \nu_e$ appearance and $\bar{\nu}_\mu \to \bar{\nu}_e$ appearance, it is followed by a term not identical between ν_e and $\overline{\nu}_e$, which is known as a CP-violating term:

$$\pm \cos\theta_{13} \sin 2\theta_{13} \sin 2\theta_{12} \sin 2\theta_{23} \sin\delta \times \sin\left(\frac{\Delta m^2_{32}L}{4E_\nu}\right) \sin\left(\frac{\Delta m^2_{31}L}{4E_\nu}\right) \sin\left(\frac{\Delta m^2_{21}L}{4E_\nu}\right), \tag{2.17}$$

with the $+$ $(-)$ sign for ν_e $(\bar{\nu}_e)$ appearance. Neutrinos do not fly in vacuum in the real experiment, hence a correction to the Hamiltonian is needed due to matter effects. Considering only electron neutrinos coherently interact with electrons in

matter, the propagation in time is corrected by using an extra potential V:

$$i\frac{\mathrm{d}}{\mathrm{d}t}|\nu_i(t)\rangle = (H_{\text{vacuum}} + V)|\nu_i(t)\rangle, \tag{2.18}$$

$$V = \begin{pmatrix} \pm\sqrt{2}G_F n_e & 0 & 0 \\ 0 & 0 & 0 \\ 0 & 0 & 0 \end{pmatrix}, \tag{2.19}$$

where H_{vacuum} is the Hamiltonian in the case of vacuum, G_F is the Fermi constant, and n_e is the electron density in the matter, with the + (−) sign for ν_e ($\bar{\nu}_e$).

Probability of electron neutrino appearance, including the matter effect, and non-leading terms, is calculated as:

$$\begin{aligned} P(\nu_\mu \to \nu_e) &= 4c_{13}^2 s_{13}^2 s_{23}^2 \sin^2\Phi_{31} \quad \text{(dominant term)} \\ &+ 8c_{13}^2 s_{12}s_{13}s_{23}(c_{12}c_{23}\cos\delta - s_{12}s_{13}s_{23})\cos\Phi_{32}\sin\Phi_{31}\sin\Phi_{21} \\ &\qquad \text{(CP conserving term)} \\ &- 8c_{13}^2 c_{12}c_{23}s_{12}s_{13}s_{23}\sin^2\Phi_{32}\sin^2\Phi_{31}\sin^2\Phi_{21} \\ &\qquad \text{(CP violating term)} \\ &+ 4s_{12}^2 c_{13}^2(c_{12}^2 c_{23}^2 + s_{12}^2 s_{23}^2 s_{13}^2 - 2c_{12}c_{23}s_{12}s_{13}\cos\delta)\sin^2\Phi_{21} \\ &\qquad \text{(solar term)} \\ &- 2c_{13}^2 s_{12}^2 s_{23}^2 \frac{aL}{E}(1-2s_{13}^2)\cos\Phi_{32}\sin\Phi_{31} \\ &\quad +8c_{13}^2 s_{13}^2 s_{23}^2 \frac{a}{\Delta m_{31}^2}(1-2s_{13}^2)\sin\Phi_{31}, \quad \text{(matter effect)} \end{aligned} \tag{2.20}$$

where $\Phi_{ij} = \Delta m_{ij}^2 L/4E_\nu$, and $a = 2\sqrt{2}G_F n_e E_\nu = 7.56\times10^{-5}(\text{g/cm}^3)\times E_\nu$. For $\overline{\nu}_\mu \to \overline{\nu}_e$, some signs are inverted: $\delta \to -\delta$ and $a \to -a$. Figure 2.1 shows the calculated probability of ν_e and $\overline{\nu}_e$ appearance, with contributions from each term. For the calculation, a distance of 295 km, which is the length of baseline in T2K, and the current best-fit values shown in Table 2.1, except for δ_{CP} assigned to be maximum, $\pi/2$, are assumed.

2.3 Measurement of neutrino oscillation

2.3.1 Measurement of neutrino oscillation parameters

So far, the neutrino oscillation parameters have been measured by various neutrino energies (E_ν) and lengths of the baseline (L). Among the parameters in the PMNS matrix, θ_{12} and Δm_{21}^2 have been measured by solar neutrino experiments,

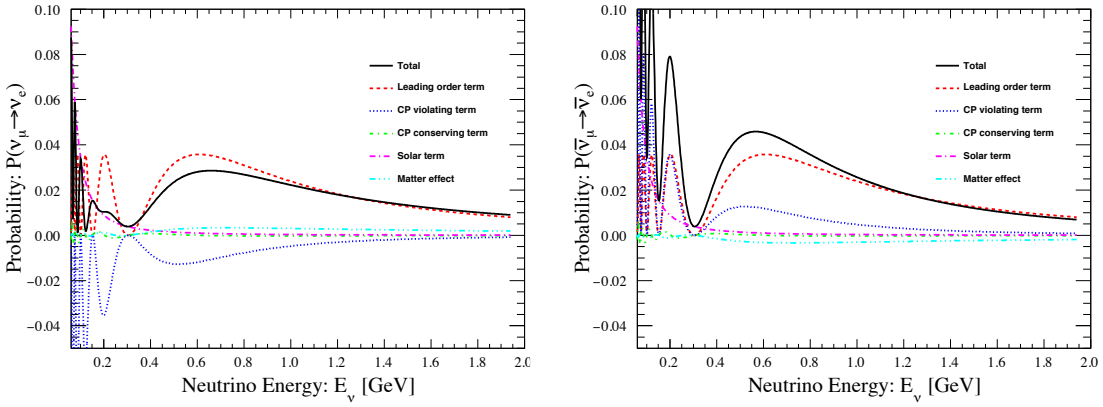

Figure 2.1: Probability of neutrino oscillation for $\nu_\mu \to \nu_e$ (left) and $\overline{\nu}_\mu \to \overline{\nu}_e$ (right).

such as Homesake[7], SK[16], SNO[17], and Borexino[18], by using electron neutrino disappearance. Those parameters are also measured by KamLAND[19] via a survival probability of $\overline{\nu}_e$ from reactors. θ_{23} and $|\Delta m^2_{32}|$ have been measured by atmospheric neutrino experiments, such as SK[20] and IceCube[21], and long-baseline accelerator neutrino experiments, such as K2K[22], MINOS[23], T2K[24], and NOνA[25]. θ_{13} has been measured by reactor neutrino experiments, Daya Bay[26], Double Chooz[27], and RENO[28]. θ_{13} has been also measured by accelerator neutrinos in T2K[29]. δ_{CP} is able to be measured by accelerator experiments with using the measured values of θ_{13} from reactor measurements and Δm^2_{21} and θ_{12} from solar neutrino experiments. Currently it is partially limited by results from T2K[24] and NOνA[25]. The current status for the measurements of neutrino oscillation parameters is summarized in Table 2.1.

2.3.2 Remaining questions

Despite significant progress in the measurement of neutrino oscillation parameters, there remain several properties to be experimentally determined, such as observation of the CP violation, determination of mass hierarchy, and understanding of large mixing angles. The neutrino CP violation at present is accessible only through accelerator experiments, and the δ_{CP} in the PMNS matrix is only partially constrained by the measurement by T2K and NOνA.

The neutrino oscillation measurements are not sensitive to the value of the neutrino absolute masses. However, the order of the three values of neutrino mass eigenvalues, which is known as mass hierarchy, can be determined by precise measurements of neutrino oscillation. The NOνA experiment reports in 2018 that

Table 2.1: Current status of measurements of neutrino oscillation parameters[30]. NO is "normal mass order" and IO is "inversed mass order".

Parameter	Mass hierarchy	Best-fit	3σ range
$\sin^2\theta_{12}$	NO, IO	0.297	0.250 – 0.354
$\sin^2\theta_{23}$	NO	0.425	0.381 – 0.615
	IO	0.589	0.384 – 0.636
$\sin^2\theta_{13}$	NO	0.0215	0.0190 – 0.0240
	IO	0.0216	0.0190 – 0.0242
Δm^2_{21} $[10^{-5}$ eV$^2]$	NO,IO	7.37	6.93 – 7.96
$\Delta m^2_{31(23)}$ $[10^{-3}$ eV$^2]$	NO	2.56	2.45 – 2.69
	IO	2.54	2.42 – 2.66
$\delta_{\rm CP}/\pi$	NO	1.38	(2σ: 1.0-1.9)
	IO	1.31	(2σ: 0.92-1.88)

the inverted mass hierarchy is disfavored at the 95% confidence level[25].

It is required to understand the large values of the neutrino mixing angles in the PMNS matrix compared with those in the CKM matrix. In particular, the measured value of θ_{23} is close to 45 degrees, which indicates a possible symmetry behind flavor mixings.

In order to understand those properties, precise measurements of the neutrino oscillation parameters are necessary. Table 2.2 shows an example of the systematic uncertainty in the T2K neutrino oscillation analysis[24]. The uncertainties in the neutrino beam flux and cross section models are constrained by measurements with the near detector, but the constraint is limited due to the differences between the near and far detectors in the nuclear targets and in the acceptance. The remnant uncertainty due to cross section models dominate the total systematic uncertainty for the ν_e events, which is estimated to be 7.8%.

In the next phase of T2K, T2K-II[31], high statistics is expected. Improvement of the systematic uncertainties is certainly required, in order to increase the sensitivity to the CP-violation up to 3σ level. The projected systematic uncertainty in total will be about 4% for ν_e events, as shown in Table 2.3. The dominant uncertainty in T2K-II will be still due to the neutrino cross sections, which is estimated to be about 3%. In order to reduce the present uncertainty down to this level, a better treatment of nuclear effect for neutrino-nucleus interactions is indispensable. Currently the uncertainties from nuclear effects are dominant among those from neutrino cross section model. It is required to obtain more information of the neutrino-nucleus interactions and their correlations between different nuclear targets for various neutrino energy range with a wide phase space.

For that purpose, there are various experiments which are ongoing or planned.

Measurements with a high granularity, such as ND280 Upgrade[32] and NINJA[33], aim to distinguish different neutrino interaction types to understand each contribution. NuPRISM[34] is planned to measure neutrino interactions by a water Cherencov detector with a wide range of neutrino energy. WAGASCI has been designed to measure correlations between water and hydrocarbon targets for a wide angular acceptance, in order to constrain neutrino cross sections at a phase space where the other detectors could not access. This thesis reports the neutrino cross section measurements using the WAGASCI detector. The results will play an important role in the process to improve the understanding of neutrino-nucleus interactions.

Table 2.2: Systematic uncertainty on the T2K far-detector event yields[24].

Source of uncertainty [%]	ν_μ	ν_e	$\nu_e\pi$	$\overline{\nu}_\mu$	$\overline{\nu}_e$
Neutrino cross section unconstrained by near detector	2.4	7.8	4.1	1.7	4.8
Neutrino flux and cross section constrained by near detector	3.3	3.2	4.1	2.7	2.9
Far detector systematics	2.4	2.9	13.3	2.0	3.8
Final or secondary hadronic interactions	2.2	3.0	11.5	2.0	2.3
Total	5.1	8.8	18.4	4.3	7.1

Table 2.3: Projected systematic uncertainties for the neutrino oscillation analysis in T2K-II[32].

Source of uncertainty [%]	ν_μ	ν_e
Neutrino cross section unconstrained by near detector	1	3
Neutrino flux and cross section constrained by near detector	1.9	1.8
Far detector systematics	1	1
Final or secondary hadronic interactions	1	1
Total	2.8	3.8

Chapter 3

Neutrino interactions

3.1 Overview of neutrino interactions

The goal of this thesis is to present measurements of cross sections of neutrino-nucleus charged-current interactions on water and hydrocarbon targets. This chapter describes the basic idea of neutrino interaction models, as well as the status of other neutrino cross section measurements.

Neutrinos only interact via the weak force, which is mediated by weak bosons $W^{\pm}$ and Z^0. Figure 3.1 shows Feynman diagrams of the vertices of a charged-current interaction and a neutral-current interaction, and those interactions are well understood in the framework of the Standard Model. The charged current and neutral current are expressed as:

$$j_{\mu}^{\pm} = \bar{u}\frac{-ig_W}{2\sqrt{2}}\gamma^{\mu}(1-\gamma^5)u, \tag{3.1}$$

$$j_{\mu}^{0} = \bar{u}\frac{-ig_Z}{2}\gamma^{\mu}(g_V - g_A\gamma^5)u, \tag{3.2}$$

where u, $\bar{u}$ are Dirac spinors, and γ^{μ} are the four Dirac gamma matrices, $\gamma^5 = i\gamma^0\gamma^1\gamma^2\gamma^3$, g_W and g_Z are coupling-strengths, and g_V and g_A are vector and axial-vector coupling constants, respectively.

As one of the simplest cases of neutrino scatterings, a muon-neutrino (ν_{μ}) scattering off an electron is shown in Fig 3.2, which is known as inverse muon decay. Since this process is only expressed with the charged-current interaction, the corresponding tree-level amplitude is constructed as:

$$\mathcal{M} = -\frac{G_F}{\sqrt{2}}\left(\bar{\mu}(k')\gamma^{\mu}(1-\gamma^5)\nu_{\mu}(p)\right)\left(\bar{\nu}_e(p')\gamma_{\mu}(1-\gamma^5)e(k)\right), \tag{3.3}$$

where $G_F = \frac{g_W^2}{4\sqrt{2}M_W^2} = 1.1663 \times 10^{-5}$ GeV^{-2} is the Fermi constant, assuming that the four-momentum of the $W^{\pm}$ boson is sufficiently smaller than its mass. In the

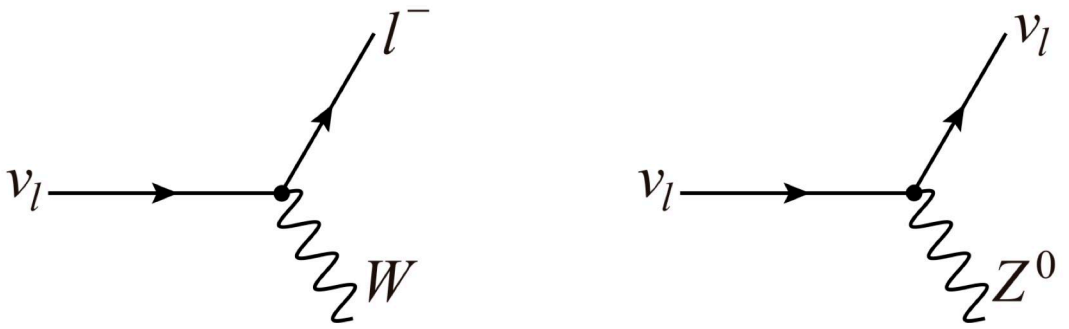

Figure 3.1: Feynman diagrams of vertices of neutrino interactions for charged-current (left) and neutral-current (right).

high-energy limit where masses of charged leptons are negligible compared with the neutrino energy, the cross section in the center of mass frame is expressed as:

$$\frac{\mathrm{d}\sigma}{\mathrm{d}\Omega} = \frac{G_F^2 s}{4\pi^2}, \tag{3.4}$$

where $s = (k+p)^2$ is the squared energy in the center of mass frame, which is expressed as:

$$s = m_e^2 + 2m_e E_\nu \simeq 2m_e E_\nu \tag{3.5}$$

in the laboratory-frame. Hence, it is seen that the neutrino cross section linearly increases on the neutrino energy in such an energy region.

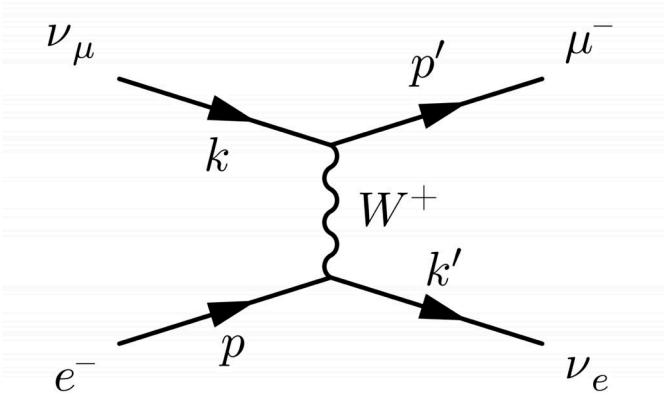

Figure 3.2: Feynman diagrams of a muon neutrino scattering off an electron.

Eq 3.4 is in common for neutrino-quark interactions, such as $\nu_\mu + d \to \mu^- + u$. In the case of anti-neutrino counterpart, $\overline{\nu}_\mu + u \to \mu^+ + d$, the cross section is suppressed by a factor of $\frac{1}{4}(1-\cos\theta)^2$ due to the helicity conservation.

Modern neutrino experiments are performed with nuclear targets. In order to consider the neutrino-nucleus interactions, neutrino-nucleon interactions are the basis of modeling. In the energy range of 0.1-30 GeV, the main interaction modes are:

- Quasi-elastic (QE)
- Resonance scattering (RES)
- Deep inelastic scattering (DIS)

Neutrino-nucleon interactions are described more in Sec. 3.2. At the basic level, neutrino-nucleon interactions are often computed assuming free nucleons. This well describes the cases of light nuclear targets, such as deuteron used in the early bubble chamber experiments. However, in the case of using heavy nuclear targets, such as carbon, oxygen, and nucleus even heavier, the neutrino interactions are influenced by the nuclear effects. The nuclear effect accounts for the initial momentum distribution of nucleons in the nucleus, distortion of final states of the outgoing particles from the neutrino interactions, and multi-nucleon processes. Those processes are described in Sec. 3.3.

Figure 3.3 shows the cross sections of neutrino-nucleus interactions for the energy range up to 5 GeV. At the sub-GeV energy, which corresponds to the target range of this analysis, the dominant interaction comes from charged-current quasi-elastic interaction (CCQE), and charged-current resonance interaction (CC RES) follows.

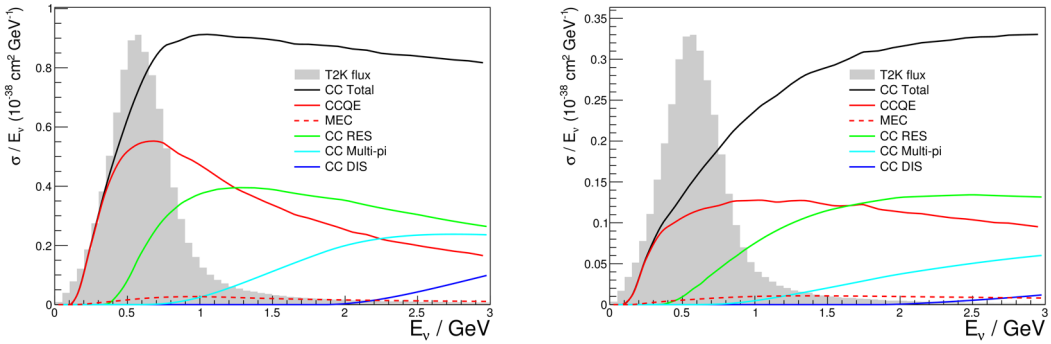

Figure 3.3: Cross sections of neutrino-nucleus interactions with different modes for ν_μ (left) and $\overline{\nu}_\mu$ (right), computed by the Monte Carlo simulation. In this figure, DIS only represents processes with a large invariant mass of the hadronic system, $W > 2.0$ GeV/c^2. The shape of the expected neutrino beam flux in T2K is shown with the shaded area.

3.2 Neutrino-nucleon interactions

3.2.1 Charged-current quasi-elastic interaction

Charged-current quasi-elastic (CCQE) interactions are the dominant interaction mode at the sub-GeV neutrino energy range, and constitutes the major fraction of the signal in this analysis. Figure 3.4 shows the diagram of CCQE.

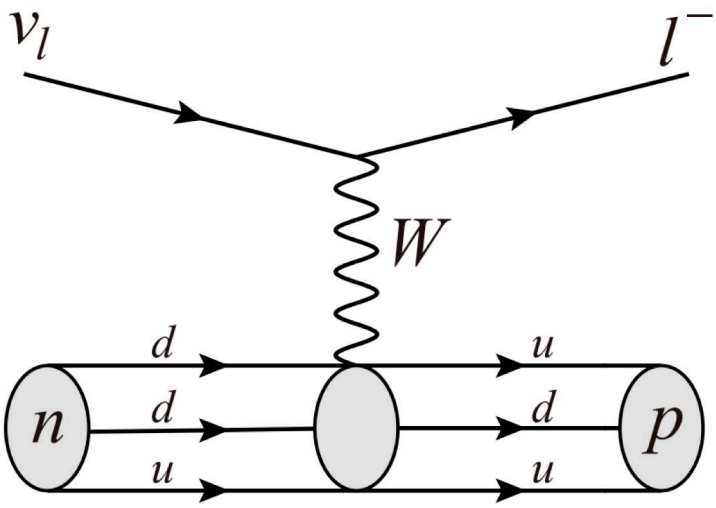

Figure 3.4: A diagram for CCQE.

Ignoring the nuclear effects, CCQE interaction is well modeled by Llewellyn-Smith formalism[35]:

$$\frac{\mathrm{d}\sigma}{\mathrm{d}Q^2}\left(\begin{array}{c}\nu n \to l^- p \\ \overline{\nu} p \to l^+ n\end{array}\right) = \frac{M^2 G_F^2 \cos^2\theta_c}{8\pi E_\nu^2}\left(A(Q^2) \pm B(Q^2)\frac{s-u}{M^2} + C(Q^2)\frac{(s-u)^2}{M^4}\right), \tag{3.6}$$

where the differential cross sections of neutrino (anti-neutrino) is expressed by $\pm$ respectively, M is the nucleon mass, G_F is the Fermi coupling constant, θ_c is the Cabbibo angle, E_ν is the neutrino energy, and s and u are the Mandlestam kinematics variables corresponding to the square center of mass energy squared and the four momentum squared respectively ($s - u = 4ME_\nu - Q^2 - m^2$ with an outgoing lepton mass, m). A, B, C are composed from Dirac (F_V^1) and Pauli (F_V^2) electromagnetic isovector form factors, an axial vector form factor (F_A), and

a pseudoscaler form factor (F_P):

$$A(Q^2) = \frac{m_l^2+Q^2}{M^2}\left[(1+\tau)F_A^2-(1-\tau)(F_V^1)^2+\tau(1-\tau)(\xi F_V^2)^2+4\tau F_V^1\xi F_V^2 - \frac{m_l^2}{4M^2}\left((F_V^1+\xi F_V^2)^2+(F_A+2F_P)^2-4(1+\tau)(F_P)^2\right)\right] \quad (3.7)$$

$$B(Q^2) = 4\tau F_A(F_V^1+\xi F_V^2) \quad (3.8)$$

$$C(Q^2) = \frac{1}{4}\left(F_A^2+(F_V^1)^2+\tau(\xi F_V^2)^2\right) \quad (3.9)$$

where $\tau = Q^2/4M^2$, $\xi = (\mu_p/\nu_N - \mu_n/\mu_N) - 1$, $\mu_p(n)$ are the proton (neutron) magnetic moments, μ_N is the nuclear magneton.

By those form factors, the internal charge distribution of nucleons are described. As one of the simplest forms, an exponential distribution of charge density with respect to the nucleus radius,

$$\rho(r) = \rho(0)\exp(-Mr), \quad (3.10)$$

is transformed to a dipole form factor by the Fourier transformation:

$$F(Q^2) = \frac{F(0)}{(1-Q^2/M^2)^2}. \quad (3.11)$$

The electromagnetic form factors from nucleon currents, F_V^1 and F_V^2, are determined by electromagnetic scattering experiments, such as electron scattering measurements. Those form factors are expressed with the dipole forms, and consistent to the electro-magnetic measurements for the low Q^2 region ($Q^2 < 2.0$ GeV^2). This dipole form factors are represented as:

$$F_V^1(Q^2) = (1+\tau)^{-1}\left[G_E^V(Q^2)+\tau G_M^V(Q^2)\right], \quad (3.12)$$

$$F_V^2(Q^2) = (1+\tau)^{-1}\left[G_M^V(Q^2)-G_E^V(Q^2)\right], \quad (3.13)$$

using Sachs form factor[36]:

$$G_E(Q^2) = 1/\left(1+\frac{Q^2}{M_V^{QE}}\right)^2, \quad (3.14)$$

$$G_M(Q^2) = (1+\xi)/\left(1+\frac{Q^2}{M_V^{QE}}\right)^2, \quad (3.15)$$

where $M_V^{QE} \sim 0.84$ GeV/c^2 is experimentally determined. A discrepancy from the dipole form is observed at larger Q^2[37], hence the correction to those form factors

are parametrized in the BBBA05 form factors[38] in order to fit the experimental data.

The pseudoscaler form factor is written as:

$$F_P(Q^2) = \frac{2M^2}{Q^2 + M_\pi^2} F_A(Q^2) \tag{3.16}$$

using the following axial vector form factor. The axial vector part takes a dominant role in the neutrino-nucleon cross sections. It is usually parametrized with a dipole form:

$$F_A(Q^2) = \frac{F_A(0)}{(1 + Q^2/M_A^2)^2} \tag{3.17}$$

where the normalization, $F_A(0) = 1.2723 \pm 0.0023$ is determined by neutron β decay measurements[30]. The axial mass term, M_A^{QE}, is measured for a neutrino-deuterium scattering in bubble chamber experiments to be 1.026 ± 0.021 GeV[39]. However, a discrepancy of the fitted M_A^{QE} values has been observed in measurements with heavier nucleus. This has been well known as "MiniBooNE M_A puzzle", which is discussed in Sec. 3.5.1. It has also been pointed out that it is not necessary to assume the dipole form factor. In the neutrino interaction simulation, models implemented into neutrino interaction generators provide some tuning to the form factor, as described Sec. 3.4.1.

3.2.2 Resonant pion production

For neutrino energies above 400 or 500 MeV, a nucleon struck by a neutrino is able to be excited to a baryon resonant state, to decay into a final state with a single pion and a nucleon. Such a process is described as:

$$\nu_l + N \to N^* + l^- \to N' + l^- + \pi \tag{3.18}$$

where N, $N' = n$, p, and N^* is the resonant state. The possible resonant single pion reaction channels via ν_μ ($\overline{\nu}_\mu$) charged-current are:

$$\begin{aligned}
\nu_\mu p &\to \mu^- p \pi^+ && (3.19)\\
\nu_\mu n &\to \mu^- p \pi^0 && (3.20)\\
\nu_\mu n &\to \mu^- n \pi^+ && (3.21)\\
\overline{\nu}_\mu p &\to \mu^+ p \pi^- && (3.22)\\
\overline{\nu}_\mu p &\to \mu^+ n \pi^0 && (3.23)\\
\overline{\nu}_\mu n &\to \mu^+ n \pi^- && (3.24)
\end{aligned}$$

The resonant pion production is able to occur via neutral-current as well. Figure 3.5 shows the diagram for the process expressed in Eq. 3.19.

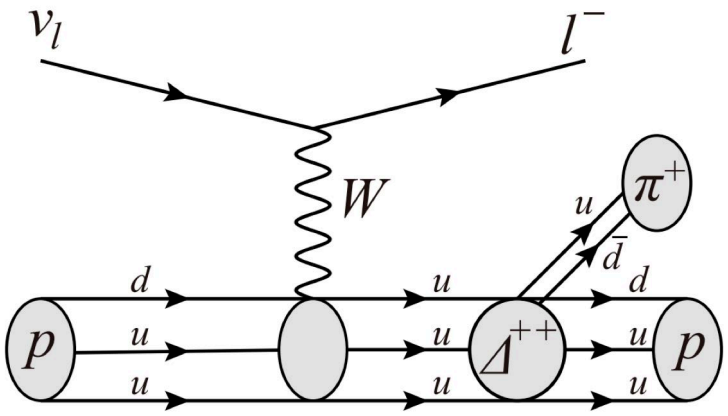

Figure 3.5: A diagram for CC resonant pion production, $\nu_\mu p \to \mu^- p \pi^+$.

Those processes are calculated in the framework of the Rein-Sehgal model[40]. It describes singl-pion productions by all interfering resonances below 2 GeV, based on the model of Feynman, Kislinger and Ravndal[41], supplemented with non-resonant background of isospin $\frac{1}{2}$. The calculation in the Rein-Sehgal model is similar to that in the Llewellyn-Smith model, and the four-momentum conservation term is replaced by a factor corresponding to excitation of bayron resonance, which is described by the Breit-Wigner distribution[42]. The vector form factors to express the hadronic part are fixed from pion electro-production data. On the other hand, the axial form factors are determined by assuming partially conserved axial current[43], and not well constrained by electron scattering data. The axial form factor has the dominant contribution to the cross section:

$$\frac{\mathrm{d}\sigma}{\mathrm{d}q^2} \simeq \frac{G_F^2 \cos\theta_c}{12\pi} \frac{s - m_\Delta^2}{s - m_N^2} \left(\frac{m_\Delta + m_N}{m_\Delta} \right)^2 |C_5^A(q^2)|^2 \tag{3.25}$$

where m_Δ is the mass of Δ and m_N is the mass of a nucleon. One of the axis form factor, C_5^A, is mainly parametrized by the axial-vector mass, M_A^{Res}, and its normalization, $C_5^A(0)$.

3.2.3 Deep inelastic scattering

Deep inelastic scattering (DIS) occurs at even higher neutrino energies, where neutrinos are able to directly interact with quarks inside a nucleon via the weak bosons. It typically results in breaking the nucleon and producing a jet of hadrons, as shown in Fig 3.6. The energy range where the DIS interactions dominantly contribute is around 10 GeV or more, so that it is less significant in the sub-GeV neutrino energy range compared with the quasi-elastic and pion production.

However, it still has small contribution by an interaction with a small invariant mass of the hadronic system in the final state. For instance, a process leaves at least two pions on top of the outgoing baryons, which is known as "multi-pion" process. The DIS interactions are understood by a number of data at a neutrino energy more than 10 GeV, and models such as PYTHIA[44] are well established in such a high energy region. However, an extrapolation toward the lower energy region is needed, and only few measurements are available[45][46]. The agreements between data and models are in a level of 10% accuracy.

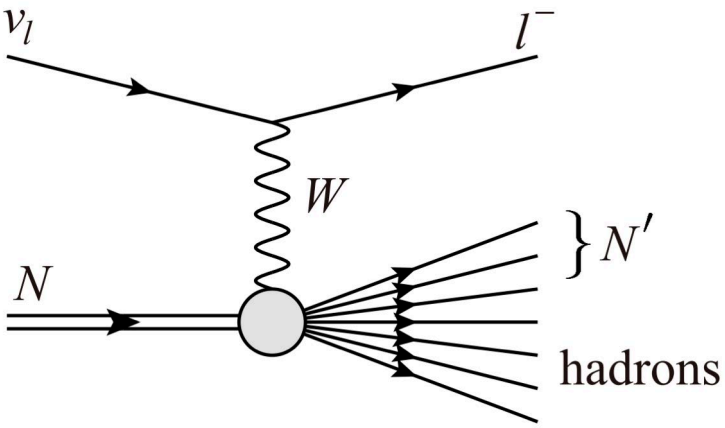

Figure 3.6: A diagram for CC DIS.

3.3 Neutrino-nucleus interactions

The neutrino-nucleon scattering was discussed in Sec. 3.2, assuming a free nucleon. In the case of heavy nucleus targets, however, this assumption is only reliable in the case of a momentum transfer more than 300 MeV[47]. In the lower momentum transfer cases, the initial state of nucleons needs to be considered so that a distribution of nucleon momentum is corrected. In addition, the impact from the dense nuclear medium around the initial nucleon should affect the scattering process. Furthermore, the final state particles produced by the initial interaction are interfered by other nucleons before leaving the nucleus.

It should be noted that the nuclear models adopted in the neutrino interaction models are often out-of-date, but they have been partially understood with the previous measurements and remain to be improved.

3.3.1 Initial state effects

The initial state motion of nucleons inside the nucleus affects any neutrino interactions on a nucleon. However, it is not possible to exactly describe it due to a complicated structure of nucleus, it is usually expressed by using a spectral function, which attempts to collectively model the nucleon momentum distribution. Three different models, the global relativistic Fermi gas model (RFG)[48], the local Fermi gas model (LFG)[49] [50], and the spectral function model from Omar Benhar (SF)[51], are shown in Fig. 3.7.

In the RFG model, all nucleons inside the nucleus are considered as interaction-free fermions, and uniformly distributed in the momentum states from its ground state up to the highest momentum, which is known as the Fermi momentum (p_F). The Fermi momentum is determined according to the number of nucleons in the nucleus, and the typical values are 217 MeV/c for ^{12}C, and 225 MeV for ^{16}O. The nucleon removal energies (E_b) are typically 25 MeV for ^{12}C, and 27 MeV for ^{16}O. Those values of p_F and E_b are determined from electron scattering data. Since the model assumes all nucleons are fermions which occupy all of the states with momentum less than p_F, momentum of the final state protons or neutrons is required to be larger than p_F.

In the RFG model, the density of the nuclear matter is assumed to be constant, while it does not describe the real nucleus. The LFG model, as an extension from the RFG model, is built to set the density of the nuclear matter to depend on the radial position in the nucleus and to modify the momentum distribution.

The SF model describes the nucleon distribution in the nucleus based on the two-dimensional distribution of the nucleon momentum and nucleon removal energy, which is obtained by the local density approximation[52]. This model includes short range correlations between the initial nucleons, which increases neutrino-nucleon interactions at the high momentum tail.

In the nominal simulation in this analysis, the RFG model is implemented, with the correction from correlation in the nuclear medium, as described in Sec. 3.3.2.

3.3.2 Correlation in the nuclear medium

It has been known from experimental data, such as MiniBooNE puzzle, that neutrino-nucleus interactions should be corrected to include scattering off a bound state of multiple nucleons inside the nucleus. Models describing the multi-nucleon interactions is provided by Nieves[50] and Martini[54]. Those models consider the short range correlations between nucleons, which is characterized by n particles - n holes excitation (np-nh). In this expression, the CCQE interaction is described as 1p-1h. It also includes neutrino interactions with correlated nucleons, such as 2p-2h interactions. The meson exchange current (MEC) is the dominant process for

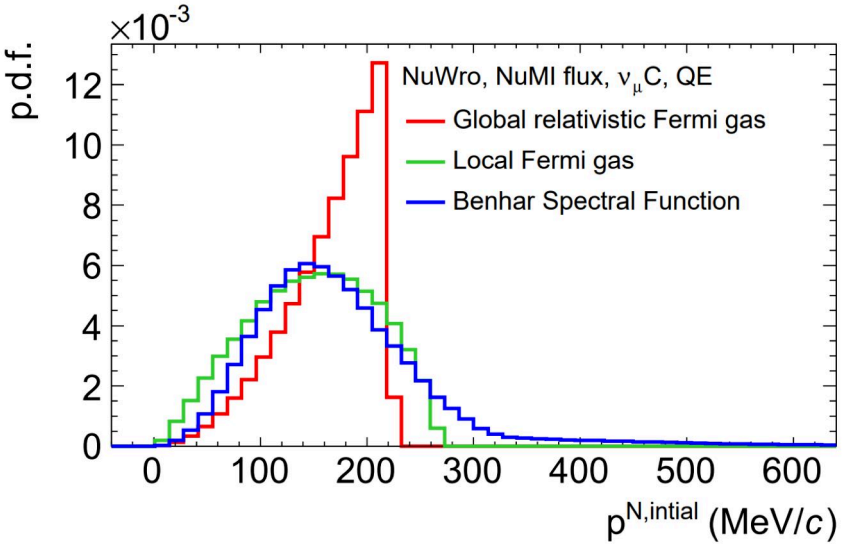

Figure 3.7: Distributions of nucleon momentum with RFG, LFG, and Benhar spectral function (SF). This figure is adapted from [53].

the 2p-2h interaction. The 2p-2h interaction has two nucleons in its final state, but it is possibly absorbed before leaving the nucleus so that it may contribute to be an indistinguishable background event to the CCQE interaction. Figure 3.8 shows the diagrams of 2p-2h interactions, including the MEC process and nucleon-nucleon correlations (NN).

The long range correlations between nucleons inside the nucleus should also be considered. The random phase approximation [57] (RPA) is commonly used to estimate such effects. Collective screening effects on the electroweak propagator due to interactions and correlations between nucleons are estimated according to pion nucleus scattering data, so that it results in the overall neutrino-nucleus interactions corrected as a function of Q^2. The RPA correction factor is seen in Fig. 3.9.

It is seen in Fig. 3.10 that those multi-nucleon mechanisms are essential. The interaction model with the LFG spectral function with the 2p-2h interaction and the RPA correction agrees with the MiniBooNE data, as keeping the M_A^{QE} values compatible to those from bubble chamber experiments.

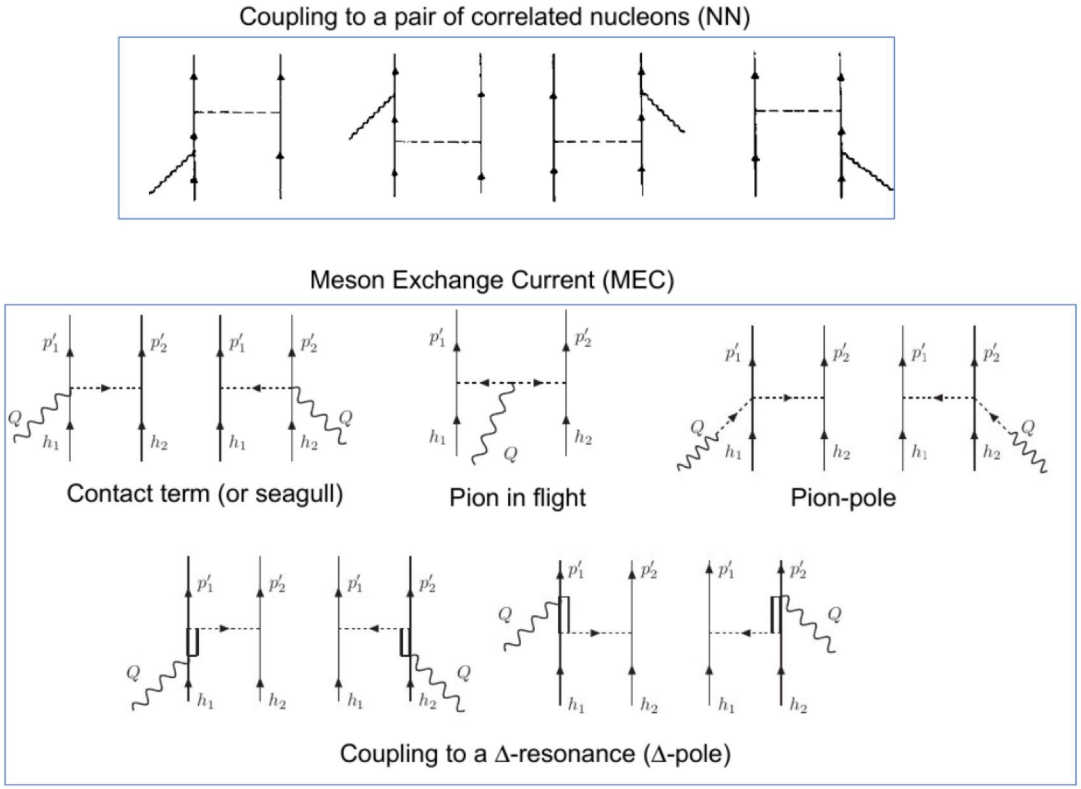

Figure 3.8: Diagrams for the 2p-2h interactions. Single lines are nucleons, double lines are Δ, dashed lines are π, and curly lines are W. This figure is adapted from [55] [56].

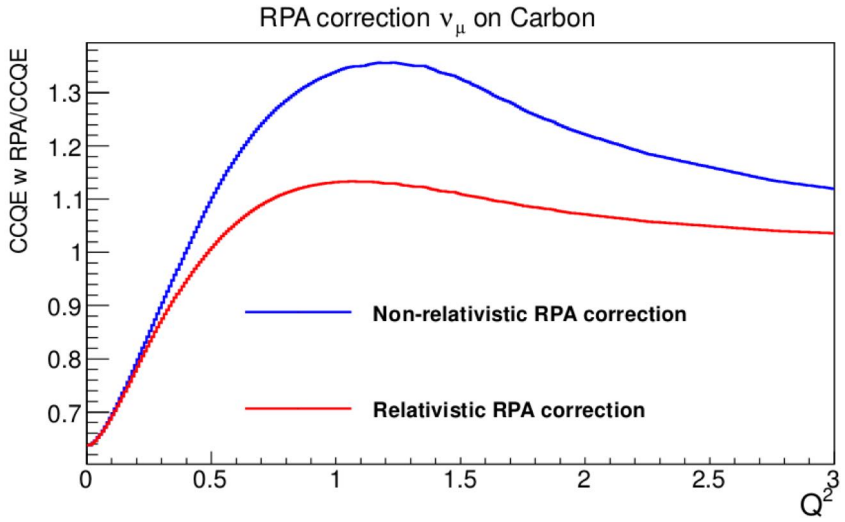

Figure 3.9: Ratio of differential CCQE cross section of ν_μ-^{12}Cwith the RPA correction to nominal CCQE cross section. In blue is Nieves' non-relativistic RPA model and in red is Nieves' relativistic RPA model.

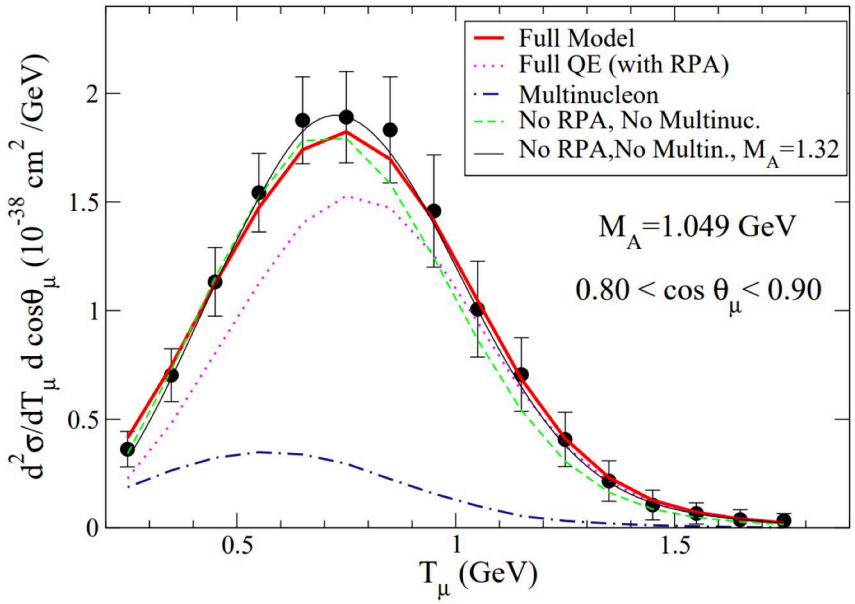

Figure 3.10: ν_μ-^{12}C double differential cross section as a function of the muon kinematic energy and for the $0.80 < \cos\theta_\mu < 0.90$ angular bin. This figure is adapted from [58].

3.3.3 Final state interactions

The final state particles produced at a neutrino interaction vertex are transported inside the nucleus, and re-interact inside the nuclear medium. Those particles are possible to be absorbed, to have their kinematics distorted, and to eject additional hadrons. Those interactions are called the final state interactions (FSI) and significantly perturb the overall cross sections.

The FSI is modeled by using a intra-nuclear cascade model in most of the neutrino interaction generators, where particles from their creation are propagated in a finite step within the nuclear medium. Every step, the probability of interactions, such as quasi-elastic, charge exchange, and absorption, is calculated based on the local density of the nuclear matter. The pion interactions in the case of low momentum ($p_\pi < 500$ MeV/c) are computed according to the Oset model[59], while interactions of higher momentum pions ($p_\pi > 500$ MeV/c) are calculated from $\pi^\pm$ scattering off free proton and deuteron cross section data[60]. The calculation is continued until each particle leaves the nucleus.

3.4 Event generator of neutrino interaction

3.4.1 NEUT

NEUT[61] is a simulation program library which is usually used as the nominal neutrino interaction generator in the T2K analysis. This covers a neutrino energy range from 100 MeV to 100 TeV, to simulate the following interactions :

- charged/neutral-current quasi-elastic scattering : $\nu\ N \to l\ N'$
- charged/neutral-current single π production : $\nu\ N \to l\ N'\ \pi$
- charged/neutral-current single K production : $\nu\ N \to l\ \Lambda\ K$
- charged/neutral-current single η production : $\nu\ N \to l\ N'\ \eta$
- charged/neutral-current single γ production : $\nu\ N \to l\ N'\ \gamma$
- charged/neutral-current deep inelastic scattering : $\nu\ N \to l\ N'$ hadrons
- charged/neutral-current coherent π production : $\nu\ \to l\ \pi\ X$
- 2p-2h interaction : $\nu\ N\ N' \to l\ N''\ N'''$

where l is a lepton, Ns represent a nucleon, and A and X represent a nuclei. Figure 3.11 shows the cross sections calculated with NEUT. Total charged-current

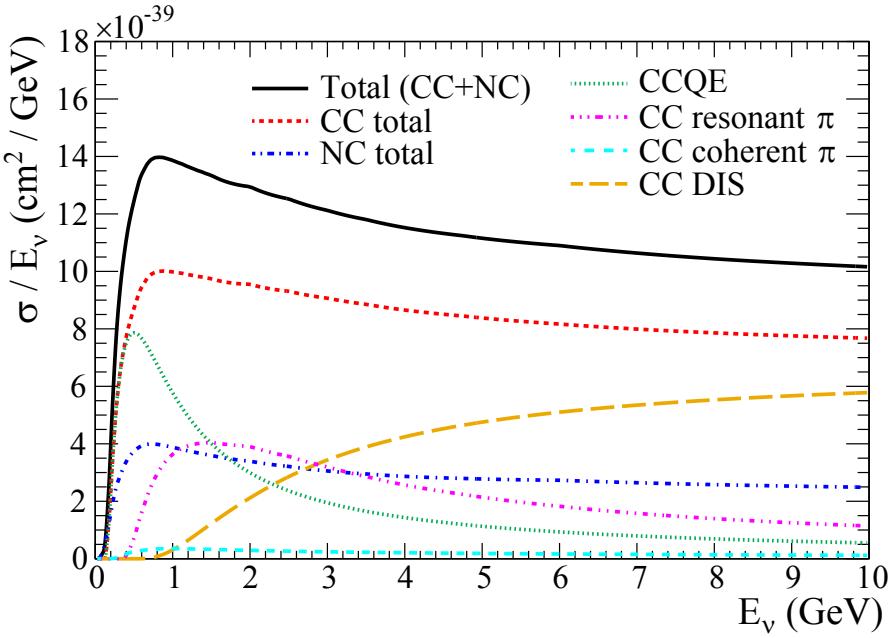

Figure 3.11: Neutrino-nucleus cross sections per nucleon computed in NEUT. Extracted from [62].

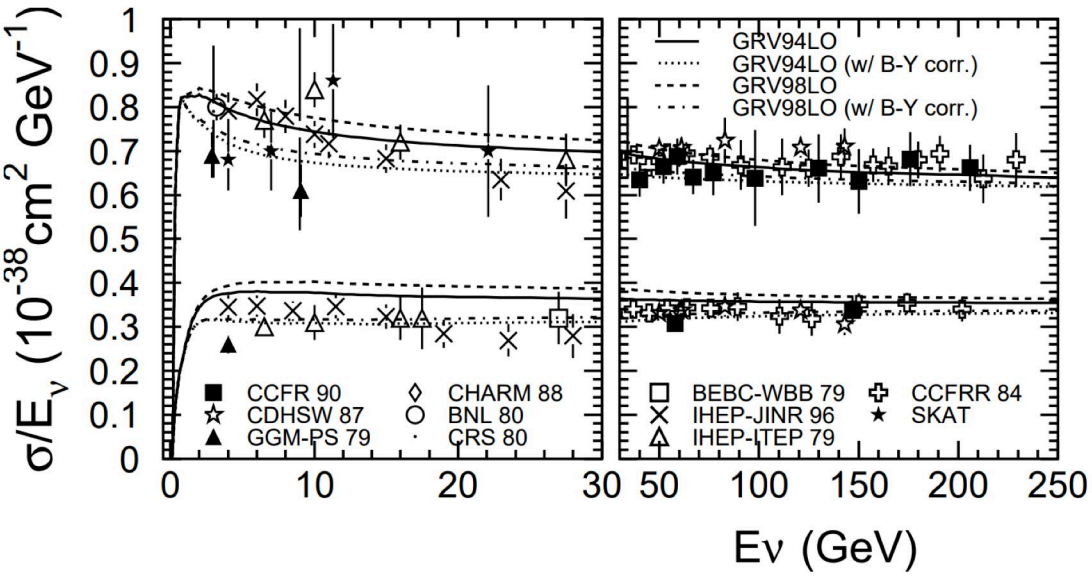

Figure 3.12: Comparison of the cross sections for charged current total cross sections between the NEUT calculation and experimental data. Taken from [61].

cross sections including quasi-elastic scattering, single meson productions and deep inelastic scattering are shown in Fig. 3.12.

The CCQE cross section is calculated based on the Llewellyn-Smith model, with a correction by using the BBBA05 form factors. The nuclear model assumes the RFG spectral function, with a relativistic RPA correction. The main parameters for this model is M_A^{QE}, p_F and E_b, and they are constrained based on measurements with the T2K near detector. Figure 3.13 shows the comparison of the CCQE cross sections between the NEUT calculation and the previous experimental data.

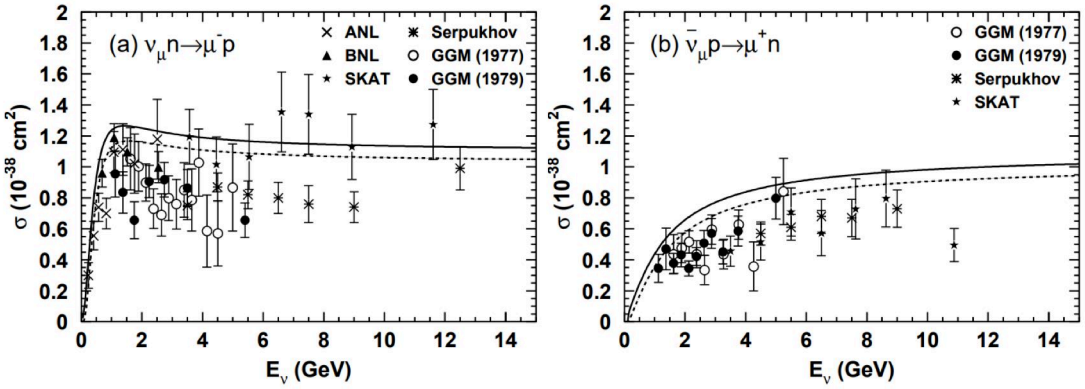

Figure 3.13: Comparison of the CCQE cross sections on a nucleon between the NEUT calculation and experimental data. The solid lines show the calculated cross sections for free targets and the dashed line shows those for targets bound in a nucleus, respectively. Taken from [61].

2p-2h is implemented with the Nieves model, and is composed of the MEC process, the NN process, and their interference. Since understanding of the 2p-2h interactions by experiments is poor, 100% uncertainty is assigned on the overall normalization. As an additional degree of freedom on 2p-2h, the "2p-2h shape" is controlled according to distribution of bias on the neutrino energy reconstruction. The "Δ-like" term, which is in the reference to the process intermediated via a virtual Δ exchange, leaves the largest bias among the 2p-2h interactions. When the uncertainty due to the 2p-2h interactions is estimated, the distribution is altered between non-Δ-like terms only and Δ-like term only.

Single pion resonant production is calculated by the Rein-Sehgal model, with a correction using the Graczyk-Sobczyk form factors. The parameters of this model, such as M_A^{Res}, C_A^5, and non-resonant background events from isospin 1/2, are constrained by fitting data from the bubble chamber experiments and MiniBooNE, with a level of 15% accuracy. This model also describes the production of K, η, and γ by changing the decays of the resonances. Figure 3.14 show the comparison

between the NEUT calculation and data.

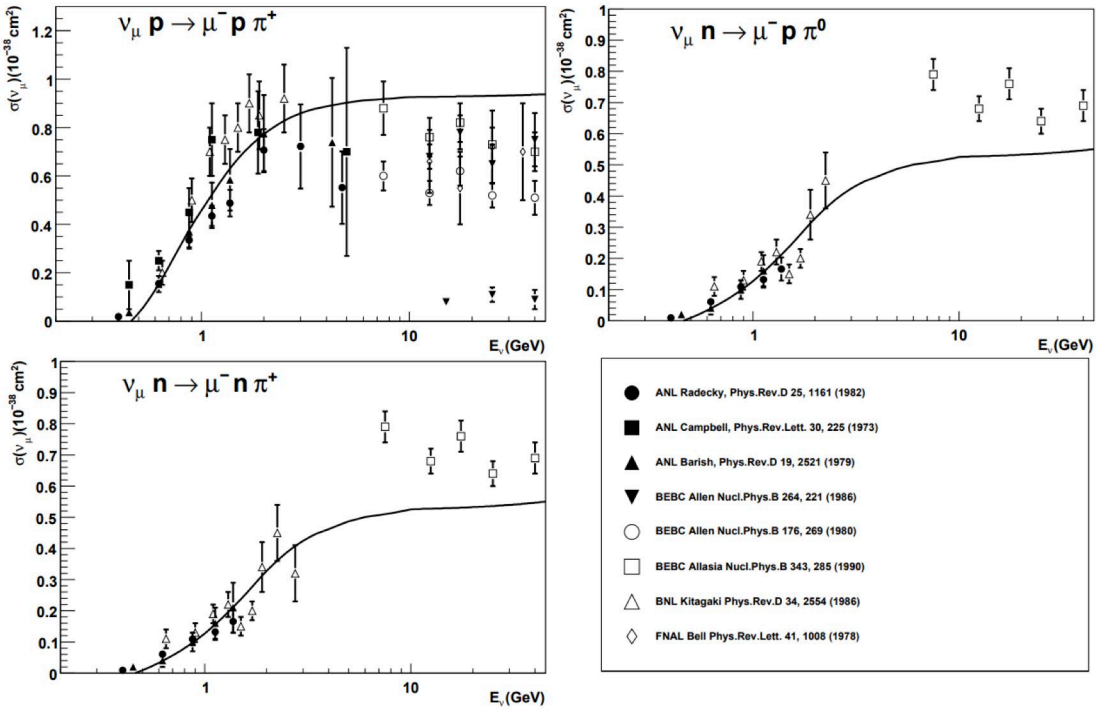

Figure 3.14: Comparison of the cross sections for CC single pion production between the NEUT calculation and experimental data. Taken from [61].

Coherent pion productions are implemented with the Berger-Sehgal model. According to a comparison to the MINERνA data[63], the uncertainty on its normalization is set to be 30%. However, 100% uncertainty is assigned in this analysis in order to be conservative.

The DIS cross section is calculated in the range of $W > 1.3$ GeV, where W is the invariant mass of the hadronic system. It is generated by an external library, PYTHIA[44], which is well developed based on the many of the experimental data in a high energy region, $W > 2.0$ GeV. The necessary input for the cross section calculation is the parton distribution function, and NEUT uses GRV98[64] with modifications by Bodek and Yang[65]. In a low energy region, the uncertainty on the Bodek-Yang corrections become large due to few inputs from experimental data. When the uncertainty due to the DIS interactions is estimated, the scaling factor, $1 + x/E_\nu$ (GeV), has the parameter x altered from the nominal $x = 0$ to $x = 0.4$.

3.4.2 Summary of neutrino interaction generators

There are many neutrino generators other than NUET, such as GENIE[66], NUANCE[67], NUGEN(ANIS)[68], GiBUU[69], and NuWro[70]. In this analysis, another version of NEUT using some different models and GENIE are used for validation of the cross section extraction, discussed in Sec. 8. Table 3.1 summarizes the models adapted in each generator among two different versions of NEUT and GENIE.

Table 3.1: Summary of three different neutrino generators.

	NEUT (nominal)	NEUT (updated)	GENIE
CCQE	RFG	LFG	BE-RFG[71]
	Llewellyn-Smith with rel. RPA	Nieve 1p1h with rel. RPA	-
	BBBA05	BBBA05	BBBA05
	$M_A^{QE} = 1.15$ GeV/c^2	$M_A^{QE} = 1.21$ GeV/c^2	$M_A^{QE} = 0.99$ GeV/c^2
2p2h	Nieves *et al.*[50]		-
FSI	Intra-nuclear cascade		Intra-nuclear cascade (INTRANUKE / hA)[72]

The main parameters of NEUT are summarized in Table 3.2. For some parameters related to the nuclear structure, there are correlations between ^{12}C and ^{16}O in NEUT. In this analysis, however, no correlation is assumed for p_F, E_b, 2p-2h, and CC coherent in order to be conservative for the cross section ratio measurement between these two nucleus.

Table 3.2: Summary of the nominal values of the used parameters of neutrino interaction model and their uncertainties

Parameter	Nominal value	Uncertainties (1σ)
CCQE: the Llewellyn-Smith model		
RFG with the RPA correction		
M_A^{QE}	1.15 GeV	0.18 GeV
P_f ^{12}C	223 MeV	31 MeV
P_f ^{16}O	225 MeV	31 MeV
E_b ^{12}C	25 MeV	9 MeV
E_b ^{16}O	27 MeV	9 MeV
2p2h		
2p2h normalization ^{12}C	—	100 %
2p2h normalization ^{16}O	—	100 %
2p2h shape ^{12}C	—	100 %
2p2h shape ^{16}O	—	100 %
CC1π model: the Rein-Sehgal model		
M_A^{Res}	0.95 GeV	0.15 GeV
C_{A5}	1.01	0.12
Isospin $\frac{1}{2}$ bg	1.30	0.20
CC coherent model: the Barbar-Sehgal model		
CCcoh normalization ^{12}C	—	100 %
CCcoh normalization ^{16}O	—	100 %
DIS		
DIS correction factor	$x = 0$	$x = 0.40$
NC interactions		
NCcoh norm	—	30 %
NCother norm	—	30 %
Secondary interaction of pions		
Pion Absorption normalization	—	50 %
Pion Charge Exchange (low E) normalization	—	50 %
Pion Charge Exchange (high E) normalization	—	30 %
Pion Quasi Elastic (low E) normalization	—	50 %
Pion Quasi Elastic (high E) normalization	—	30 %
Pion Inelastic normalization	—	50 %
Final state interactions of nucleons		
Nucleon FSI	—	100 %

3.5 Status of the current neutrino cross section measurements

Historically, neutrino cross sections have been measured in a various neutrino energy range with different nucleus targets. Especially for the charged-current interactions, there are many experimental data available as shown in Fig. 3.15. It is seen that measured cross sections linearly increase as a function of neutrino energy in a region of the high neutrino energy where it is dominated by the DIS interactions, as it is assumed in interaction models discussed in Sec. 3. However, deviation from the linear relation is observed at a low neutrino energy. In such an energy region, the nuclear effect, as discussed in Sec. 3.3, makes it complicated to estimate the overall cross sections, except for the case of using very light nucleus such as hydrogen and deuteron. However, many of the accelerator-based neutrino oscillation measurements use such a region of neutrino energy from sub-GeV to few GeV, as summarized in Table 3.3, and suffer from the uncertainty due to the poor understanding of the neutrino cross section. Since the CCQE interaction gives the dominant contributions in this energy range, it is important to measure the CCQE, or CCQE-like, interaction with various nucleus targets. In addition, there are only few experiments available for the $\overline{\nu}_\mu$ interactions for this energy region.

Table 3.3: Accelerator-based neutrino experiments at present. Table is adapted from [30].

Experiment	Beam	Mean neutrino energy [GeV]	Neutrion target	Run period
ArgoNeuT	ν, $\overline{\nu}$	4.3, 3.6	Ar	2009-2010
ICARUS (at CNGS)	ν	20.0	Ar	2010-2012
K2K	ν	1.3	CH, H2O	1999-2004
MicroBooNE	ν	0.8	Ar	2015-
MINERvA	ν, $\overline{\nu}$	3.5/5.5	He, C, CH, H2O, Fe, Pb	2009-
MiniBooNE	ν, $\overline{\nu}$	0.8, 0.7	CH2	2002-2012
MINOS	ν, $\overline{\nu}$	3.5, 6.1	Fe	2004-2016
NOMAD	ν, $\overline{\nu}$	23.4, 19.7	C–based	1995-1998
NOvA	ν, $\overline{\nu}$	2.0, 2.0	CH2	2010-
SciBooNE	ν, $\overline{\nu}$	0.8, 0.7	CH	2007-2008
T2K	ν, $\overline{\nu}$	0.6, 0.6	CH, H2O, Fe	2010-

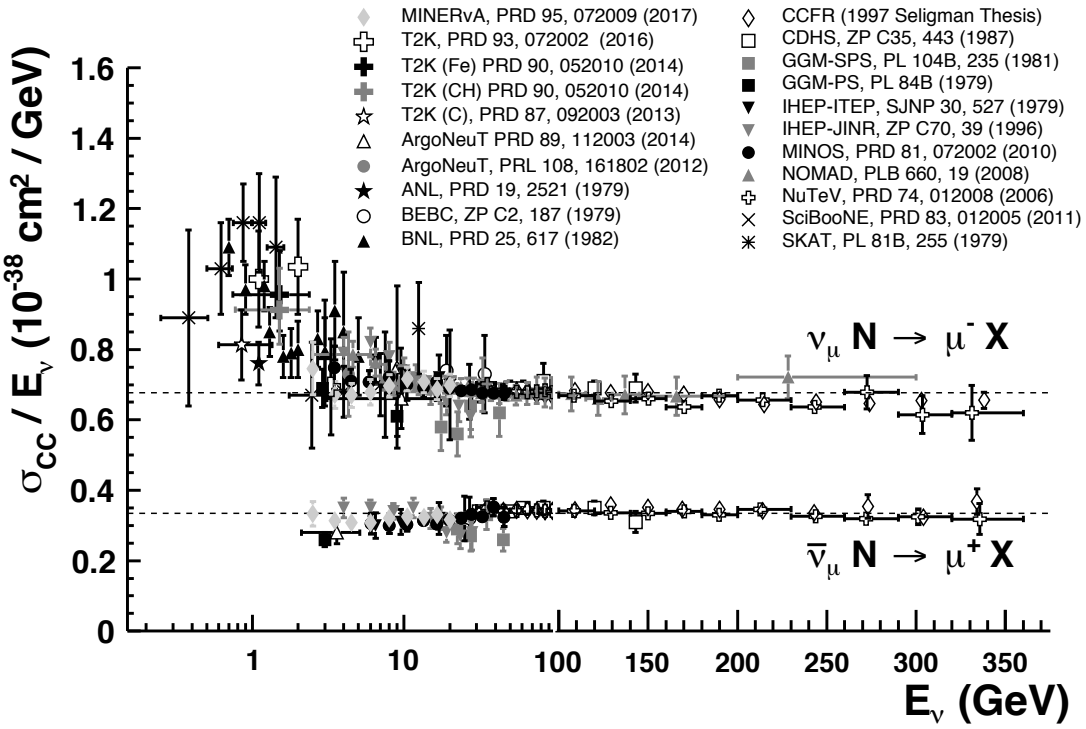

Figure 3.15: Measurements of ν_μ and $\overline{\nu}_\mu$ CC inclusive cross sections as a function of neutrino energy. This figure is adapted from [30].

3.5.1 Previous measurements of CCQE interactions

The early measurements of the CCQE cross sections started with bubble chamber experiments in 1970s and 1980s[73] [74] [75] [76] [77], using hydrogen and deuteron targets. Those measurements do not significantly suffer from nuclear effect, and it is also possible to detect both of a muon and a nucleon in the final state. The results show a good agreement with the neutrino interaction model described in Sec. 3.2.1, with a value of $M_A^{QE} \sim 1.0$ GeV.

The modern experiments, using the heavy nuclear targets, have released the CCQE cross section measurements, such as MiniBooNE[78] and NOMAD[79] using a carbon target, and K2K[80] using a water target. However, it has been observed that the CCQE prediction with free nucleons does not fully describe all of those data. For example, as shown in Fig. 3.16, the MiniBooNE data around $E_\nu \sim 1.0$ GeV have an apparent discrepancy from the prediction with $M_A^{QE} = 1.0$ GeV. This is know as the MiniBooNE puzzle.

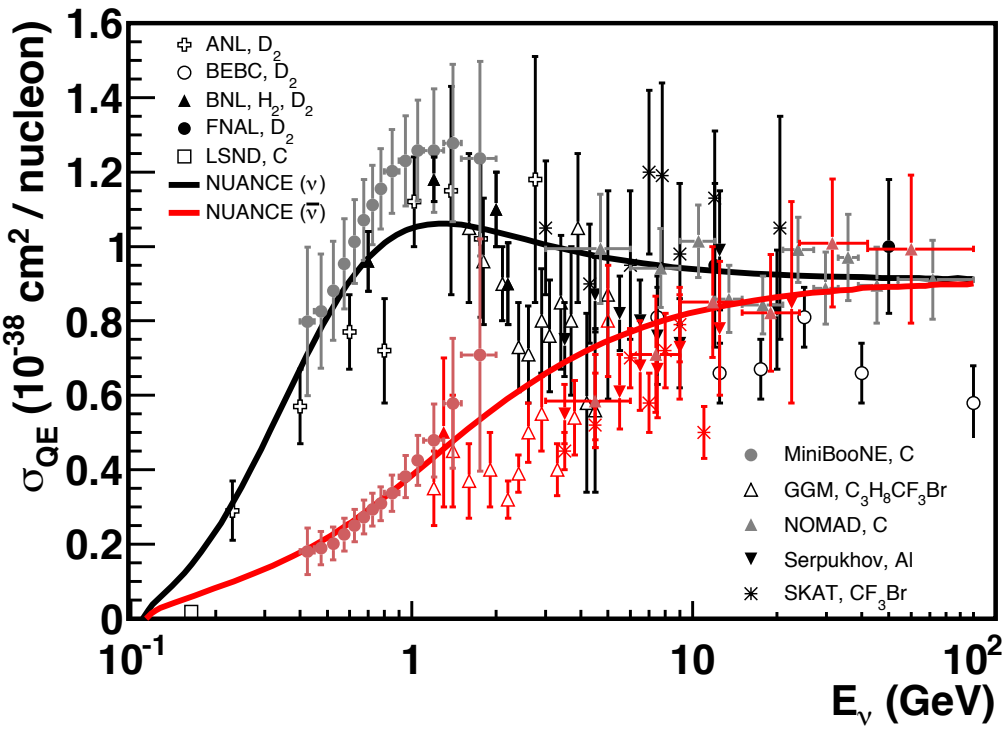

Figure 3.16: Measurements of ν_μ (black) and $\overline{\nu}_\mu$ (red) CCQE scattering cross sections per nucleon as a function of neutrino energy. Data are shown with a various targets. A CCQE prediction with free nucleon from NUANCE[67] assuming $M_A^{QE} = 1.0$ GeV is shown together. Figure is adapted from [81].

In the more recent measurements, importance of including the effects from multi-nucleon interaction and correlation in the nuclear medium has been understood as discussed in Sec. 3.3. Some experiments, such as MiniBooNE[82], MINERνA[83][84], and T2K[85], show the agreement with the model including those nuclear effects without largely shifting the value of M_A^{QE} from the bubble chamber measurement. In order to accurately measure the CCQE interaction considering the nuclear effects, it has been desired to measure kinematics of both of a muon and a nucleon in the final state, and to measure the cross sections in wide range of neutrino energy with various nucleus. However, the detectors in reality are not sensitive to the whole phase space of the nucleon kinematics. In addition, any experiments suffer from a bias on the correction from the nuclear effects to access the target signal with a variable which is not directly accessible from the detector. For those reasons, the current experiments moved to measurements of the cross section for the signal defined based on kinematics of the final state muon and hadrons, which is known as the topology-based cross section, rather than the pure neutrino interaction measurements.

3.5.2 Recent CCQE-like cross section measurements

Recent experiments have started to report the cross section for the charged-current interactions with no pions in the final state, that is CC0π, rather than the CCQE cross sections. Such measurements make it more difficult to directly compare the results between different experiments, but are less model-dependent and provide better samples for testing the models. MiniBooNE[78][82] and T2K[86] released the double-differential cross sections, $\mathrm{d}\sigma/\mathrm{d}T_\mu\mathrm{d}\theta_\mu$, on the carbon target. One of the results from the T2K data is shown in Fig. 3.17. The results are compared with both the Nieves model[87] and the Martini model[88], for both cases of including and removing 2p-2h interactions. Those models include the RPA correction. The result shows an agreement with the model including the correction from the nuclear effects and 2p-2h contribution. However, it is not able to conclude the best model of nuclear effects and 2p-2h interactions with the current uncertainty level.

3.5.3 Current understanding of the neutrino-nucleus interactions

The present neutrino interaction models have attempted to describe the nuclear effect by using electron scattering experiments. However, information from the present experimental data for neutrino interactions is limited, and further investigation is needed to understand the nuclear models. For example, nuclear models for the initial state nucleon are not determined. In the simulation currently used

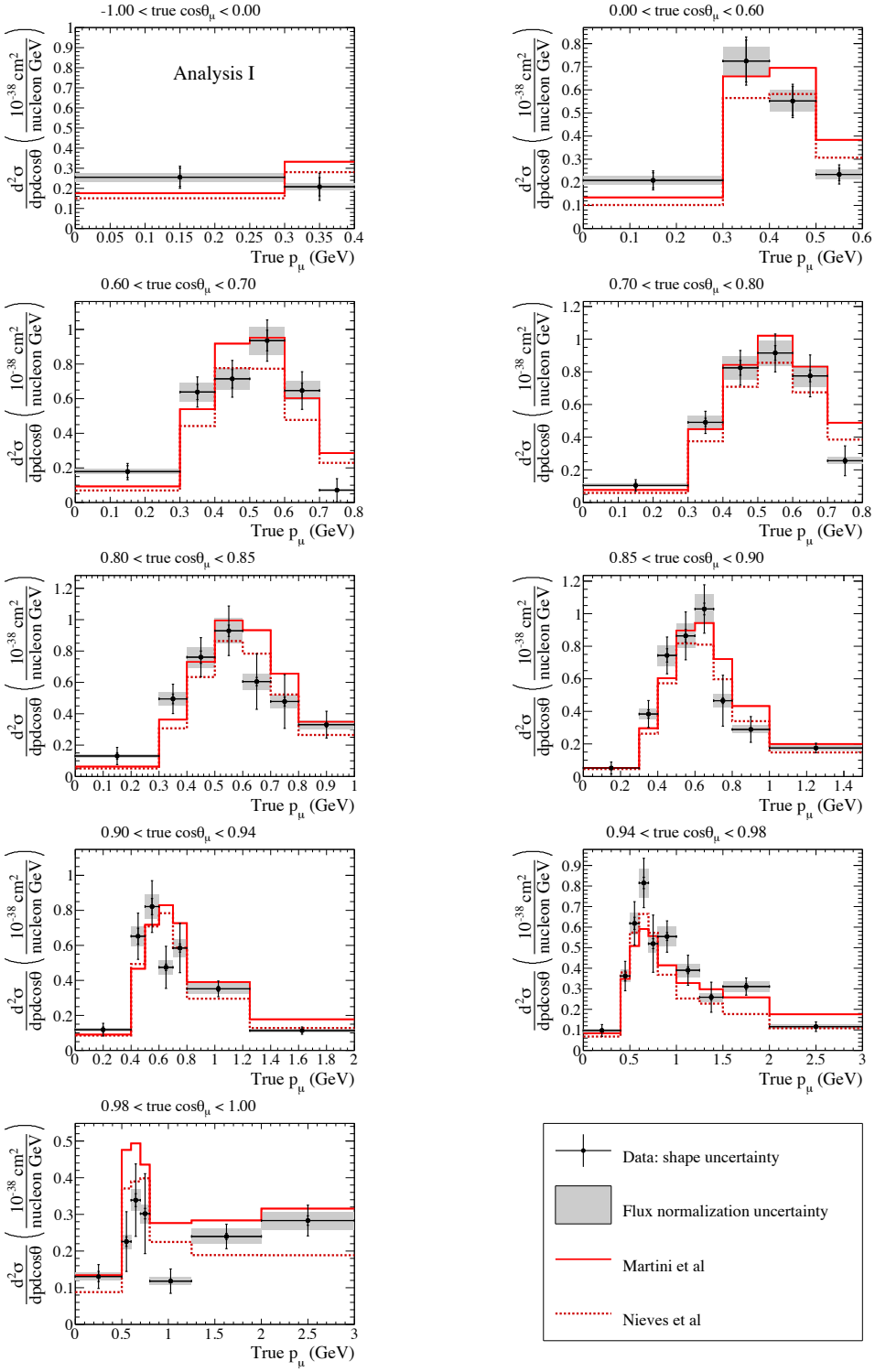

Figure 3.17: CC0π cross sections measured in T2K[86]. The results are compared with the Nieves model and the Martini model.

in T2K, NEUT, RFG with the RPA correction is adopted as the nuclear model, as described in Sec. 3.4. RFG is the simplest model of the nuclear matter, and it is sufficient to explain the present experimental data within their uncertainties. In reality, however, the nuclear medium density should be dependent on the position inside the nucleus. LFG, for example, adopts the position-dependent density, and the next version of NEUT will adopt LFG. Since it is not possible to determine a nuclear model by the current data, more input with a better precision is required.

In addition, correlations between different nuclei and between neutrino and anti-neutrino need to be understood. The parameters for the nuclear model, such as the Fermi momentum (p_f) and nucleon removal energy (E_b), are currently defined to be common between carbon and oxygen and between neutrino and anti-neutrino with no correlations. In reality, those should not be identical but correlated to each other. However, it is difficult to estimate the correlation with the present experimental data of neutrino-nucleus interactions. Hence it is important to measure the relations between carbon and oxygen targets for both neutrino and anti-neutrino interactions.

Among the nuclear effects, multi-nucleon correlations have non-negligible contribution on the CCQE signal with a 10 to 20% level. The 2p-2h interaction is one of the models to describe the multi-nucleon effects. This interaction model has been established by using electron scattering data and extrapolated to neutrino interactions. Since no direct measurements for neutrino are available so far, the normalization of 2p-2h largely depends on models and can differ by up to a factor of two. In addition, different models predict largely different contributions of the 2p-2h interaction depending on neutrino and anti-neutrino. It is very challenging to measure the final state protons for more information about the 2p-2h interactions, as it requires a good control of the other nuclear effects. At present, it is important to precisely measure the neutrino and anti-neutrino interactions with various nuclear targets to constrain the entire nuclear effect as much as possible.

3.6 Motivation of this analysis

In the neutrino oscillation analysis using a muon neutrino beam with sub-GeV neutrino energy region, the main signal for neutrino detection is CCQE:

$$\nu_\mu + n \rightarrow \mu^- + p \tag{3.26}$$
$$\overline{\nu}_\mu + p \rightarrow \mu^+ + n \tag{3.27}$$

where a neutrino interacts with a nucleon. For the calculation of neutrino oscillation probabilities, it is important to extract incoming neutrino energy. In order to access the signal events, it is indispensable to estimate indistinguishable background events, where good understanding of neutrino interaction including

the nuclear effects is desired. In addition, the nuclear models considering differences of nuclear types are required to constrain the flux uncertainty at the far detector by using measurements at the near detector, which often has a different neutrino target from the far detector. For the purpose to achieve the improved neutrino interaction models, the cross section measurements with much less model-dependence are attempted. Recent measurements define the signal not by the pure neutrino interaction such as CCQE, but by kinematic topologies of the final state particles, in order to have signal events directly accessible from detectors. In the case of anti-muon-neutrino CCQE, for instance, the final state typically has a muon with no pions and no protons, which is defined as CC0π0p.

As discussed in Sec. 2.3.2, the reduction of the systematic uncertainties in the neutrino oscillation analysis is desired for the future experiments. In order to achieve the required level, the uncertainties due to poor understanding of nuclear effects on neutrino-nucleus interactions need to be reduced. In order to improve the understanding of the nuclear models, measurements with various nuclear targets are required. For the T2K experiment, modeling the difference between ^{16}O and ^{12}C needs to be improved for the better constraint on the neutrino oscillation analysis. Among the recent topology-based cross section measurements using the near detector, there are only few measurements available on the water (^{16}O) target. T2K has reported the cross section measurements, such as ν_μ charged-current interactions with a final state pion (CC1π) by FGD2[89], ν_μ and $\overline{\nu}_\mu$ CC inclusive by P0D[90], and ν_μ CC0π by P0D[85]. However, all of them suffer from large uncertainty from the neutrino beam prediction. A method to suppress this uncertainty by using the same neutrino beam between different detectors and measuring the cross section ratio has been established. There are few measurements which report the cross section ratio measurement with various nucleus from T2K[62] and from MINERνA[84], although they do not release the topology-based cross section but the CCQE cross sections.

In this thesis, the CC0π0p cross sections on water (H_2O) and hydrocarbon (CH) are reported, with the cross section ratio between the two targets, using the anti-neutrino beam with the sub-GeV neutrino energy. It is the first measurement of the $\overline{\nu}_\mu$ cross section ratio related to ^{12}C and ^{16}O in this neutrino energy range. In addition the differential cross sections as a function of scattered muon's angle are presented. The results provide constraints on neutrino interaction models by being compared with their predictions including the nuclear effects.

Chapter 4

Experimental apparatus

4.1 The J-PARC accelerator

The Japan Proton Accelerator Research Complex (J-PARC) accelerator, as shown in Fig. 4.1, is composed of three parts: a linear accelerator (LINAC), a rapid-cycling synchrotron (RCS), and a main ring synchrotron (MR). At LINAC, H^- ions from an ion source are accelerated up to 400 MeV and pass through a thin carbon foil to be converted into protons by stripping two electrons. RCS accelerates protons from LINAC to 3 GeV with 25 Hz cycle. Each cycle consists of two bunches, and four cycles out of 62 are extracted to MR and the rest is to the Material and Life Science (MLF). MR has the 1567 m circumference, and is capable of producing eight proton bunches with about 100-ns width and separated by 581 ns. Protons are accelerated to 30 GeV. They are directed to the neutrino beamline by the fast extraction with the repetition period of 2.48 s. In the case of the hadron beamline, the operation mode is changed to the slow extraction.

4.2 The T2K neutrino beamline

The Tokai to Kamioka (T2K) experiment[91] is a long-baseline neutrino oscillation experiment with the neutrino beamline in J-PARC. The overview of the T2K experiment is shown in Fig 4.2. It has achieved an observation of a neutrino oscillation by measuring the neutrino beam with two different detectors, one of which is a near detector (ND280) located at 280 m downstream from the beam target and a far detector known as Super-Kamiokande (SK) at 295 km downstream. Two modes of neutrino oscillation, electron neutrino appearance and muon neutrino disappearance, have been studied, and the oscillation parameters, θ_{13}, θ_{23}, and $|\Delta m^2_{32}|$, have been measured.

The T2K neutrino beamline is composed of two parts: the primary beamline

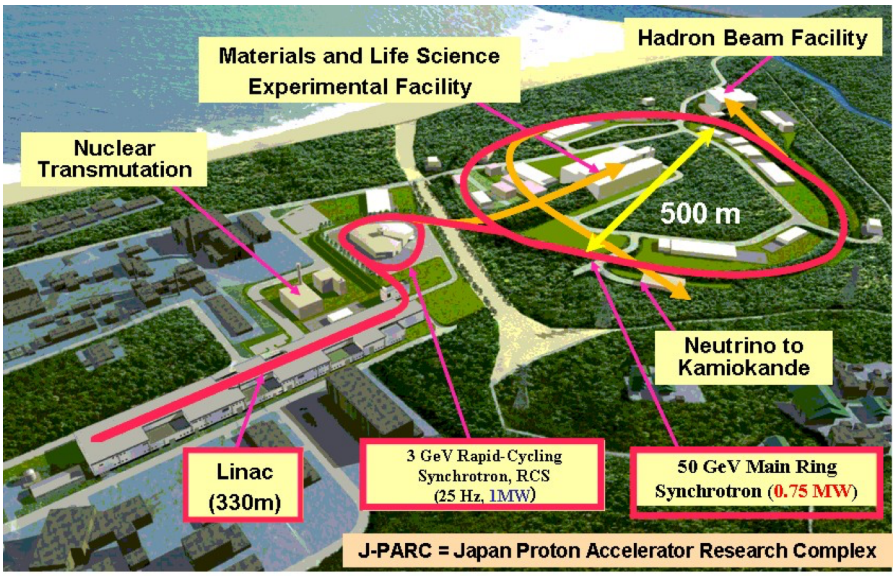

Figure 4.1: The J-PARC accelerator complex. The acceleration sequence is shown from the LINAC to the main ring. The figure is adapted from http://www.teilchen.at/news/334.

and the secondary beamline. Protons accelerated to 30 GeV strike a graphite target, to create secondary pions and other hadrons. Pions among those charged particles are mainly focused by magnetic horns, and decay into muon neutrinos. Figure 4.3 shows the overview of the T2K neutrino beamline.

4.2.1 Primary beamline

The primary beamline contains a preparation section, an arc section, and a final focusing section. The preparation section has a length of 54 m and contains 11 normal-conducting magnets: four steering magnets, two dipole magnets, and five quadrupole magnets. The proton beam is focused and deflected by those magnets. The arc section, which spreads for 147-m long, receives the beam from the preparation section and bend it by 80.7 degrees toward the far detector. This is performed by 14 super-conducting combined function magnets (SCFMs), which are cooled to 4.5 K by the helium cooling system and provide magnetic fields of 2.6 T dipole and 19 T/m quadrupole. In addition, three super-conducting steering magnets work for a correction of the beam orbit. The 37-m-long final focusing section consists of 10 normal-conducting magnets: four steering magnets, two dipole magnets, and four quadrupole magnets. Along this section, the proton beam is bent downward by 3.637 degrees and guided to the secondary beamline. In order to achieve a stable operation, the primary beamline is equipped with a number of

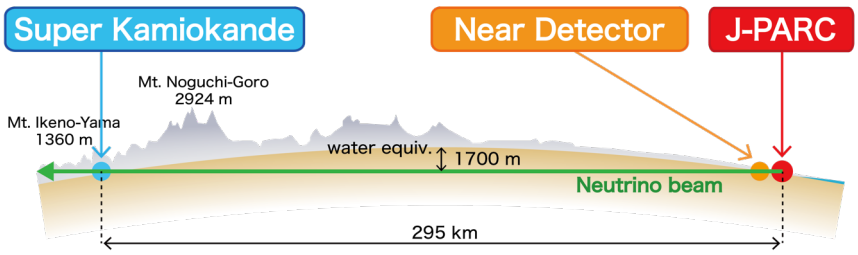

Figure 4.2: The overview of the T2K experiment. Cited from [91].

beam monitors[91]:

- 5 current transformer (CT) monitoring the beam intensity
- 21 electrostatic monitors (ESMs) monitoring the beam position
- 19 segmented secondary emission monitors (SSEMs) monitoring the beam profile
- 50 beam loss monitors (BLMs)

4.2.2 Secondary beamline

The secondary beamline contains a target station, a decay volume, and a beam dump, as shown in Fig. 4.4. In the target station, a graphite target with a length of 91.4 cm and a diameter of 2.6 cm is located on the beamline. The target is surrounded by a 2-mm-thick graphite tube and a 0.3-mm-thick titanium case, and placed inside the first magnetic horn. The 30 GeV proton beam strikes this graphite target, to emit pions with other hadrons. There are three magnetic horns, and each of them is composed of a pair of coaxial conductors made of an aluminum alloy. The magnetic horn produces a toroidal magnetic field, to collect and focus the charged pions. The amplitude of the average current is stable to be 250 ± 5 kA for providing 1.7 T magnetic field. In order to alter the beam modes between a neutrino beam and an anti-neutrino beam, the horn polarity is controlled. The polarity for the neutrino beam mode is defined as a forward horn current (FHC), while that for the anti-neutrino beam mode is defined as a reversed horn current (RHC).

The oriented charged pions enter into the decay volume. As transferred though the 96 m long volume filled with helium, pions decay into muon neutrinos. The

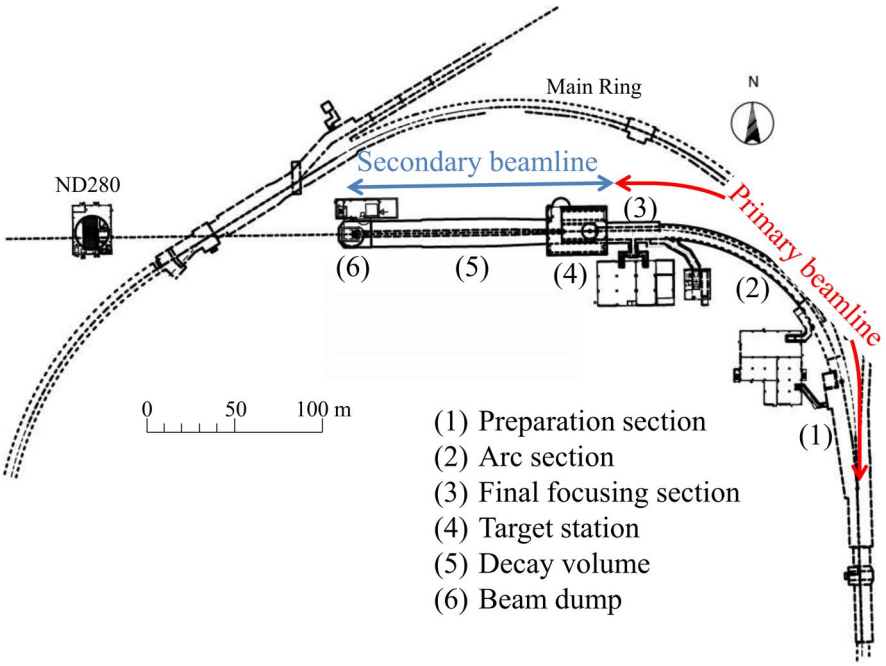

Figure 4.3: The T2K neutrino beamline[91].

dominant decay modes are:

$$\pi^+ \rightarrow \mu^+ + \nu_\mu \text{ (FHC)} \tag{4.1}$$
$$\pi^- \rightarrow \mu^- + \overline{\nu}_\mu \text{ (RHC)} \tag{4.2}$$

There are also contributions from kaons:

$$K^+ \rightarrow \mu^+ + \nu_\mu \tag{4.3}$$
$$K^+ \rightarrow \pi^0 + \mu^+ + \nu_\mu \tag{4.4}$$
$$K^- \rightarrow \mu^- + \overline{\nu}_\mu \tag{4.5}$$
$$K^- \rightarrow \pi^0 + \mu^- + \overline{\nu}_\mu \tag{4.6}$$

which are expected to be about 5% among muon neutrinos. An imperfect focusing causes a wrong-sign neutrino contamination for each mode with a level of 5–10%. In addition, there is a subtle contamination with a level of 1% from electron neutrinos generated via the following decays from a kaon and a muon:

$$K^+ \rightarrow \pi^0 + e^+ + \nu_e \tag{4.7}$$
$$\mu^+ \rightarrow e^+ + \nu_e + \overline{\nu}_\mu \tag{4.8}$$
$$K^- \rightarrow \pi^0 + e^- + \overline{\nu}_e \tag{4.9}$$
$$\mu^- \rightarrow e^- + \overline{\nu}_e + \nu_\mu \tag{4.10}$$

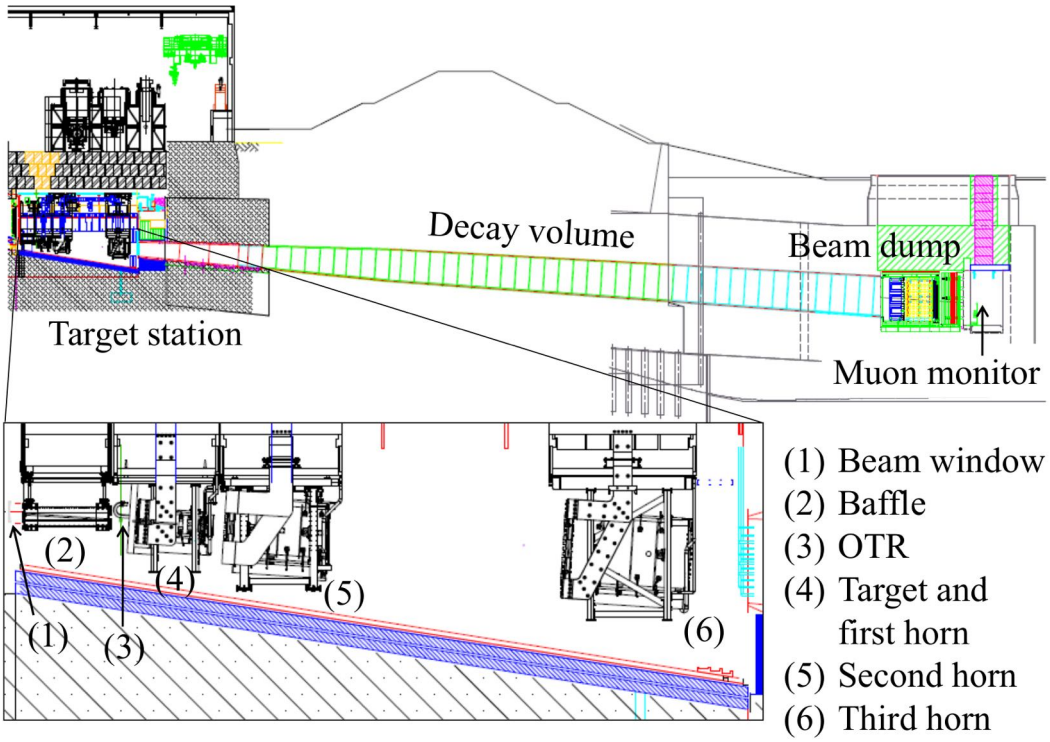

Figure 4.4: The secondary beamline[91].

The beam dump, composed of graphite blocks and concrete walls, is located at 109 m downstream form the target, for the purpose to stop all particle from the beamline except for neutrino and high-energy muons with $E_\mu >\sim 5$ GeV.

In order to measure the beam profile at the secondary beamline, an optical transition radiation (OTR) monitor is set right before the target. The OTR monitor uses a thin titanium-alloy foil and is capable of measuring the beam position and width with an accuracy better than 0.5 mm[92].

The high energy muons penetrating the beam dump are measured by a muon monitor (MUMON)[93]. MUMON is composed of two independent detectors: ionization chambers and silicon PIN photodiodes, as shown in Fig. 4.5. Both cover the 1.5×1.5 m^2 area perpendicular to the beam direction, and measure two-dimensional profile of the muons. Those allow reconstructions of neutrino beam direction on a bunch-by-bunch basis with an accuracy of 0.25 mrad, as well as a stability of the beam intensity with an accuracy of 3%.

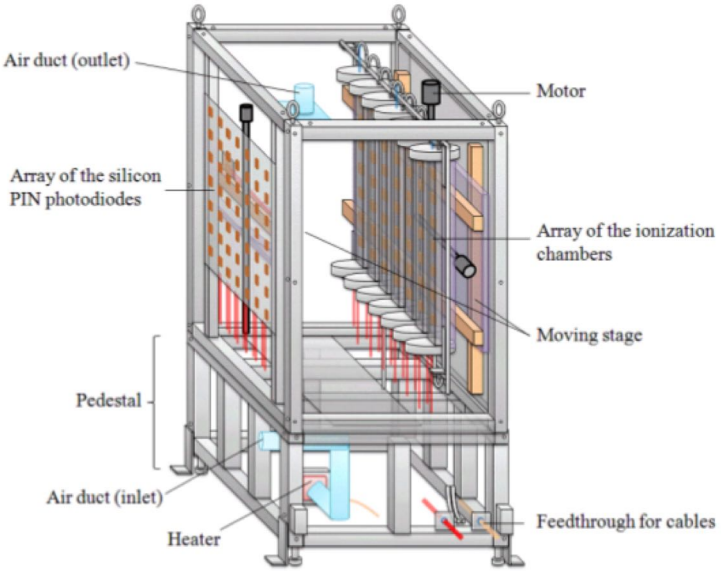

Figure 4.5: The muon monitor[93].

4.2.3 Off-axis method

In the T2K experiment, the neutrino beam is oriented to a slightly different direction from the near and far detectors, as shown in Fig. 4.6. This is known as an "off-axis method" to achieve the neutrino beam with a narrow neutrino energy spectrum: a "narrow-band" neutrino beam. In the case of a two-body decay of a pion, as described in Eq. 4.1 and 4.2, the neutrino energy is calculated as:

$$E_\nu = \frac{m_\pi^2 - m_\mu^2}{2(E_\pi - p_\pi \cos\theta_\nu)}, \tag{4.11}$$

where m_π and m_μ are masses of a pion and a muon respectively, p_π represents a pion momentum, and θ_μ is an angle between the initial pion and the neutrino. As shown in the left of Fig. 4.7, whilst the neutrino energy linearly grows as a function of the pion momentum in the case of on-axis beam, the neutrino energy has less dependency on the pion momentum when θ_μ is shifted from zero. In the T2K far detector, 2.5° off-axis degree is adopted in order to set a peak energy of the neutrino beam to be around 600 MeV, which maximizes the neutrino oscillation probabilities at 295 km. In addition, the narrow-band structure allows to suppress background neutrino interactions to CCQE which is the main signal of the T2K experiment. On the other hand, the off-axis neutrino beam is sensitive to off-axis angle. When the neutrino beam direction is deviated by 1 mrad in T2K, the neutrino beam intensity and peak energy are varied at the far detector by 5% and

3% respectively. Hence, it is important to control and monitor the neutrino beam direction with a high accuracy.

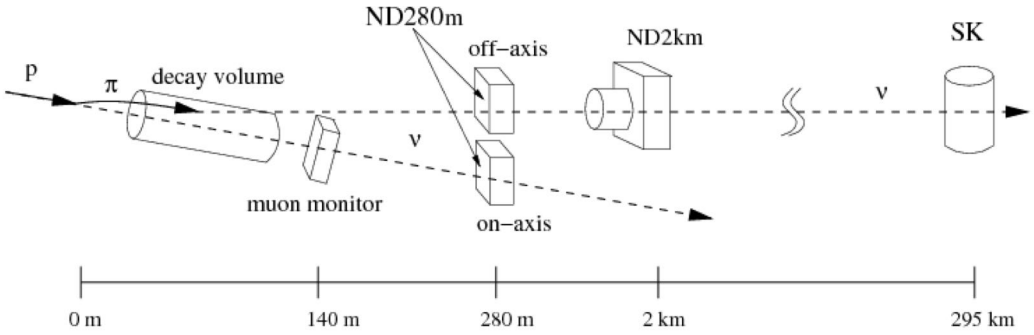

Figure 4.6: Concept of the T2K neutrino beam[94].

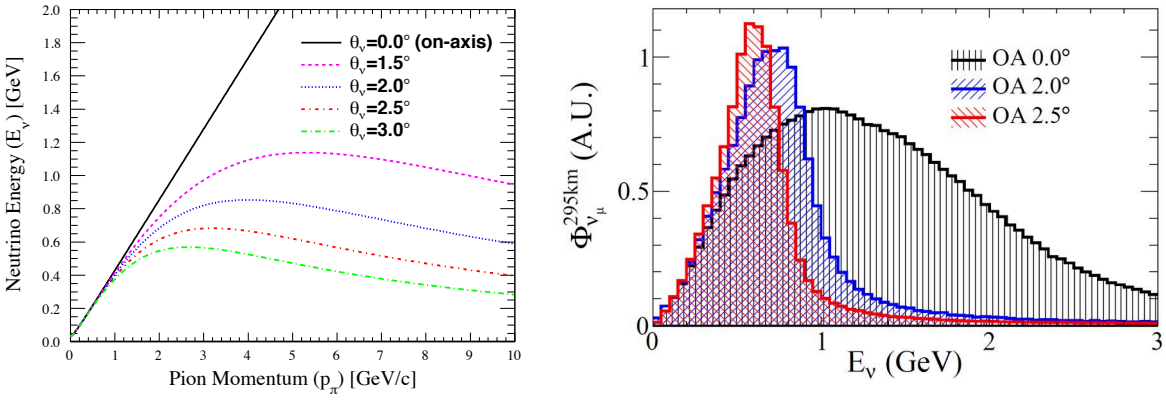

Figure 4.7: Left: relations between neutrino energy and pion momentum for several off-axis angles. Right: Distributions of neutrino energy for different off-axis angles[95].

4.2.4 Neutrino beam simulation

In the prediction of the neutrino beam flux, the processes from the primary proton interactions at the graphite target to decays of particles into neutrinos are simulated. First, hadron production and secondary interactions in the target and the baffle is simulated by using FLUKA software[96] [97]. Properties of the incident proton are parametrized based on the beam monitor measurements.

Tracks of the secondary particles generated by FLUKA are transferred to the JNUBEAM simulation[95], which is a GEANT3[98]-based Monte Carlo simulation. JNUBEAM simulates propagation of particles along the secondary beamline until they decay into neutrinos. Hadronic interactions out of the graphite target, where JNUBEAM controls the simulation, are modeled with GCALOR[99]. The obtained kinematics of neutrinos are extrapolated towards the detectors in T2K. The generated neutrino flux is tuned based on the external hadron interaction experiments, NA61/SHINE[100][101], Eichten *et al*[102], Allaby *et al.*[103], and BNL-E910[104]. The uncertainties are estimated for each of hadron interaction uncertainty and beamline uncertainty, as discussed in Sec. 7.3.1.

4.3 Near detectors

4.3.1 The off-axis detectors: ND280

The ND280 detector, Fig 4.8, is a complex of several sub-detectors and measures the neutrino beam in the J-PARC site at 280 m downstream from the neutrino beam target. Each sub-detectors is described in the followings:

- A magnet is set at the most outer layer, and also serves as a side muon range detector (SMRD) with plastic scintillator bars inserted at gaps between the magnet yokes. It provides 0.2 T magnetic fields, and the other sub-detectors are placed inside the magnet.

- A pi-zero detector (P0D) is located at the most upstream part of ND280, and mainly composed of alternating layers of plastics scintillators, lead or brass radiators, and water bags. The primary motivation of P0D is to measure neutral current π^0 interactions, which contributes as one of the dominant background sources to ν_e appearance signal in T2K.

- Each of three time projection chambers (TPCs), at the downstream of P0D, consists of an inner box filled with an argon-based drift gas and an outer box filled with CO_2 as an insulating gas. It determines track curvature to measure momentum of charged particles and their charge.

- Two fine-grained detectors (FGDs) are alternately arranged with the three TPCs. Each FGD has plastic scintillator tracking planes, which also work as the main target of neutrino interactions at ND280. The FGD module at the upstream (FGD1) is fully composed of the scintillators, while the downstream one (FGD2) contains water target parts sandwiched between the scintillator layers.

- Electromagnetic calorimeters (ECals) surround the P0D, TPCs, and FGDs.

The location of ND280 is on the same off-axis angle as the far detector, so that it measures neutrino cross sections with various targets by using the almost same beam flux and to provide constraints on the neutrino oscillation analysis.

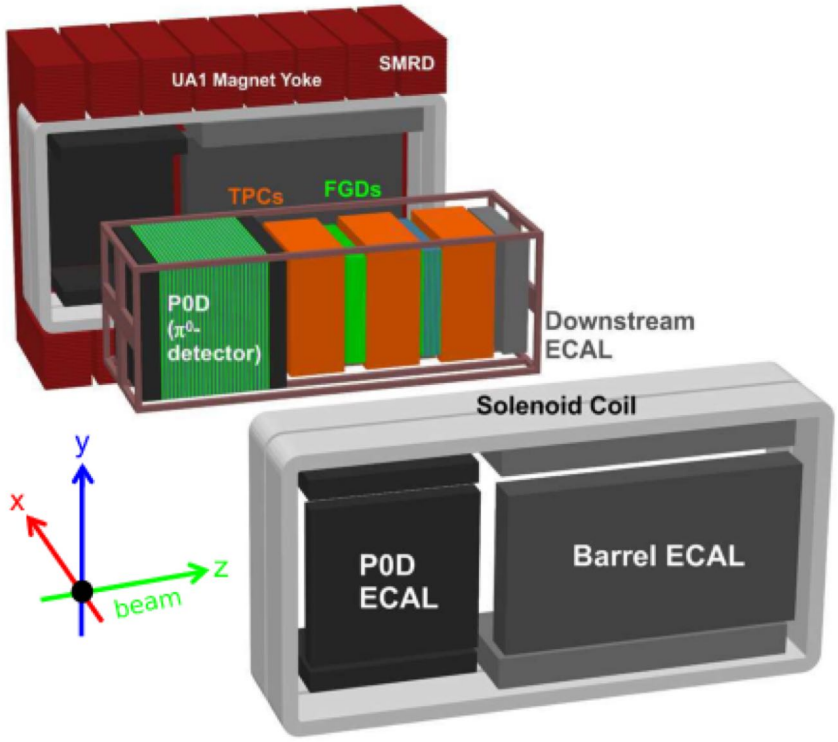

Figure 4.8: The ND280 detectors. [105].

4.3.2 The on-axis detectors: INGRID and Proton Module

The INGRID modules are located on the neutrino beam axis in the same hall as the ND280 detectors, in order to monitor the neutrino beam intensity and the beam direction by directly measuring neutrinos. 14 INGRID modules are arranged to form a cross as shown in Fig. 4.9, seven of which are placed in a horizontal direction and the rest seven are in a vertical direction. The whole of the 14 modules cover an area of 10 m $\times$ 10 m, and measure the neutrino beam profile center with an accuracy better than 28 cm which corresponds to 1 mrad of beam direction, using differences in neutrino event rates between the modules. There are two additional modules, which were originally placed on off-diagonal places as shown in Fig. 4.9 in

order to measure an asymmetry of the beam profile. They are ubiquitous modules, and one of the two modules is currently located on a different floor with WAGASCI as described in Sec. 4.6.

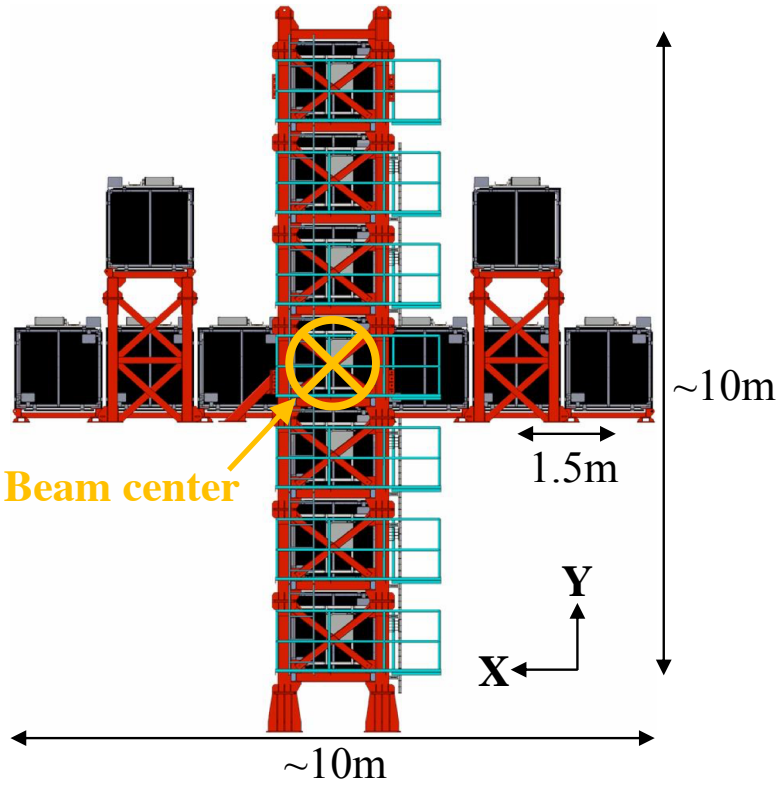

Figure 4.9: The whole view of the INGRID modules[62].

An INGRID module consists of an alternating layer structure of 9 iron target plates and 11 plastic tracking scintillator planes, surrounded by four veto scintillator planes, as shown in Fig. 4.10. Each iron plate has an area of 1240 mm×1240 mm perpendicularly and 6.5 cm thickness with respect to the beam axis. Each of scintillator planes is formed by a pair of scintillator layers, each of which has 24 scintillator bars horizontally and vertically arranged every 5 cm respectively. Sizes of a scintillator bar are 1200 mm × 50 mm × 10 mm, and a scintillator layer covers an area of 1200 mm × 1200 mm. Scintillation light is collected via a wavelength shifting (WLS) fiber which is inserted into a hole at the center of each plastic scintillator bar, and detected by a multi-pixel photon counter (MPPC) attached on an end of the WLS fiber. Signals of the MPPCs are readout by the same electronics and data acquisition system as the other ND280 detectors.

Proton Module, as shown in Fig. 4.11, is a fully-active tracking detector, which used to be located in front of the INGRID module on the neutrino beam axis.

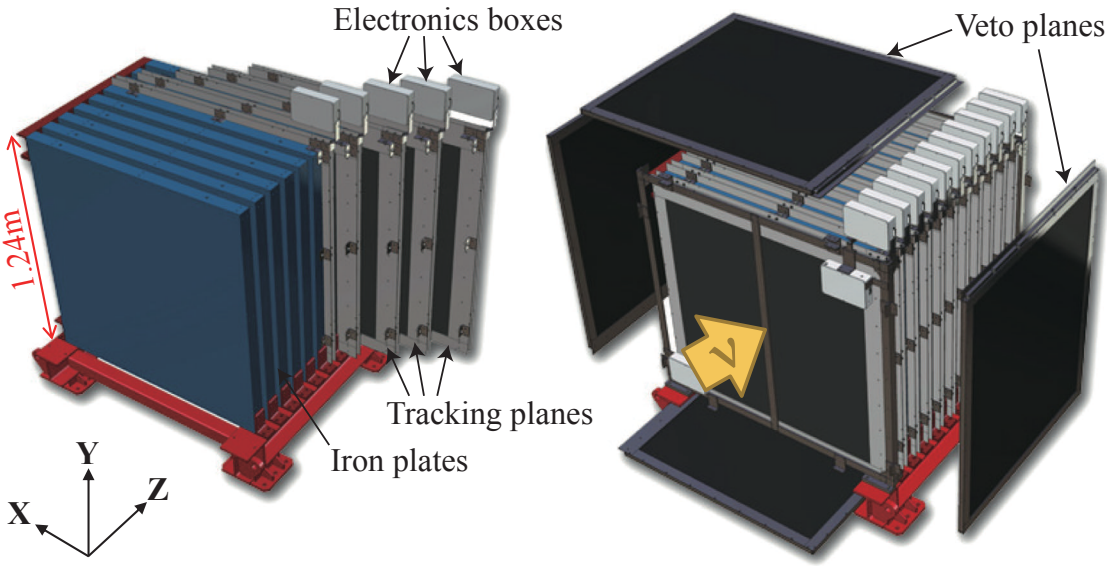

Figure 4.10: An INGRID module[62].

It is only composed of plastic scintillator bars, to separate neutrino interaction modes by measuring protons and pions in addition to a muon. A structure of Proton Module is formed by 36 scintillator tracking planes, which are alternately arranged with horizontal layers and vertical layers. Each layer consists of two types of scintillators: one has the size of 1200 mm × 50 mm × 10 mm as the INGRID scintillator bars, and the other has 1200 mm × 25 mm × 13 mm which was originally used in the SciBar detector[106]. Since the SciBar-type scintillators have a finer segmentation, they are arranged at the inner region to achieve a better reconstruction of tracks. For the outer region and one plane at the most upstream, the INGRID-type scintillators are used. Scintillator light is readout as the same procedure as INGRID. Figure 4.12 shows an example of simulated event display of Proton Module and INGRID from the side view.

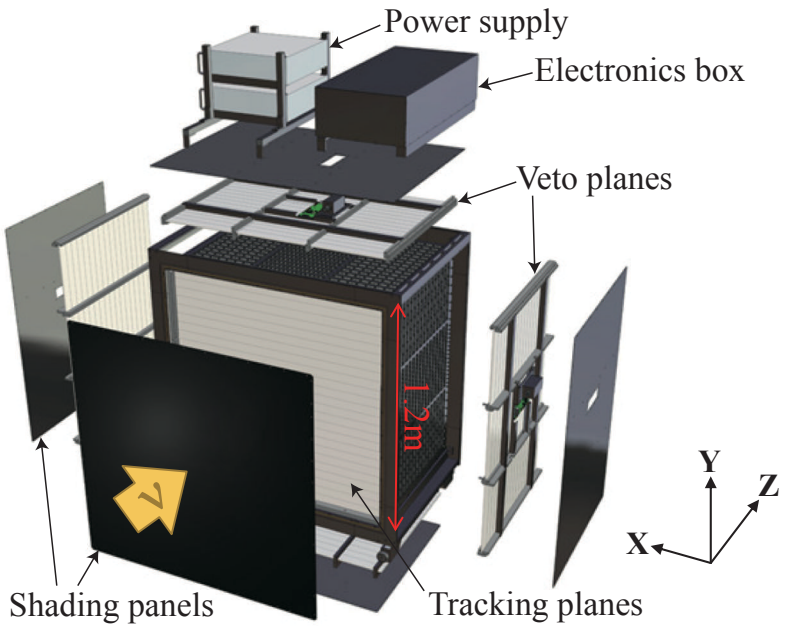

Figure 4.11: Proton Module[62].

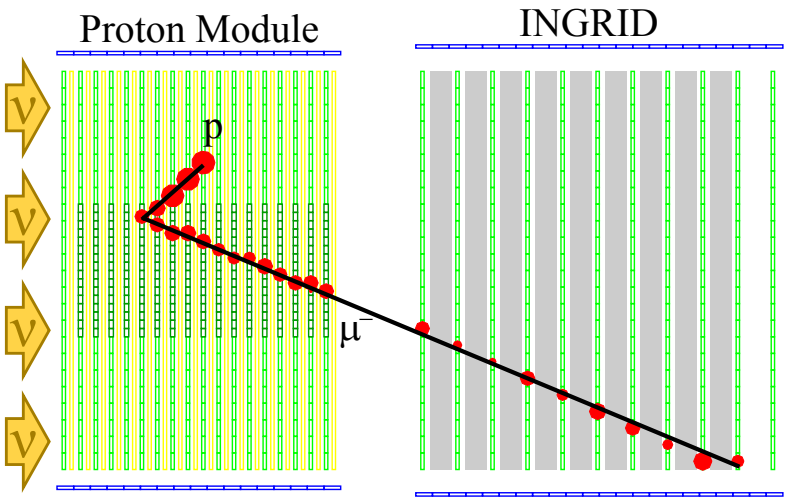

Figure 4.12: An event display of a simulated CCQE event at the on-axis configuration[62]. Green boxes are plastic scintillator channels. Yellow boxes show scintillator bars perpendicularly arranged to this view, and they are active channels in the other view. Gray filled boxes are iron plates.

4.4 Super-Kamiokande

Super-Kamiokande (SK), as shown in Fig 4.13, is a 50 ktons pure water detector with a cylindrical steel tank, 39.3 m in diameter and 41.4 m in height. The detector is separated into optically isolated two volumes, the inner detector (ID) and the outer detector (OD), and a large number of photomultiplier tubes (PMT) are installed on the walls inward for ID and outward for OD. The neutrino events are detected in ID by Chrenkov light of charge particles from the neutrino interactions, and discriminated from the external background by the OD veto. The ID detector is able to measure the charged particles with 4π solid angle.

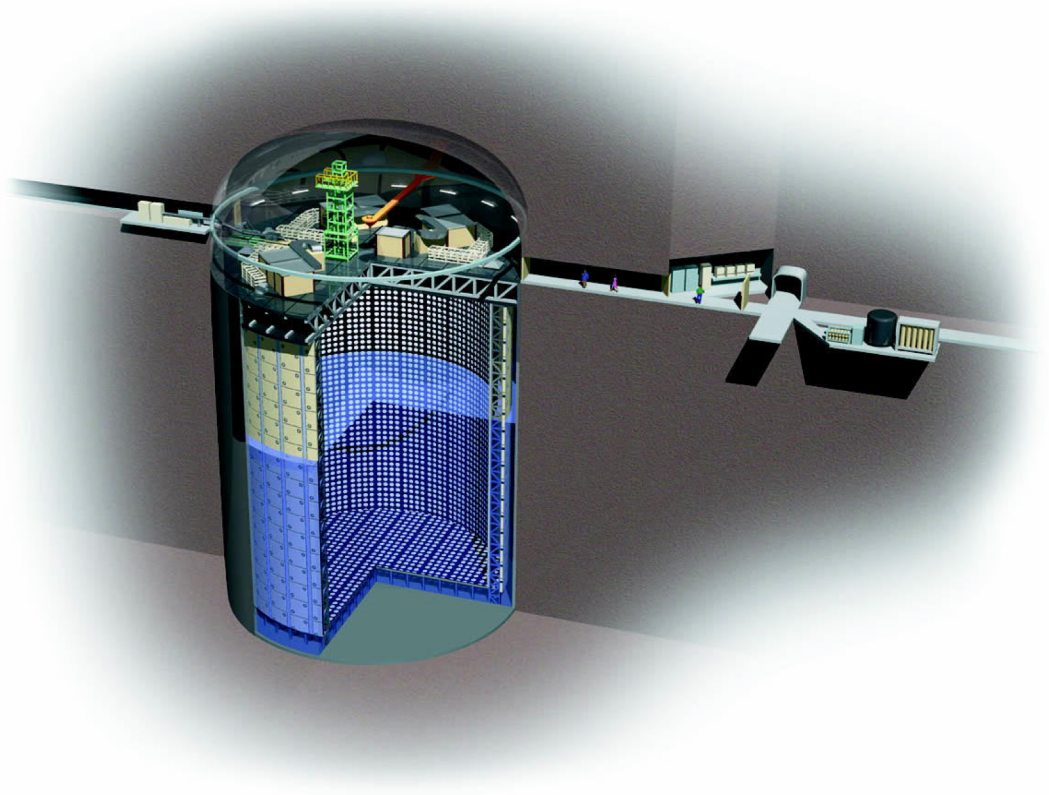

Figure 4.13: The Super-Kamiokande detector.

4.5 WAGASCI

4.5.1 Overview of the WAGASCI/Baby-MIND project

The WAGASCI/Baby-MIND project, approved as the J-PARC E69 experiment, aims to measure neutrino-nucleus interactions on water and hydrocarbon targets with various exclusive interaction channels, using the T2K neutrino beamline. Using the same neutrino beam with slightly different spectra from ND280 allows better understanding of neutrino interactions around 1 GeV. The detectors are installed on a different floor (B2 floor) in the T2K near detector hall as ND280.

The detector in the final configuration contains several sub-components: the WAGASCI modules and muon range detectors (MRDs). Main neutrino interaction targets are on two WAGSCI modules. The WAGASCI module, which has a water tank filled with 0.6-ton water, has high ratio of water target to tracking scintillators and is able to measure neutrino interactions on water target.

The WAGASCI modules are surrounded by MRDs: a pair of side-MRDs, and a downstream MRD. Since the WAGASCI modules have a three-dimensional lattice structure as described in Sec. 4.5.2, measurements of neutrino interactions with wide-angle scattering is possible by combining with the side-MRDs. The downstream MRD, known as Baby-MIND, is a magnetized iron muon spectrometer, which provides a muon momentum measurement and an identification of particle charge. The charge identification is motivated especially for the anti-neutrino beam since contaminations from wrong-sign neutrinos among all interactions are about 30%. Proton Module is located at the most upstream part, and works as a hydrocarbon target to provide a larger statistics.

One of the two WAGASCI modules and Proton Module were installed at Aug. 2017, and an operation in the first phase started at Oct. 2017. Baby-MIND was installed at May. 2018, and installations of side-MRDs and the other WAGASCI module are planned at the beginning of 2019. Data taking with the final configuration will be started at the first neutrino beam in 2019.

4.5.2 The WAGASCI module

The WAGASCI module is a water target neutrino detector[107], as shown in Fig. 4.14, and has been developed in order to measure neutrino-nucleus interactions with a high signal purity for a large acceptance. The main advantages of the WAGASCI module are as follows:

- It has a large fraction of water target in the module for reducing background events from neutrino interaction in non-water materials.

- It has a large angular acceptance for measuring neutrino interactions for the entire phase space.

The other near detectors with a water target, such as FGD2[108], have relatively large amount of non-water materials in the module, and mainly have their focus on the forward scattering region. The characteristic points of the WAGASCI module allow measurements with a better signal purity for the phase space inaccessible with the other detectors.

The WAGASCI module is mainly composed of 0.6 ton water and 3-mm-thick plastic scintillators. Adopting the thin plastic scintillators allows a large fraction of water in the target region, about 80%, for well suppressing background events from neutrino interactions in the scintillators in the target region. This is one of the main background events in the previous analysis in FGD2[109], since its ratio of water to scintillators is about 50%. In addition, WAGASCI is designed to have the scintillators forming a three-dimensional lattice structure, so that the entire solid angle acceptance from the water target is covered by the tracking scintillators. It allows the WAGASCI module to have an advantage of large angular acceptance to measure the phase space which is inaccessible with the other near detectors.

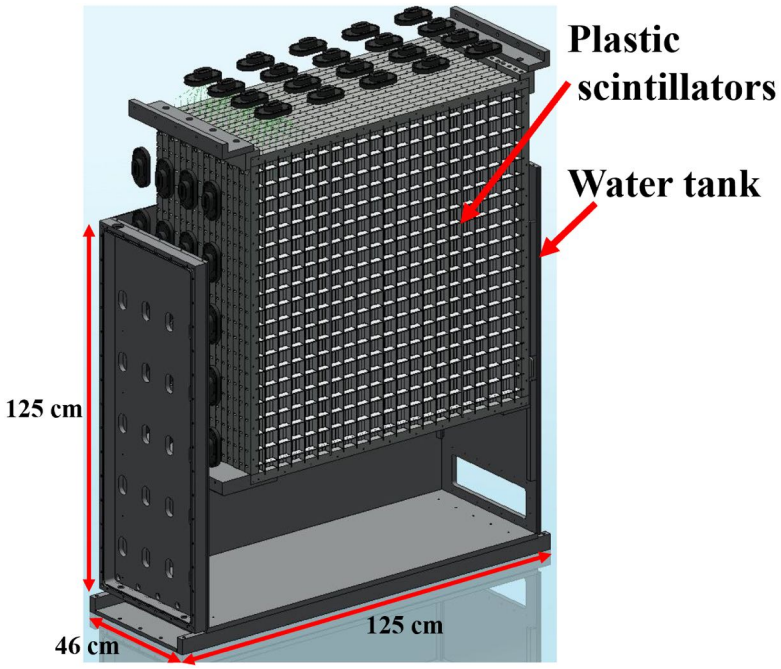

Figure 4.14: Schematic view of WAGASCI.

WAGASCI has 16 scintillator tracking planes inside a stainless steel tank, which is filled with 0.6 ton water. Each scintillator plane consists of 80 scintillator bars:

40 bars, called plane scintillators, are placed perpendicularly to the beam axis, and the other 40 bars, called grid scintillators, are placed parallel to the beam, as shown in Fig. 4.15. The measured geometry of each scintillator is shown in Fig. 4.15. The grid scintillators have 20 slits, so that a grid layer is formed by engaging a set of 20 grid scintillator bars and another set. Figure 4.16 shows the view of the scintillators from x-direction and y-directions, where the coordinate is defined with z along the beam axis, y in the vertical direction, and x in the horizontal direction.

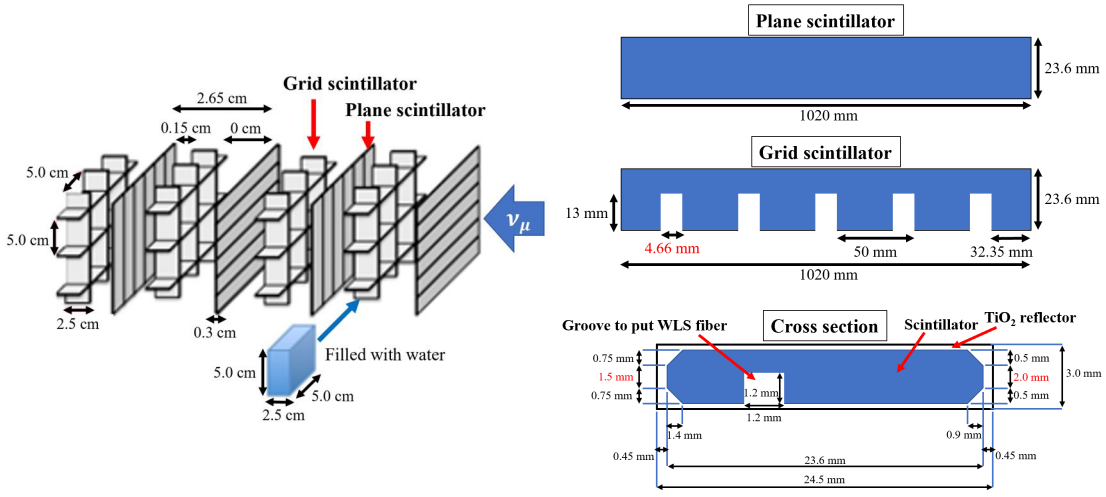

Figure 4.15: Left: schematic view of the scintillators of the WAGASCI. The written size is the design values. Right: geometry of the scintillators of the WAGASCI.

4.5.3 Detector components

4.5.3.1 Scintillator and WLS fiber

In order to detect charged particles from neutrino interactions, a combination of plastic scintillator and a WLS fiber is used, in the same way as INGRID, Proton Module, and most of the other ND280 detectors. As shown in the Fig. 4.15, each scintillator bar in WAGASCI has a groove with a depth of 1.2 mm and a width of 1.2 mm, where a 1500-mm-long WLS fiber is embedded and fixed by using optical cement.

Chemical robustness and stability in water of the plastic scintillators were confirmed in test measurements. The 3-mm thickness has been optimized during a prototype construction[107], in order to reduce the total mass of scintillator in the water target region and to keep the light yield large enough to detect charged particle. The plastic scintillators are produced at the Fermi National Accelerator

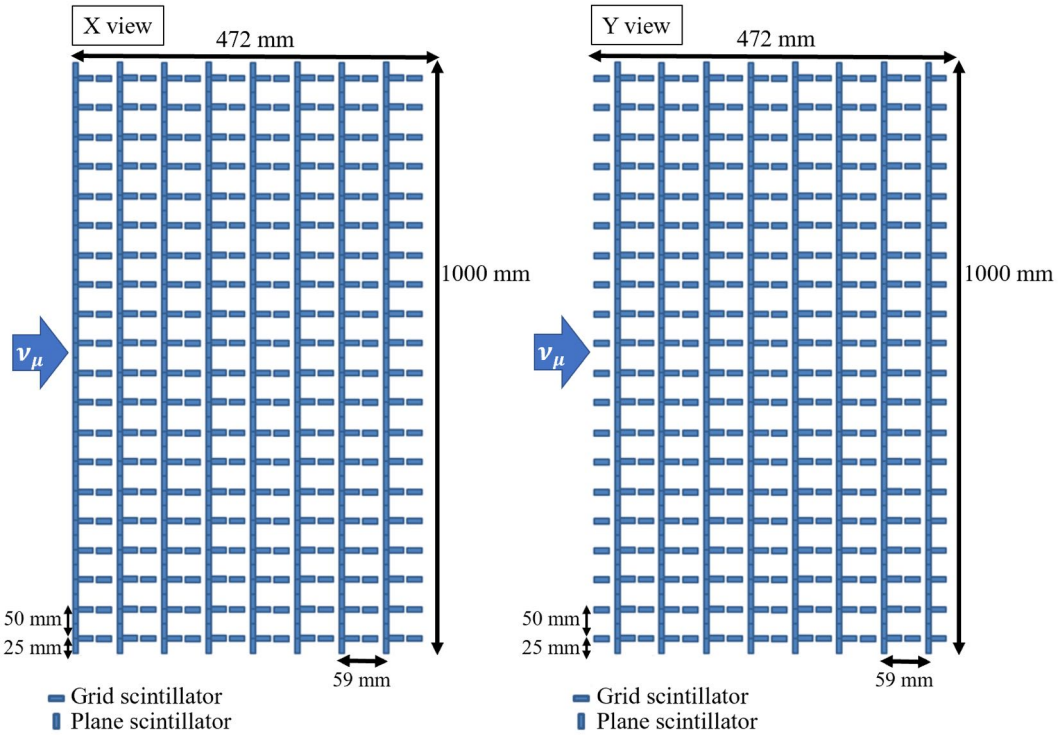

Figure 4.16: View of the scintillators of the WAGASCI from x-direction (left) and y-direction (right).

Laboratory with an extrusion method, and machined by G-tech company for their slits.

The plastic scintillator is mainly composed of polystyrene (C_8H_8), infused with PPO ($C_{15}H_{11}NO$) and POPOP ($C_{24}H_{16}N_2O_2$). Its scintillation light has a wavelength of 420 mm at the peak of the spectrum. It has a co-extruded reflective coating, composed of TiO_2 infused in polystyrene, in order to optically separate each scintillator and increase the light yield. At the most outer surface, a scintillator is coated with black silicon painting, which serves to reduce optical crosstalk between scintillators.

Figure 4.17 shows a picture during construction of a tracking plane from 40 scintillator bars. The scintillator bars are fixed to a frame made of ABS resin. Four of the scintillator planes are combined to form a sub-module, shown in Fig 4.18. An edge of the WLS fibers is extracted from the scintillator bar, and 32 of the fiber edges are bundled by a plastic jig named a fiber bundle, as shown in Fig. 4.18. The WLS fibers are fixed to the fiber bundle by optical cement, and its surface is polished by a diamond polisher to keep uniformity and increase the light yield. The WAGASCI module is formed by combining four sub-modules.

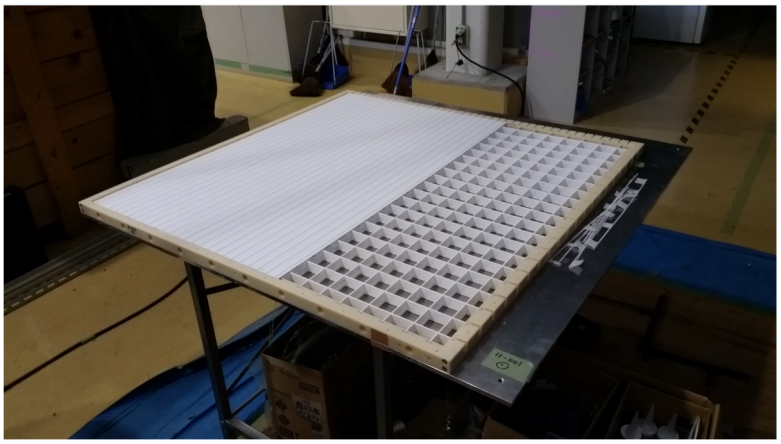

Figure 4.17: Construction of a scintillator layer.

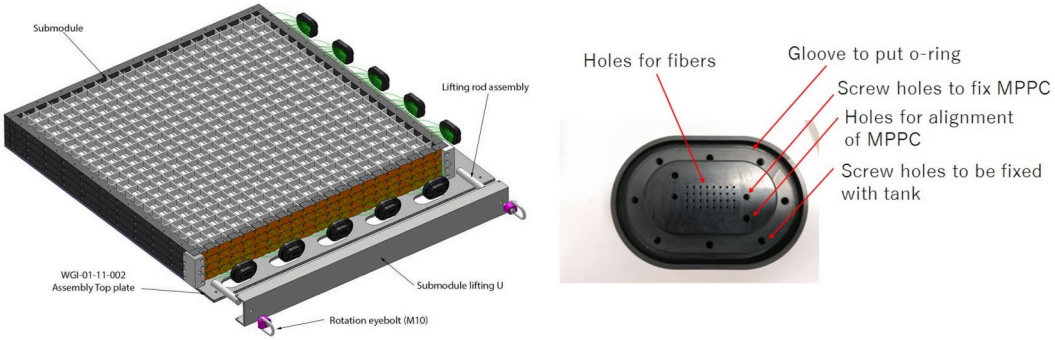

Figure 4.18: Left: a sub-module. Right: a fiber bundle.

4.5.3.2 MPPC

Scintillation light is collected by WLS fibers and detected by MPPCs. In the WAGASCI module, a 32-channel arrayed MPPC (S13660[110]) shown in Fig. 4.19 is adopted, and each fiber bundle is directly attached to an MPPC array. The MPPC has been developed by Hamamatsu Photonics[111]. Specifications of the MPPC are summarized in Table. 4.1. In total, the WAGASCI module has 1280 channels of MPPCs, corresponding to 40 MPPC arrays.

4.5.3.3 Electronics and data acquisition system

The WAGASCI electronics and data acquisition system have been newly developed for this experiment, which is operated independently of ND280. Details of the electronics[112][113] are described in Appendix A. The hit threshold for the WAGASCI electronics is set to 2.5 photoelectrons. All hits in every spill are

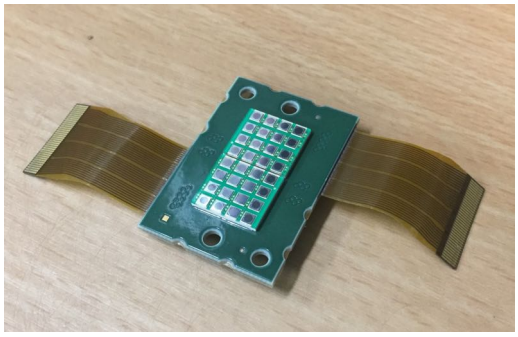

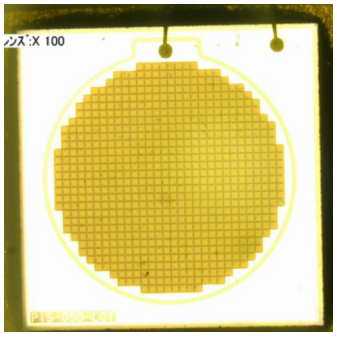

Figure 4.19: A 32-channel arrayed MPPC (left) and an enlarged picture of an MPPC channel (right).

Table 4.1: Specifications of a 32-channel arrayed MPPC.

Parameter	Value
Size of a pixel	$50 \times 50 \mu\text{m}^2$
Number of pixels	716
Size of a device	$\phi = 1.5\text{mm}^2$
Breakdown voltage	$\text{V}_{\text{bd}} = 54.0$ V
Operation voltage	$\text{V}_{\text{bd}} + 3.5$ V
Gain	2.6×10^6
Dark noise rate	36 kHz
Crosstalk and afterpulse rate	0.052
Photo detection efficiency	40% (500 mm)

recorded. Timings of those hits are measured bunch-by-bunch, which are synchronized to the neutrino beamline by a timing trigger delivered from the accelerator. In addition, an event tag of each spill is recorded together, in order to match the WAGASCI data to the other detectors operated by the ND280 electronics spill-by-spill in the off-line analysis. The whole electronics in each view is placed inside a metal housing, and its temperature is controlled by cooling fans, in order to keep a stable operation as well as stable MPPC gains.

4.5.3.4 Water tank

The water tank is made of stainless steel (SUS304). Sizes of the water tank are an area of 125 cm $\times$ 125 cm and a width of 46 cm. On one of side surfaces of the water tank are 20 holes for the fiber bundles to be extracted. Each hole is embedded with a fiber bundle whose diameter is designed to be the same size as an inner diameter of the hole, and is sealed by using an o-ring at a contact between them. Once the tank is filled with water, eight water sensors attached on the top part

of the side surface monitor the water level, as shown in Fig. 4.20. Two sensors among eight are set above the water level, to measure it with an accuracy of 1 cm. Additional two water sensors are placed at the floor underneath the module, in order to detect a water leak.

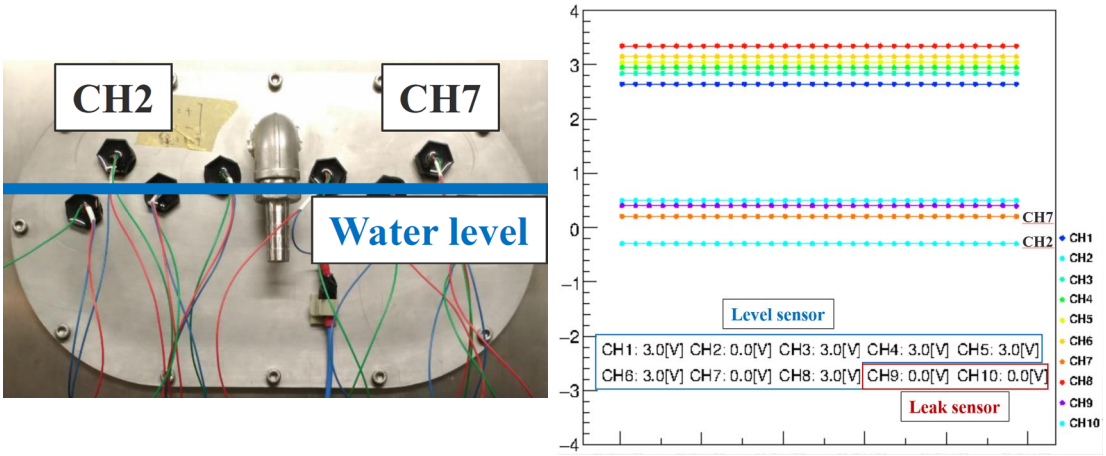

Figure 4.20: watersensor

4.6 Data taking

4.6.1 Detector configuration

The anti-neutrino beam measurement for the analysis in this thesis was performed since Oct. 2017 to May. 2018. In the summer 2017, the B2 floor in the near detector hall was arranged with three detectors: Proton Module, a WAGASCI module, and an INGRID module in an order from the upstream of the neutrino beam, as shown in Fig. 4.21. Proton Module and the INGRID module were moved from their original location in the floor on the neutrino beam axis. WAGASCI and Proton Module are used as neutrino interaction targets for water and hydrocarbon respectively. Proton Module is also used for subtracting background events from the scintillator in WAGASCI. In this analysis, INGIRD is only used as a downstream MRD for WAGASCI and Proton Module, and not used as a neutrino interaction target since the detector configuration is largely different from the other two modules.

In order to set heights of WAGASCI and Proton Module to be the same as each other, four legs were newly produced for Proton Module. On the other hand, the INGRID module is kept with its original height, though it is lower than the other two detector by 10 cm. While this is a disadvantage with respect to statistics

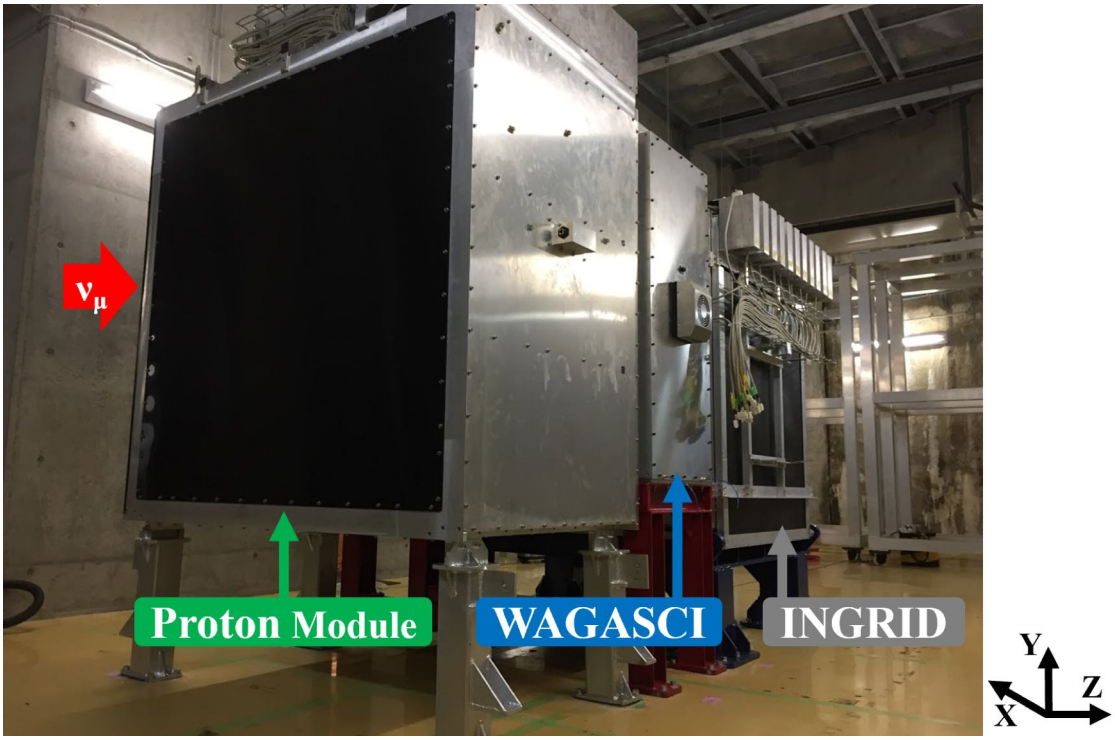

Figure 4.21: Installed detectors at the B2 floor in the J-PARC neutrino monitor building. The coordinate system used in this note is shown: The beam axis corresponds to Z axis.

about by 10%, a slightly larger acceptance for a scattering angle of a muon is available than that in the case of a common height between modules.

This detector configuration is only for commissioning of the WAGASCI module along the WAGASCI/Baby-MIND project. Although the biggest advantage of grid scintillators is the ability to reconstruct tracks for largely scattering muons, the acceptance for detection of muons from the WAGASCI module in this configuration is limited to the forward scattering, since the side-MRDs are not installed.

4.6.2 Commissioning and data taking

During the beam data taking with the anti-neutrino beam, stable data acquisition was achieved. The accumulated statistics are shown in Fig. 4.22, and the averaged data taking efficiency is 96.8% after selecting spills with data in all of WAGASCI, Proton Module and INGRID. Although the operation continued until 27th May, the data for the last three days are not used in this analysis, since the temperature for those period increased due to the operation of another detector and it is possible to affect the data quality. The used data set is shown in Sec. 4.6.3.

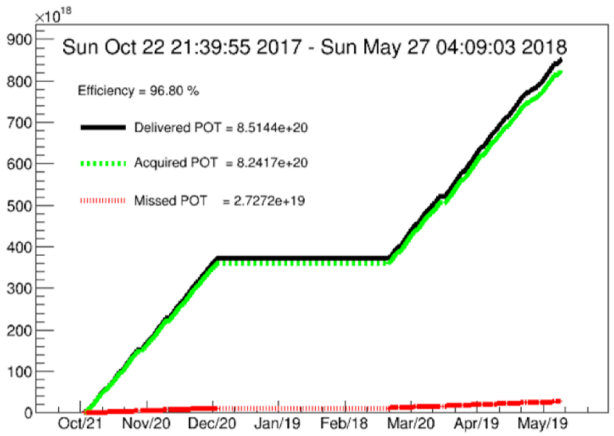

Figure 4.22: The accumulated statistics with respect to number of protons on target (POT) during data taking.

4.6.2.1 Stability during the anti-neutrino beam data taking

In order to confirm that the data quality during the operation is good, MPPC gains and scintillator light yield are monitored for the whole period.

Gains of all 1280 channels of MPPCs in WAGASCI are monitored by measuring distances between the pedestal peak and 1 photo-electron peak calculated by double Gaussian function fitting, and the mean value of the distances is set to be 40 ADC counts. Two among the 1280 channels are masked for the whole operation due to their unstable behavior, and those channels are also masked in the Monte Carlo simulation. Proton Module has one channel masked, and the gains are monitored in the same method as WAGASCI, while the distance between pedestal peak and 1 photo-electron peak is set to be 10 ADC counts. The MPPC gain history is shown in the left column of Fig. 4.23, and it is seen that all of the non-masked channels have their gains stable within 10% deviation from its nominal value for the whole period.

The light yield of the scintillators is monitored by using muons from interactions of neutrinos in the beam on the external materials such as upstream walls. Those muons are known as sand muons, and they have much more statistics than neutrino interaction inside the modules. The mean light yield of the WAGASCI scintillators is around 9.9 photo-electrons/3mm, and this is enough to detect minimum ionizing particles (MIP). There are five channels in WAGASCI with low light yield due to the damage on wavelength shifting fiber during the detector construction work. They are masked for this analysis, and reflected to the simulation as well. The stability of the scintillator light yield for the whole period of data taking is shown in the right column in Fig. 4.23. There is no low light yield channel for Proton Module.

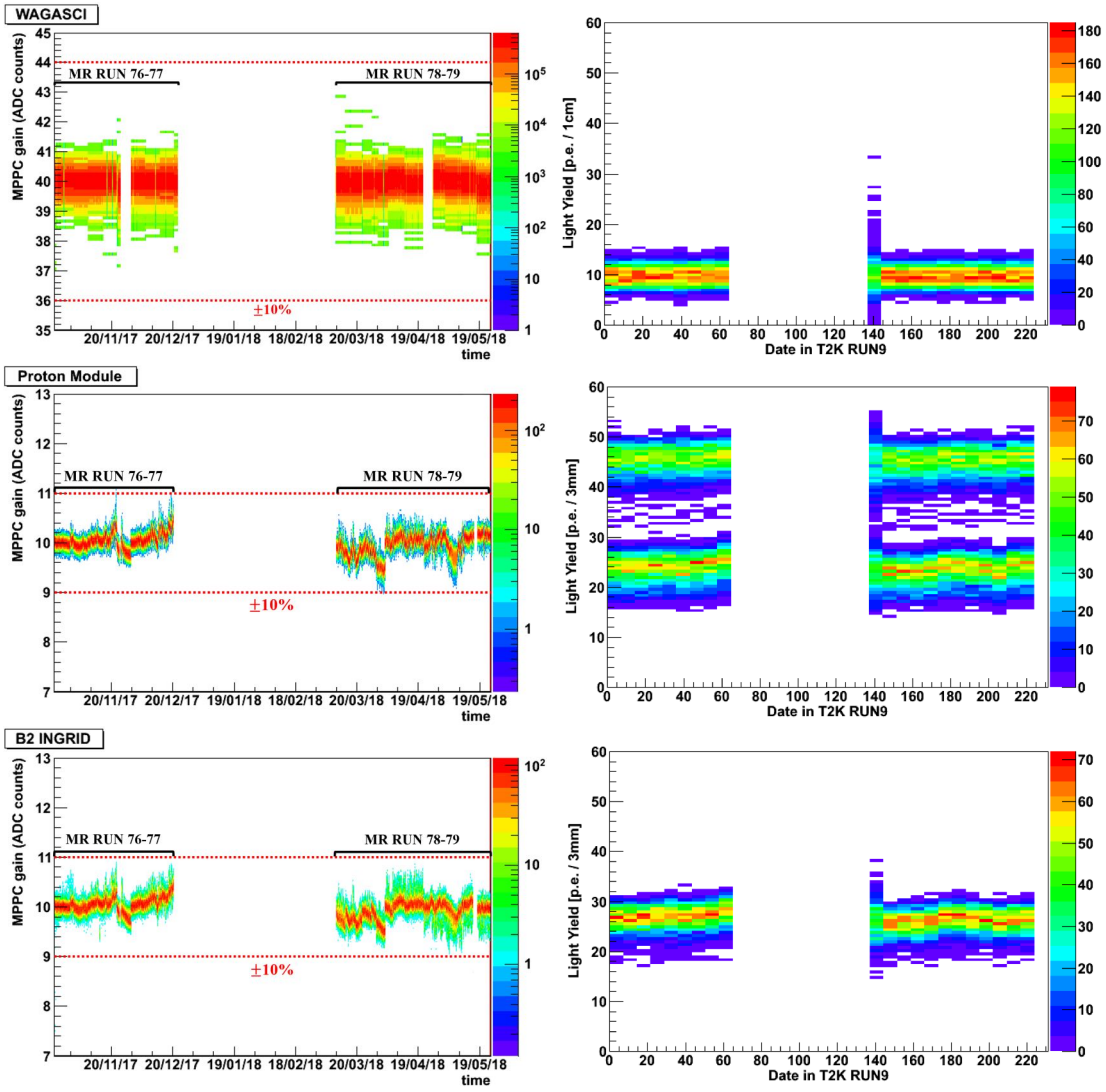

Figure 4.23: History of MPPC gains (left) and mean light yield of sand-muon hit (right). Top: WAGASCI. Middle: Proton Module. Bottom: INGRID.

4.6.2.2 Detector performance check

Since the WAGASCI module is a newly constructed module before the anti-neutrino beam data taking, the detector performances, such as hit efficiency and tracking efficiency, were checked by using the cosmic muons and sand muons, and it is confirmed that the Monte Carlo simulation described in Sec. 4.7 well describes the detector.

Hit efficiency of the scintillator layers are measured by sand muon and cosmic ray, as shown in Fig. 4.24. For calculation of the hit efficiency, the scintillators

are divided into 8 and 20 blocks in each view to check both forward and large angle events. Sand muon samples are used to estimated the hit efficiency for the 8 blocks along the beam axis, and cosmic muon samples are used for that for the 20 blocks along the perpendicular directions. The hit efficiency of a block is calculated when both of the neighboring blocks have the muon hits. Figure 4.25 shows the calculated hit efficiency as a function of the reconstructed three-dimensional track angle with respect to the neutrino beam. The data and Monte Carlo simulation expectation agree within 2%. The main reason for the inefficiency is gaps between each scintillator.

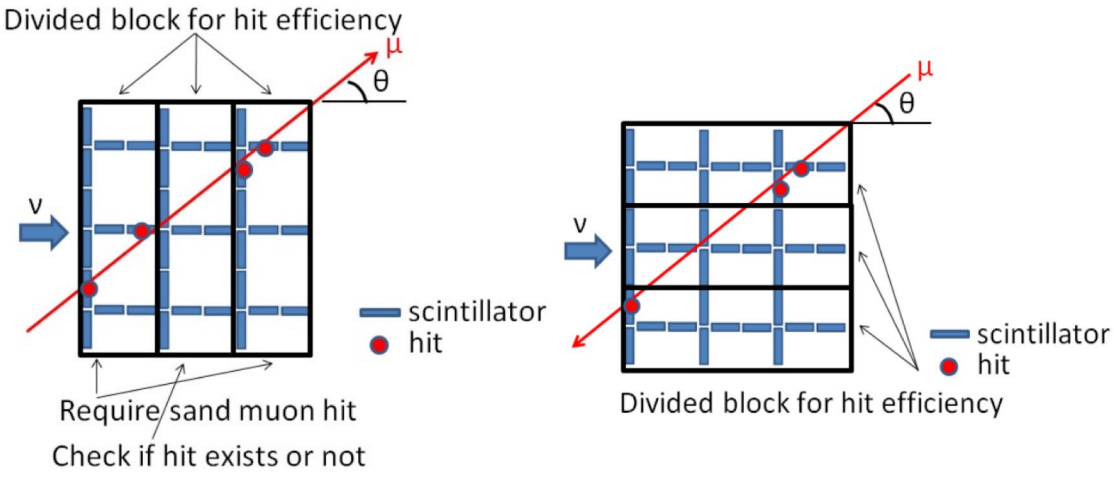

Figure 4.24: The calculation method for hit efficiency.

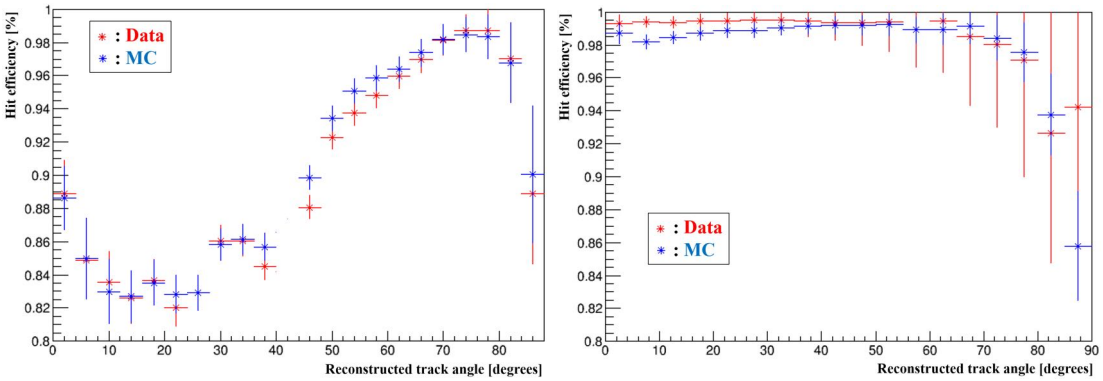

Figure 4.25: Hit efficiency estimated by cosmic muons (left) and sand muons (right).

The efficiency of two-dimensional track reconstruction with WAGASCI is checked by using the reconstructed INGRID tracks, as shown in Fig. 4.26. When INGRID

Table 4.2: Hit efficiency estimated by sand muons for each angle.

Track angle	Data [%]	MC [%]	|Data - MC| [%]
0-5deg	99.33	98.88	0.45
5-10deg	99.40	98.20	1.20
10-15deg	99.38	98.44	0.94
15-20deg	99.45	98.70	0.75
20-25deg	99.46	98.88	0.58
25-30deg	99.53	98.90	0.63
30-180deg	97.99	97.37	0.62

has a reconstructed three-dimensional track, the track is extended to WAGASCI and the distance between the track and hits of the WAGASCI is calculated. In the case of more than 3 hits within 20 cm, it is checked whether a two-dimensional track is reconstructed or not in WAGASCI for those hits. An efficiency of the track reconstruction is estimated as a function of the reconstructed INGRID track angle. Figure 4.27 and Table 4.3 show the results for the data and the Monte Carlo simulation. The Data and the Monte Carlo simulation agree with 1% level, except for the region of angle more than 30 degrees.

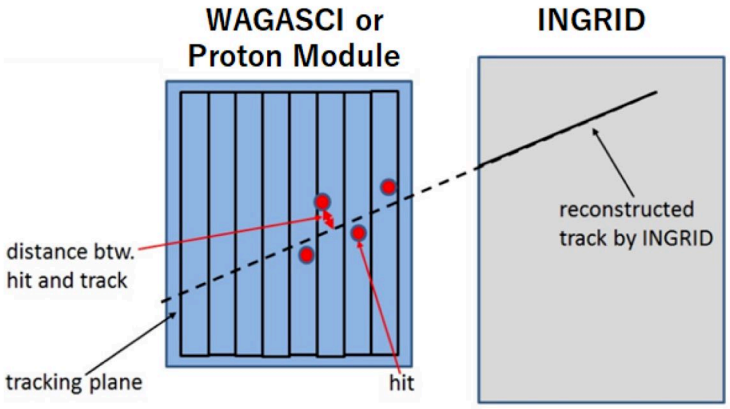

Figure 4.26: Concept of the method to evaluate the two-dimensional track reconstruction efficiency.

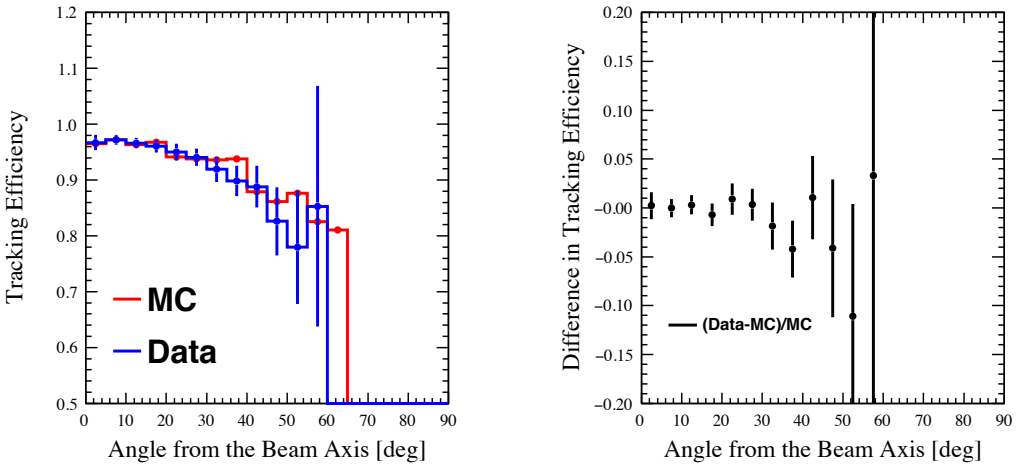

Figure 4.27: Two-dimensional track reconstruction efficiency in WAGASCI.

Table 4.3: Two-dimensional track reconstruction efficiency for each angle.

Track angle	Data [%]	MC [%]	Data - MC [%]
0-5deg	96.73	96.49	0.24
5-10deg	97.22	97.23	-0.01
10-15deg	96.62	96.30	0.32
15-20deg	96.08	96.74	-0.66
20-25deg	95.02	94.16	0.86
25-30deg	94.08	93.76	0.32
30-180deg	89.97	92.23	-2.26
Total	95.84	96.14	-0.30

4.6.3 Data set

The data set used for this analysis are from the anti-neutrino beam measurement from Oct. 2017 to May. 2018. The total number of protons on target (POT) is 7.908×10^{20}, which corresponds to 94.1% of the delivered neutrino beam spills. Table 4.4 shows the summary of data set for each sub-period within the data taking.

Table 4.4: Summary of the data set for WAGASCI, Proton Module and INGRID

MR Run	Run period	Beam good spills	Detector good spills	POT
76	Oct. 22 - Nov. 16, 2017	663378	653500	1.505×10^{20}
77	Nov. 16 - Dec. 22, 2017	932995	757003	1.796×10^{20}
78	Mar. 9 - Apr. 2, 2018	624486	615049	1.473×10^{20}
79	Apr. 4 - May 24, 2018	1334452	1276823	3.134×10^{20}
Total	Oct. 2017 - May. 2018	3555311	3302375	7.908×10^{20}

4.7 Monte Carlo simulation

In order to estimate the detection efficiency, background events, and detector responses, the Monte Carlo (MC) simulation is used. The whole simulation is composed of three separated parts;

- JNUBEAM [95] for neutrino flux expectation,
- NEUT [114] for neutrino interaction with a nucleus,
- and GEANT4-based dedicated detector simulation.

JNUBEAM simulates the neutrino productions via hadron decays, from the hadron production after 30 GeV protons striking on a graphite target, though propagation of the outgoing hadrons until the the detector, considering the secondary interactions. Neutrino interactions at the detector is generated by the NEUT program, combined with the generated neutrino flux. The details of the detector simulation are described in Sec 4.7.1

4.7.1 Detector simulation

In the GEANT4-based simulation, each detector among WAGASCI, Proton Module, and INGRID is generated, and they are placed in the detector hall surrounded by the concrete wall. The relative position of the installation are set according to the survey with a precision of 1 mm during the detector installation. The WAGASCI module is composed of a stainless tank, water in the stainless tank, scintillators in the water. The materials corresponding to the other detector components such as electronics are not implemented into the simulation, since their amount is negligibly small. It composes Proton Module only with scintillators, and INGRID with iron layers and scintillators. The configurations of Proton Module and INGRID are established since the previous analysis [62], while each component

of scintillators and electronics for the WAGASCI module is parametrized for this analysis according to the commissioning data taking since it is newly constructed. The relative positions of the scintillators within the detector are measured with precision of 1 mm during the construction, and the measured values are implemented into the detector simulation.

The modeling of the scintillator's structure is defined based on the measurement during the detector construction, as shown in Fig 4.15. The energy deposit of the charged particles on the scintillators are computed by GEANT4, and converted to the number of photons by parameters determined by the measurement during the anti-neutrino beam data taking. The effects for each step are implemented in the simulation:

- Quenching effect of the scintillator
- Dependency on hit position
- Attenuation by the propagation in the scintillator and in the wave-length shifting fiber
- Reflections at an edge of the fiber in the opposite side to the MPPC
- MPPC's response, including crosstalk, after-pulse, and saturation
- Scintillator's crosstalk
- Statistical fluctuation of the number of photons

In addition, the random noise from the MPPCs is implemented with 0.025 hits per beam bunch. The parametrization of those effects is summarized in Table 4.5. In oder to reproduce the individual difference, the mean light yield of each scintillator channel is corrected according to the measurement using the sand muons. Figure 4.28 shows the distribution of the mean light yield from the sand muons, comparing the data and the simulation. The mapping of the light yield for all of the 1280 scintillator channels in WAGASCI is shown in Fig. 4.29, including the five masked channels.

4.7.2 Generated neutrino interaction

In the WAGASCI simulation, neutrino interactions of $\overline{\nu}_\mu$, ν_μ, $\overline{\nu}_e$, and ν_e are generated on the whole region of water filled in the stainless water tank, the scintillators, and the stainless water tank, respectively. For Proton Module and INGRID, interactions on the scintillators and the iron layers are generated. The statistics used in the MC simulation corresponds to 1×10^{21} POT, to be normalized by the

Table 4.5: Parameters for the conversion from energy deposits to photons in the simulation.

Paramter	Value	Formula / Correction factor
Conversion from Energy deposit (dE) to p.e.	$\alpha = 20.5$ p.e./MeV	p.e. $= \alpha \times$ dE
Birk's constant	$\alpha = 0.0208$ cm/MeV	$1/(1 + \alpha \times \mathrm{dE}/\mathrm{d}x)$
Position dependency in the scintillator	$\lambda = 3.5$ cm	$\exp(-x/\lambda)$ x = distance from the fiber
Attenuation length in the wave-length shifting fiber	$\lambda = 241.7$ cm	$\exp(-x/\lambda)$ x = propagation length
Crosstalk between the scintillator channels	$\alpha = 0.64\%$	crosstalk $= \alpha \times$ p.e.
MPPC's saturation	$\mathrm{N_{pixel}} = 716$	$\mathrm{N_{pixel}} \times (1 - \exp(-\mathrm{p.e.}/\mathrm{N_{pixel}}))$
Crosstalk and after-pulse rate of MPPC	R = 2.7%	1 + R (R = Crosstalk rate + after-pulse rate)
Electronics noise	$\sigma_{\mathrm{pedestalwidth}} = 4.0\%$	$\mathrm{Gaus}(\mathrm{p.e.}, \mathrm{p.e.} \times \sigma_{\mathrm{pedestalwidth}})$

recored statistics for the cross section analysis. Figure 4.30 shows an example of the generated CCQE interactions on the scintillator of Proton Module.

The interactions on the walls of the detector hall are also generated, as shown in Fig. 4.31. Since the walls spread for the wide region so that it is rare for the interactions on those materials to contaminate the selected events in the detectors, the MC statistics is increased by 1000 times of that in the interactions on the detectors. The region of the interaction points is determined so that the effect from the interactions out of the region for the location of the detectors is negligible.

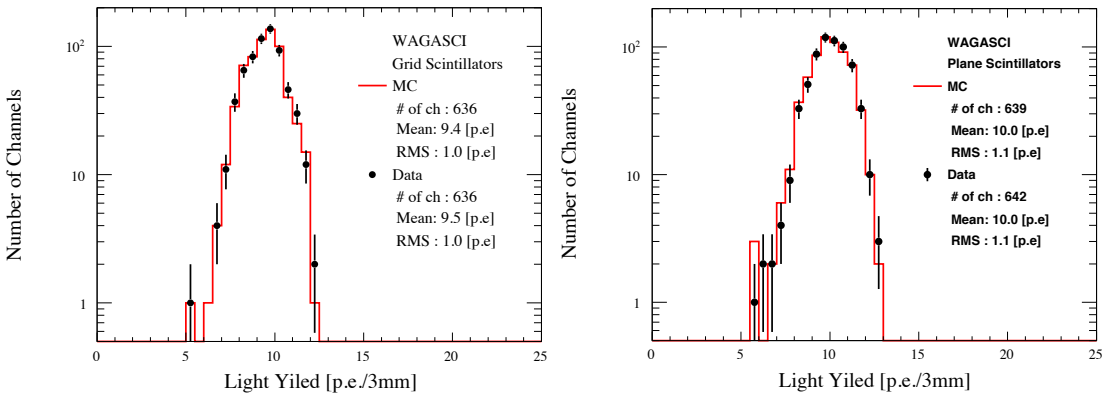

Figure 4.28: Distribution of the mean light yield for all of grid (top) and plane (bottom) scintillators in WAGASCI, using the sand muons.

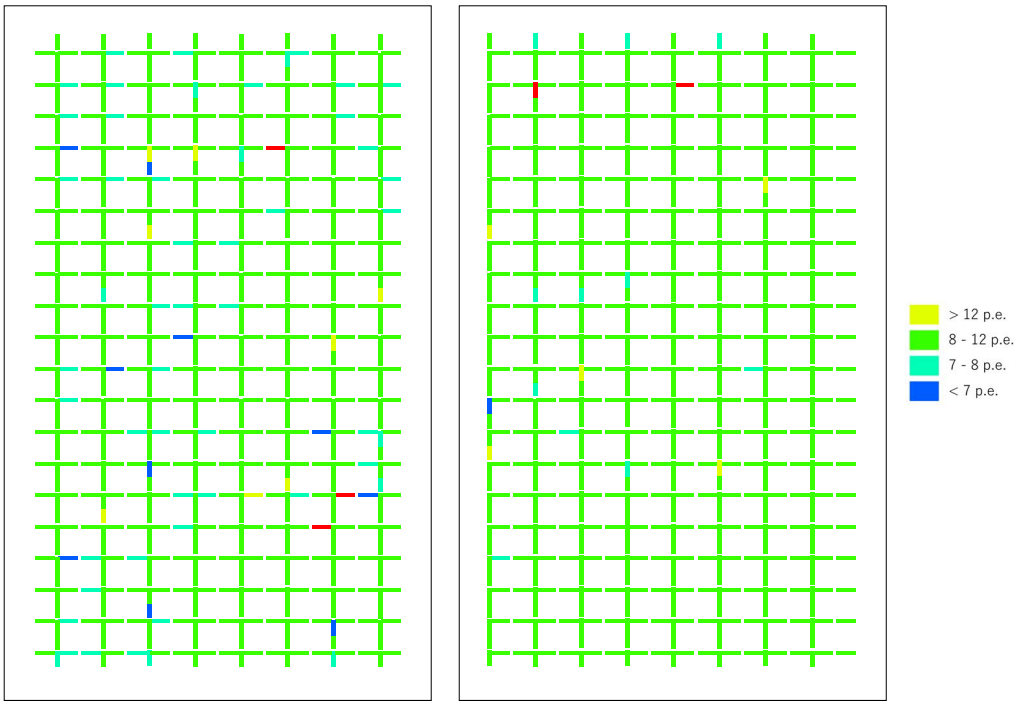

Figure 4.29: Distribution of the mean light yield in the top view (left) and side view (right) scintillators in WAGASCI, using the sand muons data. The masked channels are shown in the red color.

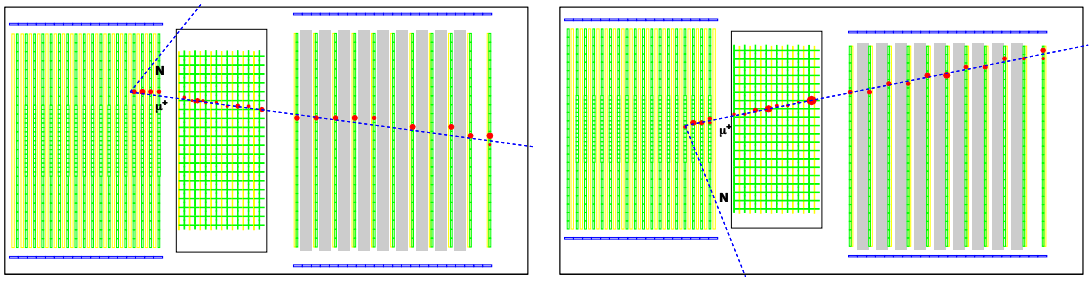

Figure 4.30: An example of the $\overline{\nu}_\mu$ CCQE event generated in the simulation. Left: the top view. Right: the side view. Green boxes: the scintillator channels active in each view. Yellow boxes: the scintillator bars active on the other view. Blue boxes: the veto layers, which is not used in this analysis. Gray boxes: the iron layers. Red circles show the energy deposit by their diameter. Water target is not shown in this display. Dotted lines show the initial direction of the generated particles.

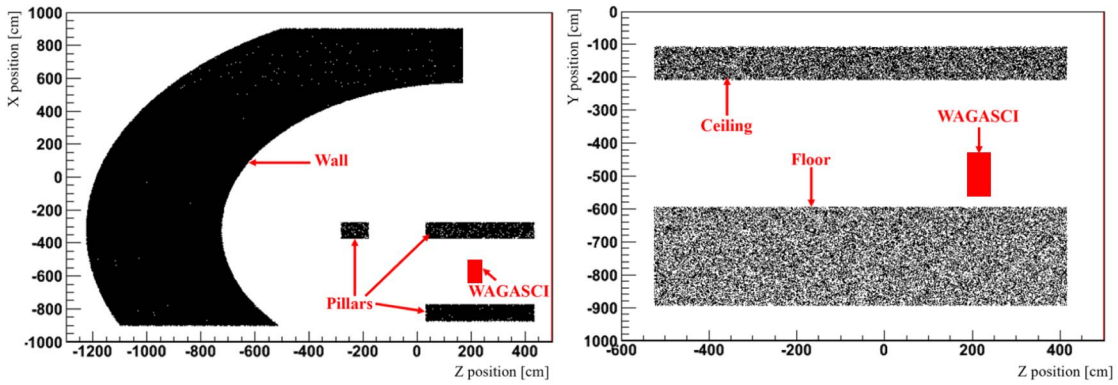

Figure 4.31: Black point shows the vertices of the generated neutrino interaction on the wall, pillars (right), ceiling and floor (left) in the J-PARC neutrino monitor building.

Chapter 5

Analysis strategy

5.1 Analysis overview

For the precise measurements of the neutrino oscillation parameters, understanding of the neutrino interactions on nucleus is crucial. In the future experiments, aiming at the observation of CP-violation in the neutrino sector, it is planed to reduce the systematic uncertainties on both of the ν_e appearance and $\overline{\nu}_e$ appearance down to few percents, hence the cross-section knowledge with the comparable level of precision is required. In T2K, the near detector, whose main target material is hydrocarbon, is present to constrain the neutrino beam flux and interaction rate, while the far detector, Super-Kamiokande, detects neutrino interactions on the water target. A proper modeling of neutrino interactions on different nucleus, especially on water (H_2O) and hydrocarbon (CH), is required to correctly extrapolate the constraints from the near detector to the far detector. However, there have been only few cross-section measurements with H_2O and CH target using the T2K anti-neutrino beam.

This analysis uses the data taken with the WAGASCI detector, Proton Module, and an INGRID module with the T2K anti-neutrino beam, in order to measure the neutrino charged-current cross sections on H_2O and CH nucleus as well as their ratio. The INGRID module is not used as the iron target in this analysis, since it has a large amount of materials between the tracking planes so that it is much less capable of detecting most of hadrons than the other two detectors are.

The focus of this analysis is on providing the flux-integrated $\overline{\nu}_\mu$ charged-current interactions with no charged pions nor proton in the final state, which is known as CC0π0p. The signal is defined based with the topology of the particles in the final state, instead of being defined with the neutrino interaction level such as CCQE. The topology defined as CC0π0p is what is expected in the $\overline{\nu}_\mu$ CCQE interactions, which has only a muon in the final state. This topology-based definition is prefer-

able since it is relatively less dependent of the indistinguishable background events, such as background events from 2p2h interactions with protons absorbed to the signal defined by CCQE. The signal in this analysis is defined with kinematics of muons, charged pions, and protons according to the detection efficiencies in the WAGASCI detector and Proton Module.

In the case of $\overline{\nu}_\mu$ cross sections, ν_μ interactions contribute as one of the dominant background events, since ν_μ interaction has a cross section larger than $\overline{\nu}_\mu$ interaction does and needs to be subtracted based on the Monte Carlo simulation. For the purpose to improve the experimental precision, cross sections including both $\overline{\nu}_\mu$ and ν_μ, which is defined as $\overline{\nu}_\mu + \nu_\mu$ cross sections, are provided as well as $\overline{\nu}_\mu$ cross sections. The neutrino event selections are in common between the $\overline{\nu}_\mu$ and $\overline{\nu}_\mu + \nu_\mu$ cross sections, and the subtraction of the background events is the only difference between those two measurements.

The neutrino cross sections are extracted using the number of selected events on WAGASCI and Proton Module. The neutrino event selection is applied to enrich the charged-current inclusive interactions, and the selected events are categorized according to the number of reconstructed track and the reconstructed angle. Among the calculated cross sections, those of non-CC0π0p and CC0π0p with a large muon angle have strong dependency on the neutrino interaction model due to their small signal purities and low selection efficiencies. Hence, the total cross section is only calculated for CC0π0p with a forward scattering muon, ignoring the two categories largely dependent on the simulation. Most of the background events are estimated by the Monte Carlo simulation and subtracted from the selected events, except for the background events from neutrino interactions on the plastic scintillators in WAGASCI, which are calculated based on the number of selected events in Proton Module. For the cross section extraction, the D'Agostini unfolding method[115] is used, and the true phase space is iteratively recovered by using the reconstructed phase space in the real data, in order to achieve the prior distribution independent of the simulation. In the final results, the total cross sections of CC0π0p with a muon angle less than 30 degrees and the differential cross sections with respect to the muon's angle are presented. The total cross section is calculated as a sum of the differential cross sections.

Due to the limited statistics, the statistical error is one of the dominant errors on the final results, to be about 5-6% for absolute cross sections, $\sigma_{\mathrm{H_2O}}$ and σ_{CH}, and about 8% for the cross section ratio, $\sigma_{\mathrm{H_2O}}/\sigma_{\mathrm{CH}}$. The systematics errors are estimated with three different sources; neutrino beam flux prediction, neutrino interaction model, and detector response. The absolute cross section measurements suffer from about 10% uncertainty of the neutrino flux, but those uncertainties are mostly canceled in the cross section ratio measurement since the same neutrino beam is measured between the detectors. The uncertainties from neutrino interac-

tion model mainly affect the estimation of detection efficiency and the subtraction of background events. Each parameter relevant to this analysis is varied to cover the current understanding of the model.

The expected anti-neutrino beam flux is shown in Fig. 5.1. The anti-neutrino beam is composed with 91.0% of $\overline{\nu}_\mu$, 8.0% of ν_μ, 0.8% of $\overline{\nu}_e$, and 0.2% of ν_e. The energy distribution of $\overline{\nu}_\mu$ has the mean energy of 0.86 GeV, the peak energy of 0.66 GeV, and $^{+0.40}_{-0.25}$ GeV for its 1σ spread. The mean direction of neutrinos is not in parallel with the global z axis with the detector coordinates. Figure 5.2 shows the distribution of $\overline{\nu}_\mu$ in the expected anti-neutrino beam, and its mean directions are shown in Table 5.1. All of the angles used to measure the neutrino cross section in this analysis are defined with respect to the mean direction of $\overline{\nu}_\mu + \nu_\mu$, -1.37 degrees along the horizontal axis and -4.76 degrees in the vertical axis.

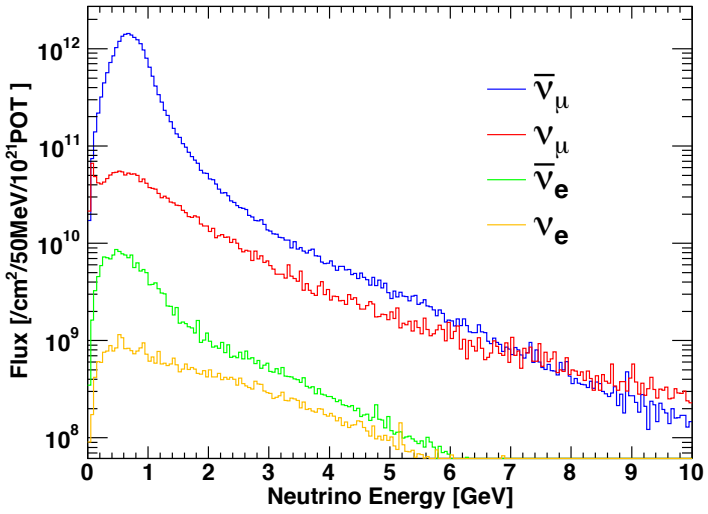

Figure 5.1: The neutrino beam flux expected by JNUBEAM.

Table 5.1: Mean directions of neutrino in the expected neutrino beam [deg]

	Horizontal	Vertical
ν_μ	-1.34	-4.73
$\overline{\nu}_\mu$	-1.37	-4.76
$\overline{\nu}_\mu + \nu_\mu$	-1.37	-4.76

The neutrino interactions in the WAGASCI module are simulated with JNUBEAM and NEUT, and the distribution as a function of true neutrino energy is shown

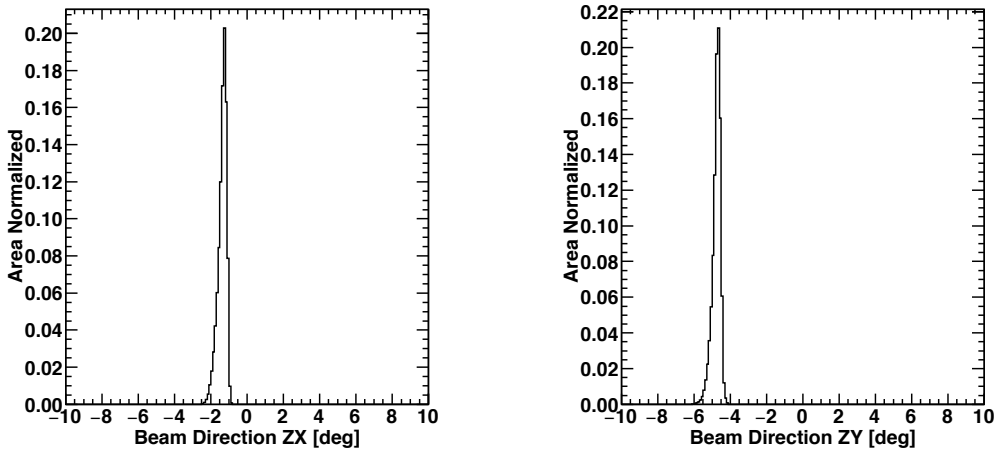

Figure 5.2: Directions of $\overline{\nu}_\mu$ in the expected neutrino beam, along the horizontal direction (left) and vertical direction (right).

in Fig. 5.3. Table 5.2 shows fractions for each neutrino interaction type. The charged-current interactions in the range of sub-GeV neutrino energy are dominated by CCQE, followed by CC1π. Among all the interactions, ν_μ interactions are about the same amount as $\overline{\nu}_\mu$ CCQE interactions, since the ν_μ cross sections are larger by about three times than $\overline{\nu}_\mu$ cross sections. Figure 5.4 shows the two-dimensional distribution of momentum and angle of muons from $\overline{\nu}_\mu$ charged-current interactions in WAGASCI.

The expected inclusive cross sections for σ_{H_2O}, σ_{CH}, and $\sigma_{H_2O}/\sigma_{CH}$ are summarized in Table 5.3. The difference in the cross section ratios between H_2O and CH mainly comes from the final state interactions in the nucleus. The two cross sections with different nuclear effects are shown. For the modeling of CCQE, RFG with RPA corrections is considered as the nuclear effect.

5.2 Analysis methodology

5.2.1 Flux-integrated cross section

In neutrino cross section measurements, the differential cross section values are extracted by the number of signal events on each of bin for true phase space (N_i^{sig}), corrected by the detection efficiency expected by the Monte Carlo simulation ($\varepsilon_i^{\mathrm{MC}}$),

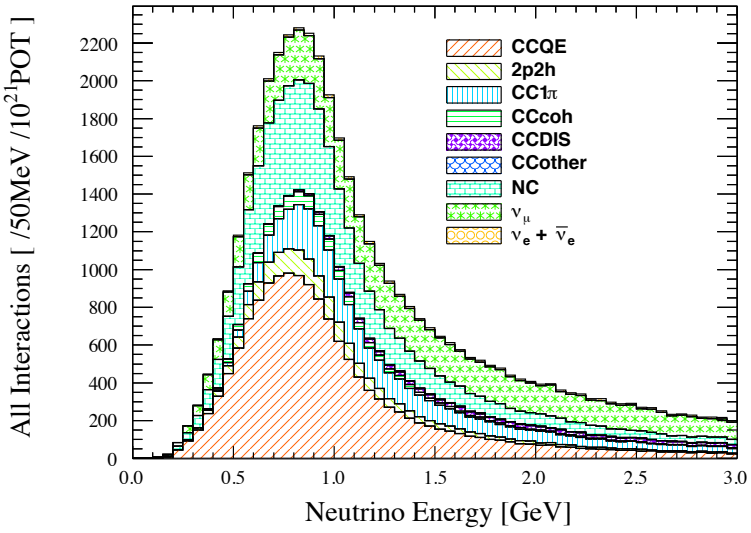

Figure 5.3: Expected number of events as a function of true neutrino energy simulated with JNUBEAM and NEUT.

number of target nucleons in the fiducial volume (T), and neutrino beam flux (Φ):

$$\frac{\mathrm{d}\sigma}{\mathrm{d}x_i} = \frac{N_i^{\mathrm{sig}}}{\varepsilon_i^{\mathrm{MC}}\Phi T} \times \frac{1}{\Delta x_i}, \tag{5.1}$$

where x_i is a differential kinematic variable, Δx_i is the width of the bin (Δx_i should be the bin area in the case of double-differential cross sections). In order to directly compare the measured cross sections between different experiments, the result should be fully corrected with the neutrino beam flux and provided as a "flux-unfolded" cross section:

$$\frac{\mathrm{d}\sigma}{\mathrm{d}x_i} = \frac{N_i^{\mathrm{sig}}}{\varepsilon_i^{\mathrm{MC}} \int_{E_\nu^{\mathrm{min}}(i)}^{E_\nu^{\mathrm{max}}(i)} \omega_i(E_\nu)\Phi(E_\nu)\mathrm{d}E_\nu T} \times \frac{1}{\Delta x_i}, \tag{5.2}$$

where $\omega_i(E_\nu)$ is a neutrino energy distribution in i-th bin for the kinematic variable, x_i, and $E_\nu^{\mathrm{max\ (min)}}(i)$ is the maximum (minimum) energy of the distribution. In this case it is indispensable to know a proper neutrino energy distribution in each bin for the kinematic variable, hence the measurement has a strong dependence on the neutrino beam flux prediction used for this correction. There is another option to estimate the flux-contributions on each bin:

$$\frac{\mathrm{d}\sigma}{\mathrm{d}x_i} = \frac{N_i^{\mathrm{sig}}}{\varepsilon_i^{\mathrm{MC}} \int_{E_\nu^{\mathrm{min}}(i)}^{E_\nu^{\mathrm{max}}(i)} \Phi(E_\nu)\mathrm{d}E_\nu T} \times \frac{1}{\Delta x_i}, \tag{5.3}$$

Table 5.2: Expected number of interactions with 1×10^{21} POT in the WAGASCI module, and fractions of each interaction mode.

Interaction mode	Number of events	Fraction [%]
$\overline{\nu}_\mu$ CCQE	15867.2	30.4
$\overline{\nu}_\mu$ 2p2h	2282.6	4.4
$\overline{\nu}_\mu$ CC1pi	5701.2	10.9
$\overline{\nu}_\mu$ CCcoh	1093.2	2.1
$\overline{\nu}_\mu$ CCDIS	1651.2	3.2
$\overline{\nu}_\mu$ CCother	245.5	0.5
$\overline{\nu}_\mu$ NC	10676.3	20.4
ν_μ	13936.6	26.7
$\nu_e + \overline{\nu}_e$	819.8	1.6
Total	52273.7	100.0

Table 5.3: Expected flux averaged $\overline{\nu}_\mu$ CC0π0p cross section with $\theta_\mu < 30$ deg and $P_\mu > 0.4$ GeV/c on H_2O and CH by NEUT. Neutrino interaction parameters used for calculation are described in Sec. 7.3.2.

	NEUT expectation
σ_{H_2O}	1.013×10^{-39}cm^2
σ_{CH}	1.051×10^{-39}cm^2
$\sigma_{H_2O}/\sigma_{CH}$	0.964

where the result is more dependent on the experiment since it is not fully unfolded according to the proper distribution of neutrino energy within each bin. The result still has model-dependency due to the estimation of the minimum (maximum) neutrino energy in each bin, $E_\nu^{\mathrm{min(max)}}(i)$, to extract the average flux in the bin.

Cross sections provided in this thesis are "flux-integrated" cross sections, where the neutrino beam flux, Φ in Eq. 5.1, is simply taken as a an integrated beam flux for the whole region. These cross sections are dependent on experiments, but no assumption is required on the neutrino energy distribution in each bin for the kinematic variable. In this case, the results can be convoluted with the shape of the flux used in the analysis.

5.2.2 Topology-based signal definition

Cross sections of true neutrino interactions, such as CCQE, have been measured in various experiments. However, it is impossible to completely access to such a pure neutrino-nucleon interaction even in the case of an ideal detector, since any neutrino interactions are distorted by the final state interactions and suffer from

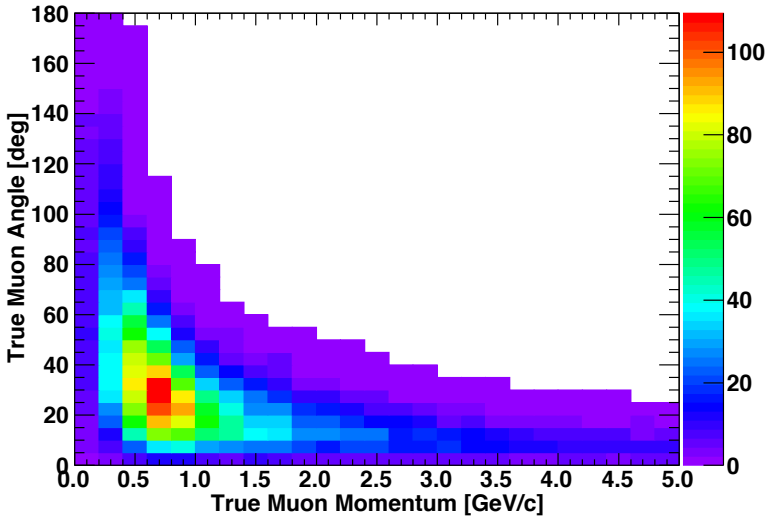

Figure 5.4: Expected angle and momentum distribution of muons from the $\overline{\nu}_\mu$ charged-current interactions in WAGASCI.

indistinguishable background events. For example, in the case of a CCQE cross section measurement, CC interactions with a single-pion production effectively becomes such an inevitable background when the produced pion is absorbed inside the nucleus. In order to subtract such background events, the result must fully rely on the neutrino interaction model. Hence, it is recently preferable to extract cross section according to the interaction topology, such as CC0π. In the case of the topology-based interactions, the signal is defined with kinematics of outgoing particles in the final state, which can be directly measured in the detector. Although the cross section measurement with the interaction topology makes it more difficult to directly compare the result with theories since the signal is composed of various true interactions, the result is less dependent on the simulation.

For calculations of differential cross sections, variables accessible with the detector should be selected in order to avoid dependency on neutrino interaction model. Variables directly related to neutrino interactions, such as neutrino energy (E_ν) and four momentum transfer (Q^2), should be avoided since the smearing between those true variables and the reconstructed variables strongly depends on the neutrino interaction model. On the other hand, variables related to kinematics of observable particles, such as momentum and angles of muons and protons, only have dependency on the detector response in association between its true value and reconstructed value.

In addition, when a measurement includes undetectable phase space, correc-

tions on such a region lead to a bias due to the interaction model applied. Hence, phase space of the signal should be restricted in order to focus on a region within the detector acceptance.

The analysis in this thesis provides CC0π0p cross sections with respect to momenta and angles of muons, with additional restriction based on kinematics of proton and charged pion.

5.2.3 Multiple bin measurements

5.2.3.1 How to define binning

In order to obtain as much information as possible, it is ideal to provide differential cross sections with respect to all meaningful variables including angles and momentums of outgoing particles. In addition, it is desirable to provide differential cross section in a higher dimension, such as $\mathrm{d}\sigma/\mathrm{d}\theta_\mu \mathrm{d}p_\mu$. However, it is difficult to calculate such higher-dimensional differential cross sections in a real measurement in the case of finite statistics and limited detector resolutions. Hence it is required to select a proper binning for each measurement. First, the number of entries in each bin should be kept sufficient so that its statistical uncertainty is comparable to systematic uncertainty on each bin. Second, the width of the bin should be comparable with the detector resolution in the variable, otherwise each bin in the true phase space has a wide template with respect to bins in the reconstructed phase space so that it results in a strong anti-correlation between the bins.

In the analysis of this thesis, events from CC0π0p with a muon angle less than 30 degrees are separated into 6 bins every 5 degrees with respect to muon's angle, so that entries on each bin become a level of 100 events.

5.2.3.2 Unfolding method

An unfolding, that is also called a deconvolution, is applied in order to remove the detector smearing, since the detector resolution is limited:

$$\frac{\mathrm{d}\sigma}{\mathrm{d}x_i} = \sum_j \frac{\tilde{U}_j^{-1}(N_j^{\mathrm{sel}} - N_j^{\mathrm{BG}})}{\varepsilon_i^{\mathrm{MC}} \Phi T} \times \frac{1}{\Delta x_i}, \tag{5.4}$$

where the number of selected events (N_j^{sel}) after subtracted by the number of background events (N_j^{BG}) is corrected by an unfolding matrix ($\tilde{U}_j^{-1}$). The simplest method is to invert the smearing matrix, $\mathbb{P}(X_j^{\mathrm{reco}}|C_i^{\mathrm{true}})$, to obtain the unfolding matrix.

In this analysis, the D'Agostini unfolding[115] is adapted, where the unfolding matrix is iteratively computed using the number of selected events and the smearing matrix estimated by the Monte Carlo simulation.

Chapter 6

Neutrino event selection and categorization

6.1 Signal definition

In this analysis, the signal is defined as charge-current interaction with no pions nor protons (CC0π0p) and the cross sections are extracted for two samples:

- CC0π0p events including $\overline{\nu}_\mu$ interactions only ($\overline{\nu}_\mu$ cross section)
- CC0π0p events including both $\overline{\nu}_\mu$ interactions and ν_μ interactions ($\overline{\nu}_\mu$ + ν_μ cross section)

In order to restrict the phase space to the region with a high detection efficiency for each of main charged particles, kinematics of muons, charged pions, and protons are limited in the the CC0π0p signal events

6.1.1 Kinematics of muons

Characteristics of charged-current interactions are emitting a muon: μ^+ from $\overline{\nu}_\mu$ interactions and μ^- from ν_μ interactions. Muons are able to penetrate large amount of materials compared with the other particles, hence a muon track is identified by setting a threshold on path length. In this analysis, the muon identification is performed by tracking with the INGRID module, which works as a muon range detector for WAGASCI and Proton Module. The minimum path length for tracks in INGRID is 6.5-cm iron as a width of a layer, hence the detection efficiency of muons whose momentum is less than 400 MeV/c is very low. The detectable phase space for muons are defined as:

- $P_\mu > 400$ MeV/c.

6.1.2 Kinematics of protons and pions

The detectable phase spaces for pions and protons are determined by the detection efficiencies for each detector. Figures 6.1–6.3 show the detection efficiencies of proton and pion in WAGASCI, and Fig. 6.4–6.6 show those in Proton Module. Regions where the detection efficiencies are flat are defined as detectable phase spaces. The WAGASCI detector has plastic scintillators forming three-dimensional cellular structure so that the water target is surrounded by them for almost 4π solid angle. Hence, the detection efficiencies for the region of a large scattering angle in WAGASCI are better than those in Proton Module.

The phase space for each particle in order to measure the cross sections in this analysis is defined with an overlapped region between the two detectors, since it is required to have a common phase space for the cross section ratio, $\sigma_{H_2O}/\sigma_{CH}$. In addition, for subtracting the background events from interactions on plastic scintillators of the WAGASCI detector by using the Proton Module data, it is preferable to define a unified phase space between those two modules. Hence the detectable phase space for pions and protons in this analysis is defined as follows:

- $P_p > 0.6$ GeV/c and $\theta_p < 70$ degrees.
- $P_\pi > 0.2$ GeV/c and $\theta_\pi < 70$ degrees.

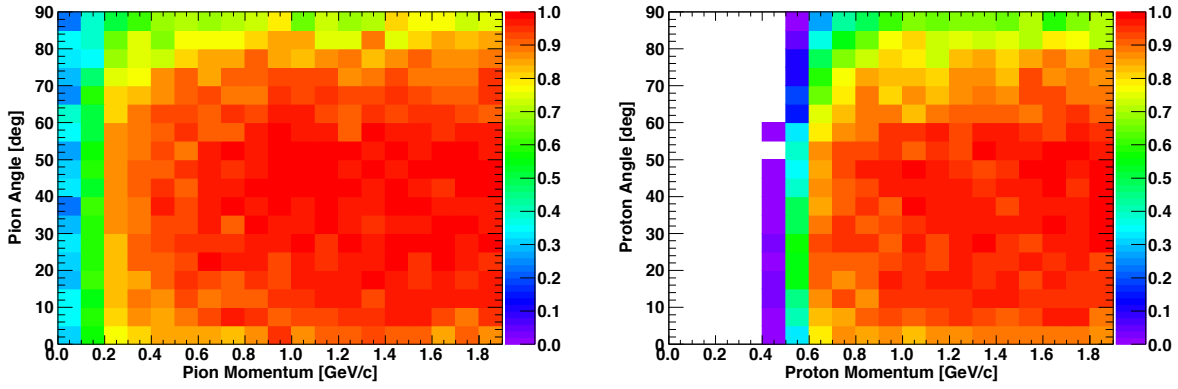

Figure 6.1: Detection efficiency of charged pion (left) and proton (right) in WAGASCI.

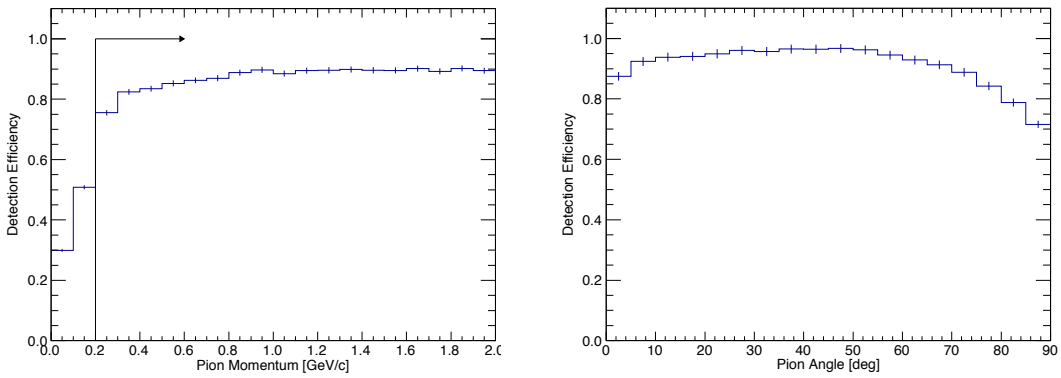

Figure 6.2: Detection efficiency of charged pion in WAGASCI. Left: Distribution as the function of true pion momentum. Right: Distribution as the function of true pion angle, when its momentum is larger than 0.2 GeV/c.

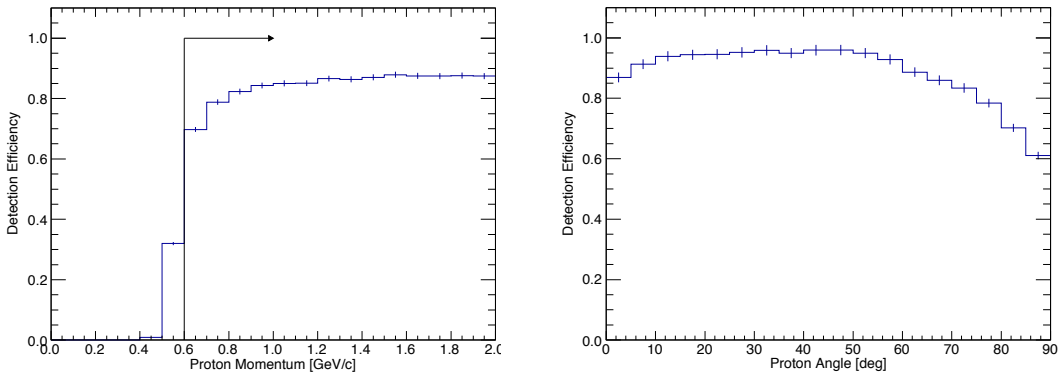

Figure 6.3: Detection efficiency of proton in WAGASCI. Left: Distribution as the function of true proton momentum. Right: Distribution as the function of true proton angle, when its momentum is larger than 0.6 GeV/c.

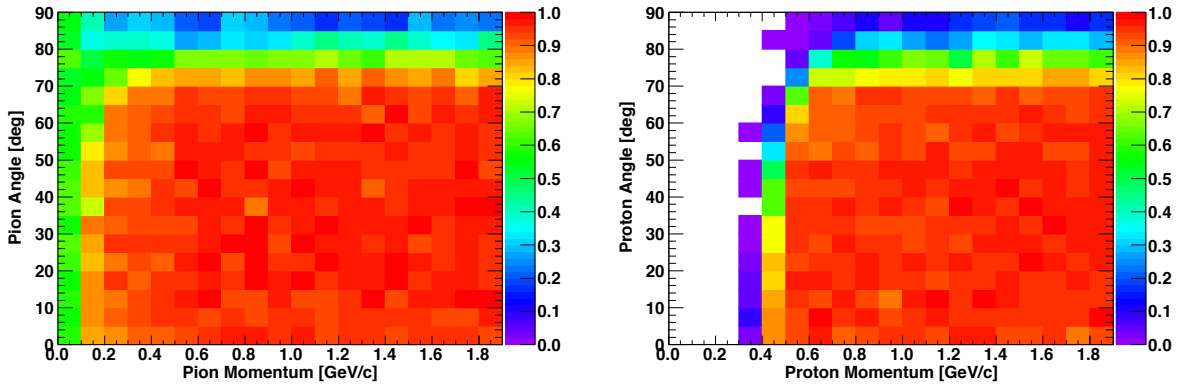

Figure 6.4: Detection efficiency of charged pion (left) and proton (right) in Proton Module.

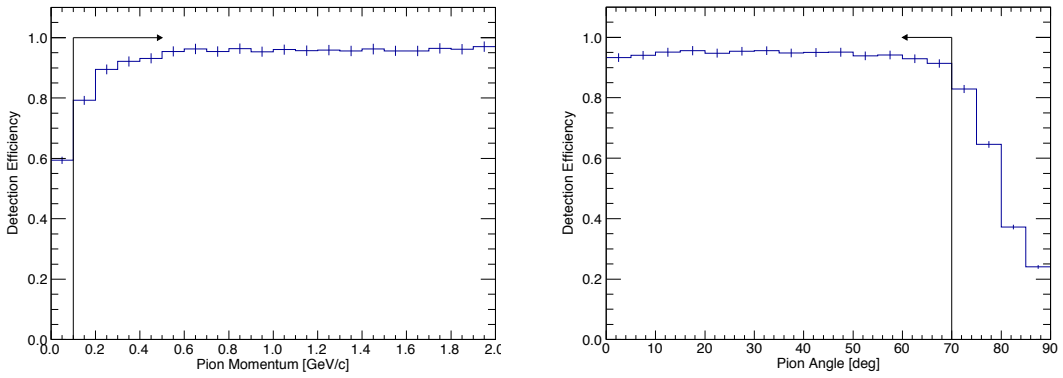

Figure 6.5: Detection efficiency of charged pion in Proton Module. Left: Distribution as the function of true pion momentum, when its angle is less than 70 degrees. Right: Distribution as the function of true pion angle, when its momentum is larger than 0.1 GeV/c.

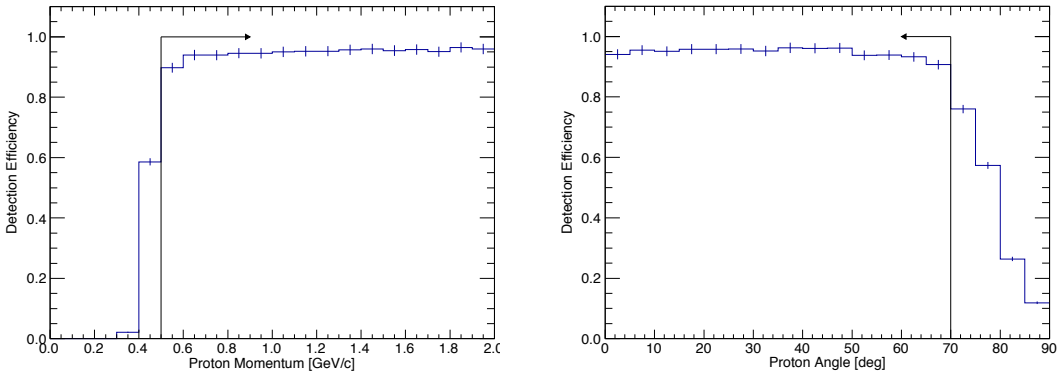

Figure 6.6: Detection efficiency of proton in Proton Module. Left: Distribution as the function of true proton momentum, when its angle is less than 70 degrees. Right: Distribution as the function of true proton angle, when its momentum is larger than 0.5 GeV/c.

6.2 Event selection

6.2.1 Overview of the event selection

The main target of this analysis is $\overline{\nu}_\mu$ CC0π0p with a muon angle less than 30 degrees. The $\overline{\nu}_\mu$ CC0π0p events are expected to only have a muon track in the detectable region, while the other charged-current events have additional tracks from other charged particles such as pions and proton. Hence the signal purity of $\overline{\nu}_\mu$ CC0π0p events is enriched by restricting the number of reconstructed tracks to be one and the reconstructed angle to be less than 30 degrees. Those events, however, are affected by background events from charged-current interactions out of the target phase space, such as

- non-CC0π0p events that pass the CC0π0p selection, and
- CC0π0p events out of the restricted phase space,

especially for the regions around boundaries of the defined phase space. In order to avoid dependence on the Monte Carlo simulation for subtraction of those background events as much as possible, the event selection is only applied to enrich the charged-current interactions and the whole of the selected events, which is defined as "analysis sample", are used to measure the cross sections.

The event selection is applied to reconstruct a muon track with a vertex in the fiducial volume of each detector. It is based on information of track reconstruction,

which uses hit information including position, charge, and timing. The overall flow of the event selection is as follows:

1. Time clustering
2. Two-dimensional track reconstruction on each detector
3. Two-dimensional track matching between detectors
4. Three-dimensional track reconstruction
5. Vertex reconstruction
6. Beam timing cut
7. Upstream veto cut
8. Fiducial volume cut
9. Acceptance cut

In order to distinguish the region with a high purity of CC0π0p with a muon angle less than 30 degrees from the other region, the analysis samples are categorized according to

- the number of reconstructed tracks, and
- the reconstructed angle.

Figure 6.7 shows the basic idea of a part of the event selections until the vertex extraction.

6.2.2 Categorization of events

The analysis sample is separated into 8 categories according to the number of reconstructed tracks and reconstructed angle. Categorization of the true phase space is determined based on the definition of CC0π0p, so that the charged-current events are separated into 8 bins, including CCother events and CC0π0p events with a muon angle larger than 30 degrees. The categorization based on true phase space and reconstructed tracks is shown in Table 6.1. Most of CCother events are expected to correspond to the multi-track sample.

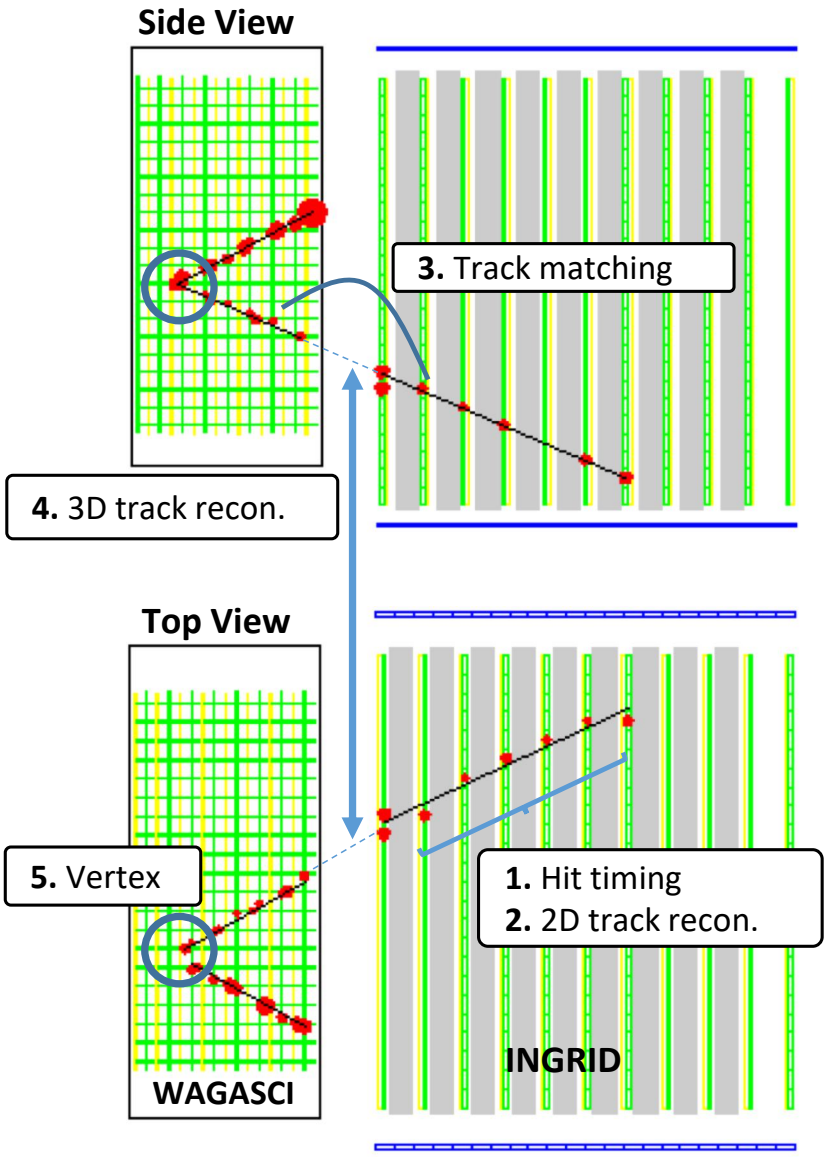

Figure 6.7: The summary of the event selections from the hit timing clustering to the vertex extraction.

Table 6.1: Categorization based on true phase space and reconstructed tracks.

Bin number	True phase space	Reconstructed tracks
0	CCother	Multi-track
1	CC0π0p : muon's angle 0-5 deg	Single-track : 0-5 deg
2	CC0π0p : muon's angle 5-10 deg	Single-track : 5-10 deg
3	CC0π0p : muon's angle 10-15 deg	Single-track : 10-15 deg
4	CC0π0p : muon's angle 15-20 deg	Single-track : 15-20 deg
5	CC0π0p : muon's angle 20-25 deg	Single-track : 20-25 deg
6	CC0π0p : muon's angle 25-30 deg	Single-track : 25-30 deg
7	CC0π0p : muon's angle 30-180 deg	Single-track : 30-180 deg

6.2.3 Selection criteria

6.2.3.1 Time clustering

A "hit" is defined as a channel with a signal larger than 2.5 photo-electrons. For WAGASCI, all hits in a neutrino beam bunch are clustered together if there are more than or equal to three hits in the bunch, since electronics for the WAGASCI detector is not capable of recording the exact hit timing within a beam bunch.

In Proton Module and INGRID, three hits or more are required within 100 nsec, to start clustering by the hit timing. All the hits within 50 nsec from the average time are classified into a cluster. By this clustering, random MPPC noise hits are reduced. Figure 6.8 shows distribution of the hit timings for all hits recorded and hits selected after the time clustering.

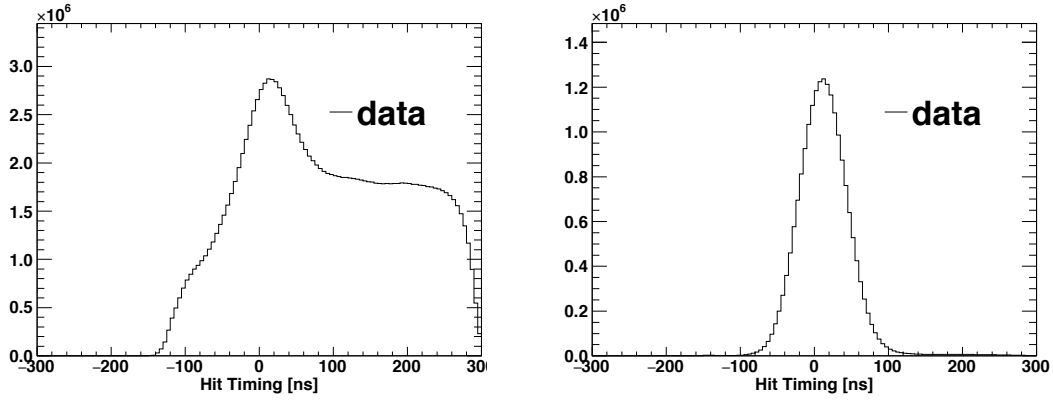

Figure 6.8: Measured timings of hits in Proton Module from the expected beam timing. Left: all hits. Right: hits clustered by the timings.

6.2.3.2 Two-dimensional track reconstruction

Hits which pass the time clustering are reconstructed as a linear track in each of the x-z (top) and y-z (side) views on each detector. The cellular automaton algorithm [116] [117] [107] is used for the reconstruction. A cell is defined as a pair of two neighbor hits, if they are one plane or two planes away from each other. The cells are connected as a track based on a likelihood fitting with a linear function. The hit position is basically assumed to be the center of the scintillator channel. As there are multiple hits next to each other in a plane, they are combined and the position is calculated based on the light yield of the hits. The minimum length to be a track is defined as two cells, which corresponds to three hits.

6.2.3.3 Two-dimensional track matching between detectors

Reconstructed two-dimensional tracks on each detector are matched in each view between any combinations of two detectors among WAGASCI, Proton Module, and INGRID:

- WAGASCI – INGRID
- Proton Module – WAGASCI
- Proton Module – INGRID

If a pair of tracks are found in the same neutrino beam bunch, the difference in the track angle and distance between the two tracks are checked if it meets the following criteria to be matched:

- Upstream edge of the track in the downstream detector is in either of the first two layers in the detector.
- Downstream edge of the track in the upstream detector is in either of the last two layers in the detector.
- Difference in the reconstructed angle between the two tracks must be less than 35 degrees.
- At the halfway point between the two detectors, the distance between the two tracks is less than 150 mm.

Figure 6.9 shows the difference of the angle and distance for matching tracks between WAGASCI and INGRID.

In order to select a muon track with a high purity, a track in WAGASCI or Proton Module is required to be matched with a track in INGRID. In the case that a track in Proton Module is matched with an INGRID-matched WAGASCI track, it is also identified as an INGRID-matched track.

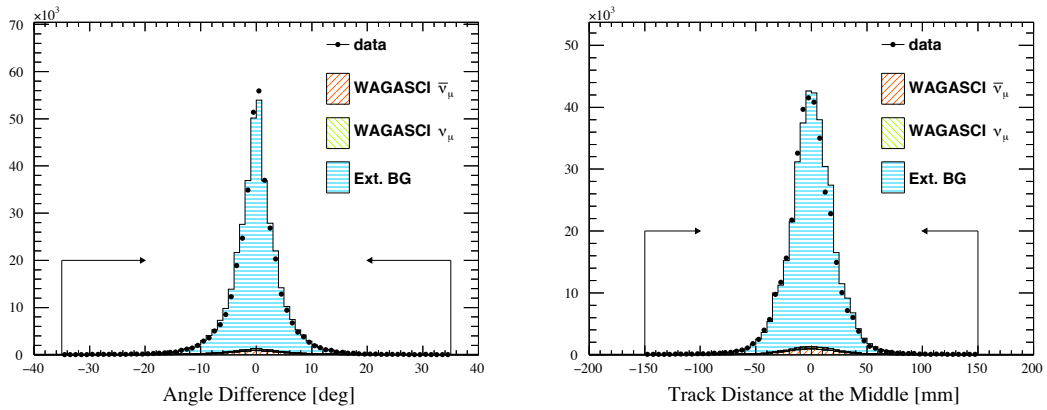

Figure 6.9: Difference in angle (left) and distance (right) of the reconstructed track between WAGASCI and INGRID. For these plots, all of the reconstructed two-dimensional tracks are used.

6.2.3.4 Three-dimensional track reconstruction

In order to reconstruct a three-dimensional track, a pair of two-dimensional tracks in a different view from each other is required to meet a criteria in their upstream points. The difference of the upstream point z of a track in the x-z view and one in the y-z view should be less than or equal to one parallel plane. If there are more than one candidate of pair of two-dimensional tracks, the pair with their stopping points closest between xz-plane and yz-plane is taken as a three-dimensional track.

6.2.3.5 Vertex reconstruction

A vertex in WAGASCI or Proton Module is defined as the initial point of the longest three-dimensional INGRID-matched track from each detector, since a muon track is required for selecting charged-current interactions. If there is an extra track around the vertex and its initial point is close to the vertex with respect to the following criteria, it is identified as a track outgoing from the same vertex:

- Sum of the z position differences between the upstream edges of the two tracks in the side and top views is less than three parallel planes:

$$|\Delta z_x| + |\Delta z_y| < 3 \text{ plane}. \tag{6.1}$$

  where Δz_x and Δz_y are the z position differences between the upstream edges of the two tracks in the x and y views.

- Distance between the upstream edges of the two tracks in the xy-plane is less than 150 mm:

$$\sqrt{\Delta x^2 + \Delta y^2} < 150 \text{ mm}. \tag{6.2}$$

  where Δx and Δy are the distances between the x and y positions of the upstream edges of the two tracks.

Figure 6.10 shows the $|\Delta z_x| + |\Delta z_y|$ and $\sqrt{\Delta x^2 + \Delta y^2}$ distributions used for this cut. Every single vertex reconstructed by this criteria is expected to correspond to a single neutrino interaction, otherwise multiple external charged particles accidentally leave the initial points close to each other.

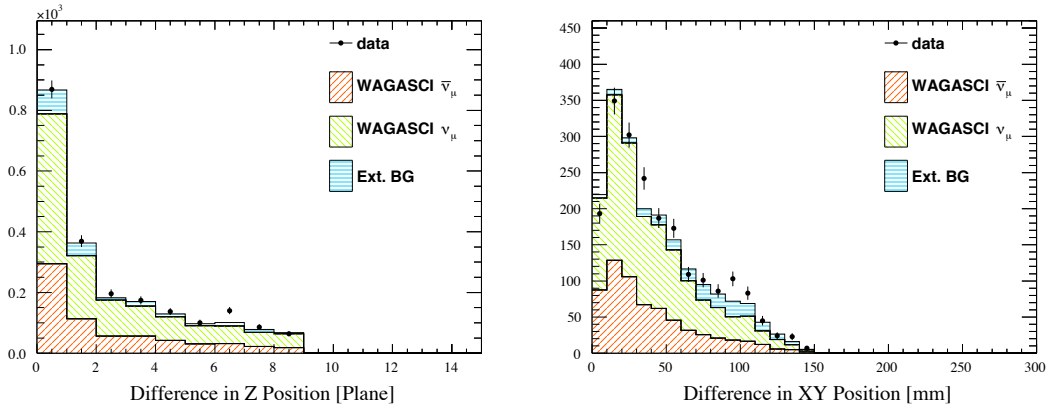

Figure 6.10: $|\Delta z_x| + |\Delta z_y|$ (top) and $\sqrt{\Delta x^2 + \Delta y^2}$ (bottom) distributions used for the vertex reconstruction. These plots only contain the multi-track sample after the vertex reconstruction.

6.2.3.6 Beam timing cut

After reconstructing vertices on the detectors, they are still contaminated by accidental events such as cosmic-rays, which is not related to the neutrino beam. In order to suppress those background events, event timing for a vertex is required to be within 100 nsec from the expected beam bunch timing, as shown in Fig. 6.11. The event timing of a vertex is computed by using the hit timings measured in Proton Module and INGRID among hits used to reconstruct tracks from the vertex. Hit timing of a channel with the largest charge among those hits is defined as the event timing for the vertex. Hit timings measured in WAGASCI are ignored because of their poor resolution.

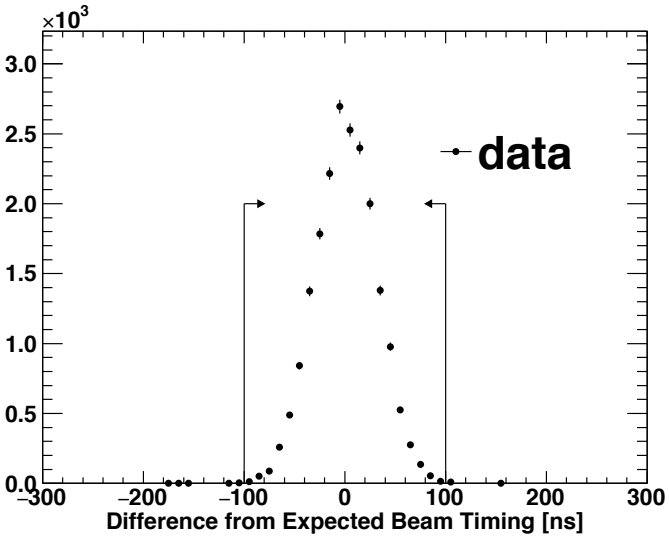

Figure 6.11: Distribution of observed event timing from the expected timing. This plot contains the events after the vertex reconstruction.

6.2.3.7 Upstream veto cut and fiducial cut

Events after the beam timing cut are still dominated by the beam-related external background events: mainly neutrino interactions in the surrounding materials around the detectors. In order to suppress those background events, the reconstructed vertex is required to be in the fiducial volume defined as follows. The fiducial volume for WAGASCI is the region

- between the 5th tracking plane and 14th one along z-axis, and
- within the central 70 cm $\times$ 70 cm transverse area,

as shown in Fig. 6.12. The fiducial volume contains about 82.4 kg of water and 19.3 kg of scintillators. The fiducial volume for Proton Module is the region

- between the 2th tracking plane and 15th one along z-axis, and
- within the central 70 cm $\times$ 70 cm transverse area,

as shown in Fig. 6.13. The fiducial volume contains about 155.3 kg of scintillators.

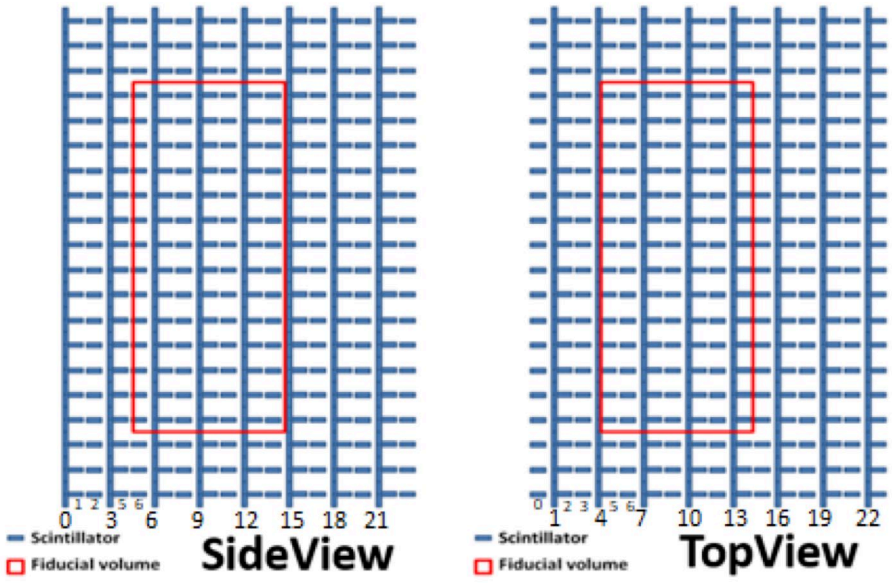

Figure 6.12: The fiducial volume in the WAGASCI detector for each view.

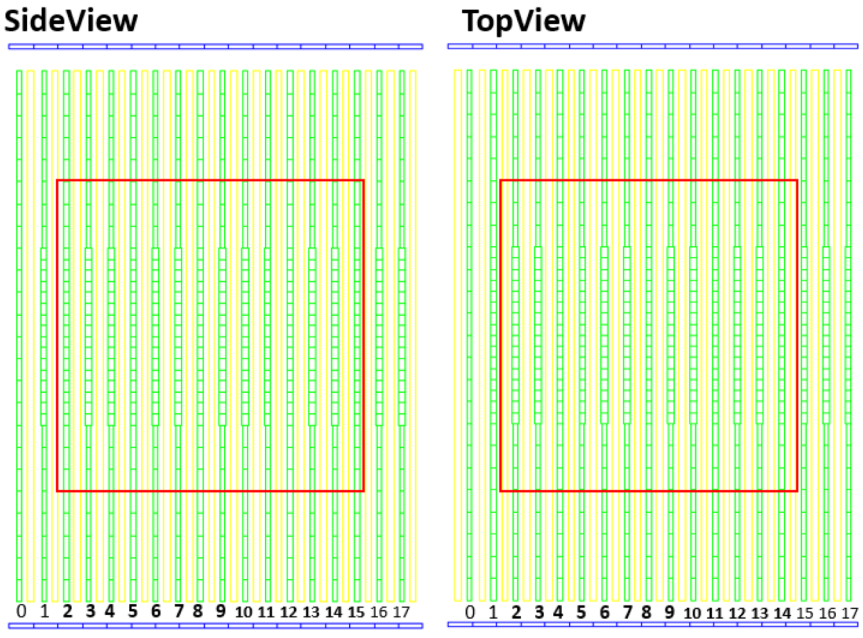

Figure 6.13: The fiducial volume in Proton Module for each view.

First, events with a reconstructed vertex in more upstream than the defined fiducial volume are rejected. Figure 6.14 shows a distribution of the reconstructed vertex along z-axis before this upstream veto cut. Second, events with an reconstructed vertex in the outer region than the defined fiducial area are rejected. Figure 6.15 shows distributions of the extracted vertex along x-axis and y-axis respectively, just after the upstream veto cut.

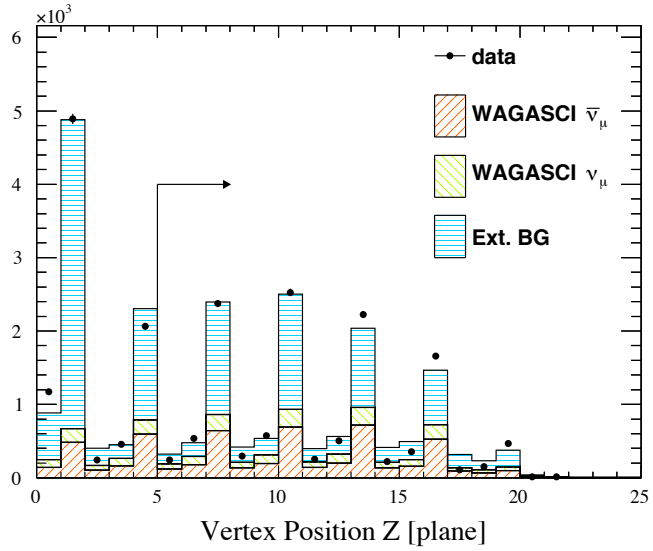

Figure 6.14: Distribution of the extracted vertices in WAGASCI along z-axis after the beam timing cut and before upstream veto cut.

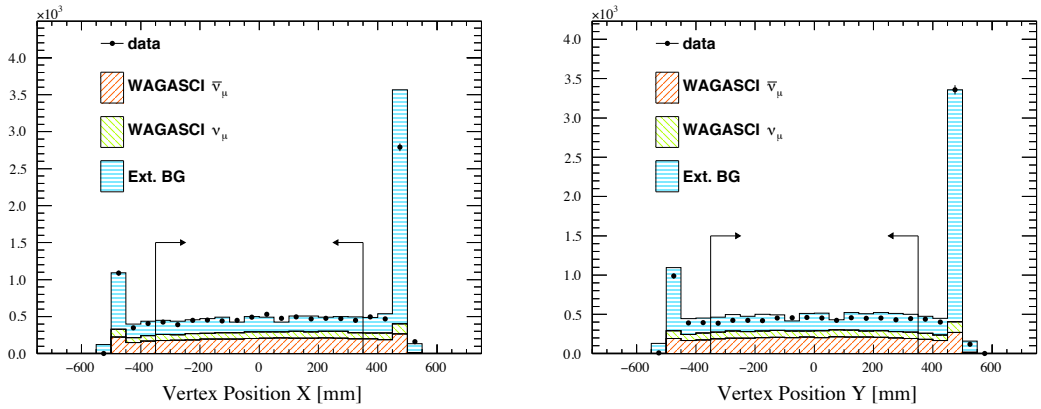

Figure 6.15: Distribution of extracted vertex along x-axis (left) and y-axis (right) after the upstream veto cut and before the fiducial cut.

6.2.3.8 Acceptance cut

For events with an reconstructed vertex in the fiducial volume of WAGASCI, the reconstructed angle of the longest INGRID-matched track is limited in order to obtain a similar acceptance to that of events from Proton Module. An imaginary INGRID module is defined at the INGRID shifted toward its downstream, to set the distance between the imaginary INGRID and WAGASCI the same as the distance between INGRID and Proton Module. An extrapolation of the reconstructed track from WAGASCI is required to reach this imaginary INGRID.

6.2.3.9 Categorization by number of tracks and reconstructed angle

In the CC0π0p interactions, we expect a single-muon final state. The analysis sample is categorized them into three groups according to the number of reconstructed tracks and the reconstructed angle:"single track forward" sample, "single track backward" sample, and "multi-track" sample. The distribution of the number of reconstructed tracks for the whole of the analysis sample is shown in Fig. 6.16. Figure 6.17 shows the reconstructed track angle only for the single track samples.

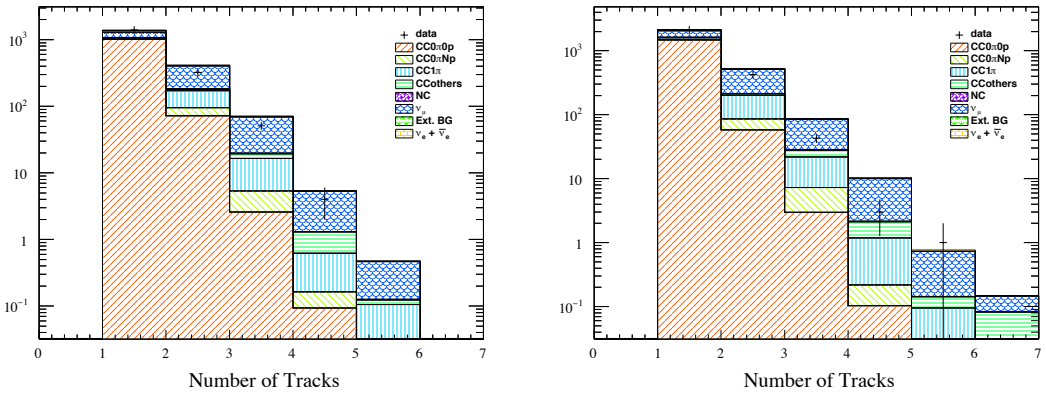

Figure 6.16: Number of reconstructed tracks of the selected events in WAGASCI (left) and Proton Module (right).

6.2.4 Event selection summary

The numbers of selected events in each selection from the vertex extraction are summarized in Table 6.2 and 6.3. In the data set, the analysis sample has 1783 events in WAGASCI and 2623 events in Proton Module. The difference in the

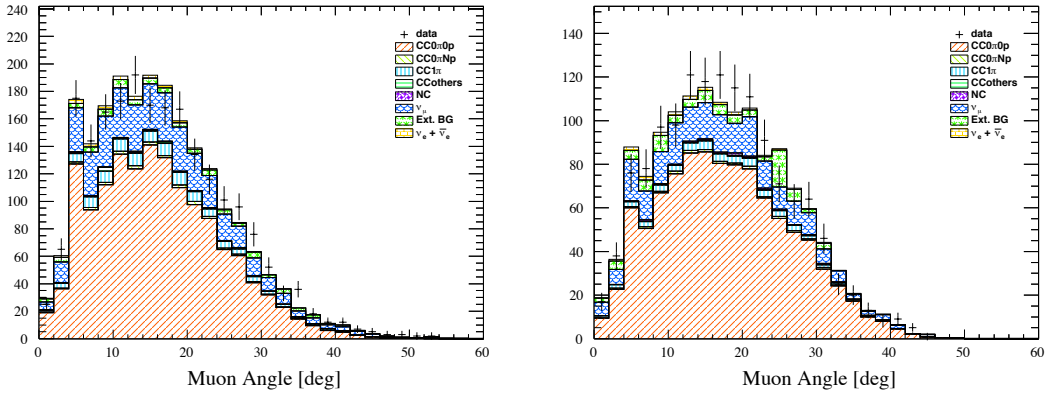

Figure 6.17: Reconstructed angle of the longest INGRID-matched track with respect with mean neutrino direction in WAGASCI (left) and Proton Module (right). These plots only contain the single-track samples.

selected number of events are basically explained by the difference in mass of the materials in the fiducial volume. Table 6.4 and 6.5 show the number of event in each bin for the analysis sample and their components. Sources of the background events to be subtracted by the Monte Carlo simulation in the case of $\overline{\nu}_\mu$ cross section analysis are as follows:

- ν_μ charged-current interactions
- $\overline{\nu}_\mu$ charged-current interactions on the other elements than H_2O and CH
- $\overline{\nu}_\mu$ charged-current interactions out of the fiducial volume
- Neutral-current interactions
- ν_e and $\overline{\nu}_e$ interactions
- neutrino interaction on the surrounding materials around the detectors

The ν_μ charged-current interactions are included into the signal in the case of $\overline{\nu}_\mu + \nu_\mu$ cross section analysis. The dominant background event in the case of the $\overline{\nu}_\mu$ cross section analysis is contamination from ν_μ charged-current interactions (20%). For the WAGASCI event, the sub-dominant component is the charged-current interactions of the fiducial volume (16%), which has a reconstructed vertex inside the fiducial volume. This migration is caused by the relatively low hit efficiency in WAGASCI, due to gaps between scintillator channels. This less often happens in Proton Module, since it is a full active detector and resolution of vertex

reconstruction is better than that of WAGASCI. The other background events occupy less than 5% for each in total number of the selected events. Figure 6.18 shows the number of selected events. Small discrepancy between the data and MC are observed, especially for the multi-track sample, but they are covered by the systematics errors as discussed in Sec. 7.4.

Table 6.2: Summary of the event selection for WAGASCI

Selection	MC					Data	Data/MC
	$\overline{\nu}_\mu$	ν_μ	$\nu_e + \overline{\nu}_e$	External BG.	Total		
Vertexing	5559.1	2597.9	149.9	10582.9	18889.7	20728	1.10
	(29.4%)	(13.8%)	(0.8%)	(56.0%)	(100.0%)		
Beam timing	5485.5	2462.8	142.3	10439.1	18529.7	20095	1.08
	(29.6%)	(13.3%)	(0.8%)	(56.3%)	(100.0%)		
Upstream veto	3925.3	1755.0	83.0	6081.8	11845.1	12236	1.03
	(33.1%)	(14.8%)	(0.7%)	(51.3%)	(100.0%)		
Fiducial volume	1936.9	812.8	38.7	112.3	2900.7	2797	0.96
	(66.8%)	(28.0%)	(1.3%)	(3.9%)	(100.0%)		
Additional acceptance	1279.9	497.4	28.3	81.5	1887.1	1783	0.94
	(67.8%)	(26.4%)	(1.5%)	(4.3%)	(100.0%)		
One-track sample	1075.7	224.5	17.3	76.5	1394.0	1406	1.01
	(77.2%)	(16.1%)	(1.2%)	(5.5%)	(100.0%)		
Reconstructed track angle	969.5	203.5	16.5	72.3	1261.9	1279	1.01
	(76.8%)	(16.1%)	(1.3%)	(5.7%)	(100.0%)		

Table 6.3: Summary of the event selection for Proton Module.

Selection	MC					Data	Data/MC
	$\overline{\nu}_\mu$	ν_μ	$\nu_e + \overline{\nu}_e$	External BG.	Total		
Vertexing	4813.4	2219.1	104.1	195761.9	202898.5	191554	0.94
	(2.4%)	(1.1%)	(0.1%)	(96.5%)	(100.0%)		
Beam timing	4807.8	2201.8	103.3	195691.1	202804.0	191118	0.94
	(2.4%)	(1.1%)	(0.1%)	(96.5%)	(100.0%)		
Upstream veto	4223.2	1883.3	88.6	31118.6	37313.7	40593	1.09
	(11.3%)	(5.0%)	(0.2%)	(83.4%)	(100.0%)		
Fiducial volume	1865.8	792.0	39.0	71.3	2768.2	2623	0.95
	(67.4%)	(28.6%)	(1.4%)	(2.6%)	(100.0%)		
Additional acceptance	1865.8	792.0	39.0	71.3	2768.2	2623	0.95
	(67.4%)	(28.6%)	(1.4%)	(2.6%)	(100.0%)		
One-track sample	1620.6	429.0	25.0	68.5	2143.1	2152	1.00
	(75.6%)	(20.0%)	(1.2%)	(3.2%)	(100.0%)		
Reconstructed track angle	1514.5	390.1	23.7	54.8	1983.1	1967	0.99
	(76.4%)	(19.7%)	(1.2%)	(2.8%)	(100.0%)		

Table 6.6 shows the fraction of the neutrino interaction modes in the single-track sample with a reconstructed angle less then 30 degrees. Among the $\overline{\nu}_\mu$ interactions, CCQE (about 55%), 2p2h (about 7%) and CC1π (about 12%) dominate

Table 6.4: The number of events in each bin and their components for the analysis sample of WAGASCI.

Reconstructed Bin	MC								Data
	$\bar{\nu}_\mu$ CC	ν_μ CC	Not on H2O/CH	Out of FV	NC	$\nu_e + \bar{\nu}_e$	Ext.BG	Total	
Multi-Track	168.3	221.4	3.8	68.0	15.6	11.0	5.0	493.1	377
	(34.1%)	(44.9%)	(0.8%)	(13.8%)	(3.2%)	(2.2%)	(1.0%)	(100.0%)	
One-Track:0-5 deg	59.1	14.9	0.7	19.6	1.7	2.0	7.9	105.9	96
	(55.8%)	(14.1%)	(0.7%)	(18.5%)	(1.6%)	(1.9%)	(7.4%)	(100.0%)	
One-Track:5-10 deg	128.7	25.3	1.5	29.9	2.7	4.1	14.4	206.7	210
	(62.3%)	(12.2%)	(0.7%)	(14.5%)	(1.3%)	(2.0%)	(7.0%)	(100.0%)	
One-Track:10-15 deg	188.5	31.0	2.1	35.1	4.9	4.0	10.2	275.9	282
	(68.3%)	(11.2%)	(0.8%)	(12.7%)	(1.8%)	(1.5%)	(3.7%)	(100.0%)	
One-Track:15-20 deg	180.2	28.0	2.0	38.5	4.7	3.2	10.8	267.4	291
	(67.4%)	(10.5%)	(0.8%)	(14.4%)	(1.8%)	(1.2%)	(4.0%)	(100.0%)	
One-Track:20-25 deg	148.1	23.7	1.7	43.9	3.4	2.1	19.1	241.9	241
	(61.2%)	(9.8%)	(0.7%)	(18.2%)	(1.4%)	(0.9%)	(7.9%)	(100.0%)	
One-Track:25-30 deg	96.4	15.4	1.1	37.4	2.7	1.2	9.9	164.1	159
	(58.8%)	(9.4%)	(0.7%)	(22.8%)	(1.7%)	(0.7%)	(6.0%)	(100.0%)	
One-Track:30-180 deg	72.0	9.3	0.8	42.0	3.0	0.8	4.2	132.1	127
	(54.5%)	(7.0%)	(0.6%)	(31.8%)	(2.3%)	(0.6%)	(3.2%)	(100.0%)	
Total	1041.5	369.0	13.7	314.4	38.7	28.3	81.5	1887.1	1783
	(55.2%)	(19.6%)	(0.7%)	(16.7%)	(2.1%)	(1.5%)	(4.3%)	(100.0%)	
OneTrk $0° - 30°$	801.1	138.3	9.1	204.4	20.1	16.5	72.3	1261.9	1279
	(63.5%)	(11.0%)	(0.7%)	(16.2%)	(1.6%)	(1.3%)	(5.7%)	(100.0%)	

Table 6.5: The number of events in each bin and their components for the analysis sample of Proton Module.

Reconstructed Bin	MC								Data
	$\bar{\nu}_\mu$ CC	ν_μ CC	Not on CH	Out of FV	NC	$\nu_e + \bar{\nu}_e$	Ext.BG	Total	
Multi-Track	230.8	336.9	8.2	16.6	15.8	14.0	2.8	625.1	471
	(36.9%)	(53.9%)	(1.3%)	(2.7%)	(2.5%)	(2.2%)	(0.4%)	(100.0%)	
One-Track:0-5 deg	144.4	34.6	2.6	7.4	2.3	3.4	8.0	202.6	195
	(71.3%)	(17.1%)	(1.3%)	(3.6%)	(1.1%)	(1.7%)	(4.0%)	(100.0%)	
One-Track:5-10 deg	261.8	76.7	4.9	9.4	4.3	5.9	9.7	372.8	379
	(70.2%)	(20.6%)	(1.3%)	(2.5%)	(1.2%)	(1.6%)	(2.6%)	(100.0%)	
One-Track:10-15 deg	352.9	79.8	6.3	13.4	5.6	6.2	12.5	476.6	453
	(74.0%)	(16.7%)	(1.3%)	(2.8%)	(1.2%)	(1.3%)	(2.6%)	(100.0%)	
One-Track:15-20 deg	316.3	70.7	5.6	12.7	7.7	4.3	8.6	425.8	417
	(74.3%)	(16.6%)	(1.3%)	(3.0%)	(1.8%)	(1.0%)	(2.0%)	(100.0%)	
One-Track:20-25 deg	230.7	52.0	4.1	11.6	3.4	2.6	8.4	312.7	317
	(73.8%)	(16.6%)	(1.3%)	(3.7%)	(1.1%)	(0.8%)	(2.7%)	(100.0%)	
One-Track:25-30 deg	135.7	34.4	2.5	9.2	1.8	1.3	7.7	192.6	206
	(70.5%)	(17.8%)	(1.3%)	(4.8%)	(0.9%)	(0.7%)	(4.0%)	(100.0%)	
One-Track:30-180 deg	96.5	28.7	1.8	16.0	2.0	1.3	13.7	160.0	185
	(60.3%)	(18.0%)	(1.1%)	(10.0%)	(1.2%)	(0.8%)	(8.5%)	(100.0%)	
Total	1769.1	713.6	36.0	96.3	42.8	39.0	71.3	2768.2	2623
	(63.9%)	(25.8%)	(1.3%)	(3.5%)	(1.5%)	(1.4%)	(2.6%)	(100.0%)	
OneTrk $0° - 30°$	1441.8	348.0	26.0	63.7	25.1	23.7	54.8	1983.1	1967
	(72.7%)	(17.5%)	(1.3%)	(3.2%)	(1.3%)	(1.2%)	(2.8%)	(100.0%)	

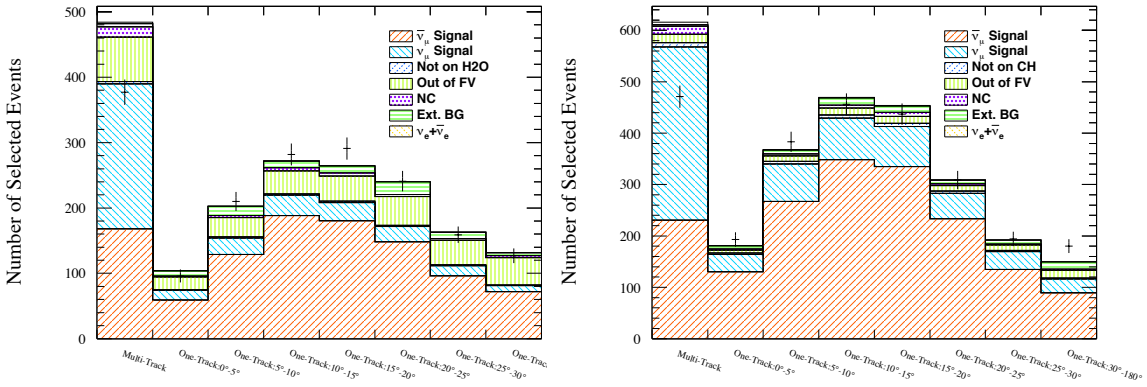

Figure 6.18: Number of selected events in WAGASCI (left) and Proton Module (right).

the selected events, and the other charged-current interactions and neutral-current interactions are well suppressed. Figure 6.19 shows distributions of the selected events as a function of neutrino energy for each interaction mode, and show distributions of charged-current interactions among the selected events in a function of muon momentum and angle.

Table 6.6: Fraction of the interaction mode in the selected events from the interactions in the fiducial volume.

Interaction mode	WAGASCI Fraction [%]	Proton Module Fraction [%]
$\overline{\nu}_\mu$ CCQE	56.7	53.1
$\overline{\nu}_\mu$ 2p2h	7.2	6.8
$\overline{\nu}_\mu$ CC1pi	11.7	12.2
$\overline{\nu}_\mu$ CCcoh	2.3	3.1
$\overline{\nu}_\mu$ CCDIS	2.6	3.0
$\overline{\nu}_\mu$ CCother	0.5	0.6
$\overline{\nu}_\mu$ NC	0.7	0.4
ν_μ	17.1	19.5
$\overline{\nu}_e + \nu_e$	1.4	1.2
Total	100.0	100.0

Figure 6.20 shows the reconstructed vertex distributions of the single track forward sample among the selected events in WAGASCI, and Fig. 6.21 shows those in Proton Module.

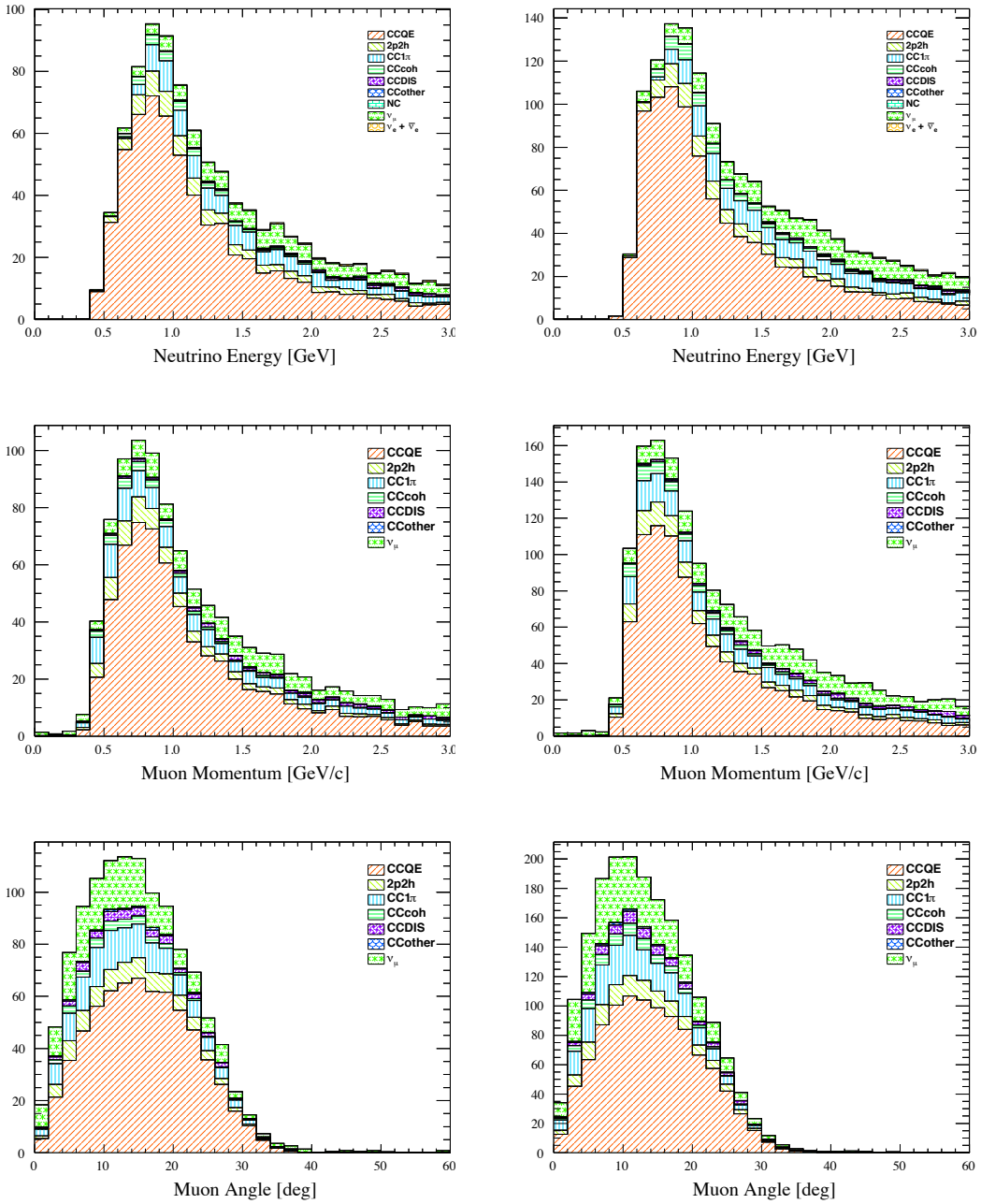

Figure 6.19: Distribution of the selected events in the fiducial volume of WAGASCI (left) and Proton Module (right) as the function of neutrino energy (top), muon momentum (middle) and muon angle (bottom). The figures in the top line show all interactions, while those in the bottom two lines show charged-current interactions.

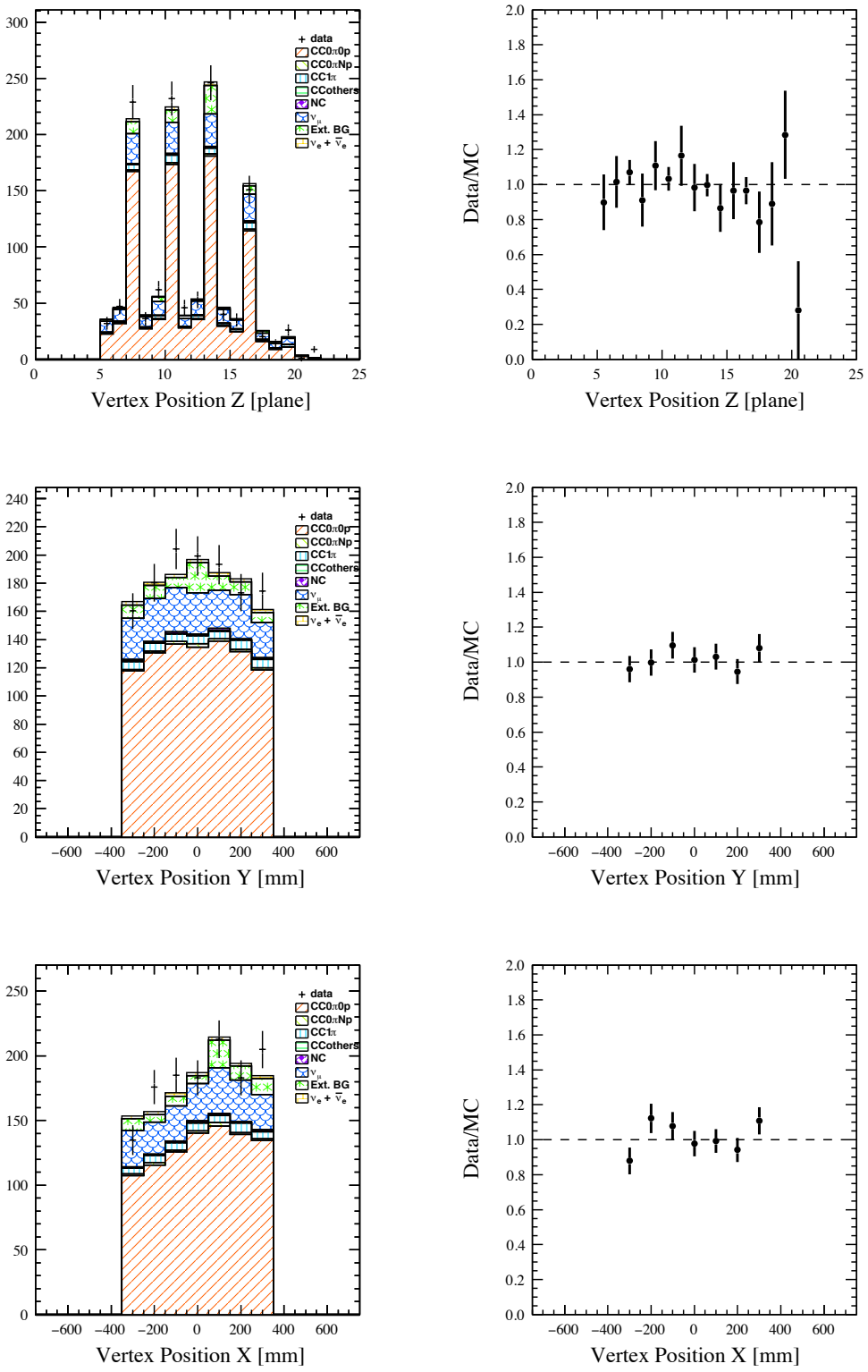

Figure 6.20: Reconstructed vertex z (top), y (middle) and x (bottom) for the selected events in WAGASCI.

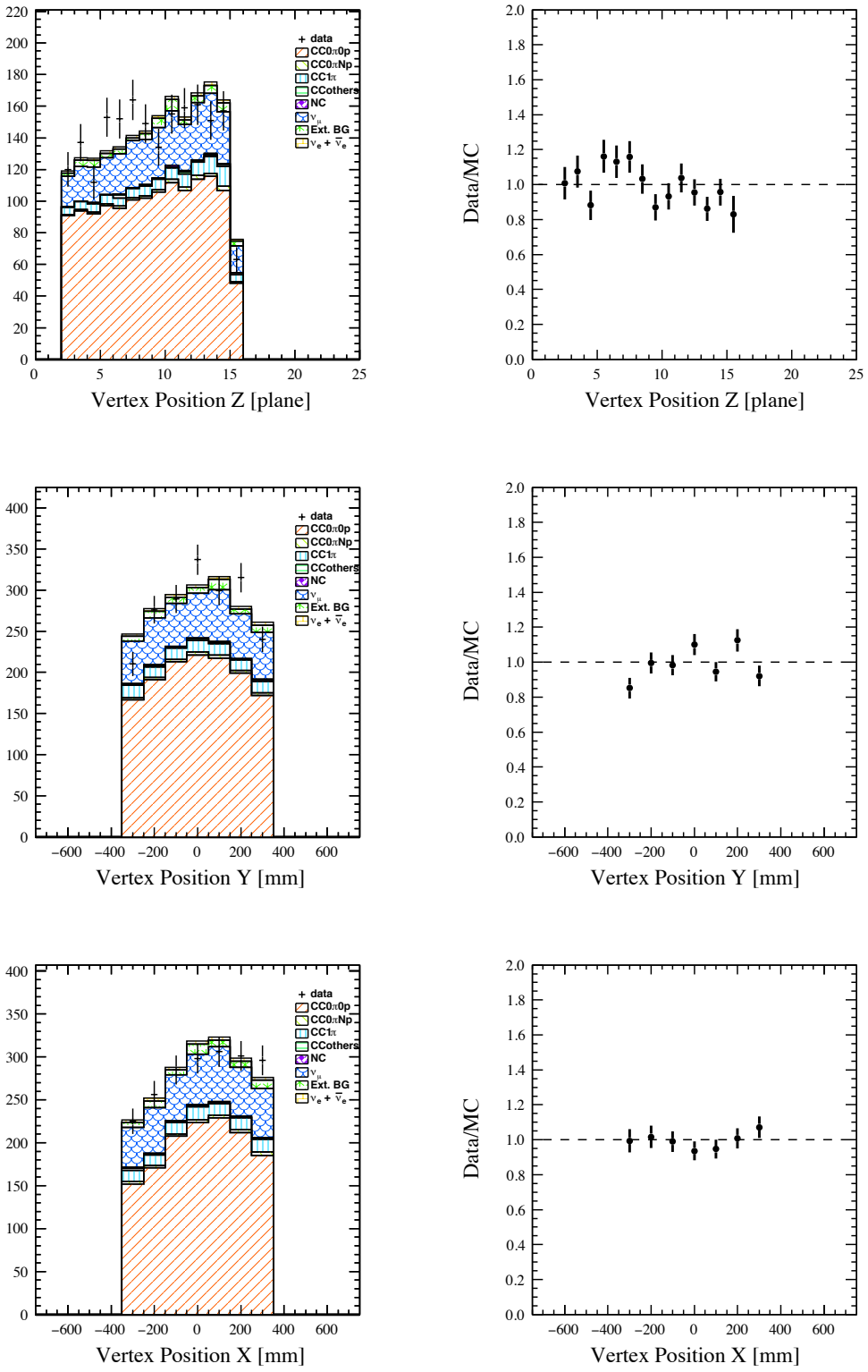

Figure 6.21: Reconstructed vertex z (top), y (middle) and x (bottom) for the selected events in Proton Module.

6.2.5 Selection efficiency

Figure 6.22 shows the selection efficiency of charged-current events for WAGASCI and Proton Module for each category, and those are summarized in Table 6.7. Here the selection efficiency is defined as the ratio of the number of selected events to the number of charged-current interactions in the fiducial volume. For CC0π0p with a muon angle less than 30 degrees, binning is every 5 degrees of muon angle. Thanks to the additional acceptance limitation cut on WAGASCI, the detection efficiencies are similar to each other among the two detectors, but the detection efficiency of WAGASCI for the forward region are smaller than that of Proton Module due to its lower hit efficiency. The two bins out of the signal phase space, corresponding to CC other and CC0π0p with a muon angle more than 30 degrees, have small selection efficiencies.

Figure 6.23 shows the detection efficiencies for each interaction type before the final state interaction. The different interaction mode have similar selection efficiencies among CC0π0p with a muon angle less than 30 degrees, except for CC DIS in WAGASCI. CC DIS emit a number of hadrons other than charged pions and protons, so that it possibly causes a failure to reconstruct a proper muon track. WAGASCI is more sensitive to those extra hadrons compared with Proton Module because of the grid scintillators.

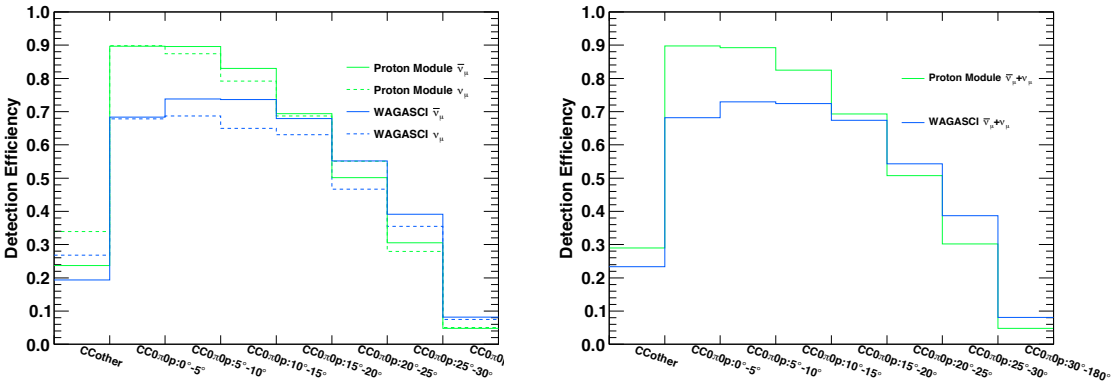

Figure 6.22: Selection efficiencies for each of $\overline{\nu}_\mu$ and ν_μ (left) and for combined sample of $\overline{\nu}_\mu + \nu_\mu$ (right).

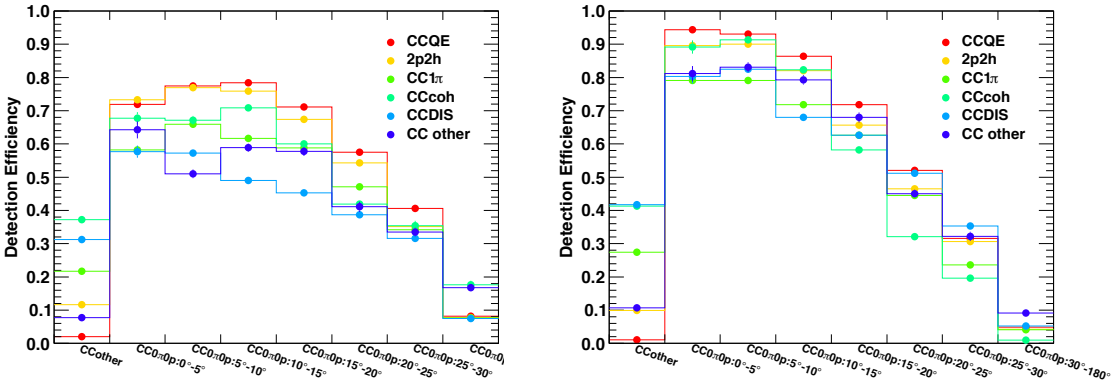

Figure 6.23: Selection efficiencies for each interaction type in WAGASCI (left) and Proton Module (right). Here those interaction modes do not consider the final state interaction, hence "CC1π" and "CC other" represent the pure neutrino-nucleus interactions and differ from those defined for the signal phase space in this analysis.

Table 6.7: Calculated detection efficiency of CC events for each of phase space bins.

	$\overline{\nu}_\mu$		ν_μ		$\overline{\nu}_\mu + \nu_\mu$	
	WAGASCI	PM	WAGASCI	PM	WAGASCI	PM
CCother	0.194	0.237	0.268	0.339	0.233	0.289
CC0π0p : $0^\circ - 5^\circ$	0.683	0.897	0.679	0.898	0.682	0.897
CC0π0p : $5^\circ - 10^\circ$	0.738	0.896	0.687	0.875	0.729	0.892
CC0π0p : $10^\circ - 15^\circ$	0.737	0.830	0.649	0.792	0.724	0.825
CC0π0p : $15^\circ - 20^\circ$	0.679	0.694	0.630	0.687	0.674	0.693
CC0π0p : $20^\circ - 25^\circ$	0.552	0.502	0.467	0.550	0.543	0.507
CC0π0p : $25^\circ - 30^\circ$	0.391	0.305	0.355	0.280	0.387	0.302
CC0π0p : $30^\circ - 180^\circ$	0.081	0.048	0.075	0.050	0.081	0.048
Total	0.372	0.397	0.315	0.391	0.355	0.395

Chapter 7

Measurement of the neutrino charged current cross section

7.1 Cross section extraction

7.1.1 Notations

In this thesis, the following notations are used:

- X_j^{reco} represents j-th category based on the number of reconstructed track and the reconstructed angle.
- C_i^{true} represents i-th category based on the true kinematics of muons, pions and protons.
- A smearing matrix, $\mathbb{P}(X_j^{\mathrm{reco}}|C_i^{\mathrm{true}})$, represents a probability that an event from C_i^{true} is reconstructed in X_j^{reco}.
- An unfolding matrix, $U_{ij} = \mathbb{P}(C_i^{\mathrm{true}}|X_j^{\mathrm{reco}})$, represents a probability that an event in X_j^{reco} derives from C_i^{true}.

7.1.2 Cross-section calculation formula

The flux-integrated differential CC0π0p cross sections are calculated as follows:

$$\sigma_{i\ \mathrm{H_2O}} = \sum_j \frac{U_{\mathrm{ij\ WM}}(N^{\mathrm{sel}}_{\mathrm{j\ WM}} - N^{\mathrm{BG}}_{\mathrm{j\ WM}})}{\Phi^{\mathrm{H_2O}}_{\mathrm{WM}} T^{\mathrm{H_2O}}_{\mathrm{WM}} \varepsilon^{\mathrm{H_2O}}_{\mathrm{i\ WM}}} \tag{7.1}$$

$$\sigma_{i\ \mathrm{CH}} = \sum_j \frac{U_{\mathrm{ij\ PM}}(N^{\mathrm{sel}}_{\mathrm{j\ PM}} - N^{\mathrm{BG}}_{\mathrm{j\ PM}})}{\Phi^{\mathrm{CH}}_{\mathrm{PM}} T^{\mathrm{CH}}_{\mathrm{PM}} \varepsilon^{\mathrm{CH}}_{\mathrm{i\ PM}}} \tag{7.2}$$

where N^{sel} is the number of selected events, N^{BG} is the number of expected background events, Φ is the integrated $\overline{\nu}_\mu$ flux, T is the number of target nucleons and ε is the selection efficiency for signal events. The subscript of i represents binning for true phase space of muons, pions, and protons, and the subscript of j represents binning for reconstructed tracks, as described in Sec. 6.2.2. U_{ij} is a unfolding matrix, which corresponds to a probability that events reconstructed in the j-th bin originate from true phase space of the i-th bin. The subscript of WAGASCI and Proton Module are WM and PM, respectively. Superscript of H_2O and CH is the target materials.

The background events for this analysis are NC events, ν_μ events, ν_e events, $\overline{\nu}_e$ events, interactions on elements other than the target elements in the detector and background events produced by neutrino interactions on the material surrounding the detector. In the case of the $\overline{\nu}_\mu$ cross section analysis, ν_μ CC events are included into the background events. All of the backgrounds are estimated by the Monte Carlo simulation, except for interactions on plastic scintillator of WAGASCI. They would become one of main background events for $\sigma_{\mathrm{H_2O}}$, since about 20% of the fiducial volume of WAGASCI is occupied by plastic scintillators. They are statistically calculated by using the number of selected events in Proton Module. Hence, total background events in WAGASCI are categorized into two parts:

$$N^{\mathrm{BG}}_{\mathrm{WM}} = N^{\mathrm{Scintillator\ BG}}_{\mathrm{WM}} + N^{\mathrm{Other\ BG}}_{\mathrm{WM}}, \tag{7.3}$$

where $N^{\mathrm{Scintillator\ BG}}_{\mathrm{WM}}$ represents the interactions on plastic scintillators in WAGASCI, and $N^{\mathrm{Other\ BG}}_{\mathrm{WM}}$ is the other background events. $N^{\mathrm{Scintillator\ BG}}_{\mathrm{WM}}$ is calculated as:

$$N^{\mathrm{ScintillatorBG}}_{j\ \mathrm{WM}} = \sum_i \mathbb{P}(X^{\mathrm{reco}}_j | C^{\mathrm{true}}_i)^{\mathrm{CH}}_{\mathrm{WM}} \times \sigma^{\mathrm{CH}}_i \times \Phi^{\mathrm{CH}}_{\mathrm{WM}} T^{\mathrm{CH}}_{\mathrm{WM}} \varepsilon^{\mathrm{CH}}_{i\ \mathrm{WM}} \tag{7.4}$$

$$= \sum_{ij'} \Bigg[\mathbb{P}(X^{\mathrm{reco}}_j | C^{\mathrm{true}}_i)^{\mathrm{CH}}_{\mathrm{WM}} \times U^{\mathrm{PM}}_{ij'} \times (N^{\mathrm{sel}}_{j'\ \mathrm{PM}} - N^{\mathrm{BG}}_{j'\ \mathrm{PM}}) \times \frac{\Phi^{\mathrm{CH}}_{\mathrm{WM}} T^{\mathrm{CH}}_{\mathrm{WM}} \varepsilon^{\mathrm{CH}}_{i\ \mathrm{WM}}}{\Phi_{\mathrm{PM}} T_{\mathrm{PM}} \varepsilon_{i\ \mathrm{PM}}} \Bigg] \tag{7.5}$$

where $^{\mathrm{CH}}_{\mathrm{WM}}$ is the scintillator of WAGASCI. Figure 7.1 shows a product between the smearing matrix on scintillators of WAGASCI and the unfolding matrix on Proton Module, $\sum_i \left[\mathbb{P}(X^{\mathrm{reco}}_j | C^{\mathrm{true}}_i)^{\mathrm{CH}}_{\mathrm{WM}} \times U^{\mathrm{PM}}_{ij'} \right]$, which mainly affects the normalization from the number of selected events on Proton Module to the number of background events on the scintillators in WAGASCI.

In order to achieve the prior distribution independent of the neutrino interaction generator, the unfolding matrix is calculated by using the D'Agostini unfolding. According to the Bayes inversion formula, the unfolding matrix is calculated

Figure 7.1: Product of the smearing matrix on scintillators of WAGASCI and U-Matrix on Proton Module, $\sum_i \mathbb{P}(X_j^{\rm reco}|C_i^{\rm true})^{\rm CH}_{\rm WM} \times U_{ij'}^{\rm PM}$.

as

$$
\begin{aligned}
U_{ij} &= \mathbb{P}(C_i^{\rm true}|X_j^{\rm reco}) && (7.6)\\
&= \mathbb{P}(X_j^{\rm reco}|C_i^{\rm true}) \times \mathbb{P}(C_i^{\rm true})/\mathbb{P}(X_j^{\rm reco}) && (7.7)\\
&= \mathbb{P}(X_j^{\rm reco}|C_i^{\rm true}) \times \mathbb{P}(C_i^{\rm true})/\sum_k \left[\mathbb{P}(X_j^{\rm reco}|C_k^{\rm true})\mathbb{P}(C_k^{\rm true})\right] && (7.8)
\end{aligned}
$$

where $\mathbb{P}(X_j^{\rm reco}|C_i^{\rm true})$, which represents a probability that a events in the i-th bin of true phase space is reconstructed in the j-th bin of reconstructed bin, is calculated by the Monte Carlo simulation. On the other hand, $\mathbb{P}(C_i^{\rm true})$ is iteratively computed using the number of selected events as follows:

1. In the beginning of iteration, $\mathbb{P}(C_i^{\rm true})$ is set to a flat prior distribution.
2. U_{ij} is calculated by Eq. 7.8.
3. $\mathbb{P}(C_i^{\rm true})$ is set to $\sum_j U_{ij}(N_j^{\rm sel} - N_j^{\rm BG})/\sum_{i'j'} U_{i'j'}(N_{j'}^{\rm sel} - N_{j'}^{\rm BG})$
4. The process 2-3 is repeated.

The number of required iterations is conservatively set to 1500, so that all differential cross sections converge into a constant value. The convergence behavior is confirmed in a validation procedure as described in Sec. 8.1. The background events on the scintillator of WAGASCI, $N_{j\ \rm WM}^{\rm Scintillator\ BG}$, are also iteratively calculated every step.

The integrated cross sections are provided as the sum of those differential cross sections.

$$\sigma_{\mathrm{H_2O}} = \sum_i \sigma_{i\ \mathrm{H_2O}} \tag{7.9}$$

$$\sigma_{\mathrm{CH}} = \sum_i \sigma_{i\ \mathrm{CH}} \tag{7.10}$$

Those integrated cross section are focused on the CC0π0p events with a muon angle less then 30 degrees, not including the other two categories, CC other and CC0π0p with a muon angle more than 30 degrees.

The CC0π0p cross section ratio is calculated as follows by using Eq. 7.1 and 7.2:

$$\frac{\sigma_{i\ \mathrm{H_2O}}}{\sigma_{i\ \mathrm{CH}}} = \sum_j \left[\frac{U_{ij}(N^{\mathrm{sel}}_{\mathrm{j\ WM}} - N^{\mathrm{BG}}_{\mathrm{j\ WM}})}{\Phi^{\mathrm{H_2O}}_{\mathrm{WM}} T^{\mathrm{H_2O}}_{\mathrm{WM}} \varepsilon^{\mathrm{H_2O}}_{\mathrm{i\ WM}}} \right] / \sum_j \left[\frac{U_{ij}(N^{\mathrm{sel}}_{\mathrm{j\ PM}} - N^{\mathrm{BG}}_{\mathrm{j\ PM}})}{\Phi^{\mathrm{CH}}_{\mathrm{PM}} T^{\mathrm{CH}}_{\mathrm{PM}} \varepsilon^{\mathrm{CH}}_{\mathrm{i\ PM}}} \right] \tag{7.11}$$

$$\frac{\sigma_{\mathrm{H_2O}}}{\sigma_{\mathrm{CH}}} = \sum_{ij} \left[\frac{U_{ij}(N^{\mathrm{sel}}_{\mathrm{j\ WM}} - N^{\mathrm{BG}}_{\mathrm{j\ WM}})}{\Phi^{\mathrm{H_2O}}_{\mathrm{WM}} T^{\mathrm{H_2O}}_{\mathrm{WM}} \varepsilon^{\mathrm{H_2O}}_{\mathrm{i\ WM}}} \right] / \sum_{ij} \left[\frac{U_{ij}(N^{\mathrm{sel}}_{\mathrm{j\ PM}} - N^{\mathrm{BG}}_{\mathrm{j\ PM}})}{\Phi^{\mathrm{CH}}_{\mathrm{PM}} T^{\mathrm{CH}}_{\mathrm{PM}} \varepsilon^{\mathrm{CH}}_{\mathrm{i\ PM}}} \right] \tag{7.12}$$

7.1.3 $\overline{\nu}_\mu$ cross sections and $\overline{\nu}_\mu + \nu_\mu$ cross sections

Between the two cross section measurements of $\overline{\nu}_\mu$ and $\overline{\nu}_\mu + \nu_\mu$, the event selection, the number of selected events (N^{sel}_j), and the number of nucleons (T) are in common. The differences between the two cross section analyses are as follows. In the case of $\overline{\nu}_\mu$ cross section analyses,

- ν_μ charged-current interactions are included into one of background events,
- the selection efficiency (ε_i) and unfolding matrix (U_{ij}) are calculated with only $\overline{\nu}_\mu$ samples, and
- the integrated neutrino flux is $\Phi = \Phi_{\overline{\nu}_\mu}$.

In the case of $\overline{\nu}_\mu + \nu_\mu$ cross section analyses,

- ν_μ charged-current interactions are included into a part of the signal,
- the selection efficiency (ε_i) and unfolding matrix (U_{ij}) are calculated with combined samples including both $\overline{\nu}_\mu$ and ν_μ, and
- the integrated neutrino flux is $\Phi = \Phi_{\overline{\nu}_\mu} + \Phi_{\nu_\mu}$.

7.1.4 Quantities

7.1.4.1 Number of selected events

Table 7.1 shows the number of selected events. Those values correspond to Tables 6.4 and 6.5, and Fig. 6.18.

Table 7.1: Summary of the number of selected events

Detector	Reconstructed tracks	N^{sel}(Data)	N^{sel}(MC)
WAGASCI	Multi-Track	377	493.1
	One-Track:0-5 deg	96	105.9
	One-Track:5-10 deg	210	206.7
	One-Track:10-15 deg	282	275.9
	One-Track:15-20 deg	291	267.4
	One-Track:20-25 deg	241	241.9
	One-Track:25-30 deg	159	164.1
	One-Track:30-180 deg	127	132.1
	Total	1783	1887.1
Proton Module	Multi-Track	471	625.1
	One-Track:0-5 deg	195	202.6
	One-Track:5-10 deg	379	372.8
	One-Track:10-15 deg	453	476.6
	One-Track:15-20 deg	417	425.8
	One-Track:20-25 deg	317	312.7
	One-Track:25-30 deg	206	192.6
	One-Track:30-180 deg	185	160.0
	Total	2623	2768.2

7.1.4.2 Integrated neutrino beam flux

Figure 7.2 shows the neutrino energy spectrum predicted by the Monte Carlo simulation and Table 7.2 shows the number of the integrated neutrino flux in the fiducial volume region of WAGASCI and Proton Module used for this analysis, which corresponds to 7.908×10^{20} POT.

7.1.4.3 Number of target nucleons

The numbers of target nucleons in the fiducial volume of WAGASCI and Proton Module are calculated as described in Appendix B. Considering the neutrino interactions with H_2O or CH, the number of nucleons contained in the whole molecule of H_2O or CH is counted. Table 7.3 summarizes the calculated number of target

Table 7.2: Integrated neutrino beam flux per used POT (7.908×10^{20}) in the fiducial volume region of each detector [cm^{-2}].

	WAGASCI	Proton Module
$\Phi_{\overline{\nu}_\mu}$	1.69×10^{13}	1.70×10^{13}
Φ_{ν_μ}	1.48×10^{12}	1.49×10^{12}
$\Phi_{\overline{\nu}_e}$	1.52×10^{11}	1.51×10^{11}
Φ_{ν_e}	3.47×10^{10}	3.51×10^{10}

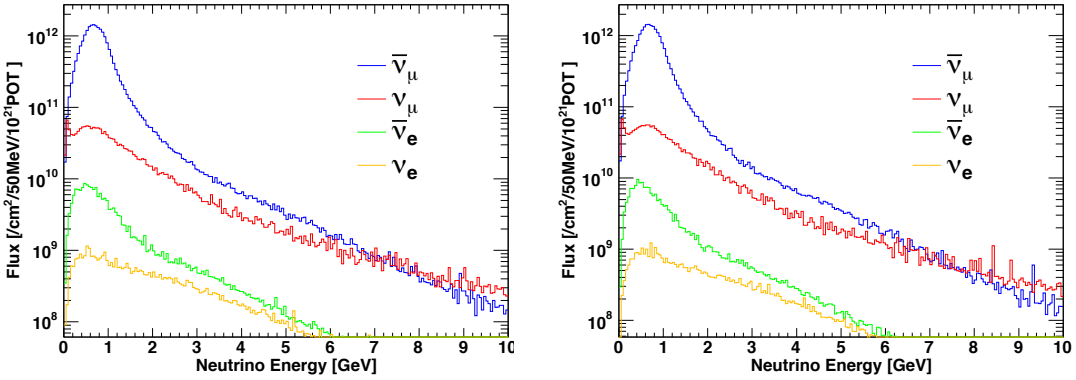

Figure 7.2: Expected neutrino flux for WAGASCI (left) and Proton Module (right).

nucleons. Interactions on the other elements are estimated by the calculated mass fractions, and subtracted as one of the background events.

Table 7.3: Summary of the number of target nucleons

Target	The number of target nucleon
$T_{\mathrm{WM}}^{\mathrm{H_2O}}$	4.957×10^{28}
$T_{\mathrm{WM}}^{\mathrm{CH}}$	1.107×10^{28}
$T_{\mathrm{PM}}^{\mathrm{CH}}$	9.210×10^{28}

7.1.4.4 Selection efficiency of charged-current events

The selection efficiencies are estimated using the Monte Carlo simulation, as shown in Table 7.4. Those values correspond to Fig. 6.22.

Table 7.4: Summary of the selection efficiency

		WAGASCI	PM
$\overline{\nu}_\mu$			
	CCother	0.194	0.237
	CC0π0p : $0^\circ - 5^\circ$	0.683	0.897
	CC0π0p : $5^\circ - 10^\circ$	0.738	0.896
	CC0π0p : $10^\circ - 15^\circ$	0.737	0.830
	CC0π0p : $15^\circ - 20^\circ$	0.679	0.694
	CC0π0p : $20^\circ - 25^\circ$	0.552	0.502
	CC0π0p : $25^\circ - 30^\circ$	0.391	0.305
	CC0π0p : $30^\circ - 180^\circ$	0.081	0.048
	Total	0.372	0.397
$\overline{\nu}_\mu + \nu_\mu$			
	CCother	0.233	0.289
	CC0π0p : $0^\circ - 5^\circ$	0.682	0.897
	CC0π0p : $5^\circ - 10^\circ$	0.729	0.892
	CC0π0p : $10^\circ - 15^\circ$	0.724	0.825
	CC0π0p : $15^\circ - 20^\circ$	0.674	0.693
	CC0π0p : $20^\circ - 25^\circ$	0.543	0.507
	CC0π0p : $25^\circ - 30^\circ$	0.387	0.302
	CC0π0p : $30^\circ - 180^\circ$	0.081	0.048
	Total	0.355	0.395

7.1.4.5 Expected number of background events

The expected numbers of the background events in WAGASCI are shown in Table 7.5 for each of the $\overline{\nu}_\mu$ cross section analysis and the $\overline{\nu}_\mu + \nu_\mu$ cross section analysis. Table 7.6 shows those in Proton Module. In those tables, CC interactions on scintillators in WAGASCI are not included because they are constrained by Proton Module. In the case of the $\overline{\nu}_\mu + \nu_\mu$ cross section, the ν_μ CC interactions are not included as background events. Those values correspond to the whole of the analysis sample.

Table 7.5: Summary of the number of background events after the event selection in WAGASCI.

	ν_μ CC	Not on H_2O	Out of FV	NC	$\nu_e + \bar{\nu}_e$	Ext.BG	Total	
							$\overline{\nu}_\mu$	$\overline{\nu}_\mu + \nu_\mu$
Multi-Track	221.4	3.8	68.0	15.6	11.0	5.0	324.8	103.4
One-Track:0-5 deg	14.9	0.7	19.6	1.7	2.0	7.9	46.8	31.8
One-Track:5-10 deg	25.3	1.5	29.9	2.7	4.1	14.4	77.9	52.6
One-Track:10-15 deg	31.0	2.1	35.1	4.9	4.0	10.2	87.3	56.4
One-Track:15-20 deg	28.0	2.0	38.5	4.7	3.2	10.8	87.2	59.2
One-Track:20-25 deg	23.7	1.7	43.9	3.4	2.1	19.1	93.8	70.1
One-Track:25-30 deg	15.4	1.1	37.4	2.7	1.2	9.9	67.7	52.3
One-Track:30-180 deg	9.3	0.8	42.0	3.0	0.8	4.2	60.1	50.8
Total	369.0	13.7	314.4	38.7	28.3	81.5	845.6	476.6

Table 7.6: Summary of the number of background events after the event selection in Proton Module.

	ν_μ CC	Not on CH	Out of FV	NC	$\nu_e + \bar{\nu}_e$	Ext.BG	Total	
							$\overline{\nu}_\mu$	$\overline{\nu}_\mu + \nu_\mu$
Multi-Track	336.9	8.2	16.6	15.8	14.0	2.8	394.3	57.4
One-Track:0-5 deg	34.6	2.6	7.4	2.3	3.4	8.0	58.2	23.7
One-Track:5-10 deg	76.7	4.9	9.4	4.3	5.9	9.7	110.9	34.3
One-Track:10-15 deg	79.8	6.3	13.4	5.6	6.2	12.5	123.8	44.0
One-Track:15-20 deg	70.7	5.6	12.7	7.7	4.3	8.6	109.5	38.8
One-Track:20-25 deg	52.0	4.1	11.6	3.4	2.6	8.4	82.0	30.1
One-Track:25-30 deg	34.4	2.5	9.2	1.8	1.3	7.7	56.8	22.5
One-Track:30-180 deg	28.7	1.8	16.0	2.0	1.3	13.7	63.5	34.8
Total	713.6	36.0	96.3	42.8	39.0	71.3	999.1	285.5

7.1.4.6 Detector smearing matrix

A detector smearing matrix, $\mathbb{P}(X_j^{\text{reco}}|C_i^{\text{true}})$, is calculated by the Monte Carlo simulation as shown in Fig. 7.3 and 7.4 for $\overline{\nu}_\mu$ and ν_μ, respectively. Smearing on the CC0π0p events reconstructed as multi-track samples is explained by high-energy charged-current interactions, such as CC DIS, emitting hadrons other than charged pions or protons. This smearing effect is larger on ν_μ samples than $\overline{\nu}_\mu$ sample, since the ν_μ component has a distribution with a larger energy. For the $\overline{\nu}_\mu + \nu_\mu$ cross section analysis, the P matrix is simply calculated by using the samples including both $\overline{\nu}_\mu$ and ν_μ, as shown in Fig. 7.5. The normalization is taken as $\sum_j \mathbb{P}(X_j^{\text{reco}}|C_i^{\text{true}}) = 1$.

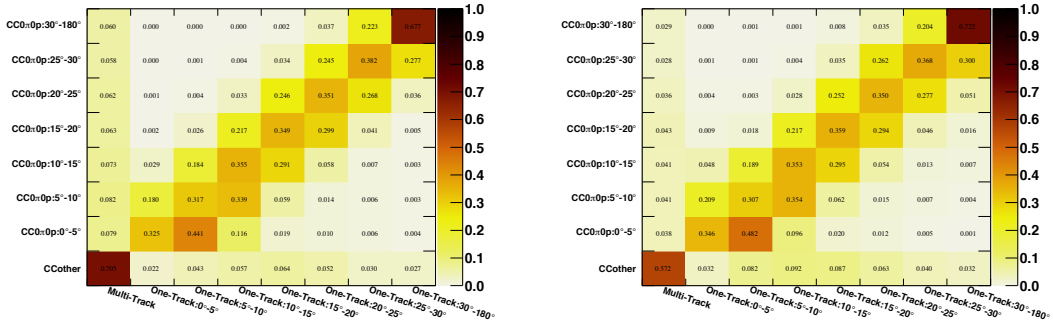

Figure 7.3: Calculated P matrix for WAGASCI (left) and Proton Module (right). The used samples only include $\overline{\nu}_\mu$.

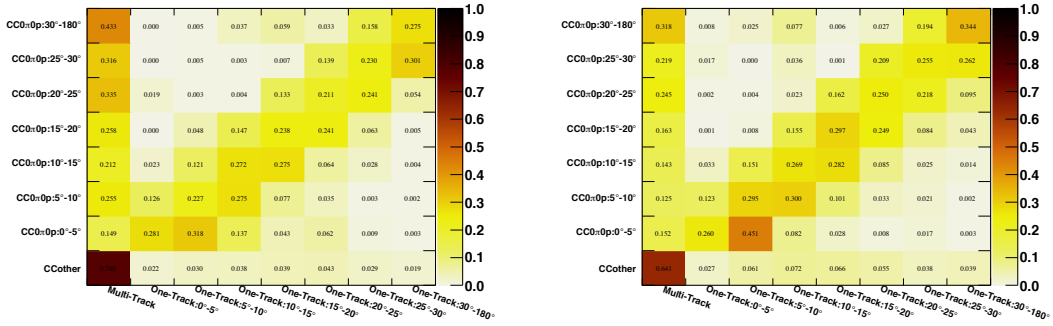

Figure 7.4: Calculated P matrix for WAGASCI (left) and Proton Module (right). The used samples only include ν_μ.

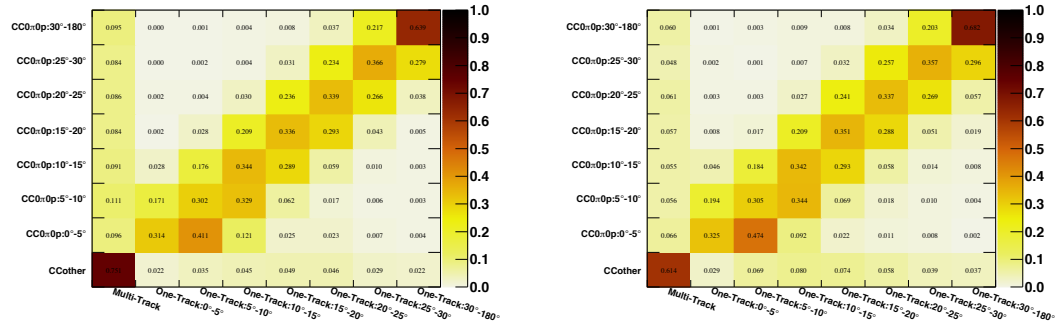

Figure 7.5: Calculated P matrix for WAGASCI (left) and Proton Module (right). The used samples include both $\overline{\nu}_\mu + \nu_\mu$.

7.2 Statistical uncertainty

A statistical error on the extracted cross section is estimated based on the number of selected events in each bin for the reconstructed tracks on each detector. Entries in each bin are fluctuated according to the Poisson distribution, and cross sections are computed by using the fluctuated number of events. The cross section computation is repeated for 10,000 times of the random fluctuations, and the 68% range of the distribution are taken as a statistical error. The statistical errors are symmetrically assigned for each of the calculated cross sections. The estimated statistical errors are summarized in Table 7.7.

Figure 7.6 shows the correlation matrices showing the correlation between σ_{H_2O} and σ_{CH} together. Those two cross section are correlated mainly via a subtraction of the background events on scintillators of WAGASCI using the number of events in Proton Module.

The detector smearing matrices, as described in Sec. 7.1.4.6, are not fully diagonal, and events from each category of the true phase space are widely distributed along categories of the reconstructed phase space. The wide distribution is due to the angular resolution of the detector and mis-reconstruction leading to a wrong number of tracks. This results in a strong anti-correlations between the unfolded cross sections on different bins, and causes the large statistical errors in the differential cross section measurements. However, the anti-correlations are basically canceled with each other when an integrated cross section is calculated by summing up the differential cross sections, so that the statistical errors on the CC0π0p with a muon angle less than 30 degrees cross sections are relatively small.

Table 7.7: Calculated statistical uncertainty

Cross section	True phase space	σ_{H_2O}	σ_{CH}	$\sigma_{H_2O}/\sigma_{CH}$
$\overline{\nu}_\mu$	CCother	±49.4%	±35.5%	±49.9%
	CC0π0p : 0-5 deg	±29.5%	±27.1%	±36.6%
	CC0π0p : 5-10 deg	±51.6%	±34.8%	±51.5%
	CC0π0p : 10-15 deg	±29.3%	±21.7%	±31.6%
	CC0π0p : 15-20 deg	±36.7%	±27.4%	±40.2%
	CC0π0p : 20-25 deg	±32.7%	±23.8%	±40.0%
	CC0π0p : 25-30 deg	±41.5%	±25.7%	±52.3%
	CC0π0p : 30-180 deg	±22.8%	±29.3%	±37.0%
	CC Total	±10.0%	±8.8%	±12.6%
	CC0π0p : 0-30 deg	±6.3%	±5.0%	±7.9%
$\overline{\nu}_\mu + \nu_\mu$	CCother	±13.6%	±7.1%	±16.0%
	CC0π0p : 0-5 deg	±29.3%	±19.4%	±33.7%
	CC0π0p : 5-10 deg	±39.4%	±25.7%	±41.5%
	CC0π0p : 10-15 deg	±16.8%	±19.0%	±23.6%
	CC0π0p : 15-20 deg	±32.0%	±22.8%	±37.8%
	CC0π0p : 20-25 deg	±19.1%	±18.2%	±26.3%
	CC0π0p : 25-30 deg	±29.4%	±21.2%	±34.6%
	CC0π0p : 30-180 deg	±31.3%	±23.5%	±41.1%
	CC Total	±6.4%	±5.8%	±8.7%
	CC0π0p : 0-30 deg	±5.5%	±4.2%	±6.9%

7.3 Systematic uncertainties

Systematic errors include effects from three categories:

- Neutrino flux
- Neutrino interaction
- Detector response

7.3.1 Systematic errors from neutrino flux uncertainties

The neutrino flux uncertainty is estimated according to understanding of hadron interactions and beamline monitors. The estimated uncertainties as a function of neutrino energy are shown in Fig. 7.7. The dominant contribution derives from hadron interactions, which is estimated based on the external hadron scattering measurements. Sources for the uncertainties on the hadron interactions are:

- Uncertainties on the hadron production cross sections (interaction length),
- Uncertainties on tuning of the hadron multiplicity:
  - uncertainties on the NA61/SHINE multiplicity measurements,
  - uncertainties on extrapolation to phase space not covered by NA61/SHINE,
  - uncertainties on energy scaling for secondary or tertiary hadron production, and
  - uncertainties on target material scaling.
- Uncertainties on secondary nucleon tuning:
  - uncertainties on changing the leading baryon definition, and
  - uncertainties on using external neutron production data.
- Uncertainties on interaction rate of secondary and tertiary pion with the target and the beamline materials (pion re-scattering).

For low neutrino energies ($E_\nu <\sim 0.3$ GeV) the uncertainty on pion re-scattering has the largest contribution, and for neutrino energies around 1 GeV or higher the dominant contributions are from the uncertainty on meson multiplicity and production cross section. In addition to the hadron interaction, the uncertainties from beamline components are based on measurements.

For systematic errors on the cross section extraction, effects on the number of background events (N^{BG}), integrated flux (Φ), detection efficiency (ε), and the

unfolding matrix (U_{ij}) are considered. Events generated in the Monte Carlo simulation are fluctuated based on the neutrino energy using the estimated uncertainty on the neutrino beam flux, and accordingly the variation of the cross section is computed. Distributions of the variation of the CC0π0p with a muon angle less than 30 degrees cross sections by using 10,000 inputs are shown in Fig. 7.8. The large correlation between WAGASCI and Proton Module results in the cancellation of the uncertainties on the cross section ratio measurement. The 68% range of the distribution is taken as the systematic errors. Correlation matrices of the cross sections are shown in Fig. 7.9.

Difference in the neutrino beam flux between WAGASCI and Proton Module is additionally taken into account for the the cross section ratio measurement and subtraction of background events on scintillator of WAGASCI. Distances from the proton beam target to WAGASCI and Proton Module are measured as 279.52 m and 278.76 m respectively. Assuming a point source of neutrinos at the target, an expected ratio of the neutrino beam flux between the two detectors is

$$(278.76/279.52)^{-2} = 1.0055. \tag{7.13}$$

While, a ratio of the expected neutrino beam flux between the two detectors is 1.0059. Difference between the point-source assumption and the expected flux ratio, 0.04%, is additionally included into the systematic errors.

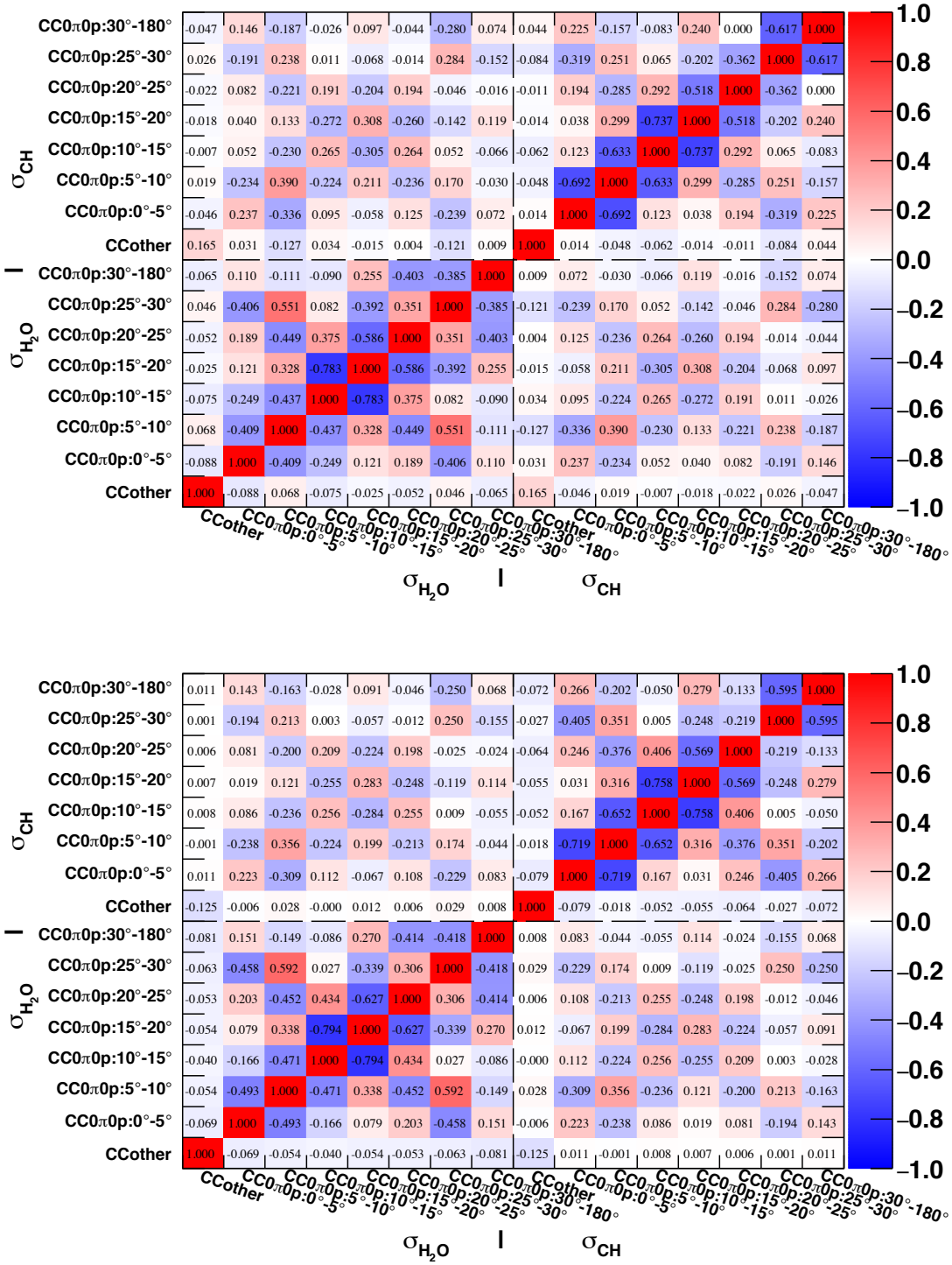

Figure 7.6: Correlation matrices from statistical uncertainties for $\overline{\nu}_\mu$ cross section (top) and $\overline{\nu}_\mu + \nu_\mu$ cross section (bottom), concerning correlation between $\sigma_{\mathrm{H_2O}}$ and σ_{CH}.

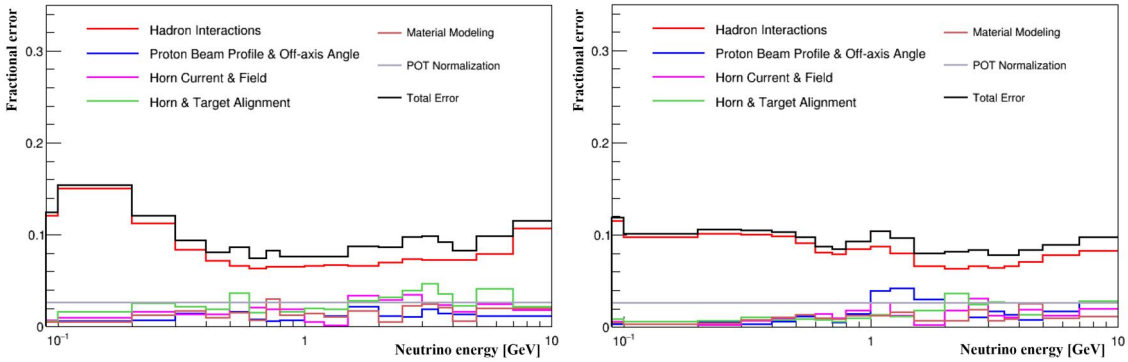

Figure 7.7: Fractional uncertainties of the anti-neutrino beam flux on WAGASCI, for ν_μ (left) and $\overline{\nu}_\mu$ (right).

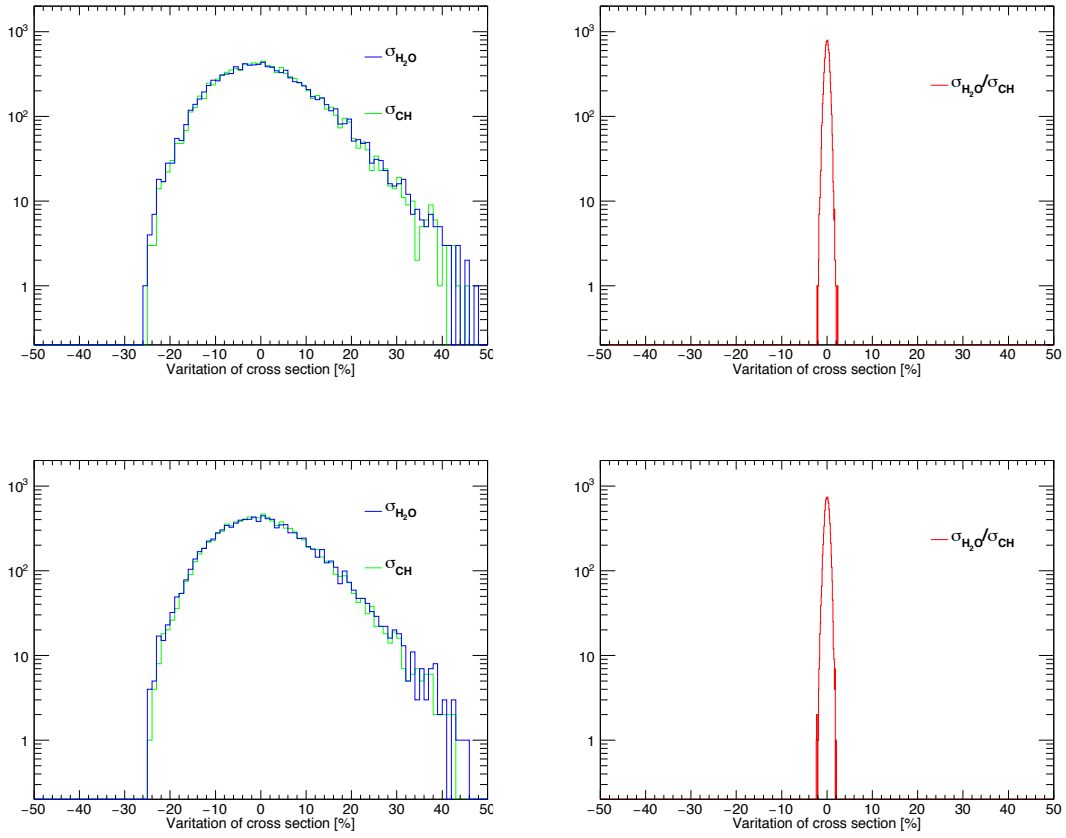

Figure 7.8: Variations of cross sections for CC0π0p with a muon angle less than 30 degrees, due to neutrino flux uncertainty for $\overline{\nu}_\mu$ (top) and $\overline{\nu}_\mu + \nu_\mu$ (bottom).

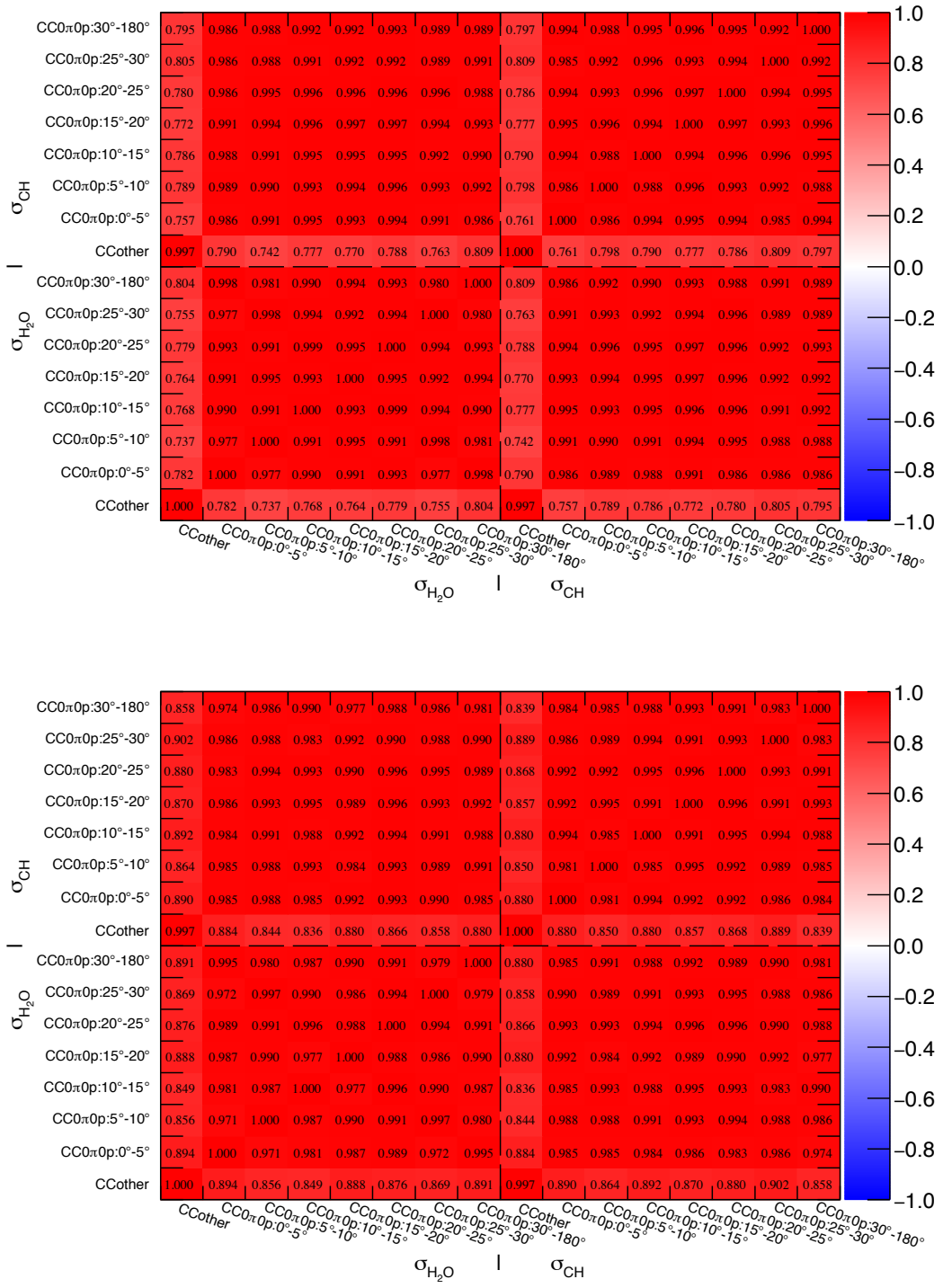

Figure 7.9: Correlation matrix due to neutrino flux uncertainty for $\overline{\nu}_\mu$ (left) and $\overline{\nu}_\mu + \nu_\mu$ (right) cross sections, concerning correlation between $\sigma_{\mathrm{H_2O}}$ and σ_{CH}.

7.3.2 Systematic errors from neutrino interaction model

Uncertainties of the neutrino interaction model affect estimations of the detection efficiency (ε), the number of background events (N_{BG}), and the unfolding matrix (U_{ij}). Each parameter related to this analysis is varied to cover understanding of the model, and propagations to the extracted cross sections are estimated. The parameters with their nominal value and 1σ variation are summarized in Table 3.2. In this analysis, only $\overline{\nu}_\mu$ and ν_μ interactions on WAGASCI and Proton Module are concerned for those variation, since the other components such as ν_e, $\overline{\nu}_e$, and interactions on external materials only affect on N_{BG} and their contaminations are negligibly small.

No correlation between ^{12}C and ^{16}O is assumed for parameters of 2p2h, Fermi momentum ($\mathrm{P_f}$), binding energy ($\mathrm{E_b}$), and CC coherent normalization, since effects from nuclear difference are not fully understood. For the other parameters, ^{12}C and ^{16}O are fully correlated. $\overline{\nu}_\mu$ and ν_μ are basically treated with a full correlation, except for the parameters related to CCQE and 2p2h interactions. CCQE and 2p2h interactions have only a muon and protons, and dominate the signal of CC0π0p, hence their uncertainties largely affect the detection efficiency estimation. In order to conservatively estimate the effect, $\overline{\nu}_\mu$ and ν_μ are uncorrelated for those interactions.

Among the uncertainties of the cross section from CCQE and 2p2h interactions, the dominant contribution is from 2p2h normalization, and $\mathrm{M_A^{QE}}$ is in the second largest contribution. Table 7.8 shows the uncertainties from the whole of parameters in the neutrino interaction model. They are dominated by effects from CCQE and 2p2h interactions, and nucleon FSI, and followed by pion production ($\mathrm{M_A^{Res}}$ and $\mathrm{C_{A5}}$) and Fermi momentum (P_f). CCQE and 2p2h interactions have the largest effect on the detection efficiency estimation, since they dominate the CC0π0p signal and largely distort the prior distribution. Nucleon FSI mainly affect the number of background events via ν_μ interactions, since more nucleons often exist in the final state of ν_μ interactions than that of $\overline{\nu}_\mu$ interactions. Hence, this effect become smaller for the $\overline{\nu}_\mu + \nu_\mu$ cross section measurement.

Figure 7.10 shows the fractional uncertainties from the neutrino interaction models on each bin of differential cross section, and contributions from each parameter. The correlation matrices are shown in Fig. 7.11. Among the differential cross sections, bins corresponding to CC other and CC0π0p with a muon angle larger than 30 degrees have large uncertainties. This is because they have low detection efficiency as described in Sec. 6.2, and multi-track sample and single-track sample with a track angle 30 degrees to 180, which mainly correspond to CC other and CC0π0p with a muon angle larger than 30 degrees respectively, have low purity of the $\overline{\nu}_\mu$ and $\overline{\nu}_\mu$interactions.

Table 7.8: Summary of the variation of the $\overline{\nu}_\mu$ and $\overline{\nu}_\mu + \nu_\mu$ cross sections of CC0π0p with a muon angle less than 30 degrees(%)

Parameter	The $\overline{\nu}_\mu$ cross section			The $\overline{\nu}_\mu + \nu_\mu$ cross section		
	σ_{H_2O}	σ_{CH}	$\sigma_{H_2O}/\sigma_{CH}$	σ_{H_2O}	σ_{CH}	$\sigma_{H_2O}/\sigma_{CH}$
CCQE − like	+3.34/-3.19	+2.68/-2.99	+4.35/-3.76	+2.61/-2.49	+2.35/-2.59	+3.55/-3.07
M_A^{Res}	+1.35/-1.49	+0.42/-0.40	+0.92/-1.09	+0.98/-1.19	+0.04/-0.15	+0.94/-1.04
C_{A5}	+1.42/-1.69	+0.30/-0.37	+1.12/-1.32	+0.89/-1.09	+0.24/-0.25	+1.14/-1.33
IsoSpin$\frac{1}{2}$bg	+0.38/-0.45	+0.23/-0.27	+0.15/-0.18	+0.26/-0.31	+0.02/-0.02	+0.25/-0.29
CCother shape	+0.34/-0.34	+0.06/-0.06	+0.40/-0.40	+0.34/-0.34	+0.05/-0.05	+0.28/-0.28
NCother norm	+0.61/-0.61	+0.16/-0.16	+0.44/-0.44	+0.58/-0.58	+0.17/-0.17	+0.41/-0.41
NCcoh norm	+0.06/-0.06	+0.01/-0.01	+0.04/-0.04	+0.05/-0.05	+0.01/-0.01	+0.04/-0.04
Pf C	+0.08/-0.15	+0.68/-0.37	+0.45/-0.83	+0.02/-0.04	+0.20/-0.09	+0.11/-0.24
Pf O	+1.68/-1.35	<0.01	+1.68/-1.35	+1.13/-0.91	<0.01	+1.13/-0.91
Eb C	+0.01/-0.01	+0.07/-0.05	+0.07/-0.08	+0.00/-0.00	+0.01/-0.01	+0.01/-0.01
Eb O	+0.12/-0.11	<0.01	+0.12/-0.12	+0.05/-0.04	<0.01	+0.05/-0.04
CCcoh norm	+0.48/-0.49	+0.17/-0.17	+0.31/-0.31	+0.66/-0.67	+0.08/-0.09	+0.76/-0.75
Pion Abs	+2.49/-0.95	+2.48/-1.83	+0.90/-0.01	+3.24/-1.57	+0.96/-0.88	+2.25/-0.69
Pion CE (low E)	+0.14/-0.10	+0.08/-0.07	+0.20/-0.18	+0.04/-0.01	+0.02/-0.01	+0.02/-0.00
Pion CE (high E)	+1.04/-0.71	+0.25/-0.04	+0.79/-0.67	+0.96/-0.56	+0.32/-0.29	+1.25/-0.88
Pion QE (low E)	+0.11/-0.12	+0.00/-0.00	+0.10/-0.11	+0.09/-0.09	+0.02/-0.02	+0.11/-0.11
Pion QE (high E)	+0.09/-0.17	+0.01/-0.01	+0.10/-0.18	+0.01/-0.07	+0.01/-0.00	+0.00/-0.06
Pion Inelastic	+0.27/-0.35	+0.06/-0.07	+0.33/-0.41	+0.10/-0.16	+0.00/-0.00	+0.10/-0.16
Nucleon FSI C	+0.01/-0.01	+2.37/-2.37	+2.30/-2.30	+0.70/-0.70	+0.66/-0.66	+1.37/-1.37
Nucleon FSI O	+2.39/-2.39	+0.25/-0.25	+2.65/-2.65	+1.34/-1.34	+0.14/-0.14	+1.21/-1.21
Total	+5.64/-5.03	+4.46/-4.31	+6.20/-5.75	+4.95/-3.97	+2.67/-2.86	+5.20/-4.32

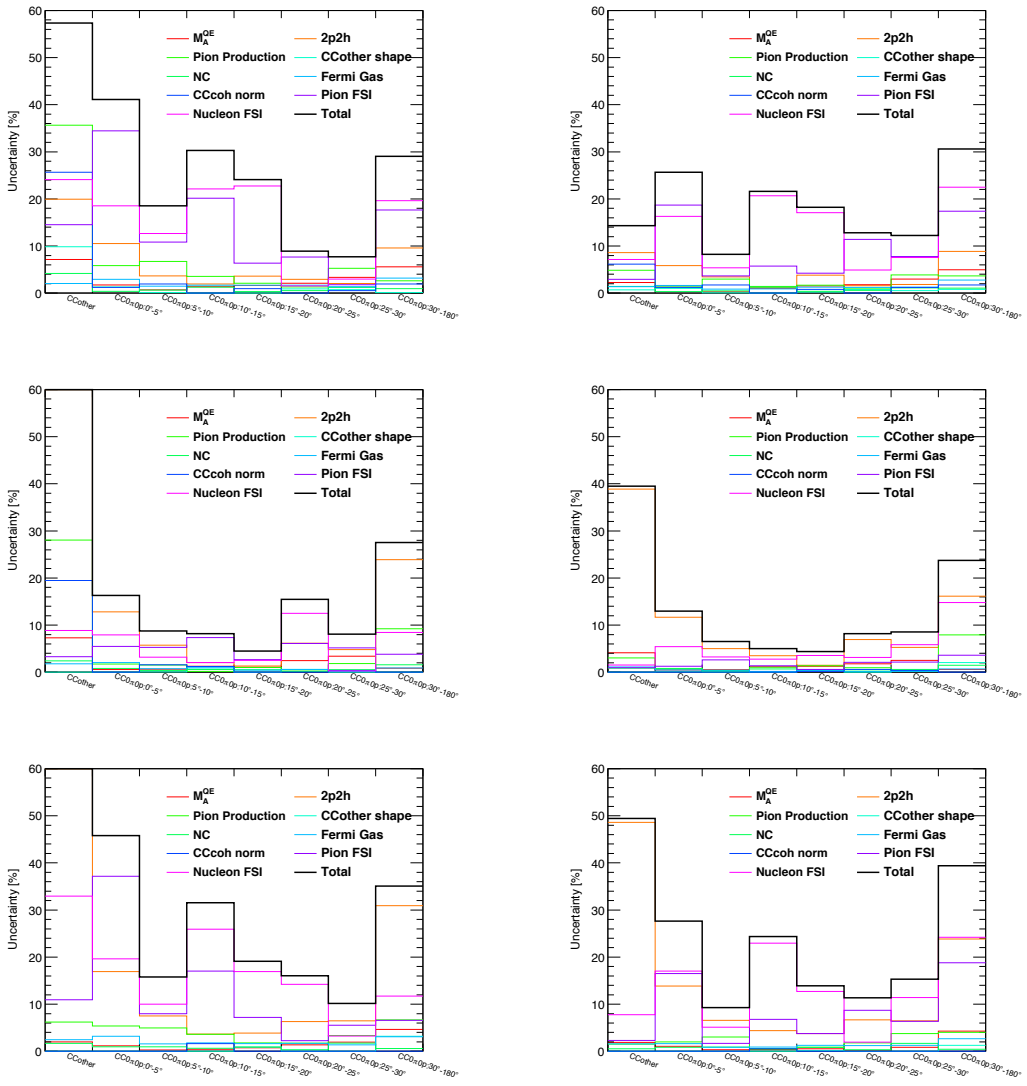

Figure 7.10: Uncertainties in each bin of differential cross section due to neutrino interaction model for $\overline{\nu}_\mu$ (left) and $\overline{\nu}_\mu + \nu_\mu$ (right) cross sections. Top line: $\sigma_{\mathrm{H_2O}}$. Middle line: σ_{CH}, Bottom line: $\sigma_{\mathrm{H_2O}}/\sigma_{\mathrm{CH}}$.

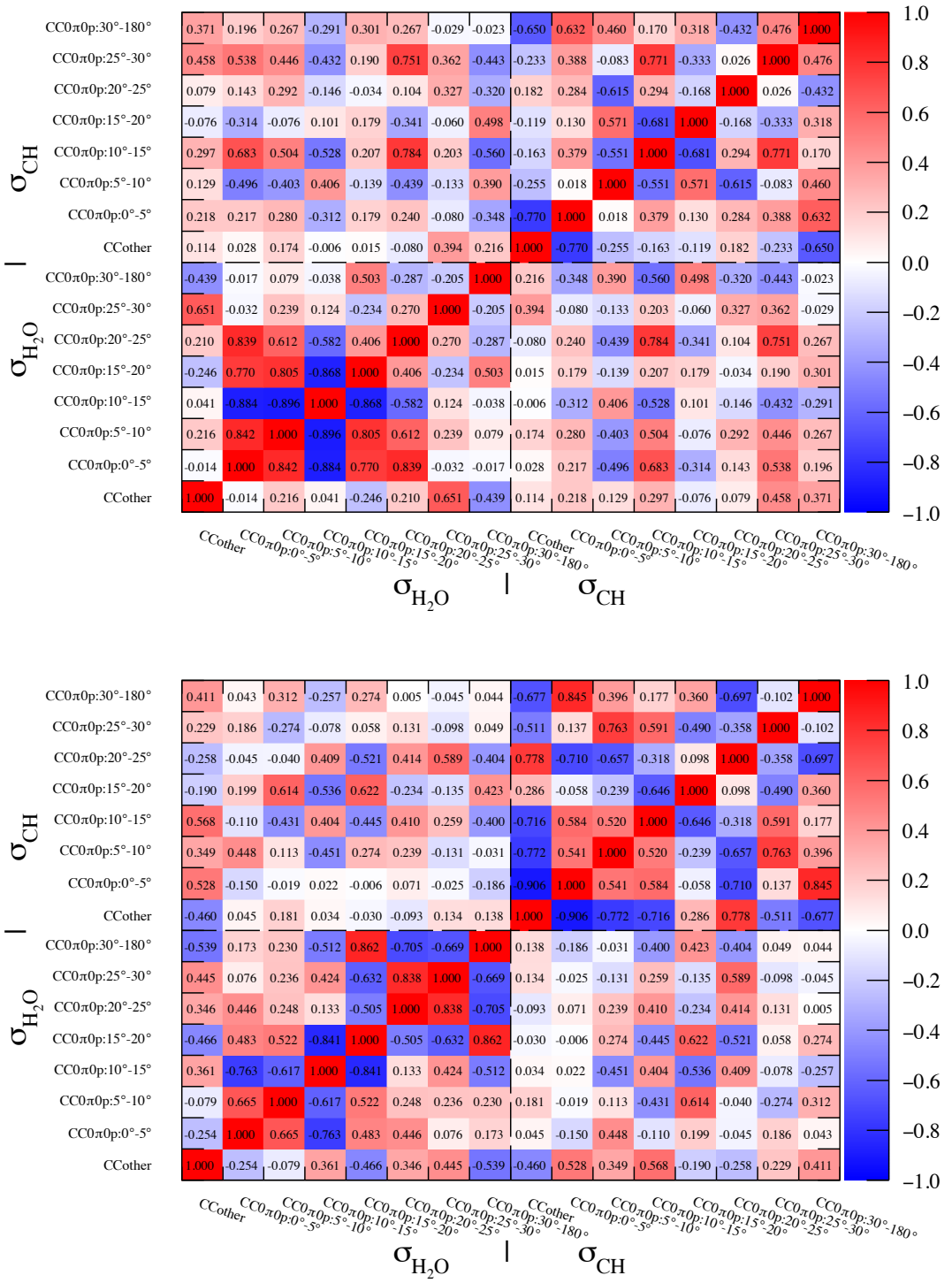

Figure 7.11: Correlation matrices for uncertainties due to neutrino interaction model for $\overline{\nu}_\mu$ (left) and $\overline{\nu}_\mu+\nu_\mu$ (right) cross sections, concerning correlation between $\sigma_{\mathrm{H_2O}}$ and σ_{CH}.

7.3.3 Systematic errors from detector response

Uncertainty on the detector response is estimated based on measurements during the detector construction, commissioning data taking with cosmic muons, and operation with the neutrino beam. Effects on the number of selected events are estimated according to the uncertainty of detector response, and the systematic uncertainty on the cross section measurement is estimated by fluctuating the measured number of selected events. In order to fluctuate the number of selected events, no correlation between WAGASCI and Proton Module is assumed, except for the beam-related background events which should be in common for both detectors. Correlations between bins of the reconstructed tracks are considered.

Sources of the uncertainty and how to determine the 1σ uncertainty on each parameter are listed as follows:

- Detector performance
  - Target mass:

    All parameters, such as scintillator positions and weights, are measured during the detector construction. The measurement accuracy is taken as the 1σ uncertainty.
  - MPPC noise:

    The noise rate is measured as 0.025 hits per beam bunch per module. The simulation is generated with different noise rates, 0 hits and 1 hits, and the difference is taken as the 1σ uncertainty.
  - Scintillator crosstalk:

    The crosstalk rate is measured as 0.64%:The simulation is generated with different crosstalk rates, 0% and 1%, and the difference is taken as the 1σ uncertainty.
  - Two-dimensional track reconstruction:

    The reconstruction efficiency is estimated by using sand muon, as described in Sec. 4.6.2.2. Difference between data and simulation is taken as the 1σ uncertainty.
- Neutrino beam
  - Event pileup:

    In order to estimate the event pileup effect, tracks are reconstructed by combining two bunches next to each other and using all hits in the double bunch. Difference in the number of selected events between the double-bunched and nominal selection is taken as the 1σ uncertainty.

– Beam-related background events:

  Difference in the number of sand muon events between data and simulation is taken as the 1σ uncertainty.

Uncertainty from the event selection is estimated by difference between data and simulation in the variation of the number of selected events as changing each selection criteria. Sources of the uncertainty and the selection criteria are listed in Table 7.9.

Table 7.9: Uncertainties from each event selection.

Event selection	Nominal criteria	Variation
Hit threshold	>2.5 p.e.	>3.5 p.e.
2D track Match	$\|\Delta\theta\| < 35$ deg	30 deg, 40 deg
	$\|\Delta x\| < 150$ mm	140 mm, 160 mm
3D track reconstruction	$\|\Delta z\| < 2$ planes	1 plane,3 planes
Vertex extraction	$\|\Delta z_x\| + \|\Delta z_y\| < 3$ planes	2 plane, 4 planes
	$\sqrt{\Delta x^2 + \Delta y^2} < 150$ mm	100 mm, 200 mm
Beam timing cut	Event timing $< \pm 100$ ns	No cut
Upstream veto cut	Vertex Z > 2nd plane	3rd plane, 4th plane
Fiducial volume cut	|Vertex X(Y)| < 35 cm	25 cm
Additional acceptance cut	Extrapolation of a reconstructed track	x,y,z ± 5 *cm*

The systematic uncertainty of the measured cross section is calculated as shown in Table 7.10 and 7.11. Uncertainties on each bin of the differential cross section and contributions from each source are shown in Fig. 7.12. The dominating parameters are upstream veto cut, three-dimensional track reconstruction, vertex extraction, and hit threshold. Figure 7.13 shows the correlation matrices.

Table 7.10: Summary of the detector systematics for the $\overline{\nu}_\mu$ cross sections.

	σ_{H_2O}		σ_{CH}		$\sigma_{H_2O}/\sigma_{CH}$	
	WAGASCI	PM	WAGASCI	PM	WAGASCI	PM
Target mass	0.68%	0.05%	< 0.01%	0.27%	0.68%	0.32%
MPPC noise	1.08%	0.56%	< 0.01%	0.78%	1.12%	0.94%
Scintillator crosstalk	0.34%	—	< 0.01%	—	0.34%	—
Hit efficiency	1.84%	0.56%	< 0.01%	0.83%	1.87%	0.99%
Event pileup	1.02%	0.56%	< 0.01%	0.73%	1.02%	0.87%
Beam-related BG	1.77%		1.76%		2.77%	
2D track reconstruction	0.74%	0.55%	< 0.01%	0.64%	0.74%	0.76%
2D track Match (WAGASCI-INGRID)	1.42%		< 0.01%		1.54%	
2D track Match (PM-WAGASCI)	0.64%		0.65%		0.96%	
2D track Match (PM-INGRID)	0.56%		0.56%		0.34%	
3D track reconstruction	1.96%	0.75%	< 0.01%	2.89%	1.96%	3.34%
Vertex extraction (pln)	1.23%	0.55%	< 0.01%	0.91%	1.23%	1.10%
Vertex extraction (ch)	1.77%	0.55%	< 0.01%	0.80%	1.77%	0.99%
Beam timing cut	0.55%		0.01%		0.56%	
Upstream veto cut	2.37%	0.56%	< 0.01%	0.94%	2.37%	1.14%
Fiducial volume cut	0.62%	0.34%	< 0.01%	1.13%	0.62%	1.36%
Additional acceptance cut	1.50%	—	< 0.01%	—	1.55%	—
Total	5.49%		3.75%		7.02%	

Table 7.11: Summary of the detector systematics for the $\overline{\nu}_\mu + \nu_\mu$ cross sections.

	σ_{H_2O}		σ_{CH}		$\sigma_{H_2O}/\sigma_{CH}$	
	WAGASCI	PM	WAGASCI	PM	WAGASCI	PM
Target mass	0.68%	0.05%	< 0.01%	0.27%	0.68%	0.32%
MPPC noise	1.02%	0.56%	< 0.01%	0.72%	1.05%	0.86%
Scintillator crosstalk	0.55%	—	< 0.01%	—	0.55%	—
Hit efficiency	1.71%	0.56%	< 0.01%	0.74%	1.74%	0.87%
Event pileup	0.94%	0.56%	< 0.01%	0.68%	0.94%	0.81%
Beam-related BG	1.63%		1.61%		2.55%	
2D track reconstruction	0.73%	0.56%	< 0.01%	0.65%	0.73%	0.78%
2D track Match (WAGASCI-INGRID)	1.31%		< 0.01%		1.41%	
2D track Match (PM-WAGASCI)	0.60%		0.62%		0.89%	
2D track Match (PM-INGRID)	0.56%		0.56%		0.56%	
3D track reconstruction	1.99%	0.69%	< 0.01%	2.62%	1.99%	3.17%
Vertex extraction (pln)	1.12%	0.56%	< 0.01%	0.83%	1.12%	1.00%
Vertex extraction (ch)	1.83%	0.55%	< 0.01%	0.78%	1.83%	0.93%
Beam timing cut	0.55%		< 0.01%		0.56%	
Upstream veto cut	2.19%	0.56%	< 0.01%	0.86%	2.19%	1.05%
Fiducial volume cut	0.58%	0.56%	< 0.01%	1.04%	0.58%	1.25%
Additional acceptance cut	1.32%	—	< 0.01%	—	1.32%	—
Total	5.15%		3.41%		6.54%	

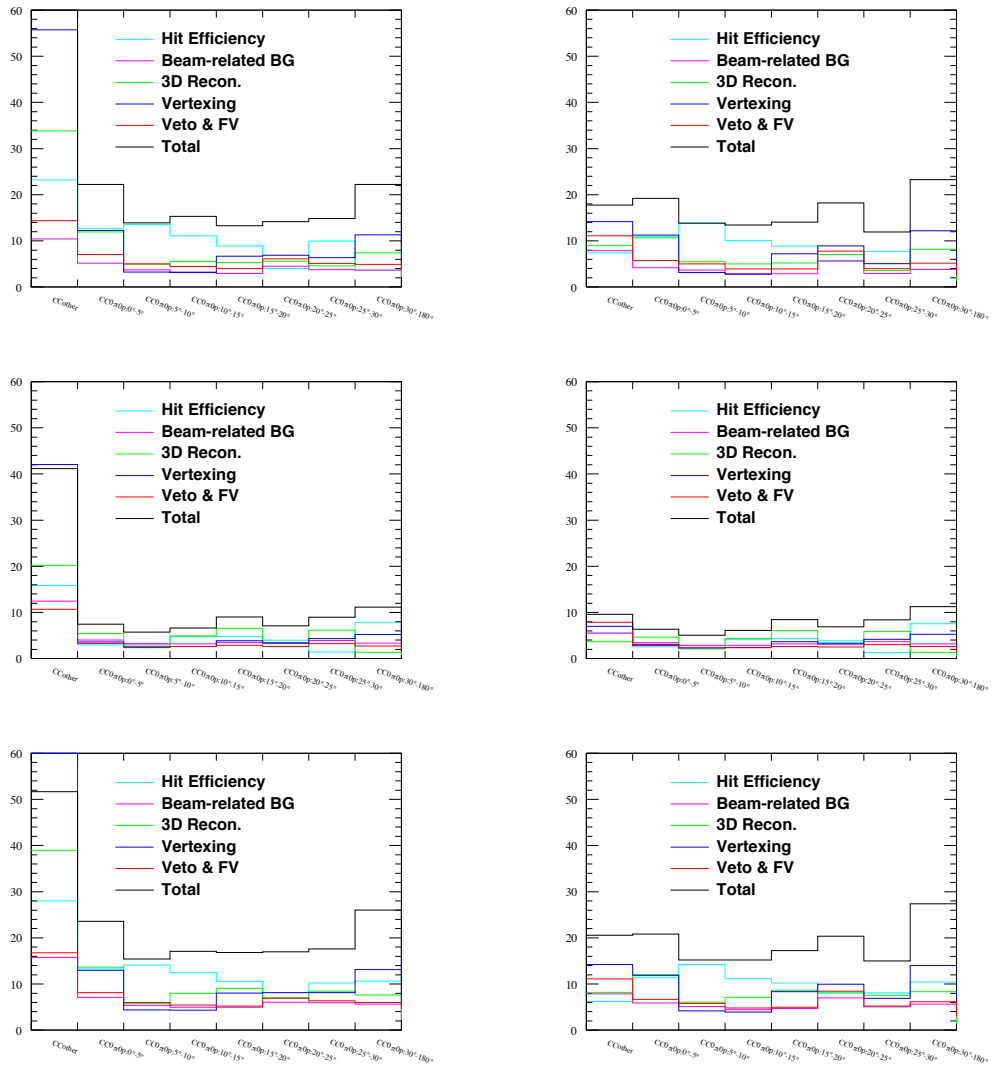

Figure 7.12: Uncertainty due to the detector response for $\overline{\nu}_\mu$ cross section (left) and $\overline{\nu}_\mu + \nu_\mu$ cross section (right). Top line: $\sigma_{\mathrm{H_2O}}$. Middle line: σ_{CH}. Bottom line: $\sigma_{\mathrm{H_2O}}/\sigma_{\mathrm{CH}}$ (bottom).

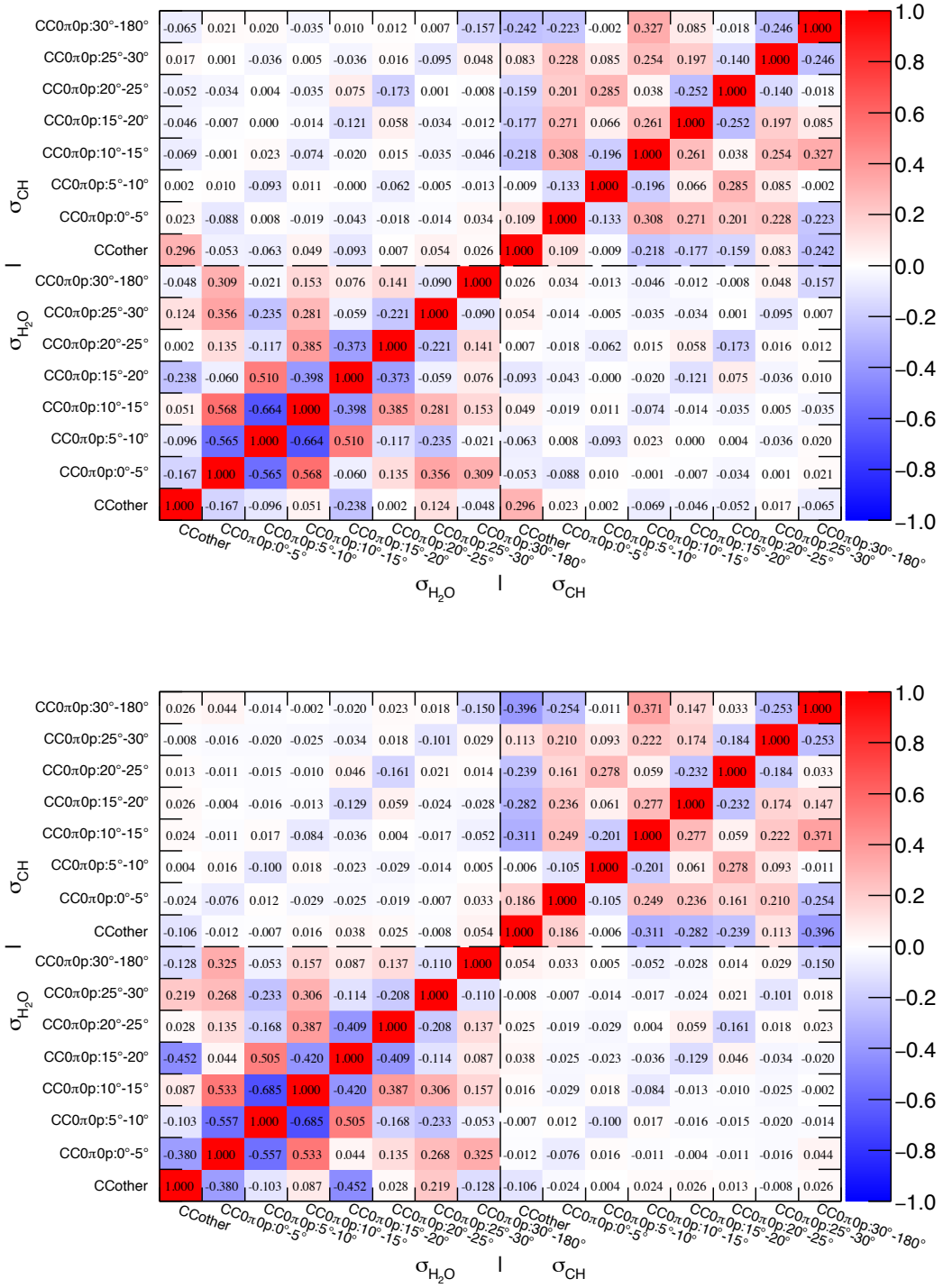

Figure 7.13: Correlation matrices from the detector systematics for $\overline{\nu}_\mu$ cross section (top) and $\overline{\nu}_\mu + \nu_\mu$ cross section (bottom), concerning correlation between $\sigma_{\mathrm{H_2O}}$ and σ_{CH}.

7.4 Summary of uncertainties

7.4.1 Summary of systematic uncertainties

Systematic uncertainties on the CC0π0p with a muon angle less than 30 degrees cross sections are summarized in Table 7.12. Quadratic sums of the uncertainties from neutrino flux, neutrino interaction and detector response are taken as total systematic uncertainties. The dominant systematic error for the absolute cross sections, σ_{H_2O} and σ_{CH}, is the uncertainty from neutrino flux with a level of about 10%. The uncertainty on the cross section ratio measurement, $\sigma_{H_2O}/\sigma_{CH}$, is dominated by that from the detector response with a level of 7%. Systematics uncertainties on each bin of the differential cross sections are shown in Fig. 7.14. Quadratic sums of three components on each bin are taken as the total systematic errors for the bin.

Table 7.12: Summary of the systematic uncertainties of the measured cross section for CC0π0p with muon angle less than 30 degrees. (%)

	σ_{H_2O}	σ_{CH}	$\sigma_{H_2O}/\sigma_{CH}$
The $\overline{\nu}_\mu$ cross section			
Neutrino flux	+10.85/-9.23	+10.56/-9.05	+0.51/-0.53
Neutrino interaction	+5.64/-5.03	+4.46/-4.31	+6.20/-5.75
Detector response	±5.49	±3.75	±7.02
Total	+13.40/-11.86	+12.06/-10.70	+9.38/-9.09
The $\overline{\nu}_\mu + \nu_\mu$ cross section			
Neutrino flux	+10.60/-9.07	+10.27/-8.86	+0.54/-0.55
Neutrino interaction	+4.95/-3.97	+2.67/-2.86	+5.20/-4.32
Detector response	±5.15	±3.41	±6.54
Total	+12.78/-11.16	+11.15/-9.92	+8.37/-7.86

7.4.2 Total uncertainty

Total uncertainties are summarized in Table. 7.13 and 7.14. The total uncertainty on the right-end column is calculated as a quadratic sum of the statistical uncertainty and the systematic uncertainties. For the cross sections measurements of CC0π0p with a muon angle less than 30 degrees, the total uncertainty on the absolute cross sections, σ_{H_2O} and σ_{CH}, is dominated by the neutrino flux uncertainty, while that on the ratio cross section, $\sigma_{H_2O}/\sigma_{CH}$, is dominated by those from statistical errors and detector response.

Table 7.13: Summary of errors on the $\overline{\nu}_\mu$ cross section [%].

	True phase space	Statistics	Neutino flux	Neutrino interactions	Detector response	Total
σ_{H_2O}	CCother	±49.40	$^{+8.46}_{-7.24}$	$^{+57.33}_{-53.24}$	±61.65	$^{+97.98}_{-95.54}$
	CC0π0p : 0 − 5deg	±29.51	$^{+10.66}_{-9.00}$	$^{+41.24}_{-37.66}$	±22.21	$^{+56.38}_{-53.51}$
	CC0π0p : 5 − 10deg	±51.56	$^{+11.36}_{-9.49}$	$^{+19.44}_{-16.06}$	±13.91	$^{+57.96}_{-56.57}$
	CC0π0p : 10 − 15deg	±29.33	$^{+11.02}_{-9.25}$	$^{+31.64}_{-28.81}$	±15.34	$^{+47.10}_{-44.85}$
	CC0π0p : 15 − 20deg	±36.72	$^{+10.90}_{-9.28}$	$^{+24.26}_{-23.96}$	±13.28	$^{+47.25}_{-46.74}$
	CC0π0p : 20 − 25deg	±32.68	$^{+10.62}_{-9.05}$	$^{+8.28}_{-6.78}$	±14.17	$^{+38.08}_{-37.37}$
	CC0π0p : 25 − 30deg	±41.45	$^{+11.14}_{-9.44}$	$^{+8.21}_{-8.92}$	±14.86	$^{+46.16}_{-45.91}$
	CC0π0p : 30 − 180deg	±22.78	$^{+10.29}_{-8.70}$	$^{+29.41}_{-24.54}$	±22.21	$^{+44.53}_{-41.11}$
	CCTotal	±10.01	$^{+9.56}_{-8.24}$	$^{+15.66}_{-14.28}$	±8.95	$^{+22.74}_{-21.27}$
	CC0π0p : 0 − 30deg	±6.32	$^{+10.85}_{-9.23}$	$^{+5.64}_{-5.03}$	±5.49	$^{+14.82}_{-13.44}$
σ_{CH}	CCother	±35.48	$^{+8.55}_{-7.35}$	$^{+81.77}_{-76.14}$	±41.18	$^{+98.56}_{-93.84}$
	CC0π0p : 0 − 5deg	±27.14	$^{+10.83}_{-9.17}$	$^{+17.29}_{-16.44}$	±7.43	$^{+34.76}_{-33.86}$
	CC0π0p : 5 − 10deg	±34.77	$^{+10.77}_{-9.14}$	$^{+9.55}_{-7.76}$	±5.76	$^{+38.07}_{-37.23}$
	CC0π0p : 10 − 15deg	±21.68	$^{+10.41}_{-8.95}$	$^{+9.27}_{-5.85}$	±6.64	$^{+26.61}_{-25.07}$
	CC0π0p : 15 − 20deg	±27.38	$^{+10.84}_{-9.16}$	$^{+4.79}_{-4.37}$	±9.04	$^{+31.17}_{-30.57}$
	CC0π0p : 20 − 25deg	±23.84	$^{+10.75}_{-9.24}$	$^{+16.18}_{-15.21}$	±7.07	$^{+31.55}_{-30.58}$
	CC0π0p : 25 − 30deg	±25.71	$^{+10.37}_{-8.80}$	$^{+7.93}_{-6.80}$	±8.96	$^{+30.19}_{-29.41}$
	CC0π0p : 30 − 180deg	±29.25	$^{+10.43}_{-8.96}$	$^{+29.05}_{-32.23}$	±11.13	$^{+43.96}_{-45.81}$
	CCTotal	±8.75	$^{+9.59}_{-8.14}$	$^{+19.45}_{-17.46}$	±5.27	$^{+23.97}_{-21.80}$
	CC0π0p : 0 − 30deg	±4.96	$^{+10.56}_{-9.05}$	$^{+4.46}_{-4.31}$	±3.75	$^{+13.04}_{-11.80}$
$\sigma_{H_2O}/\sigma_{CH}$	CCother	±49.92	$^{+0.57}_{-0.63}$	$^{+107.84}_{-86.87}$	±51.68	$^{+129.59}_{-112.74}$
	CC0π0p : 0 − 5deg	±36.62	$^{+1.66}_{-1.63}$	$^{+45.20}_{-34.81}$	±23.57	$^{+62.79}_{-55.77}$
	CC0π0p : 5 − 10deg	±51.53	$^{+1.47}_{-1.52}$	$^{+17.46}_{-22.96}$	±15.43	$^{+56.57}_{-58.50}$
	CC0π0p : 10 − 15deg	±31.61	$^{+1.11}_{-1.10}$	$^{+32.60}_{-26.81}$	±17.10	$^{+48.53}_{-44.85}$
	CC0π0p : 15 − 20deg	±40.25	$^{+0.78}_{-0.77}$	$^{+19.67}_{-20.33}$	±16.83	$^{+47.86}_{-48.13}$
	CC0π0p : 20 − 25deg	±40.00	$^{+0.87}_{-0.91}$	$^{+17.23}_{-17.71}$	±16.98	$^{+46.76}_{-46.94}$
	CC0π0p : 25 − 30deg	±52.31	$^{+1.62}_{-1.60}$	$^{+10.02}_{-8.47}$	±17.62	$^{+56.12}_{-55.86}$
	CC0π0p : 30 − 180deg	±36.99	$^{+1.38}_{-1.38}$	$^{+36.35}_{-37.90}$	±26.02	$^{+58.04}_{-59.02}$
	CCTotal	±12.60	$^{+0.37}_{-0.38}$	$^{+17.13}_{-18.97}$	±10.61	$^{+23.77}_{-25.13}$
	CC0π0p : 0 − 30deg	±7.93	$^{+0.51}_{-0.53}$	$^{+6.20}_{-5.75}$	±7.02	$^{+12.28}_{-12.06}$

Table 7.14: Summary of errors on the $\overline{\nu}_\mu + \nu_\mu$ cross section [%].

	True phase space	Statistics	Neutino flux	Neutrino interactions	Detector response	Total
σ_{H_2O}	CCother	±13.64	$^{+8.32}_{-7.03}$	$^{+14.30}_{-14.09}$	±17.76	$^{+27.84}_{-27.37}$
	CC0π0p : 0 − 5deg	±29.32	$^{+10.37}_{-8.87}$	$^{+25.94}_{-21.59}$	±19.23	$^{+44.83}_{-42.12}$
	CC0π0p : 5 − 10deg	±39.37	$^{+11.04}_{-9.21}$	$^{+8.22}_{-7.62}$	±13.84	$^{+43.95}_{-43.41}$
	CC0π0p : 10 − 15deg	±16.84	$^{+10.89}_{-9.35}$	$^{+21.48}_{-21.21}$	±13.42	$^{+32.31}_{-31.64}$
	CC0π0p : 15 − 20deg	±31.95	$^{+10.71}_{-9.06}$	$^{+18.02}_{-17.70}$	±14.06	$^{+40.72}_{-40.17}$
	CC0π0p : 20 − 25deg	±19.09	$^{+10.57}_{-9.05}$	$^{+12.93}_{-8.93}$	±18.20	$^{+31.22}_{-29.28}$
	CC0π0p : 25 − 30deg	±29.39	$^{+10.70}_{-9.17}$	$^{+12.22}_{-10.51}$	±11.93	$^{+35.64}_{-34.65}$
	CC0π0p : 30 − 180deg	±31.33	$^{+10.34}_{-8.72}$	$^{+30.67}_{-27.00}$	±23.28	$^{+50.71}_{-48.26}$
	CCTotal	±6.43	$^{+9.30}_{-7.96}$	$^{+5.78}_{-5.62}$	±7.41	$^{+14.70}_{-13.83}$
	CC0π0p : 0 − 30deg	±5.53	$^{+10.60}_{-9.07}$	$^{+4.95}_{-3.97}$	±5.15	$^{+13.93}_{-12.46}$
σ_{CH}	CCother	±7.05	$^{+8.57}_{-7.29}$	$^{+39.48}_{-37.33}$	±9.57	$^{+42.11}_{-39.85}$
	CC0π0p : 0 − 5deg	±19.40	$^{+10.37}_{-8.84}$	$^{+13.00}_{-12.94}$	±6.36	$^{+26.33}_{-25.74}$
	CC0π0p : 5 − 10deg	±25.70	$^{+10.76}_{-9.24}$	$^{+6.46}_{-6.37}$	±5.06	$^{+29.04}_{-28.50}$
	CC0π0p : 10 − 15deg	±18.95	$^{+9.99}_{-8.62}$	$^{+4.77}_{-4.68}$	±6.08	$^{+22.78}_{-22.19}$
	CC0π0p : 15 − 20deg	±22.84	$^{+10.73}_{-9.15}$	$^{+4.23}_{-4.40}$	±8.44	$^{+26.94}_{-26.38}$
	CC0π0p : 20 − 25deg	±18.22	$^{+10.30}_{-8.92}$	$^{+7.73}_{-6.31}$	±6.87	$^{+23.34}_{-22.33}$
	CC0π0p : 25 − 30deg	±21.22	$^{+9.92}_{-8.46}$	$^{+8.45}_{-8.33}$	±8.41	$^{+26.28}_{-25.73}$
	CC0π0p : 30 − 180deg	±23.54	$^{+10.31}_{-8.98}$	$^{+24.53}_{-28.38}$	±11.28	$^{+37.27}_{-39.59}$
	CCTotal	±5.81	$^{+9.35}_{-7.86}$	$^{+13.23}_{-11.97}$	±3.64	$^{+17.59}_{-15.88}$
	CC0π0p : 0 − 30deg	±4.20	$^{+10.27}_{-8.86}$	$^{+2.67}_{-2.86}$	±3.41	$^{+11.91}_{-10.77}$
$\sigma_{H_2O}/\sigma_{CH}$	CCother	±16.04	$^{+0.62}_{-0.67}$	$^{+49.39}_{-44.85}$	±20.57	$^{+55.86}_{-51.89}$
	CC0π0p : 0 − 5deg	±33.71	$^{+1.64}_{-1.63}$	$^{+27.55}_{-27.33}$	±20.85	$^{+48.30}_{-48.17}$
	CC0π0p : 5 − 10deg	±41.49	$^{+1.57}_{-1.56}$	$^{+9.47}_{-10.26}$	±15.20	$^{+45.21}_{-45.39}$
	CC0π0p : 10 − 15deg	±23.61	$^{+1.70}_{-1.72}$	$^{+24.58}_{-24.16}$	±15.18	$^{+37.35}_{-37.07}$
	CC0π0p : 15 − 20deg	±37.77	$^{+1.47}_{-1.43}$	$^{+13.94}_{-13.85}$	±17.26	$^{+43.83}_{-43.80}$
	CC0π0p : 20 − 25deg	±26.29	$^{+0.91}_{-0.87}$	$^{+11.14}_{-10.12}$	±20.34	$^{+35.07}_{-34.76}$
	CC0π0p : 25 − 30deg	±34.63	$^{+1.69}_{-1.67}$	$^{+15.33}_{-14.63}$	±15.02	$^{+40.77}_{-40.52}$
	CC0π0p : 30 − 180deg	±41.14	$^{+1.88}_{-1.76}$	$^{+40.23}_{-35.34}$	±27.39	$^{+63.76}_{-60.79}$
	CCTotal	±8.67	$^{+0.31}_{-0.32}$	$^{+14.20}_{-15.84}$	±8.64	$^{+18.75}_{-20.02}$
	CC0π0p : 0 − 30deg	±6.91	$^{+0.54}_{-0.55}$	$^{+5.20}_{-4.32}$	±6.54	$^{+10.85}_{-10.46}$

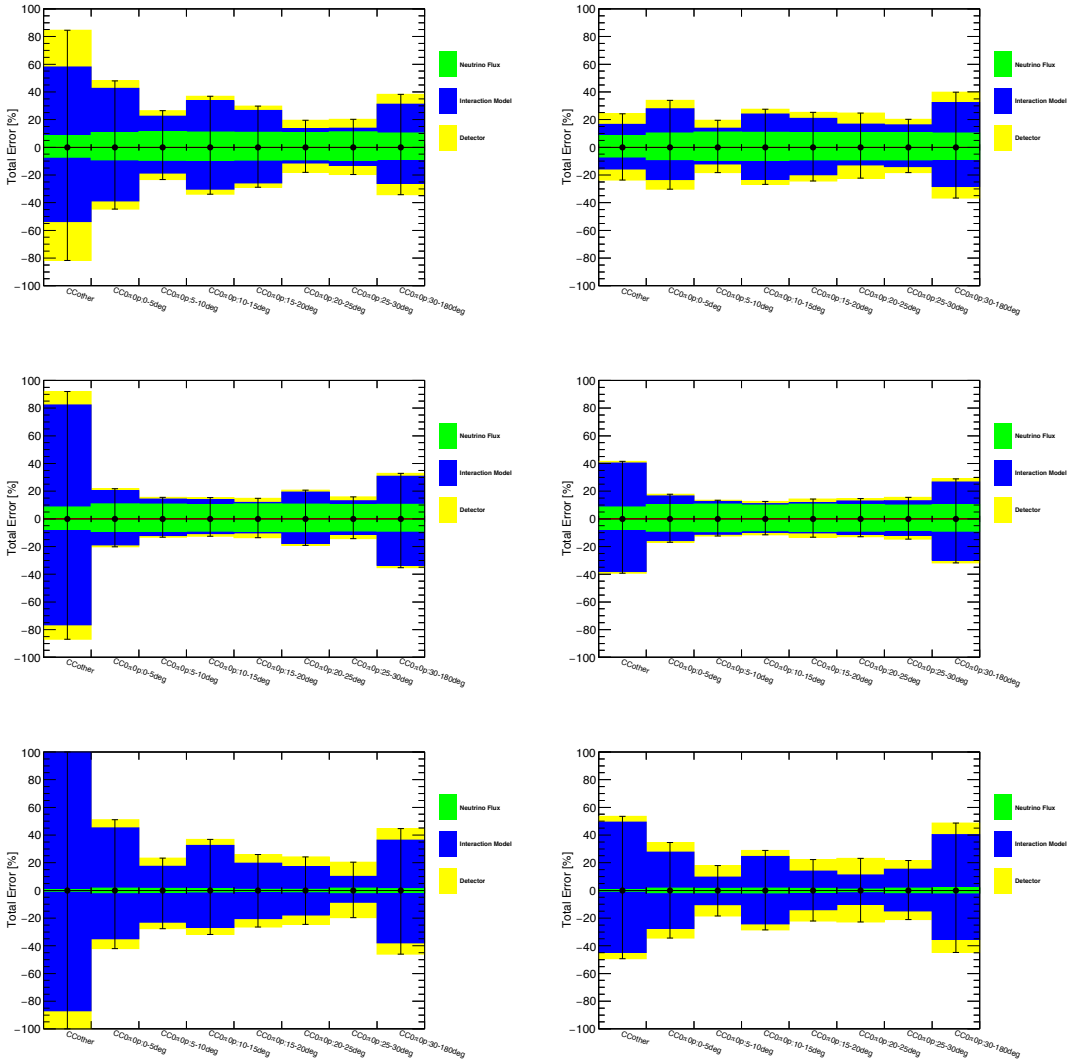

Figure 7.14: Summary of the systematic errors for $\overline{\nu}_\mu$ cross section (left) and $\overline{\nu}_\mu + \nu_\mu$ cross section (right). Top line: $\sigma_{\mathrm{H_2O}}$. Middle line: σ_{CH}. Bottom line: $\sigma_{\mathrm{H_2O}}/\sigma_{\mathrm{CH}}$ (bottom). Each plot shows the cumulative quadratic sum of the uncertainties from neutrino flux, neutrino interaction model, and detector response.

Chapter 8

Validation of analysis method

In order to validate that the cross-section extraction method functions as expected, performances with using several simulation inputs to obtain the number of selected events ($N_j^{\rm sel}$) are checked. Agreement between the extracted cross section and prediction in the used neutrino interaction generator is verified by calculating the χ^2 goodness of fit, defined as follows.

$$\chi^2 = \sum_{ii'} (\sigma_i^{\rm extracted} - \sigma_i^{\rm predicted})(V_{cov}^{-1})_{ii'}(\sigma_{i'}^{\rm extracted} - \sigma_{i'}^{\rm predicted}), \tag{8.1}$$

where $\sigma_i(i')$ is a cross section on each bin, and V_{cov}^{-1} is an inverse of the covariance matrix characterizing the extracted cross section uncertainty. In the case of a good agreement between the calculation and prediction with respect to properly estimated uncertainties, the χ^2 value is expected to be comparable with the number of degrees of freedom (N_d), $\chi^2/N_d \simeq 1$. In the case of a perfect agreement, $\chi^2 = 0$ is expected.

8.1 Validation with the nominal simulation

In order to confirm agreement of the extracted cross section with the prediction in the nominal neutrino interaction generator, which is used to estimate the quantities described in Sec. 7.1.4, the cross sections are computed using the number of selected events in the nominal Monte Carlo simulation, instead of real data.

In the case of infinite Monte Carlo statistics, the extracted cross sections are expected to exactly converge into the prediction in the neutrino interaction generator. However, the limited statistics in this analysis causes non-perfect convergence of cross sections on each bin. The cross-section extraction in this analysis is sensitive to the fluctuation of the number of events due to the strong anti-correlation.

Figure 8.1 shows evolutions of the extracted CC0π0p cross sections with a muon angle less than 30 degrees as a function of the number of iterations, comparing

cross sections computed without an iteration by using truth of the prior in the simulation ($\sigma_{\text{truth prior}}$). In the beginning, that is at the 0-th iteration, the extracted cross sections are deviated from $\sigma_{\text{truth prior}}$ by a level of 10-20%; after about 10 iterations, the cross sections are converged into the calculation with the true prior within 1%. Figure 8.2 shows evolutions of the extracted cross sections on each bin. The speed of convergence is slower than that of the total cross section, so that 100 to 200 iterations are required for each cross section to be converge into a constant value.

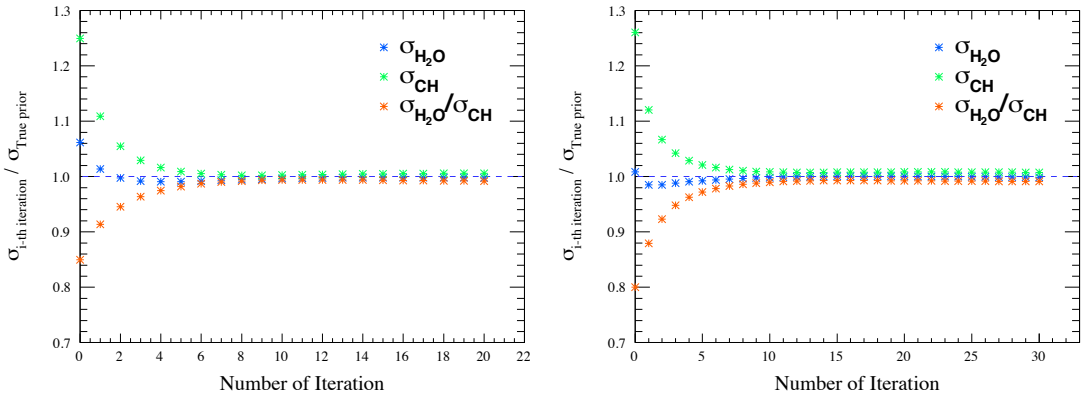

Figure 8.1: Evolutions of the extracted CC0π0p cross section with a muon angle less than 30 degrees with respect to the number of iterations. Left: $\overline{\nu}_\mu$ cross section. Right: $\overline{\nu}_\mu + \nu_\mu$ cross section. Those plots only show the first 20 iterations for $\overline{\nu}_\mu$, and 30 iterations for $\overline{\nu}_\mu + \nu_\mu$. Cross sections computed by using truth of the prior in the simulation are used as the references.

Table 8.1 shows the calculated cross sections and the expected values in the nominal simulation for CC0π0p with a muon angle less than 30 degrees, and the comparison for each bin is shown in Fig. 8.3. Whilst the total cross sections show a good agreement between the calculation and prediction, deviations up to $\sim 10\%$ are seen in the each differential cross section. Those discrepancies on each bin are explained by the anti-correlation between bins. The χ^2 values are calculated with the statistical uncertainty, as summarized in Table 8.2. Those values show good agreement between the calculated values and the predictions, since the number of degree of freedom is eight.

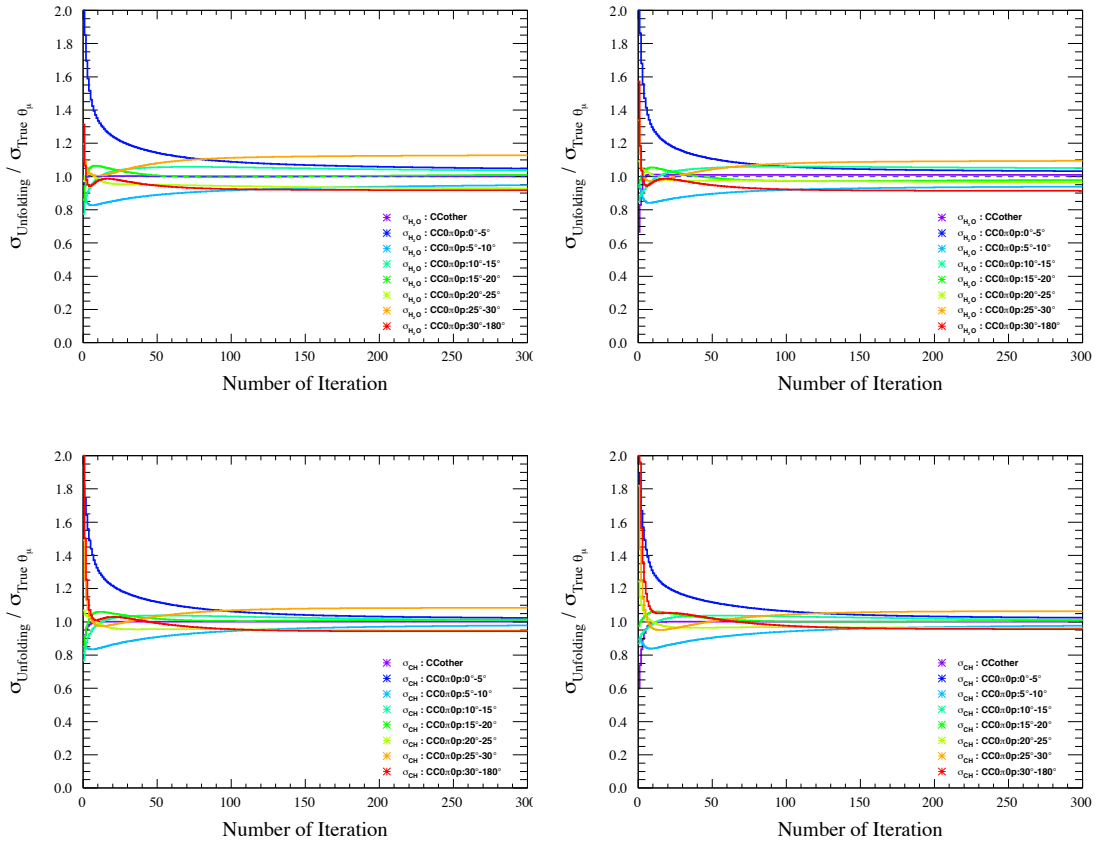

Figure 8.2: Evolutions of extracted cross sections for each true phase space bin, $\sigma_{\mathrm{H_2O}}$ (top) and σ_{CH} (bottom), with respect to the number of iterations, for $\overline{\nu}_\mu$ (left) and $\overline{\nu}_\mu + \nu_\mu$ (right), respectively.

8.2 Validation with extra input samples

In order to understand bias of the neutrino interaction model, the cross-section extraction is performed with four extra neutrino interaction generator (fake data):

- The nominal NEUT with a zigzag reweight
- The nominal NEUT with a different nuclear model
- The updated version of NEUT
- GENIE

The zigzag reweight function based on neutrino energy, shown in Fig. 8.4, is applied to the nominal simulation, for the purpose to check the effect by arbitrary

Table 8.1: Calculated cross sections for CC0π0p with a muon angle less than 30 degrees and their predictions in the nominal simulation.
Units for σ_{H_2O} and σ_{CH} are [cm$^2 \cdot$ nucleon^{-1}].

		Cross sections		Agreement
		Calculated	Expected	$(\sigma_{calc} - \sigma_{expected})/\sigma_{expected}$
$\overline{\nu}_\mu$	σ_{H_2O}	1.021×10^{-39}	1.024×10^{-39}	-0.3%
	σ_{CH}	1.068×10^{-39}	1.062×10^{-39}	+0.6%
	$\sigma_{H_2O}/\sigma_{CH}$	0.956	0.964	-0.8%
$\overline{\nu}_\mu + \nu_\mu$	σ_{H_2O}	1.080×10^{-39}	1.094×10^{-39}	-1.2%
	σ_{CH}	1.141×10^{-39}	1.139×10^{-39}	+0.2%
	$\sigma_{H_2O}/\sigma_{CH}$	0.947	0.960	-1.4%

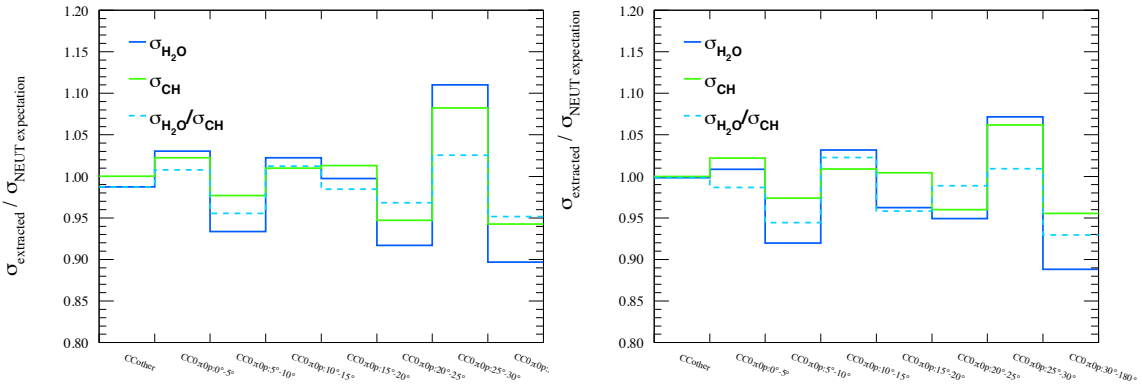

Figure 8.3: Comparison between extracted cross sections after 1500 iterations and predictions by NEUT for $\overline{\nu}_\mu$ (left) and $\overline{\nu}_\mu + \nu_\mu$ (right) .

fluctuation from the nominal value. Another input is generated with the nominal NEUT with using spectral function (SF) instead of RFG+RPA and removing the 2p-2h interactions. The update version of NEUT and GENIE adopt different the CCQE models and nuclear models from the nominal NEUT, and they serve as check of the bias on models for the dominant interaction in the signal.

The cross sections for the fake data are calculated as follows:

$$\sigma_i^{\text{Fake-data}} = \sum_j \frac{U_{ij}^{\text{Fake-data}}(N_{j\ \text{sel}}^{\text{Fake-data}} - N_{j\ \text{BG}}^{\text{Nominal}})}{\Phi T \varepsilon_i^{\text{Nominal}}}, \tag{8.2}$$

where the number of selected events ($N_{\text{sel}}^{\text{Fake-data}}$) is estimated by the fake data, and the other quantities, Φ, T, ε_i, and $N_{j\ \text{BG}}$, are taken from the nominal values shown in Sec. 7.1.4. The response matrix, $U_{ij}^{\text{Fake-data}}$, is calculated with the unfolding method using the smearing matrix estimated by the nominal generator

Table 8.2: The χ^2 values for the cross sections calculated with the nominal simulation input. Only statistical errors are taken into account for this calculation.

	σ_{H_2O}	σ_{CH}	$\sigma_{H_2O}/\sigma_{CH}$
$\overline{\nu}_\mu$	0.54	0.34	0.25
$\overline{\nu}_\mu + \nu_\mu$	0.38	0.18	0.12

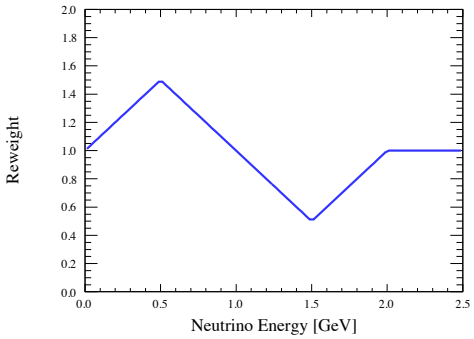

Figure 8.4: The function reweighing the distribution in the nominal NEUT.

$(\mathbb{P}(X_j^{\text{reco}}|C_i^{\text{true}}))$ and $N_{\text{sel}}^{\text{Fake-data}}$.

In order to verify the agreement between the extracted cross sections and predictions in each fake data, the bias of the fake data is calculated as follows:

$$\frac{\sigma_i^{\text{Fake-data}} - \sigma_{i\ true}^{\text{Fake-data}}}{\sigma_{i\ true}^{\text{Fake-data}}}, \tag{8.3}$$

where $\sigma_i^{\text{Fake-data}}$ is the extracted cross section with Eq 8.2, and $\sigma_{i\ true}^{\text{Fake-data}}$ is the true cross section expected in the generator used as the fake data. The bias of the fake data for the cross section of CC0π0p with a muon angle less than 30 degrees is summarized in Table. 8.3 and 8.4. Figure 8.5 shows the bias of cross sections for each bin, and the deviation is compared with quadratic sum of the statistical errors and fractional systematic uncertainty from neutrino interaction model. Those cross sections using fake data set are consistent to those by the nominal generator within the uncertainties. The χ^2 values are shown in Table. 8.5 and 8.6. For calculation of the χ^2 values, the fractional systematics errors due to neutrino interaction model and statistical errors expected from the nominal simulation are used. The small χ^2 values show that the cross-section is extracted consistently to the true values for all of the extra neutrino interaction generators.

Table 8.3: Bias of fake data for $\overline{\nu}_\mu$ cross section for CC0π0p with a muon angle less than 30 degrees. [%]

	σ_{H_2O}	σ_{CH}	$\sigma_{H_2O}/\sigma_{CH}$
Nominal NEUT with Zigzag-Reweight	+0.86	-1.34	+2.23
Nominal NEUT with SF + no 2p2h	+1.50	+0.88	+0.62
Updated NEUT	+4.44	+5.02	-0.56
GENIE	+0.78	-3.60	+4.54

Table 8.4: Bias of fake data study for $\overline{\nu}_\mu + \nu_\mu$ cross section for CC0π0p with a muon angle less than 30 degrees. [%]

	σ_{H_2O}	σ_{CH}	$\sigma_{H_2O}/\sigma_{CH}$
Nominal NEUT with Zigzag-Reweight	+0.24	-1.23	+1.49
Nominal NEUT with SF + no 2p2h	+0.64	+0.37	+0.27
Updated NEUT	+3.51	+2.65	+0.83
GENIE	+4.31	+2.05	+2.21

Table 8.5: Summary of the χ^2 values for $\overline{\nu}_\mu$ cross section. Fractional systematic errors due to neutrino interaction model and statistical errors are considered.

	σ_{H_2O}	σ_{CH}	$\sigma_{H_2O}/\sigma_{CH}$
Nominal NEUT with Zigzag-Reweight	0.41	0.08	0.15
Nominal NEUT with SF + no 2p2h	0.25	0.14	0.03
Updated NEUT	1.12	1.04	0.56
GENIE	1.13	0.87	0.57

Table 8.6: Summary of absolute χ^2 values for $\overline{\nu}_\mu + \nu_\mu$ cross section. Fractional systematic errors due to neutrino interaction model and statistical errors are considered.

	σ_{H_2O}	σ_{CH}	$\sigma_{H_2O}/\sigma_{CH}$
Nominal NEUT with Zigzag-Reweight	0.40	0.11	0.09
Nominal NEUT with SF + no 2p2h	0.16	0.27	0.09
Updated NEUT	0.24	1.59	1.07
GENIE	0.42	1.95	1.11

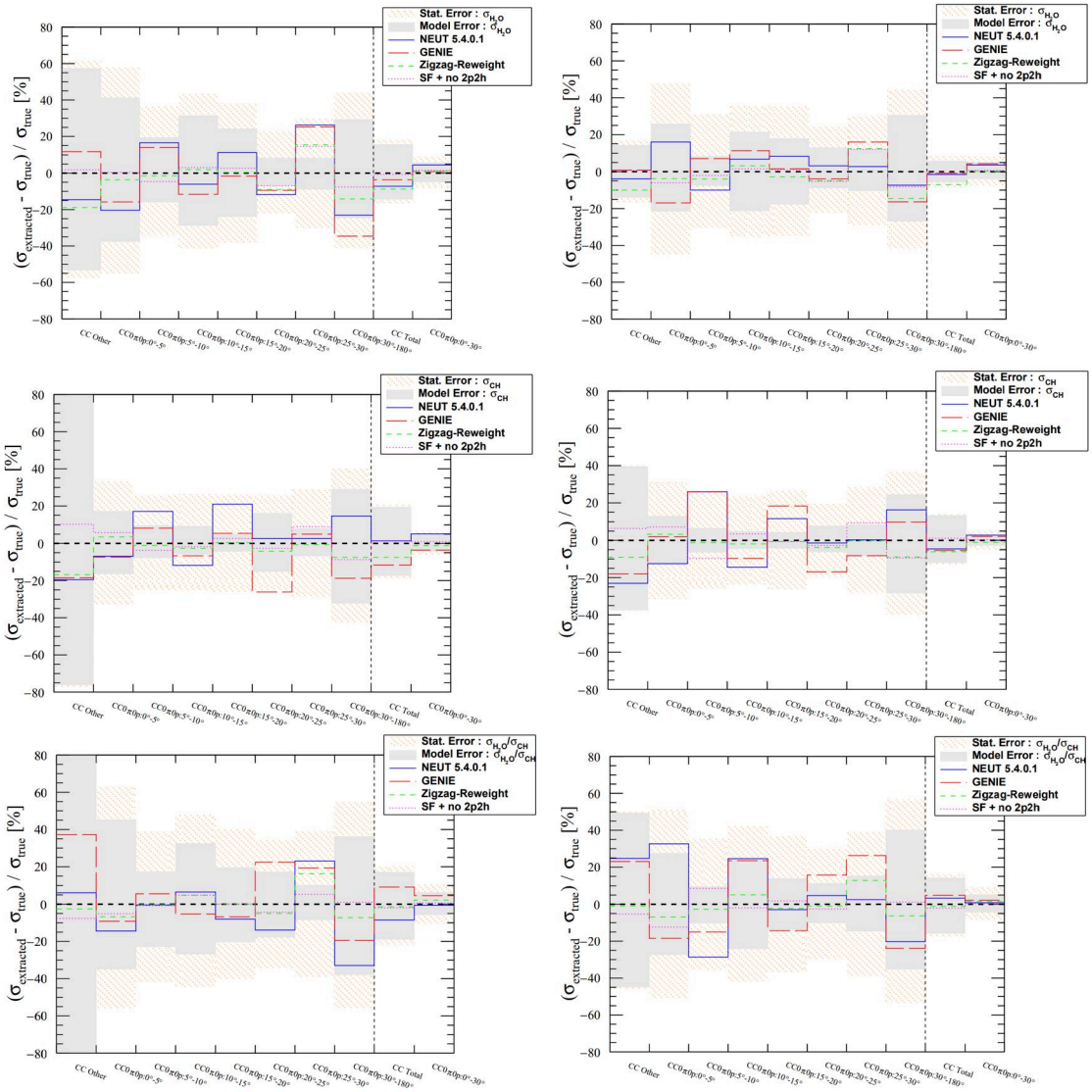

Figure 8.5: Summary of the fake data study. The gray error boxes correspond to the fractional uncertainty due to neutrino interaction model. The outer errors regions, which is the sum of the gray boxes and the red boxes, correspond to the cumulative quadratic sum of the model systematics and statistical errors. Figures correspond to $\overline{\nu}_\mu$ (left column) and $\overline{\nu}_\mu$+ν_μ (right column) cross sections, respectively. Top line: $\sigma_{\mathrm{H_2O}}$. Middle line: σ_{CH}, Bottom line: $\sigma_{\mathrm{H_2O}}/\sigma_{\mathrm{CH}}$. As for the bin for CC other events, the error sizes are over the displayed region for the $\overline{\nu}_\mu$ cross sections and for the $\overline{\nu}_\mu + \nu_\mu$ $\sigma_{\mathrm{H_2O}}/\sigma_{\mathrm{CH}}$ cross section. NEUT 5.4.0.1 represents the updated version of NEUT.

Chapter 9

Conclusions

In this thesis, we report measurements of neutrino charged-current interactions on water and hydrocarbon targets with the WAGASCI module using the T2K anti-neutrino beam. Mean of the neutrino energy is 0.86 GeV, and the peak is at 0.66 GeV with 1σ spread of $^{+0.40}_{-0.25}$ GeV. The signal is CC0π0p, defined based on kinematics of muons, pions, and protons. The differential cross sections and total cross sections are measured for each of interactions including $\overline{\nu}_\mu$ only and including both $\overline{\nu}_\mu$ and ν_μ.

9.1 Results

Figure 9.1 shows the convergence of the extracted cross section with respect to the number of iterations. Here, drifts of the extracted cross sections, which is defined as $\sigma_{i\text{-th iteration}} - \sigma_{(i-1)\text{-th iteration}}$, are shown. With 1500 iterations, each cross section is sufficiently converged into a constant value.

The measured flux-integrated CC0π0p with a muon angle less than 30 degrees on H_2O and CH are:

$$\begin{aligned}
\sigma^{\overline{\nu}_\mu}_{H_2O} &= \left[1.082 \pm 0.068(\text{stat.})^{+0.145}_{-0.128}(\text{syst.})\right] \times 10^{-39}\text{cm}^2 \cdot \text{nucleon}^{-1}, \\
\sigma^{\overline{\nu}_\mu}_{CH} &= \left[1.096 \pm 0.054(\text{stat.})^{+0.132}_{-0.117}(\text{syst.})\right] \times 10^{-39}\text{cm}^2 \cdot \text{nucleon}^{-1}, \\
\sigma^{\overline{\nu}_\mu}_{H_2O}/\sigma^{\overline{\nu}_\mu}_{CH} &= 0.987 \pm 0.078(\text{stat.})^{+0.093}_{-0.090}(\text{syst.}), \\
\sigma^{\overline{\nu}_\mu+\nu_\mu}_{H_2O} &= \left[1.155 \pm 0.064(\text{stat.})^{+0.148}_{-0.129}(\text{syst.})\right] \times 10^{-39}\text{cm}^2 \cdot \text{nucleon}^{-1}, \\
\sigma^{\overline{\nu}_\mu+\nu_\mu}_{CH} &= \left[1.159 \pm 0.049(\text{stat.})^{+0.129}_{-0.115}(\text{syst.})\right] \times 10^{-39}\text{cm}^2 \cdot \text{nucleon}^{-1}, \\
\sigma^{\overline{\nu}_\mu+\nu_\mu}_{H_2O}/\sigma^{\overline{\nu}_\mu+\nu_\mu}_{CH} &= 0.996 \pm 0.069(\text{stat.})^{+0.083}_{-0.078}(\text{syst.}),
\end{aligned}$$

where the cross sections are normalized by all nucleons in molecules of H_2O and CH. All of those integrated cross sections are consistent to the prediction from nominal NEUT within a level of 1σ.

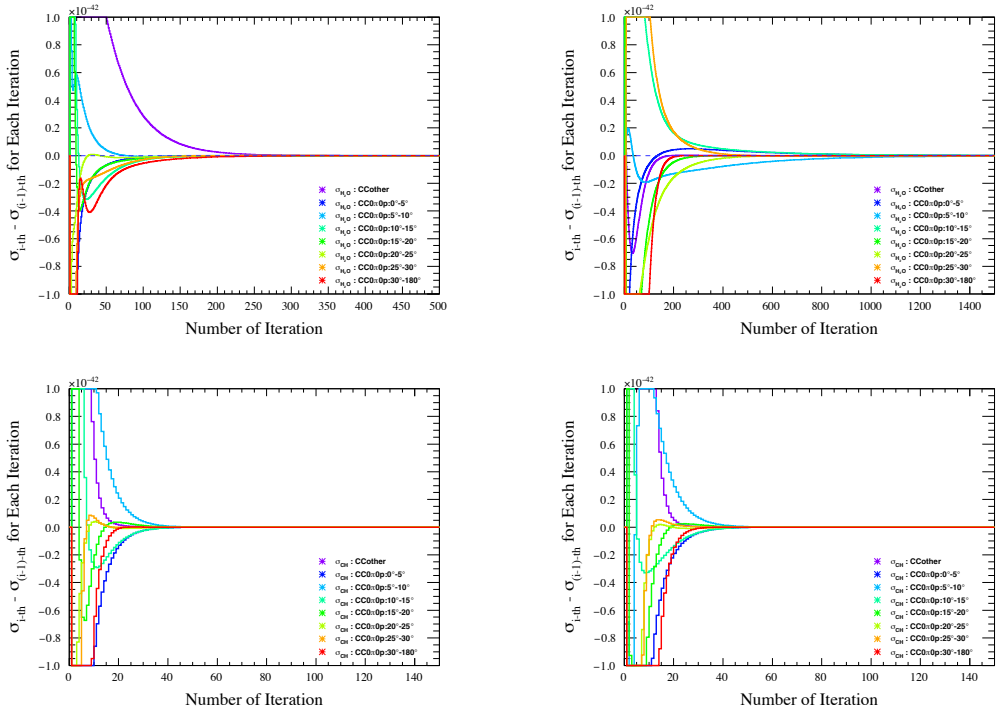

Figure 9.1: Convergence of the extracted cross section, $\overline{\nu}_\mu$ cross section (left) and $\overline{\nu}_\mu + \nu_\mu$ cross section (right). Top line: $\sigma_{\mathrm{H_2O}}$. Bottom line: σ_{CH}. The plots show the first 500 iterations for $\overline{\nu}_\mu$ $\sigma_{\mathrm{H_2O}}$, 150 iterations for $\overline{\nu}_\mu$ σ_{CH}, 1500 iterations for $\overline{\nu}_\mu + \nu_\mu$ $\sigma_{\mathrm{H_2O}}$, 150 iterations for $\overline{\nu}_\mu + \nu_\mu$ σ_{CH}

Tables 9.1 and 9.2 show the measured values of cross sections on each phase space bin with the statistical errors and the total systematics errors for the $\overline{\nu}_\mu$ cross section and the $\overline{\nu}_\mu + \nu_\mu$ cross section, respectively.

Tables 9.3 and 9.4 show comparison of the cross section between the measured and expected values by the nominal NEUT. Figure 9.2 shows the distribution of the measured differential cross sections for CC0π0p with a muon angle less than 30 degrees, with their uncertainties and expectations from NEUT. Basically, the measured cross sections on each phase space bin agree with the NEUT expectation with a level of 1σ, except for $\sigma^{\mathrm{CC0\pi0p:20-25deg}}_{\mathrm{H_2O}\ \overline{\nu}_\mu+\nu_\mu}$, and $(\sigma_{\mathrm{H_2O}}/\sigma_{\mathrm{CH}})^{\mathrm{CC0\pi0p:20-25deg}}_{\overline{\nu}_\mu+\nu_\mu}$. Figure 9.2 shows the same distribution and includes additional two bins for CC other and CC0π0p with a muon angle larger than 30 degrees.

In order to evaluate agreement of the measured differential cross sections with predictions, χ^2 values are calculated based on the total uncertainty including both the statistical error and the systematic error. Table 9.5 shows the calculated χ^2 values for the predictions from the nominal NEUT and GENIE. Assuming the

number of degree of freedom is eight, the calculated χ^2 values suggest that the measured cross sections well agree with those models.

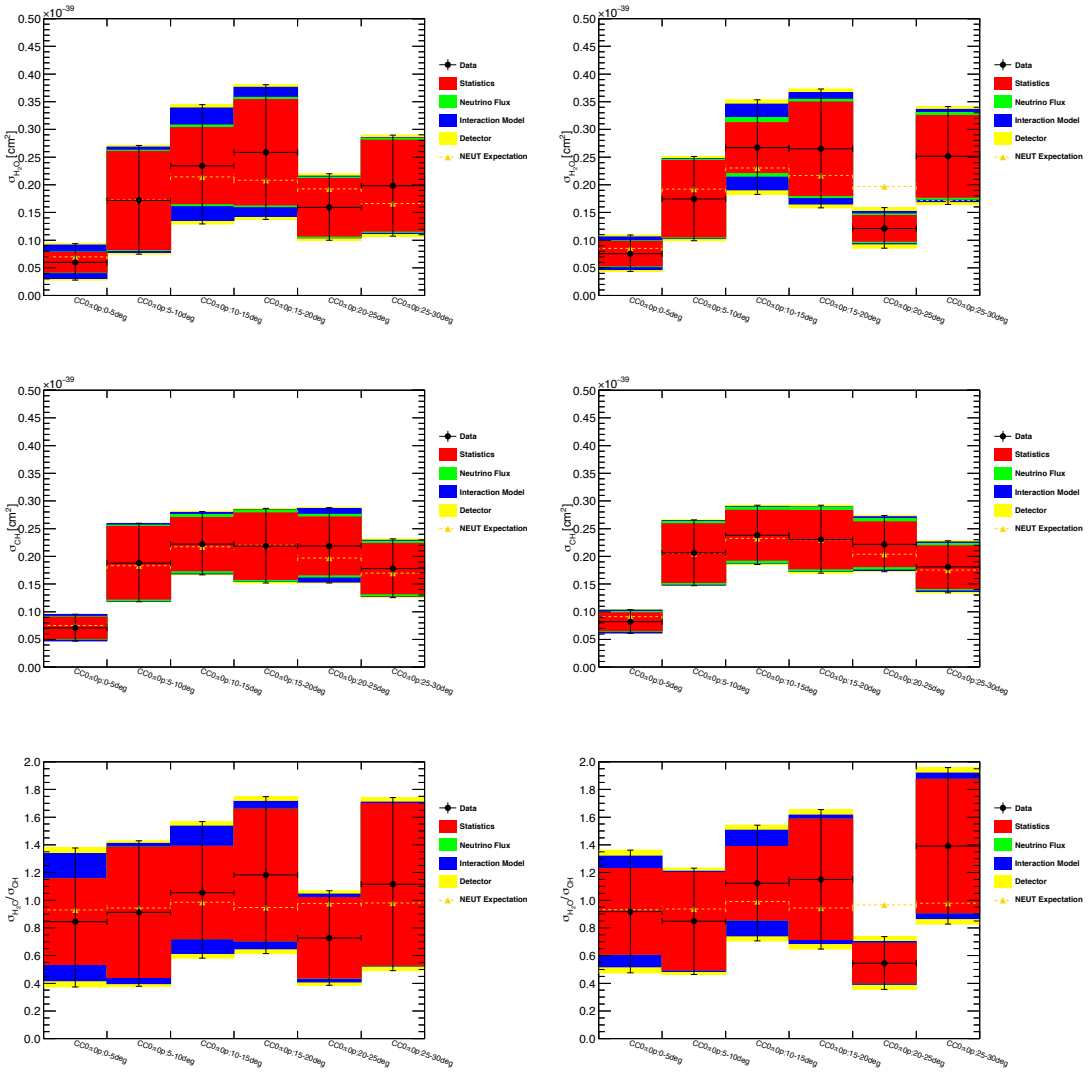

Figure 9.2: Measured values for the differential cross sections $\overline{\nu}_\mu$ cross section (left) and $\overline{\nu}_\mu + \nu_\mu$ cross section (right). Top line: $\sigma_{\mathrm{H_2O}}$. Middle line: σ_{CH}. Bottom line: $\sigma_{\mathrm{H_2O}}/\sigma_{\mathrm{CH}}$ (bottom). Each plot shows the cumulative quadratic sum of the uncertainties from statistics, neutrino flux, neutrino interaction model, and detector response.

Table 9.1: Summary of the $\overline{\nu}_\mu$ cross section measurement. Units for σ_{H_2O} and σ_{CH} are $[\times 10^{-39}\ \mathrm{cm}^2 \cdot \mathrm{nucleon}^{-1}]$.

	True phase space	Cross section	Stat. err.	Syst. err.
σ_{H_2O}	CCother	0.244	±0.120	+0.206/-0.199
	CC0π0p : 0 − 5deg	0.060	±0.018	+0.029/-0.027
	CC0π0p : 5 − 10deg	0.172	±0.089	+0.045/-0.040
	CC0π0p : 10 − 15deg	0.234	±0.069	+0.086/-0.080
	CC0π0p : 15 − 20deg	0.259	±0.095	+0.077/-0.075
	CC0π0p : 20 − 25deg	0.159	±0.052	+0.031/-0.029
	CC0π0p : 25 − 30deg	0.198	±0.082	+0.040/-0.039
	CC0π0p : 30 − 180deg	0.635	±0.145	+0.243/-0.217
	CCTotal	1.961	±0.196	+0.400/-0.368
	CC0π0p : 0 − 30deg	1.082	±0.068	+0.145/-0.128
σ_{CH}	CCother	0.162	±0.057	+0.149/-0.141
	CC0π0p : 0 − 5deg	0.071	±0.019	+0.015/-0.014
	CC0π0p : 5 − 10deg	0.188	±0.065	+0.029/-0.025
	CC0π0p : 10 − 15deg	0.222	±0.048	+0.034/-0.028
	CC0π0p : 15 − 20deg	0.219	±0.060	+0.033/-0.030
	CC0π0p : 20 − 25deg	0.219	±0.052	+0.045/-0.042
	CC0π0p : 25 − 30deg	0.178	±0.046	+0.028/-0.025
	CC0π0p : 30 − 180deg	0.975	±0.285	+0.320/-0.344
	CCTotal	2.233	±0.195	+0.498/-0.446
	CC0π0p : 0 − 30deg	1.096	±0.054	+0.132/-0.117
$\sigma_{H_2O}/\sigma_{CH}$	CCother	1.508	±0.753	+1.803/-1.524
	CC0π0p : 0 − 5deg	0.846	±0.310	+0.431/-0.356
	CC0π0p : 5 − 10deg	0.913	±0.470	+0.213/-0.253
	CC0π0p : 10 − 15deg	1.056	±0.334	+0.389/-0.336
	CC0π0p : 15 − 20deg	1.183	±0.476	+0.306/-0.312
	CC0π0p : 20 − 25deg	0.728	±0.291	+0.176/-0.179
	CC0π0p : 25 − 30deg	1.115	±0.583	+0.227/-0.219
	CC0π0p : 30 − 180deg	0.651	±0.241	+0.291/-0.299
	CCTotal	0.878	±0.111	+0.177/-0.191
	CC0π0p : 0 − 30deg	0.987	±0.078	+0.093/-0.090

Table 9.2: Summary of the $\overline{\nu}_\mu + \nu_\mu$ cross section measurement. Units for σ_{H_2O} and σ_{CH} are $[\times 10^{-39}\ \text{cm}^2 \cdot \text{nucleon}^{-1}]$.

	True phase space	Cross section	Stat. err.	Syst. err.
σ_{H_2O}	CCother	0.923	$\pm$0.126	+0.224/-0.219
	CC0π0p : 0 $-$ 5deg	0.075	$\pm$0.022	+0.026/-0.023
	CC0π0p : 5 $-$ 10deg	0.175	$\pm$0.069	+0.034/-0.032
	CC0π0p : 10 $-$ 15deg	0.267	$\pm$0.045	+0.074/-0.072
	CC0π0p : 15 $-$ 20deg	0.265	$\pm$0.085	+0.067/-0.065
	CC0π0p : 20 $-$ 25deg	0.121	$\pm$0.023	+0.030/-0.027
	CC0π0p : 25 $-$ 30deg	0.252	$\pm$0.074	+0.051/-0.046
	CC0π0p : 30 $-$ 180deg	0.590	$\pm$0.185	+0.235/-0.217
	CCTotal	2.668	$\pm$0.171	+0.353/-0.327
	CC0π0p : 0 $-$ 30deg	1.155	$\pm$0.064	+0.148/-0.129
σ_{CH}	CCother	0.877	$\pm$0.062	+0.364/-0.344
	CC0π0p : 0 $-$ 5deg	0.082	$\pm$0.016	+0.015/-0.014
	CC0π0p : 5 $-$ 10deg	0.206	$\pm$0.053	+0.028/-0.025
	CC0π0p : 10 $-$ 15deg	0.238	$\pm$0.045	+0.030/-0.027
	CC0π0p : 15 $-$ 20deg	0.230	$\pm$0.053	+0.033/-0.030
	CC0π0p : 20 $-$ 25deg	0.222	$\pm$0.040	+0.032/-0.029
	CC0π0p : 25 $-$ 30deg	0.181	$\pm$0.038	+0.028/-0.026
	CC0π0p : 30 $-$ 180deg	0.969	$\pm$0.228	+0.280/-0.309
	CCTotal	3.005	$\pm$0.175	+0.499/-0.444
	CC0π0p : 0 $-$ 30deg	1.159	$\pm$0.049	+0.129/-0.115
$\sigma_{H_2O}/\sigma_{CH}$	CCother	1.052	$\pm$0.169	+0.563/-0.519
	CC0π0p : 0 $-$ 5deg	0.919	$\pm$0.310	+0.318/-0.316
	CC0π0p : 5 $-$ 10deg	0.848	$\pm$0.352	+0.152/-0.156
	CC0π0p : 10 $-$ 15deg	1.123	$\pm$0.265	+0.325/-0.321
	CC0π0p : 15 $-$ 20deg	1.151	$\pm$0.435	+0.256/-0.255
	CC0π0p : 20 $-$ 25deg	0.546	$\pm$0.143	+0.127/-0.124
	CC0π0p : 25 $-$ 30deg	1.391	$\pm$0.482	+0.300/-0.293
	CC0π0p : 30 $-$ 180deg	0.609	$\pm$0.251	+0.297/-0.273
	CCTotal	0.888	$\pm$0.077	+0.148/-0.160
	CC0π0p : 0 $-$ 30deg	0.996	$\pm$0.069	+0.083/-0.078

Table 9.3: Comparison of the $\overline{\nu}_\mu$ cross section between the measured value and those expected by NEUT. Units for σ_{H_2O} and σ_{CH} are $[\times 10^{-39}\ \mathrm{cm}^2 \cdot \mathrm{nucleon}^{-1}]$.

	True phase space	Data	MC	Data/MC [%]
σ_{H_2O}	CCother	0.244	0.601	-59.42
	CC0π0p : $0-5$deg	0.060	0.070	-14.12
	CC0π0p : $5-10$deg	0.172	0.173	-0.49
	CC0π0p : $10-15$deg	0.234	0.214	+9.47
	CC0π0p : $15-20$deg	0.259	0.208	+24.27
	CC0π0p : $20-25$deg	0.159	0.193	-17.37
	CC0π0p : $25-30$deg	0.198	0.166	+19.21
	CC0π0p : $30-180$deg	0.635	0.542	+17.02
	CCTotal	1.961	2.167	-9.51
	CC0π0p : $0-30$deg	1.082	1.024	+5.72
σ_{CH}	CCother	0.162	0.646	-74.95
	CC0π0p : $0-5$deg	0.071	0.075	-5.47
	CC0π0p : $5-10$deg	0.188	0.183	+2.79
	CC0π0p : $10-15$deg	0.222	0.217	+2.19
	CC0π0p : $15-20$deg	0.219	0.220	-0.56
	CC0π0p : $20-25$deg	0.219	0.197	+10.96
	CC0π0p : $25-30$deg	0.178	0.170	+4.79
	CC0π0p : $30-180$deg	0.975	0.544	+79.20
	CCTotal	2.233	2.252	-0.84
	CC0π0p : $0-30$deg	1.096	1.062	+3.23
$\sigma_{H_2O}/\sigma_{CH}$	CCother	1.508	0.931	+62.02
	CC0π0p : $0-5$deg	0.846	0.931	-9.15
	CC0π0p : $5-10$deg	0.913	0.943	-3.19
	CC0π0p : $10-15$deg	1.056	0.986	+7.12
	CC0π0p : $15-20$deg	1.183	0.947	+24.98
	CC0π0p : $20-25$deg	0.728	0.977	-25.53
	CC0π0p : $25-30$deg	1.115	0.980	+13.76
	CC0π0p : $30-180$deg	0.651	0.997	-34.70
	CCTotal	0.878	0.962	-8.75
	CC0π0p : $0-30$deg	0.987	0.964	+2.42

Table 9.4: Comparison of the $\overline{\nu}_\mu + \nu_\mu$ cross section between the measured value and those expected by NEUT. Units for σ_{H_2O} and σ_{CH} are [$\times 10^{-39}$ cm$^2 \cdot$ nucleon^{-1}].

	True phase space	Data	MC	Data/MC [%]
σ_{H_2O}	CCother	0.923	1.190	-22.43
	CC0π0p : $0-5$deg	0.075	0.085	-11.39
	CC0π0p : $5-10$deg	0.175	0.192	-9.20
	CC0π0p : $10-15$deg	0.267	0.231	+15.92
	CC0π0p : $15-20$deg	0.265	0.217	+22.12
	CC0π0p : $20-25$deg	0.121	0.197	-38.59
	CC0π0p : $25-30$deg	0.252	0.172	+46.44
	CC0π0p : $30-180$deg	0.590	0.555	+6.43
	CCTotal	2.668	2.838	-6.00
	CC0π0p : $0-30$deg	1.155	1.094	+5.58
σ_{CH}	CCother	0.877	1.226	-28.46
	CC0π0p : $0-5$deg	0.082	0.091	-10.07
	CC0π0p : $5-10$deg	0.206	0.205	+0.28
	CC0π0p : $10-15$deg	0.238	0.233	+2.30
	CC0π0p : $15-20$deg	0.230	0.230	+0.07
	CC0π0p : $20-25$deg	0.222	0.204	+8.68
	CC0π0p : $25-30$deg	0.181	0.175	+3.03
	CC0π0p : $30-180$deg	0.969	0.557	+74.07
	CCTotal	3.005	2.922	+2.86
	CC0π0p : $0-30$deg	1.159	1.139	+1.75
$\sigma_{H_2O}/\sigma_{CH}$	CCother	1.052	0.970	+8.42
	CC0π0p : $0-5$deg	0.919	0.932	-1.47
	CC0π0p : $5-10$deg	0.848	0.936	-9.45
	CC0π0p : $10-15$deg	1.123	0.991	+13.31
	CC0π0p : $15-20$deg	1.151	0.943	+22.03
	CC0π0p : $20-25$deg	0.546	0.966	-43.50
	CC0π0p : $25-30$deg	1.391	0.979	+42.13
	CC0π0p : $30-180$deg	0.609	0.996	-38.86
	CCTotal	0.888	0.971	-8.61
	CC0π0p : $0-30$deg	0.996	0.960	+3.76

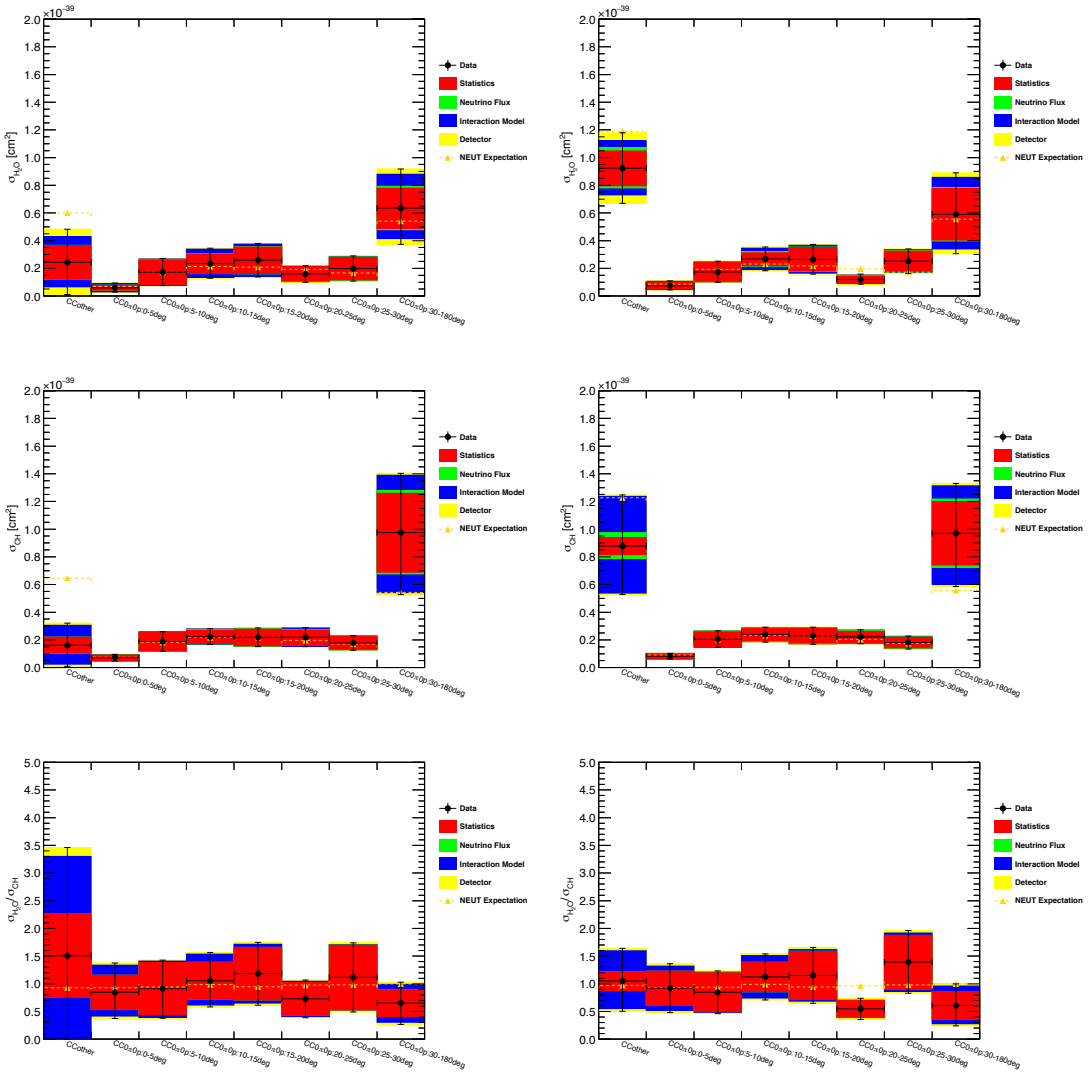

Figure 9.3: Measured values for the differential cross sections, with including the CC other and CC0π0p:30-180deg, $\overline{\nu}_\mu$ cross section (left) and $\overline{\nu}_\mu + \nu_\mu$ cross section (right). Top line: $\sigma_{\mathrm{H_2O}}$. Middle line: σ_{CH}. Bottom line: $\sigma_{\mathrm{H_2O}}/\sigma_{\mathrm{CH}}$ (bottom). Each plot shows the cumulative quadratic sum of the uncertainties from statistics, neutrino flux, neutrino interaction model, and detector response.

Table 9.5: Absolute χ^2 values for the $\overline{\nu}_\mu$ and $\overline{\nu}_\mu + \nu_\mu$ cross sections, concerning the total uncertainty.

	$\overline{\nu}_\mu$ cross section			$\overline{\nu}_\mu + \nu_\mu$ cross section		
	σ_{H_2O}	σ_{CH}	$\sigma_{H_2O}/\sigma_{CH}$	σ_{H_2O}	σ_{CH}	$\sigma_{H_2O}/\sigma_{CH}$
NEUT	3.19	11.34	1.71	7.06	2.63	6.87
GENIE	4.25	14.26	1.83	7.09	3.38	7.55

9.2 Discussion

This thesis reports CC0π0p cross sections using the sub-GeV anti-neutrino beam with water and hydrocarbon targets, and the cross section ratio between those two targets. They are the first measurements of direct relations of anti-neutrino-nucleus interactions between water and hydrocarbon with the sub-GeV neutrino energy range. These results play important roles as new input to constrain the neutrino-nucleus interaction models.

In the T2K oscillation analysis, the neutrino beam flux and neutrino interactions at Super-Kamiokande is constrained by fitting the event rates at the ND280 detectors. Due to the limited knowledge of neutrino-nucleus interactions, the extrapolation between the different nuclear targets, water and hydrocarbon, largely depends on the nuclear model. The results in this thesis verify the modeling of nuclear dependency between water and hydrocarbon for the anti-neutrino interactions for the first time.

In order to improve understanding of neutrino-nucleus interaction models, measurements which are less model dependent have been desired. For this reason, CC0π0p cross sections instead of CCQE are calculated. The results are provided with both integrated and differential cross sections with respect to muon angle, in order to have more information. In addition, cross sections including both of the $\overline{\nu}_\mu$ and ν_μ interactions are calculated with smaller uncertainties than those of the $\overline{\nu}_\mu$ cross sections. In future developments of neutrino interaction models, which have to be designed to be consistent with the existing experimental data, all of the results can constrain the models by being fitted with the neutrino beam flux and covariance matrix provided in this thesis.

There are a few analyses ongoing in the ND280 detectors such as FGD1 and P0D, which will report $\overline{\nu}_\mu$ cross sections on H_2O and CH for CC0π. It should be noted that those results are calculated with slightly different signal definition and with different phase space from the analysis in this thesis. Energy spectra of the neutrino beam are also slightly different. However, the selected samples are dominated by CCQE interactions, muon's kinematics is basically restricted to

be forward scattering angle region, and neutrino beam spectra have the sub-GeV mean energy and the peak around at 0.6-0.7 GeV. Thus, it is reasonable that the measured flux-integrated CC0π0p cross sections with muon angle less than 30 degrees on H_2O and CH in the analysis of this thesis are comparable with those ND280 results. By briefly comparing the analysis in this thesis with the preliminary results from those analysis, they all agree with each other within the uncertainties.

Similar analyses have been done with a different neutrino energy range. For instance, MINERνA reported a double-differential $\overline{\nu}_\mu$ cross section with respect to muon transverse and longitudinal momentum for topology-based CCQE-like signal at $E_\nu \sim 3.5$ GeV[118]. Combining the MINERνA results with the results in this thesis, which is measured with a sub-GeV neutrino energy range, neutrino interaction models can be compared with experimental data for a wide neutrino energy range.

The WAGASCI project is still ongoing, and data taking with the full configuration is planned in 2019. Combining the other sub-detectors, side-MRDs and Baby-MIND, more precise measurements with larger acceptance are expected. The side-MRDs allow detection of large-angle scattering muons. The magnetic field of Baby-MIND allows charge identification to discriminate the wrong sign neutrino contamination, which is one of the dominant background events in the case of $\overline{\nu}_\mu$ cross section analysis.

In the future, this analysis is expected to be improved by reduction of uncertainties. Preliminary results from a new analysis technique using the NA61/SHINE data taken with the graphite target with the same length as the T2K beam target suggest reduction of the neutrino beam flux uncertainty by around 50%[119]. In addition, improvements of neutrino interaction models allow reduction of systematic uncertainty, especially for parameters where 100% uncertainty is assigned at present, such as nucleon FSI and 2p-2h models. Statistical uncertainty will be also reduced. T2K requests more neutrino beam corresponding to about four times statistics to that used in this analysis by 2021. Statistical uncertainty is expected to be reduced about 50% in the case of anti-neutrino beam only for all of the additional statistics.

What is desired is an accuracy comparable with the difference in the CCQE cross section between water and hydrocarbon targets, which is expected to be few percent at most. Detector systematics would be dominant in the future analysis with the suppressed uncertainties. Further tuning of the detector simulation by using the whole data taken so far will improve understanding of our detector. By a better precision of measurements in the future, we would achieve various measurements following the results in this thesis, such as:

- measurements of two-dimensional differential cross sections with muon's an-

gle and momentum with a wider phase space,

- measurements of other interaction channels such as CC1π, and
- comparison with different analyses using the same neutrino beam but different energy spectrum.

This thesis, which presents the first results of the cross section measurement using the WAGASCI detector, will serve as a useful reference for the future analysis.

Appendix A

Electronics and data acquisition system

The electronics of the WAGASCI detector, including the whole DAQ system, are being developed at Laboratoire Leprince-Ringuet (LLR) of l'Ecole polytechnique[120].

The J-PARC neutrino beam has 2.48-second-period spill structure, and each spill contains 8 bunches with 581ns gaps. To readout 1280 channels of photodetector (MPPC) to the neutrino beam and to control them, a new electronics with a Silicon PM Integrated Read-Out Chip (SPIROC) has been developed. SPIROC is a 36-channel auto-triggered front-end ASIC, and is produced by OMEGA/IN2P3[121]. The adopted version in WAGASCI is SPIROC2D, which is capable of adjustment of MPPC gains, charge measurement with a wide dynamic range from one to 2,000 photoelectrons, and time measurement with about 100 ps step.

The whole electronics system of WAGASCI is shown in Fig. A.1. The front-end board for WAGASCI, named Active Sensor Unit (ASU), has been developed with the SPIROC2D, and designed to directly attached to a 32-channel arrayed MPPC on the surface of the WAGASCI detector, as shown in Fig. A.2. The ASU boards are connected in a daisy chain, and the data readout and the chip configuration are serially performed. The configuration of the SPIROC2D and the wrapping of the data are performed by the detector interface board (DIF), and one of back-end boards, GDCC, performs the data transfer between a data acquisition server and front-end boards. The whole system is synchronized to 50 MHz clock generated on the other back-end board, CCC.

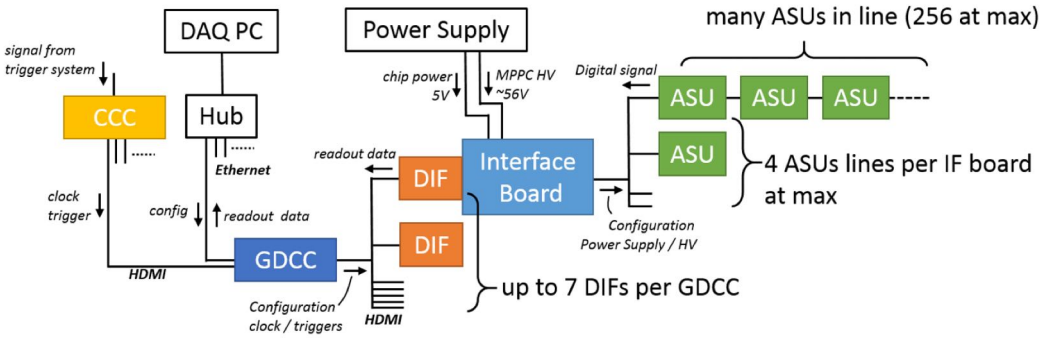

Figure A.1: Front-end and back-end electronics boards.

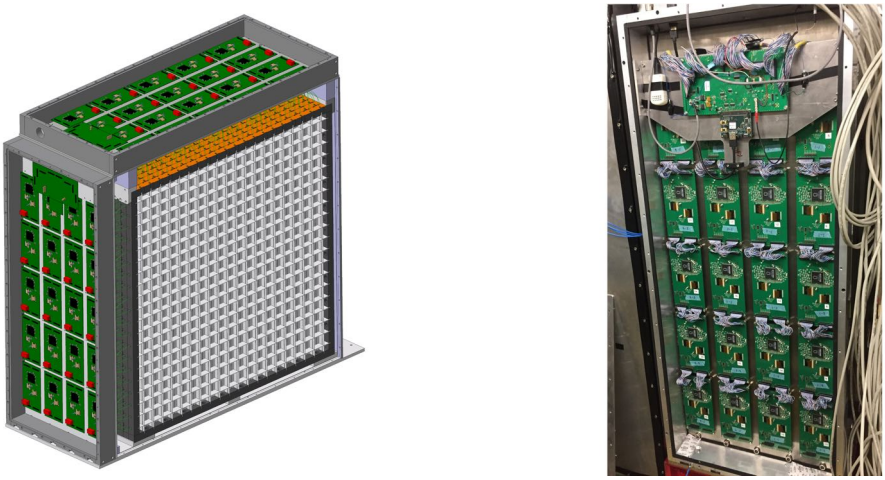

Figure A.2: ASUs attached to the WAGASCI module.

A.1 Electronics boards

The WAGASCI detector adopts the SPIROC2D chip as its front-end electronics. The SPIROC2D chip is a newly developed, and the WAGASCI detector is its first application. For the readout of 1280 MPPCs on the WAGASCI detector, 40 of the SPIROC2D chips are used. The boards in the WAGASCI electronics are described as follows:

ASU (Active Sensor Unit). The ASU board, as shown in Fig A.3, has a SPIROC2D chip, and is connected to one 32-channel arrayed MPPC.

It also has connections to an Interface board and another ASU via two 50-pin connectors for each.

Interface. The interface board, as shown in Fig A.4, has connections to four ASUs and a DIF, and transfers signals between the DIF and the four ASUs in parallel. It also has a NIM connection for MPPC bias voltage supply, which is sent to MPPCs through ASUs. Power for the chips such as FPGA on DIF and SPIROC on ASU is also provided through this board.

DIF (Detector InterFace). The DIF board, as shown in Fig A.5, has an FPGA, which controls the SPIROC chips. It sends DAQ signals and configuration data to the chips, and receives response signals and output data from the chips through the Interface board. The firmware is controlled by the GDCC board through an HDMI connection.

GDCC (Giga Data Concentrator Card). The GDCC board, as shown in Fig A.6, has HDMI connections of seven DIFs. It has an FPGA, which only works as signal transfer between an Ethernet to a DAQ PC and HDMIs to DIFs. The GDCC board can also function as CCC mode if the corresponding firmware is loaded on the FPGA.

CCC (Clock & Control Card). The CCC board provides all the GDCCs connected to it with clock signals and fast controls.

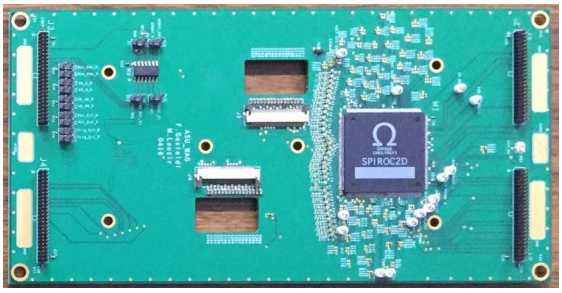

Figure A.3: Picture of the front side of the ASU board with SPIROC2D.

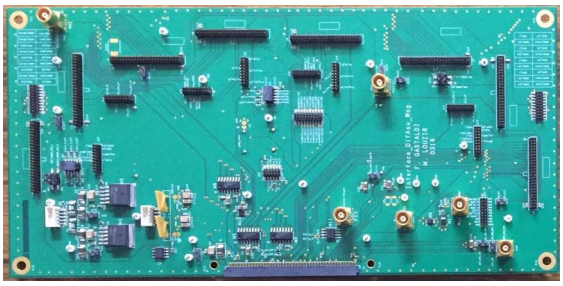

Figure A.4: Picture of the front side of the Interface board.

The numbers of boards for the WAGASCI detector are planed as shown in Table A.1.

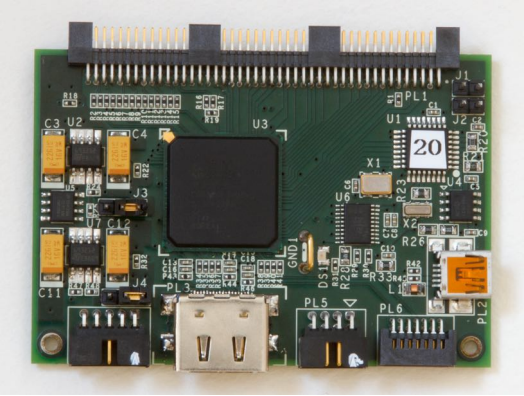

Figure A.5: Picture of the front side of the DIF board.

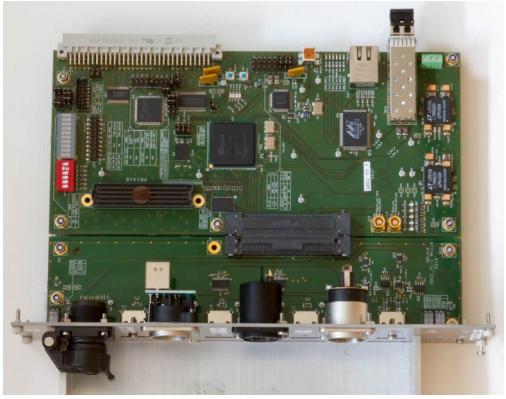

Figure A.6: Picture of the front side of the GDCC board.

Table A.1: The numbers of the WAGASCI electronics boards.

Boards	The WAGASCI detector
ASU	40
Interface	2
DIF	2
GDCC	1
CCC	1

A.2 Triggering system

The CCC board also receives trigger signals from the neutrino beamline. Firmware for a Spartan 6 FPGA has been developed to open an acquisition gate by receiving two different timing signals. The first beam timing signal (pre-beam trigger) arrives exactly 100 ms before the second one (beam trigger), and then about 30 μs later then the beam trigger, neutrino beam arrives at the near detectors. The spill number information for tagging the event is also delivered from the beamline as 16-bit ECL signal, and received by a Xilinx Zynq-7000 development board. Firmware for the Zynq-7000 has been developed to receive the 16-bit ECL signal and to send it to GDCC board on Ethernet frame.

Appendix B

Calculation of the number of target nucleons in WAGASCI

The number of target nucleons are calculated based on the measurements during the detector construction. In the fiducial volume of WAGASCI, there are materials of water, scintillators, wavelength shifting (WLS) fiber, optical cement, reflective coating on the surface of the scintillator, and silicon glue to fix the scintillators. Among them, the amount of the silicon glue is controlled during the construction and corresponds to 0.05% of the fiducial volume by weight, hence it is ignored in this analysis. The reflective coating has two types: co-extruded reflective coating and additional coating on the WLS fiber.

B.1 Scintillators

The total masses of the scintillators, including reflector, WLS fiber, optical cement and black painting, are measured before detector assembly, and the distribution of the measured weight of all scintillators are shown in Fig. B.1. The mean of the measured weight are 79.25 g (75.74 g) for the parallel (grid) scintillator bar. The scintillator mass in the fiducial volume region of WAGASCI, $M_{\mathrm{WM}}^{\mathrm{sci}}$, is calculated as follows:

$$\begin{aligned} M_{\mathrm{WM}}^{\mathrm{sci(plane)}} &= 79.25\mathrm{g} \times 168 \times \frac{70.0\mathrm{cm}}{102.0\mathrm{cm}} \\ &= 9.14 \text{ kg} \qquad \text{(B.1)} \\ M_{\mathrm{WM}}^{\mathrm{sci(grid)}} &= 75.74\mathrm{g} \times 196 \times \frac{70.0\mathrm{cm}}{120.0\mathrm{cm}} \\ &= 10.19 \text{ kg} \qquad \text{(B.2)} \\ M_{\mathrm{WM}}^{\mathrm{sci}} &= M_{\mathrm{WM}}^{\mathrm{sci(para)}} + M_{\mathrm{WM}}^{\mathrm{sci(grid)}} \\ &= 19.33 \text{ kg} \qquad \text{(B.3)} \end{aligned}$$

where 168 (196) is the number of plane (grid) scintillators in the fiducial volume, 70 cm is a size of the fiducial volume and 102.0 cm is the length of the scintillator bars. Mass of each component is also measured before the assembly.

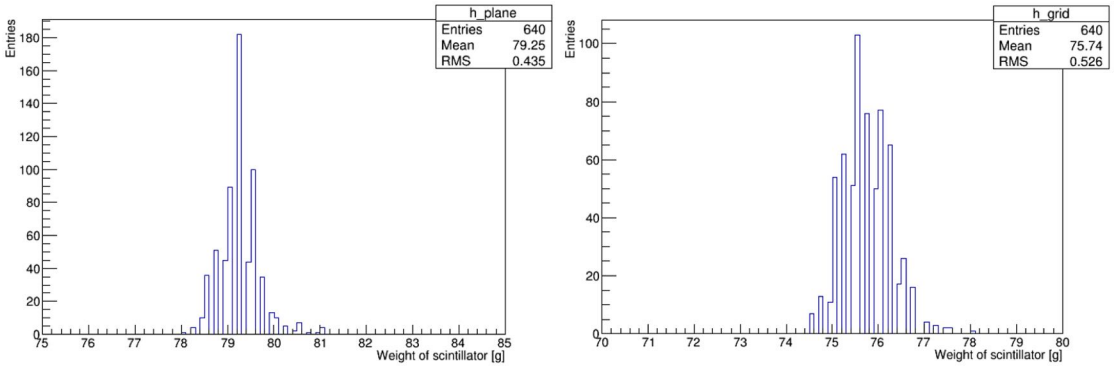

Figure B.1: Measured weight of the plane (left) and grid (right) scintillators.

The main component of the scintillator is polystyrene (C_8H_8), infused with 1 % of the fluors PPO ($C_{15}H_{11}NO$) and 0.03 % of POPOP ($C_{24}H_{16}N_2O_2$). On the surface of the scintillator is the co-extruded reflective coating, which is composed of TiO_2 infused in polystyrene (C_8H_8), and acrylic silicon black painting ($SiO_2C_5O_2H_8$) for reducing the optical cross talk. The WLS fiber is mainly composed of polystyrene (C_8H_8) and the other contribution is ignored. According to the measured mass and the elemental composition, the mass fraction of each element of the whole scintillators in the fiducial volume is estimated as shown in Table. B.1. The mass fraction of CH is 95.3% (95.0%) for the parallel (grid) scintillators.

From the masses in the fiducial volume, the number of target nucleon is calculated as follow:

$$\begin{aligned} T_{\mathrm{WM}}^{\mathrm{CH}} &= (M_{\mathrm{WM}}^{\mathrm{sci(para)}} \times R^{\mathrm{CH(para)}} + M_{\mathrm{WM}}^{\mathrm{sci(grid)}} \times R^{\mathrm{CH(grid)}}) \\ &\times \frac{n_{\mathrm{p}}^{\mathrm{C}} + n_{\mathrm{n}}^{\mathrm{C}} + n_{\mathrm{p}}^{\mathrm{H}} + n_{\mathrm{n}}^{\mathrm{H}}}{(A_r^{\mathrm{C}} + A_r^{\mathrm{H}})/N_A} \\ &= (9.14 \times 10^3 \times 0.953 + 10.19 \times 10^3 \times 0.950) \\ &\times \frac{6 + 6.0107 + 1 + 0.0001}{(12.011 + 1.008)/(6.02214 \times 10^{23})} \\ &= 1.107 \times 10^{28} \end{aligned} \tag{B.4}$$

where R is the elemental mass ratio, n_{p} and n_{n} are the number of protons and neutrons per atom, A_r is atomic weight and N_A is the Avogadro number.

Table B.1: Component of the scintillator bar

	Mass fraction	Element H	C	N	O	Ti	Si
Plane scintillator							
Scintillator	81.6%	7.71%	92.12%	0.08%	0.09%	0	0
Co-extruded reflective coating	13.1%	6.58%	78.42%	0	6.01%	8.99%	0
WLS fiber	1.04%	7.74%	92.26%	0	0	0	0
Optical cement	1.17%	4.8%	57.1%	0	38.1%	0	0
Additionally painted reflector	2.23%	1.0%	23.8%	27.7%	47.5%	0	0
Black paint	0.81%	5.0%	37.5%	0	40.0%	0	17.5%
Total		7.4%	87.9%	0.7%	2.7%	1.2%	0.1%
Grid scintillator							
Scintillator	81.0%	7.71%	92.12%	0.08%	0.09%	0	0
Co-extruded reflective coating	13.1%	6.58%	78.42%	0	6.01%	8.99%	0
WLS fiber	1.09%	7.74%	92.26%	0	0	0	0
Optical cement	1.48%	4.8%	57.1%	0	38.1%	0	0
Additionally painted reflector	2.46%	1.0%	23.8%	27.7%	47.5%	0	0
Black paint	0.81%	5.0%	37.5%	0	40.0%	0	17.5%
Total		7.3%	87.7%	0.7%	2.9%	1.2%	0.1%

B.2 Water

Total volume of the fiducial volume is calculated with the measured scintillator positions:

$$V_{\rm all}^{\rm fiducial} = 20.52{\rm cm} \times 70{\rm cm} \times 70{\rm cm}, \tag{B.5}$$

where 20.52 cm is measured distance between the most upstream and downstream scintillator layers in the fiducial volume. The density of the scintillator in WAGASCI, $d_{\rm WM}^{\rm sci} = 1.075{\rm g/cm}^3$, is measured before detector assembly. The total volume of scintillators in the fiducial volume is calculated as:

$$V_{\rm sci}^{\rm fiducial} = M_{\rm WM}^{\rm sci}/d_{\rm WM}^{\rm sci} \tag{B.6}$$

Mass of water in the fiducial volume is calculated by those volumes and the density of water, $d_{\rm WM}^{\rm water} = 0.9982{\rm g/cm}^3$, which is measured during the water filling work:

$$\begin{aligned} M_{\rm WM}^{\rm water} &= d_{\rm WM}^{\rm water} \times (V_{\rm all}^{\rm fiducial} - V_{\rm sci}^{\rm fiducial}) \\ &= 82.40 \text{ kg} \end{aligned} \tag{B.7}$$

The water is composed of 99.75% pure water and 0.25% preservative, which is made of 60 % H_2O and 40 % $C_8H_{14}N_4O_7$. Based on them, the mass fraction of each element in the fiducial volume is calculated as shown in Table B.2. The mass fraction of H_2O is 99.95%.

Table B.2: Elemental composition of the water in the fiducial region of WAGASCI.

Element	O	H	C	N
Mass fraction	88.76%	11.19%	0.03%	0.02%

From the masses in the fiducial volume, the number of target nucleon is calculated as follow:

$$\begin{aligned} T_{\mathrm{WM}}^{\mathrm{H_2O}} &= M_{\mathrm{WM}}^{\mathrm{water}} \times R^{\mathrm{H_2O}} \times \frac{n_{\mathrm{p}}^{\mathrm{O}} + n_{\mathrm{n}}^{\mathrm{O}} + 2 \times (n_{\mathrm{p}}^{\mathrm{H}} + n_{\mathrm{n}}^{\mathrm{H}})}{(A_r^{\mathrm{O}} + 2 \times A_r^{\mathrm{H}})/N_A} \\ &= 82.40 \times 10^3 \times 0.9995 \times \frac{8 + 8.0045 + 2 \times (1 + 0.0001)}{(15.999 + 2 \times 1.008)/(6.02214 \times 10^{23})} \\ &= 4.957 \times 10^{28} \end{aligned} \tag{B.8}$$

Appendix C

Supplementary of the uncertainty estimation

C.1 Statistics uncertainty

In order to check if the effect of anti-correlation between phase space bins is canceled between bins, the statistical errors are calculated with the coarse binning. In this trial estimation, the number of selected events are replaced by those generated by the nominal simulation, and only $\overline{\nu}_\mu$ cross sections are calculated. Binning is changed only for the CC0π0p with a muon angle less than 30 degrees, so that the events are separated every 10 degrees instead of 5 degrees. The calculated errors are summarized in Table. C.1. The statistical errors for each bin become smaller compared with those with the finer binning, while the statistical error on the integrated cross section is consistent with each other. Correlation matrices are shown in Fig. C.1.

Table C.1: Trial estimation of statistical uncertainties on each bin with coarse binning for forward muon angle.

Cross section	True phase space	σ_{H_2O}	σ_{CH}	$\sigma_{H_2O}/\sigma_{CH}$
$\overline{\nu}_\mu$	CCother	$\pm$26.8%	$\pm$14.7%	$\pm$31.0%
	CC0π0p : 0-10 deg	$\pm$15.3%	$\pm$7.7%	$\pm$17.6%
	CC0π0p : 10-20 deg	$\pm$10.7%	$\pm$6.3%	$\pm$13.0%
	CC0π0p : 20-30 deg	$\pm$14.4%	$\pm$9.1%	$\pm$17.5%
	CC0π0p : 30-180 deg	$\pm$29.1%	$\pm$25.3%	$\pm$36.0%
	CC Total	$\pm$9.5%	$\pm$6.8%	$\pm$12.1%
	CC0π0p : 0-30 deg	$\pm$6.5%	$\pm$4.0%	$\pm$8.1%

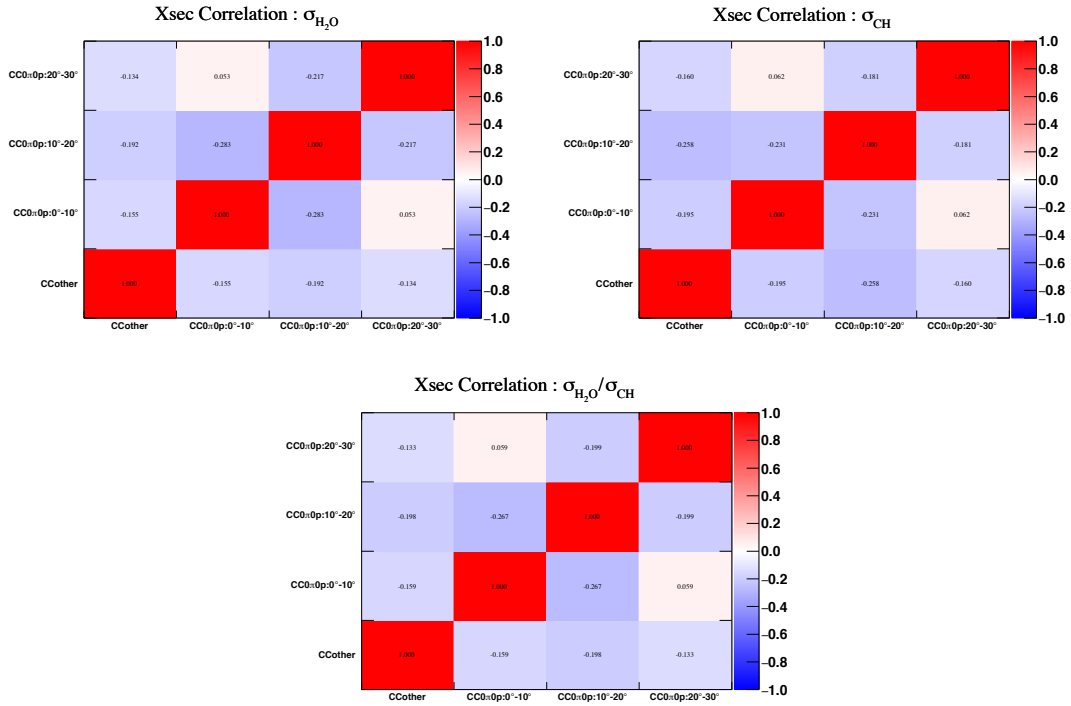

Figure C.1: Correlation matrix from statistical uncertainties calculated with coarse binning for $\sigma_{\mathrm{H_2O}}$ (top left), σ_{CH} (top right), and $\sigma_{\mathrm{H_2O}}/\sigma_{\mathrm{CH}}$ (bottom)

C.2 Nuetino beam flux

The uncertainty on the calculated cross section is estimated based on the uncertainty on the neutrino beam flux prediction, as described in Sec. 7.3.1. The uncertainty on the beam prediction is estimated as a function of neutrino energy for each of ν_μ and $\overline{\nu}_\mu$. In this analysis, twenty bins along neutrino energy are applied as shown in Table C.2. In total 40 bins are considered including ν_μ and $\overline{\nu}_\mu$, and correlations between any pair of bins are taken into account. Hence the fractional covariance matrix for the neutrino beam flux prediction with 40×40 dimension is estimated as shown in Fig. C.2.

Table C.2: Energy binning for flux uncertainty evaluation

Energy range	Number of bins	Energy width per bin
0.0-3.0 GeV	15	0.2 GeV
3.0-4.0 GeV	1	1.0 GeV
4.0-10.0 GeV	3	2.0 GeV
10.0-30.0 GeV	1	20.0 GeV

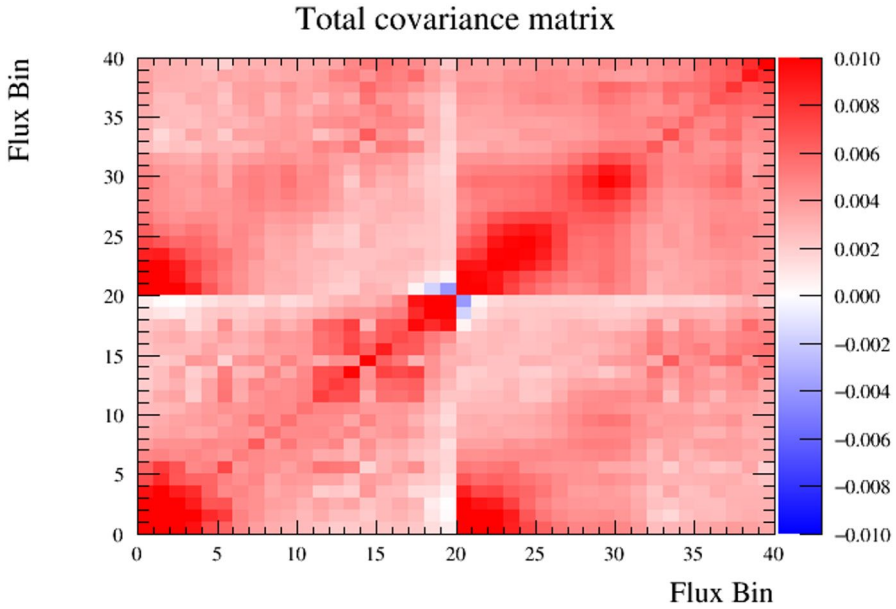

Figure C.2: Covariance matrix on the anti-neutrino beam flux uncertainty on WAGASCI. The bins 0-19 correspond to ν_μ fraction, and bins 20-39 correspond to $\overline{\nu}_\mu$ fraction.

Two categories of the uncertainty sources are hadron interaction and beam monitor. Fractional error of each uncertainty is shown in Fig. C.3 and Fig. C.4. The uncertainties from hadron interaction is categorized as, meson multiplicity, nucleon interactions, production cross section (interaction length), and pion re-scattering. The uncertainties from beam monitor is categorized as, proton beam profile, off-axis angle, absolute value of horn current, horn magnetic field asymmetry, mis-alignment of horn and target, material modeling for strip line and cooling water, and number of protons.

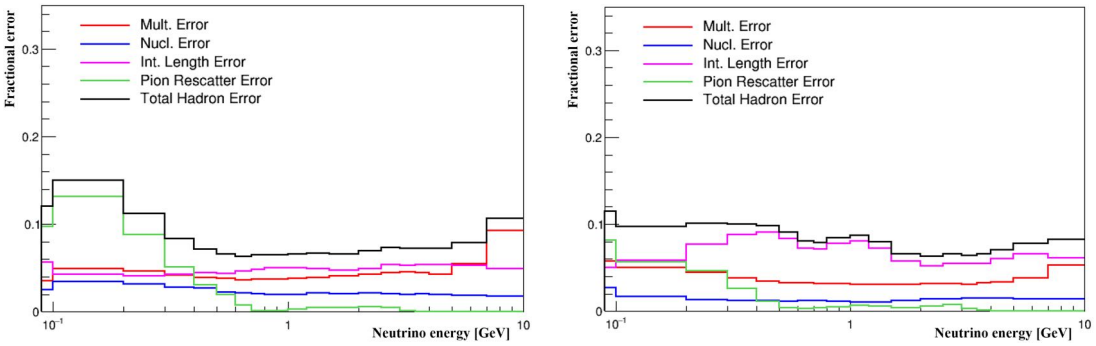

Figure C.3: The hadron interaction model uncertainties evaluated on the flux prediction for ν_μ (left) and $\overline{\nu}_\mu$ (right).

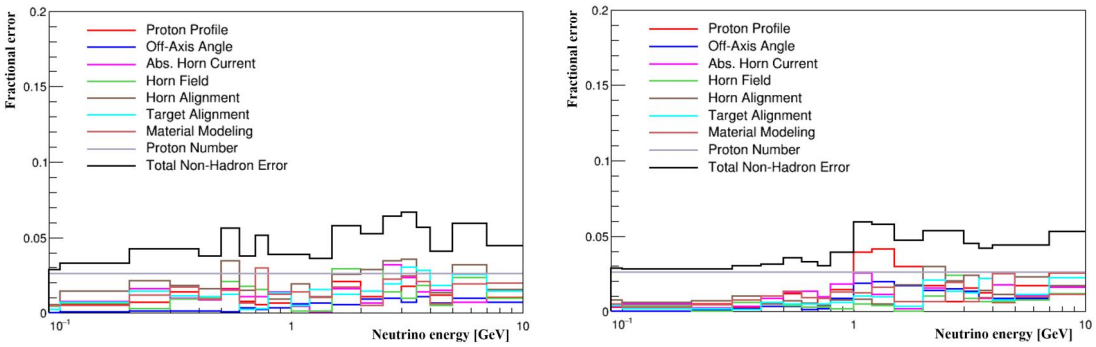

Figure C.4: The non-hadron interaction model uncertainties evaluated on the flux prediction for ν_μ (left) and $\overline{\nu}_\mu$ (right).

C.3 Neutirno interaction model

In order to estimated the uncertainty due to the neutrino interaction model, parameters in the neutrino interaction generator are varied for covering understanding of the parameter. The $\overline{\nu}_\mu$ and ν_μ interactions are independently varied only for the parameters related to CCQE or 2p-2h interactions, since those parameters would largely affect the selection efficiency and . For the other parameters, $\overline{\nu}_\mu$ and ν_μ are varied in full correlation. Table C.3 shows the variation of the calculated cross section for CC0π0p with a muon angle less than 30 degrees. Among the uncertainties on the calculated cross section from the parameters related to CCQE and 2p-2h, the dominant contribution comes from 2p-2h normalization, and M_A^{QE} follows.

Table C.3: Uncertainties on CC0π0p with a muon angle less than 30 degrees from CCQE and 2p2h interactions (%)

Parameter	σ_{H_2O}	σ_{CH}	$\sigma_{H_2O}/\sigma_{CH}$
The $\overline{\nu}_\mu$ cross section			
M_A^{QE} : $\bar{\nu}_\mu$	+1.60/-1.45	+1.29/-1.08	+0.30/-0.37
M_A^{QE} : ν_μ	+0.69/-0.44	+0.98/-0.77	+0.33/-0.28
2p2h norm C : $\bar{\nu}_\mu$	+0.43/-0.25	+1.74/-2.32	+2.81/-1.96
2p2h norm C : ν_μ	+0.27/-0.26	+1.10/-1.14	+1.43/-1.34
2p2h norm O : $\bar{\nu}_\mu$	+2.21/-2.20	<0.01	+2.21/-2.20
2p2h norm O : ν_μ	+1.58/-1.55	<0.01	+1.61/-1.58
2p2h shape C : $\bar{\nu}_\mu$	+0.04/-0.06	+0.26/-0.16	+0.20/-0.32
2p2h shape C : ν_μ	+0.17/-0.12	+0.50/-0.71	+0.89/-0.62
2p2h shape O : $\bar{\nu}_\mu$	+0.38/-0.28	<0.01	+0.39/-0.28
2p2h shape O : ν_μ	+0.55/-0.65	<0.01	+0.55/-0.64
Total	+3.34/-3.19	+2.68/-2.99	+4.35/-3.76
The $\overline{\nu}_\mu + \nu_\mu$ cross section			
M_A^{QE} : $\bar{\nu}_\mu$	+1.45/-1.32	+1.25/-1.04	+0.20/-0.28
M_A^{QE} : ν_μ	+0.31/-0.20	+0.46/-0.38	+0.17/-0.14
2p2h norm C : $\bar{\nu}_\mu$	+0.43/-0.32	+1.91/-2.33	+2.82/-2.18
2p2h norm C : ν_μ	+0.02/-0.02	+0.05/-0.08	+0.10/-0.07
2p2h norm O : $\bar{\nu}_\mu$	+2.01/-2.00	<0.01	+2.02/-2.00
2p2h norm O : ν_μ	+0.42/-0.41	<0.01	+0.45/-0.43
2p2h shape C : $\bar{\nu}_\mu$	+0.04/-0.06	+0.23/-0.17	+0.21/-0.29
2p2h shape C : ν_μ	+0.05/-0.05	+0.26/-0.21	+0.26/-0.31
2p2h shape O : $\bar{\nu}_\mu$	+0.41/-0.34	<0.01	+0.41/-0.34
2p2h shape O : ν_μ	+0.19/-0.22	<0.01	+0.20/-0.21
Total	+2.61/-2.49	+2.35/-2.59	+3.55/-3.07

C.4 Detector response

This section describes details of estimation of the uncertainties from the detector response in WAGASCI, since WAGASCI is newly constructed detector and this is the first estimation of the detector performance. In order to estimate the uncertainty with considering the correlation between event categories, variation of the number of selected events on each categories is estimated by altering each parameter of the detector response, and the covariance matrix is calculated. Uncertainty on the cross section is estimated by fluctuating the number of selected events and evaluating variation of the cross section calculated with the fluctuated number of events.

C.4.1 MPPC noise

MPPC noises accidentally make hits, and it is possible to cause mis-reconstruction of vertex or two-dimensional tracks. Accordingly the number of selected events are affected by MPPC noise rate. During the detector operation, the random noise rate is measured as 0.025 hits per bunch. In order to conservatively evaluate the effect of the random noise, random noises are generated in the simulation and the difference in the number of selected events between the cases of 0 and 1 hit/bunch is assigned as 1σ uncertainties. The covariance of the detector systematics is calculated as follows:

$$\mathrm{cov_{ij}} = \Delta \mathrm{N_i} \times \Delta \mathrm{N_j}, \tag{C.1}$$

where ΔN_i is the variation of the number of selected events in the i-th bin of the reconstructed track information calculated by the simulation between the noise rates of 0 and 1 hit/bunch. The variation of the number of selected events are summarized in Table C.4.

C.4.2 Scintillator crosstalk

Crosstalk occurs between the grid scintillators in x view and y view through the cross point of the slits, and would make additional hits and cause mis-reconstruction of vertex and tracks. The crosstalk ratio between scintillators are measured by using external muons induced by neutrino beam, as shown in Fig. C.5. A linear relation in the light yield between neighbor scintillators is observed and the crosstalk ratio is taken as the slope, 0.64%. The crosstalk is implemented the simulation. When a grid scintillator has a hit, crosstalk hits are generated on the grid scintillator in the opposite view within 5 cm distance from the hit point, and fluctuated based on the Poisson distribution. In order to conservatively estimate the uncertainty, the variation of the number of selected events between the cases of

Table C.4: Variation of the number of selected events by changing the rate of accidental noise between 0 and 1 hit/cycle for the WAGASCI by MC simulation.

Reconstructed tracks	Variation of MC (%) $\Delta N_i (= N_{i\ 1hit} - N_{i\ 0hit})$
Multi-Track	-1.223
One-Track:0-5 deg	+0.001
One-Track:5-10 deg	-0.240
One-Track:10-15 deg	-1.135
One-Track:15-20 deg	-0.406
One-Track:20-25 deg	-0.487
One-Track:25-30 deg	-0.645
One-Track:30-180 deg	-0.120
Total	-0.694

no crosstalk and 1% crosstalk is taken as 1σ uncertainties, as shown in Table C.5. The covariance matrix is calculated as follows:

$$cov_{ij} = \Delta N_i \times \Delta N_j \tag{C.2}$$

where ΔN_i is the variation of the number of selected events in the i-th reconstructed track angle bin calculated by Monte Carlo between with crosstalk rates of 0 and 1%. The variation of the number of selected events are summarized in Table C.5.

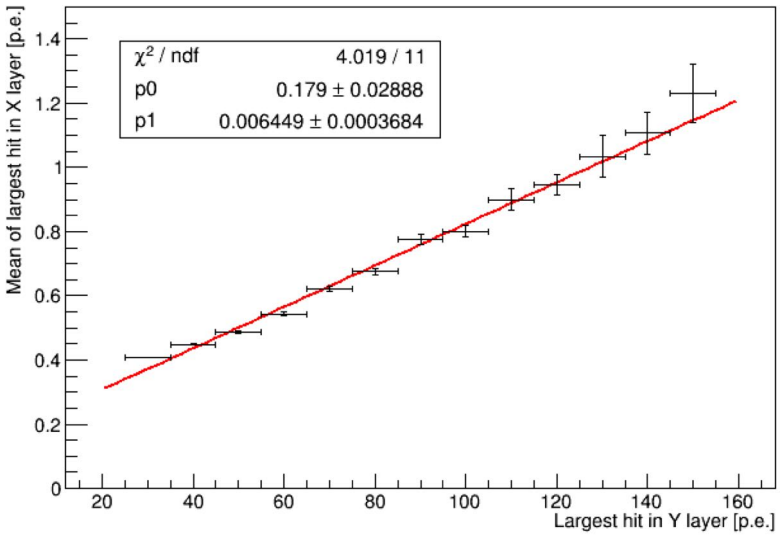

Figure C.5: Relation of the light yield between grid-x and grid-y scintillator.

Table C.5: Variation of the number of selected events by changing the crosstalk rate between 0 and 1% for the WAGASCI by MC simulation.

Reconstructed tracks	Variation of MC (%) $\Delta N_i (= N_{i\ 1\%crosstalk} - N_{i\ nocrosstalk})$
Multi-Track	+0.145
One-Track:0-5 deg	+0.956
One-Track:5-10 deg	-0.326
One-Track:10-15 deg	-0.117
One-Track:15-20 deg	+0.065
One-Track:20-25 deg	-0.062
One-Track:25-30 deg	-0.245
One-Track:30-180 deg	-0.230
Total	< 0.001

C.4.3 Two-dimensional track reconstruction

The two-dimensional track reconstruction efficiency is estimated by using external muon tracks. The difference in the reconstruction efficiency in each track angle between data and simulation is taken as 1σ uncertainty, since it directly affects the number of tracks. In order to estimated the difference in the entries of the multi-track bin, the number of reconstructed tracks and the averaged tracking efficiency are used as follows:

$$x_0 = \frac{\sum_{N_{Data}=2,3,...} \left[N_{Data} \times X^N_{Data} \right]}{N^{Multi\text{-}Track}_{sel\ Data}} - \frac{\sum_{N_{MC}=2,3,...} \left[N_{MC} \times X^N_{MC} \right]}{N^{Multi\text{-}Track}_{sel\ MC}}, \tag{C.3}$$

where x_0 is the Data-Monte Carlo of the tracking efficiency in the multi-track angle bin, N is the number of reconstructed tracks, $N^{Multi\text{-}Track}_{sel}$ is the number of selected events in the multi-track bin, and X is the averaged tracking efficiency. Based on them, the covariance of the detector systematic is calculated as follows:

$$cov_{ij} = x_i \times x_j \tag{C.4}$$

where x_i is the Data-Monte Carlo of the tracking efficiency in the reconstructed angle bin i (i = 1, 2, ..., 7), in addition to x_0 for the multi-track bin. Table C.6 shows the difference in the tracking efficiency, x_i.

C.4.4 Event pileup

Since the neutrino event rate in WAGASCI is small, the correction from the pileup events is not applied. However, to conservatively estimate the uncertainty from the

Table C.6: Difference in the tracking efficiency.

Reconstructed tracks	Difference in the efficiency (x_i [%])
Multi-Track	-4.07
One-Track:0-5 deg	0.79
One-Track:5-10 deg	0.09
One-Track:10-15 deg	-0.22
One-Track:15-20 deg	0.22
One-Track:20-25 deg	-0.44
One-Track:25-30 deg	-0.55
One-Track:30-180 deg	-1.87

event pileup, difference in the number of selected events in the double bunched data and the normal bunch structure is calculated, and the difference, 0.5%, is taken as 1σ systematic uncertainty for all reconstructed angle bins with full correlation.

C.4.5 Beam-related background

In order to estimate the uncertainty on the beam-related background events, three sources are considered: neutrino beam flux uncertainty, neutrino interaction uncertainty, and normalization of the simulated events. The uncertainties from neutrino beam flux and neutrino interactions affect the number of beam-related background events. As comparable values to the current systematics errors for neutrino beam flux and interactions, 10% uncertainty is assigned for each. In order to estimate the discrepancy between the simulated background events and the real data, the number of rejected event by the upstream veto cut is compared between the simulation and data. The difference, 20.6%, is taken as the systematic error. Total uncertainty on the beam-related background is calculated as a quadratic sum of the three components: $\sqrt{(0.10)^2 + (0.10)^2 + (0.206)^2} = 0.250$, and this uncertainty is assigned for all event categories with full correlation. The uncertainty on the cross section is estimated by fluctuating the expected number of the external background events based of the 1σ errors.

C.4.6 Non beam-related background

In order to estimate the accidental background event, that is non beam-related background events, the event selection is applied to the data taken without beam. However, no events are selected by checking data corresponding to 6.5×10^6 bunches. By assuming the Poisson distributions with 90% probability, the expected number of events is 0.1 and this is negligible.

C.4.7 Event selection

In order to estimate the uncertainty from each event selection, variations of the number of selected events are checked for both the simulation and data by altering each selection criteria as shown in Table. 7.9, and the difference in the variation of the number of selected events is taken as 1σ uncertainty. The covariance matrix of the detector systematics is calculated as follows:

$$\mathrm{cov}_{ij} = \sum_{k} \mathrm{difference}_{i}^{k} \times \mathrm{difference}_{j}^{k}, \tag{C.5}$$

where $\mathrm{difference}_{i}^{k}$ is the difference of the variation of the selected events in the i-th reconstructed angle bin between the data and Monte Carlo with the changed k-th tolerance (in the case of three-dimensional track reconstruction, < 1 planes and < 3 planes).

Beam timing cut is not applied to the simulation, and the variation of the number of selected events are estimated only by data. Veto cut and fiducial volume cut are only altered toward reducing the number of selected events, since it would suffer from the external background in the case of altering those criteria to increase the number of selected events. Statistics are limited in those cases, hence the comparison between data and simulation is applied only to the total number of selected events, without using the number of entries in each bin. The covariance matrix is calculated by assuming the full correlation for the whole events.

Table C.7: Variation of the number of selected events in tentative hit threshold, 3.5 p.e. (Nominal: 2.5 p.e.) [%]

	MC	Data - MC
Multi-Track	-3.67	+1.82
One-Track:0-5 deg	-2.14	+1.10
One-Track:5-10 deg	-2.45	-2.32
One-Track:10-15 deg	-3.95	+2.17
One-Track:15-20 deg	-0.64	-1.94
One-Track:20-25 deg	-1.42	+0.23
One-Track:25-30 deg	-2.93	+2.30
One-Track:30-180 deg	-1.27	+0.48
Total	-2.53	+0.54

Table C.8: Variation of the number of selected events from nominal by changing the criteria of the position for the track matching. (Nominal: < 150 mm) [%]

Reconstructed tracks	MC		(Data - MC)	
	< 140 mm	< 160 mm	< 140 mm	< 160 mm
Multi-Track	-0.48	+0.20	+0.27	+0.72
One-Track:0-5 deg	-0.32	+0.28	-0.72	+0.66
One-Track:5-10 deg	-0.13	+0.09	-0.82	-0.03
One-Track:10-15 deg	-0.11	+0.09	+0.01	+0.27
One-Track:15-20 deg	-0.31	+0.18	-0.04	-0.06
One-Track:20-25 deg	-0.33	+0.17	-0.09	-0.09
One-Track:25-30 deg	-0.50	+0.24	-0.76	+1.02
One-Track:30-180 deg	-0.51	+0.69	-2.64	-0.63
Total	-0.34	+0.21	-0.34	+0.25

Table C.9: Variation of the number of selected events from nominal by changing the criteria of the angle for the track matching. (Nominal: < 35 deg) [%]

Reconstructed tracks	MC		(Data - MC)	
	< 30 deg	< 40 deg	< 30 deg	< 40 deg
Multi-Track	-1.06	+0.80	-0.27	+0.53
One-Track:0-5 deg	-0.19	+0.40	-1.90	-0.40
One-Track:5-10 deg	-0.10	+0.16	-0.38	+0.32
One-Track:10-15 deg	-0.28	+0.19	-1.14	+0.16
One-Track:15-20 deg	-0.49	+0.40	-0.54	-0.05
One-Track:20-25 deg	-0.85	+0.73	+0.26	+0.52
One-Track:25-30 deg	-0.95	+0.63	-0.05	< 0.01
One-Track:30-180 deg	-2.42	+1.93	-3.09	-1.73
Total	-0.77	+0.62	-0.63	+0.07

Table C.10: Variation of the number of selected events from nominal by changing the criteria of the Z position for the three-dimensional track reconstruction. (Nominal: < 2 planes) [%]

Reconstructed tracks	MC		(Data - MC)	
	< 1 planes	< 3 planes	< 1 planes	< 3 planes
Multi-Track	-2.21	+0.07	-2.44	+0.46
One-Track:0-5 deg	-7.64	+3.31	+1.61	-0.31
One-Track:5-10 deg	-4.64	+2.16	-0.36	+0.84
One-Track:10-15 deg	-3.90	+1.41	+0.71	-1.06
One-Track:15-20 deg	-3.16	+2.01	+1.14	-1.01
One-Track:20-25 deg	-3.05	+1.21	+0.56	-0.80
One-Track:25-30 deg	-3.33	+0.80	+0.82	+0.46
One-Track:30-180 deg	-2.57	+1.24	+1.78	-0.24
Total	-3.39	+1.25	+0.04	-0.16

Table C.11: Variation of the number of selected events from nominal by changing the criteria of the Z position for the vertex reconstruction. (Nominal: < 3 planes) [%]

Reconstructed tracks	MC		(Data - MC)	
	< 2 planes	< 4 planes	< 2 planes	< 4 planes
Multi-Track	-5.56	+2.14	-1.76	+1.58
One-Track:0-5 deg	+1.59	-0.40	+0.46	-0.70
One-Track:5-10 deg	+2.35	-0.62	+0.51	+0.14
One-Track:10-15 deg	+1.41	-0.82	+0.72	+0.11
One-Track:15-20 deg	+2.64	-0.98	+0.45	-0.05
One-Track:20-25 deg	+1.78	-0.86	+0.92	+0.03
One-Track:25-30 deg	+2.18	-0.89	-0.92	-0.36
One-Track:30-180 deg	+2.23	-0.83	-1.25	-1.35
Total	+0.10	-0.06	+0.19	+0.07

Table C.12: Variation of the number of selected events from nominal by changing the criteria of the XY position for the vertex reconstruction.
(Nominal: < 150 mm) [%]

Reconstructed tracks	MC		(Data - MC)	
	< 100 mm	< 200 mm	< 100 mm	< 200 mm
Multi-Track	-5.10	+2.92	-2.48	+2.92
One-Track:0-5 deg	+1.29	-1.23	+0.64	-1.90
One-Track:5-10 deg	+1.62	-1.25	-0.14	-0.65
One-Track:10-15 deg	+2.11	-1.18	-0.03	-0.24
One-Track:15-20 deg	+1.96	-0.72	+0.79	-1.68
One-Track:20-25 deg	+1.80	-0.89	+0.28	+0.06
One-Track:25-30 deg	+1.33	-1.25	-0.86	-0.01
One-Track:30-180 deg	+2.01	-1.05	+1.93	+0.27
Total	+0.03	-0.04	+0.02	-0.02

Table C.13: Variation of the number of selected events with and without the beam timing cut. (Nominal: with beam timing cut) [%]

Selection criteria	Data
With beam timing cut (nominal)	0.0
Without beam timing cut	+0.06

Table C.14: Variation of the number of selected events from nominal by changing the criteria of the vertex z for the front veto cut. [%]

Selection criteria	Data	MC	(Data - MC)
< 3 planes (nominal)	0.0	0.0	0.0
< 4 planes	-26.45	-25.84	-0.61
< 5 planes	-52.88	-51.83	-1.05

Table C.15: Variation of the number of selected events in tentative fiducial volume. [%]

Selection criteria	Data	MC	(Data - MC)
$< \pm 35$ cm (nominal)	0.0	0.0	0.0
$< \pm 25$ cm	-45.06	-45.34	+0.28

Table C.16: Variation of the number of selected events from nominal by changing the criteria of the acceptance cut for x axis. [%]

Reconstructed tracks	MC		(Data - MC)	
	+5 cm	-5 cm	+5 cm	-5 cm
Multi-Track	+0.14	-0.89	+0.43	-0.79
One-Track:0-5 deg	< 0.01	< 0.01	< 0.01	< 0.01
One-Track:5-10 deg	+0.85	-0.65	-0.30	+0.08
One-Track:10-15 deg	+1.75	-1.51	-0.84	+0.57
One-Track:15-20 deg	+1.48	-1.80	-0.44	+0.81
One-Track:20-25 deg	+1.17	-0.52	-0.44	-0.31
One-Track:25-30 deg	+0.18	-0.61	-0.10	+0.05
One-Track:30-180 deg	+6.09	-5.63	+0.13	+0.12
Total	+1.20	-1.30	-0.15	+0.01

Table C.17: Variation of the number of selected events from nominal by changing the criteria of the acceptance cut for y axis. [%]

Reconstructed tracks	MC		(Data - MC)	
	+5 cm	-5 cm	+5 cm	-5 cm
Multi-Track	+0.70	-1.04	+0.30	-0.18
One-Track:0-5 deg	< 0.01	< 0.01	< 0.01	< 0.01
One-Track:5-10 deg	+1.04	-0.43	-0.04	-0.04
One-Track:10-15 deg	+1.49	-1.94	-0.78	-0.54
One-Track:15-20 deg	+1.41	-1.15	+0.65	-0.28
One-Track:20-25 deg	+1.11	-1.20	-0.25	+0.37
One-Track:25-30 deg	+1.44	-0.95	-0.38	-0.31
One-Track:30-180 deg	+2.84	-1.52	-0.84	-0.49
Total	+1.19	-1.11	-0.06	-0.19

Table C.18: Variation of the number of selected events from nominal by changing the criteria of the acceptance cut for z axis. [%]

Reconstructed tracks	MC		(Data - MC)	
	+5 cm	-5 cm	+5 cm	-5 cm
Multi-Track	-4.02	+4.84	+0.57	+0.20
One-Track:0-5 deg	< 0.01	< 0.01	< 0.01	< 0.01
One-Track:5-10 deg	-0.13	+0.22	+0.13	-0.22
One-Track:10-15 deg	-0.79	+1.09	-0.98	+0.32
One-Track:15-20 deg	-2.44	+2.04	+0.38	-0.66
One-Track:20-25 deg	-4.11	+3.21	-0.45	+0.90
One-Track:25-30 deg	-6.10	+6.26	+0.44	+0.66
One-Track:30-180 deg	-15.24	+16.17	+0.02	+1.94
Total	-3.67	+3.83	+0.11	+0.14

Appendix D

Covariance matrix

The calculated cross sections have a correlation between the separated categories. The covariance matrices based on the estimated uncertainties for statistics, neutrino beam flux, neutrino interaction model, and detector response are shown in Fig. D.1, D.2, D.3, and D.4, respectively. The covariance and correlation matrices for the total uncertainty are shown in Fig. D.6.

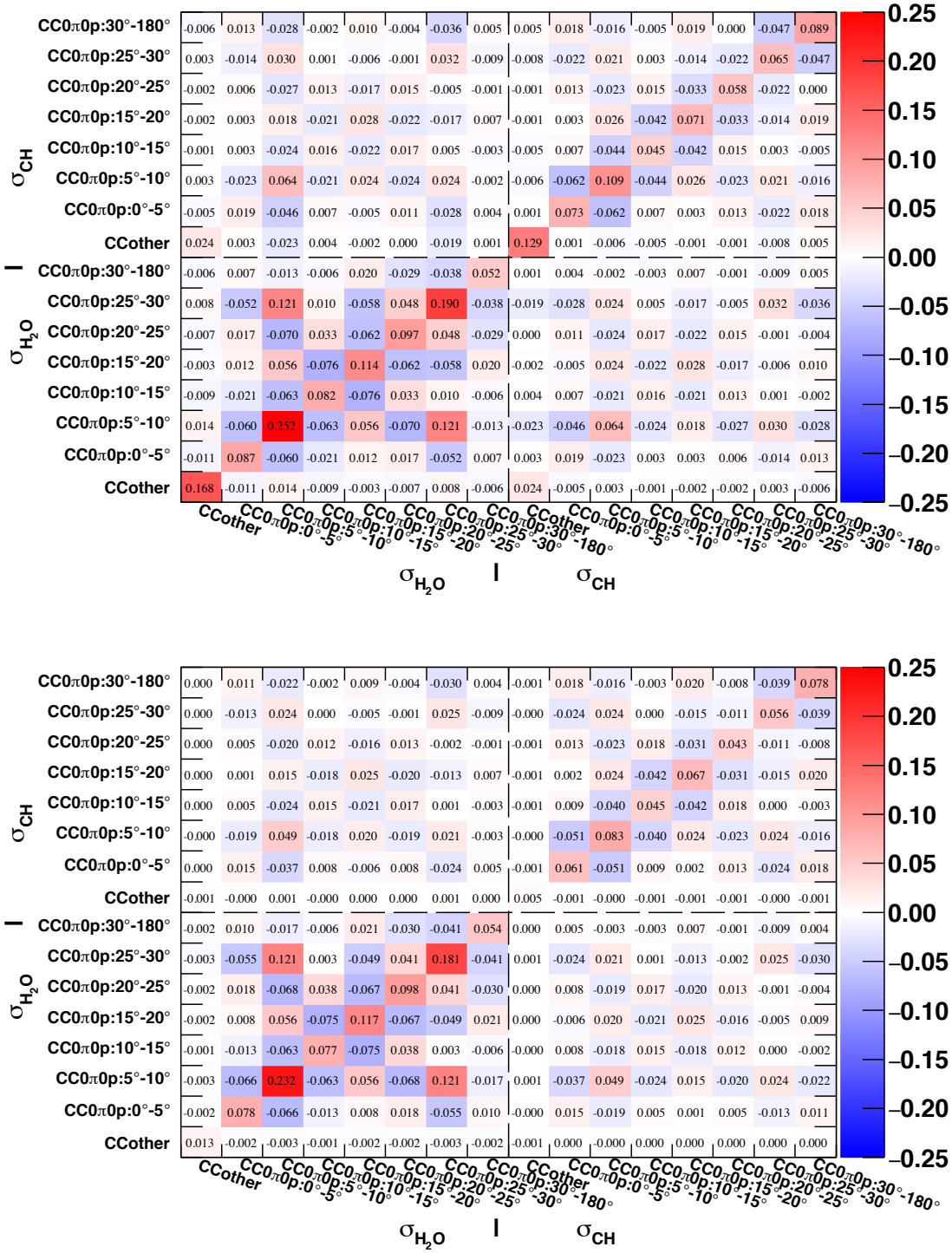

Figure D.1: Covariance matrices from statistical uncertainties for $\overline{\nu}_\mu$ cross section (top) and $\overline{\nu}_\mu + \nu_\mu$ cross section (bottom), concerning correlation between $\sigma_{\mathrm{H_2O}}$ and σ_{CH}.

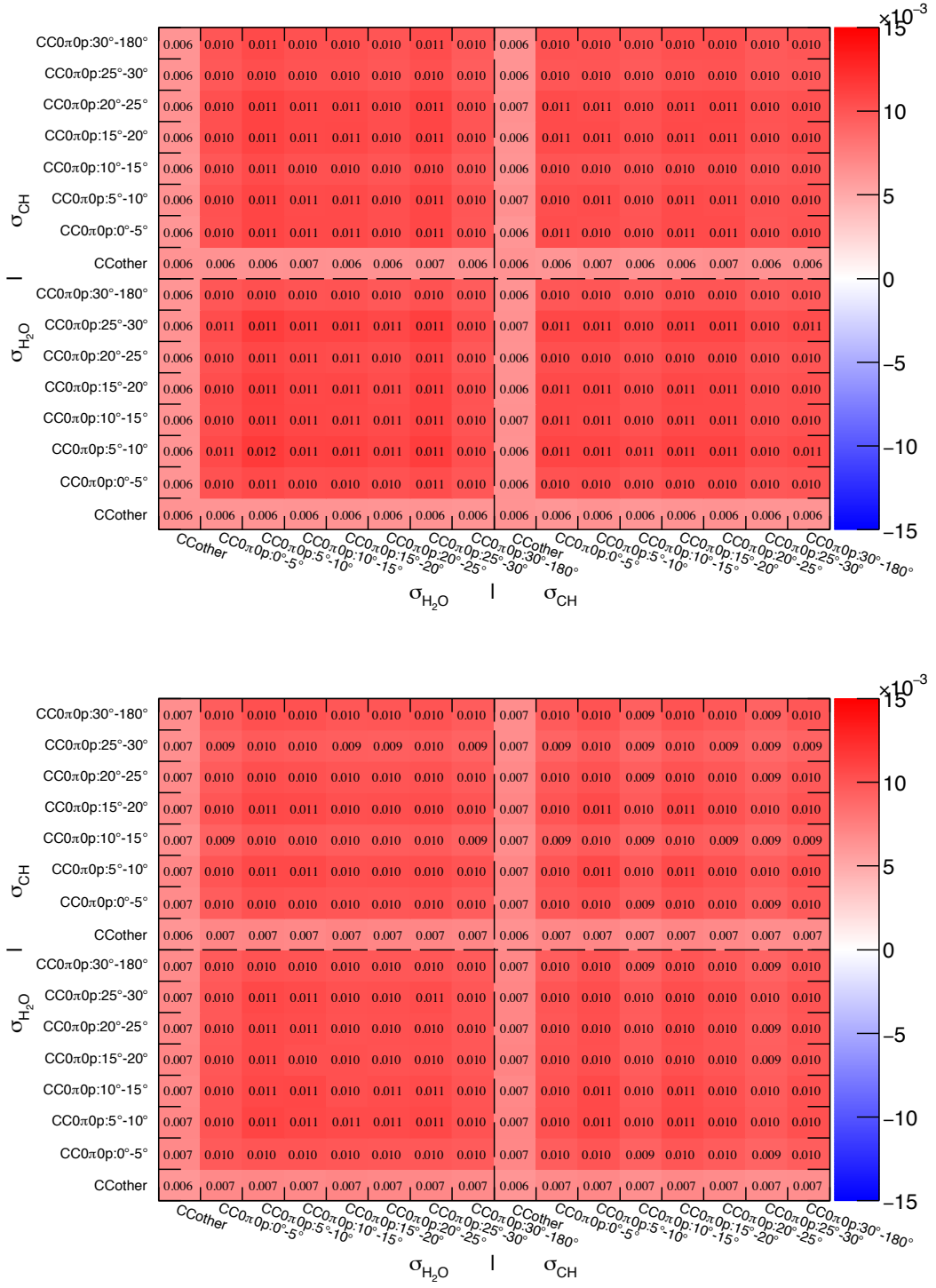

Figure D.2: Covariance matrix due to neutrino flux uncertainty for $\overline{\nu}_\mu$ (left) and $\overline{\nu}_\mu + \nu_\mu$ (right) cross sections, concerning correlation between $\sigma_{\mathrm{H_2O}}$ and σ_{CH}.

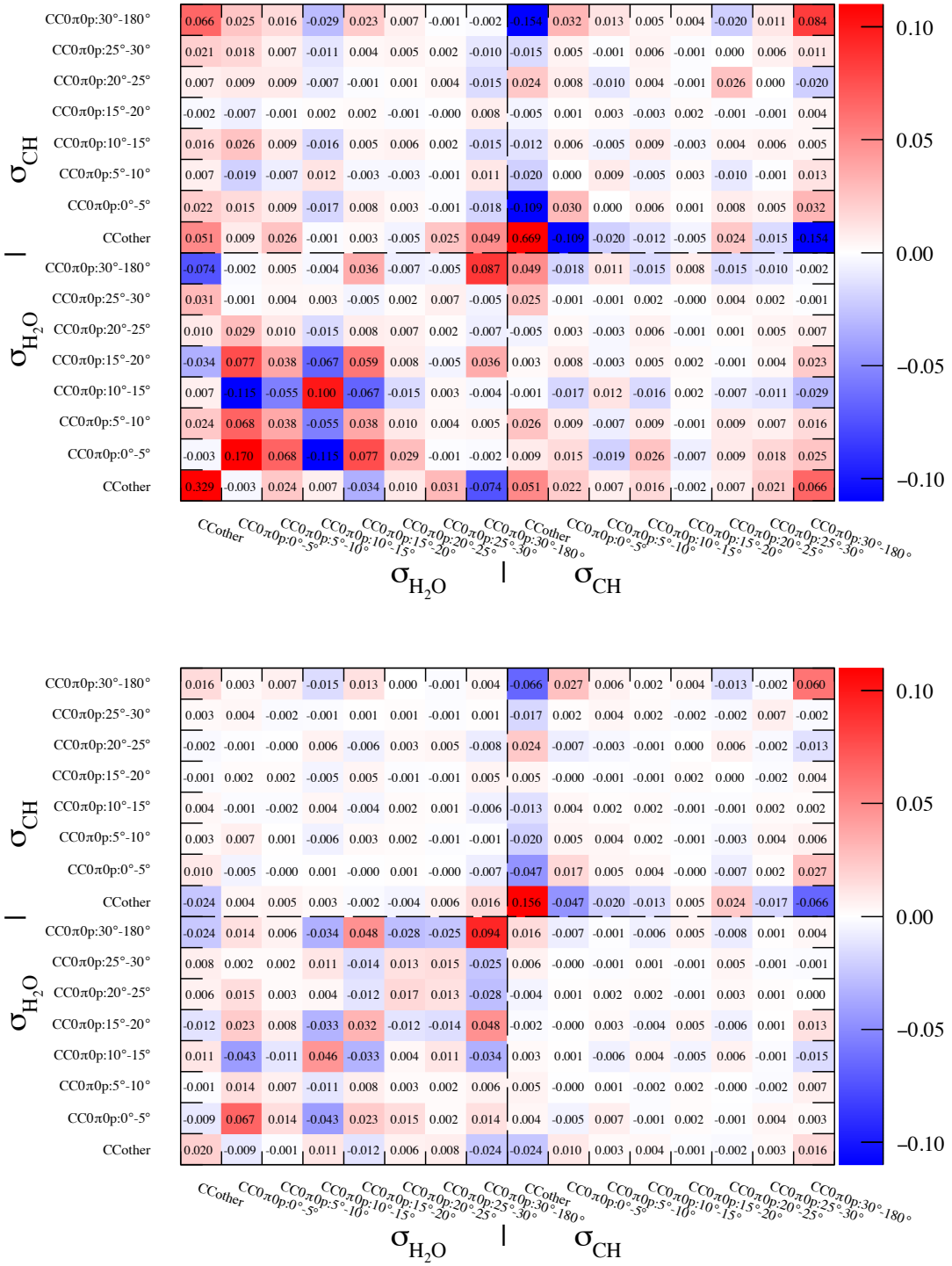

Figure D.3: Covariance matrices for uncertainties due to neutrino interaction model for $\overline{\nu}_\mu$ (left) and $\overline{\nu}_\mu+\nu_\mu$ (right) cross sections, concerning correlation between $\sigma_{\mathrm{H_2O}}$ and σ_{CH}.

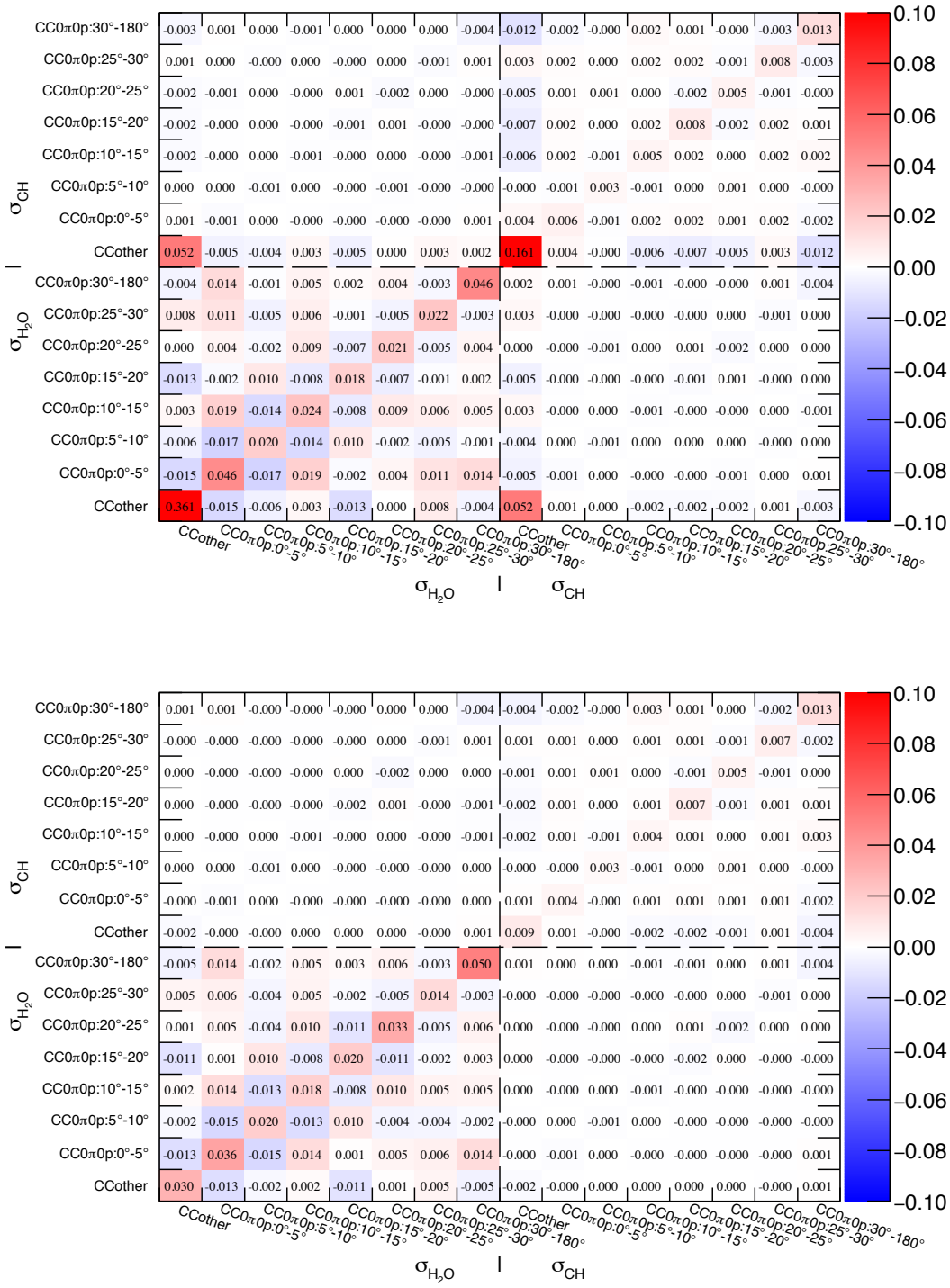

Figure D.4: Covariance matrices from the detector systematics for $\overline{\nu}_\mu$ cross section (top) and $\overline{\nu}_\mu + \nu_\mu$ cross section (bottom), concerning correlation between $\sigma_{\mathrm{H_2O}}$ and σ_{CH}.

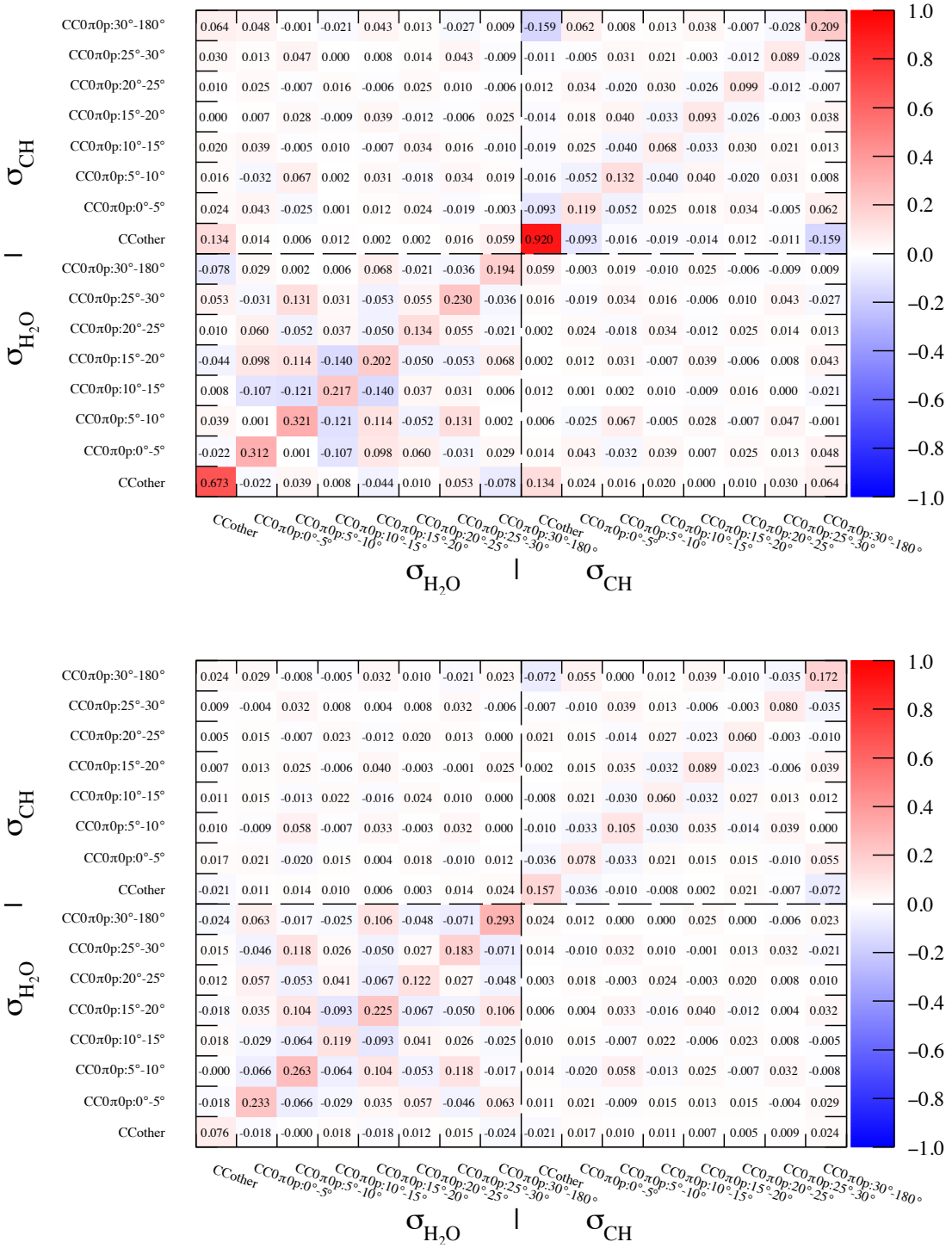

Figure D.5: Covariance matrix including all uncertainties for $\overline{\nu}_\mu$ (top) and $\overline{\nu}_\mu + \nu_\mu$ (bottom) cross sections.

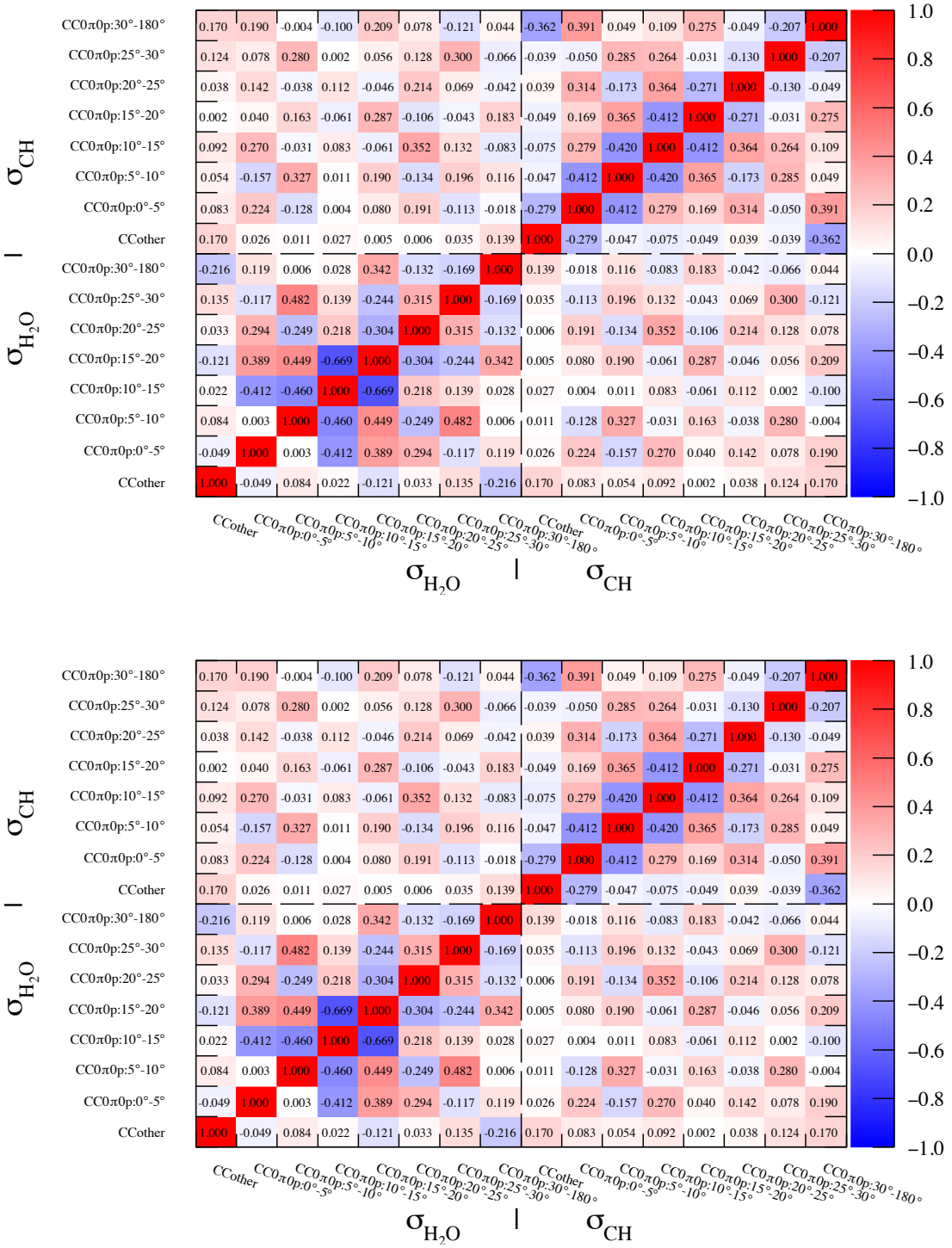

Figure D.6: Correlation matrix including all uncertainties for $\overline{\nu}_\mu$ (top) and $\overline{\nu}_\mu + \nu_\mu$ (bottom) cross sections.

List of Figures

List of Tables

Bibliography

[1] W. Pauli, "Dear radioactive ladies and gentlemen", Phys. Today **31N9**, 27 (1978).

[2] F. Reines *et al.*, "Detection of the Free Antineutrino", Phys. Rev. **117**, 159–173 (1960).

[3] G. Danby *et al.*, "Observation of High-Energy Neutrino Reactions and the Existence of Two Kinds of Neutrinos", Phys. Rev. Lett. **9**, 36–44 (1962).

[4] M. L. Perl *et al.*, "Evidence for Anomalous Lepton Production in $e^+ - e^-$ Annihilation", Phys. Rev. Lett. **35**, 1489–1492 (1975).

[5] K. Kodama *et al.*, "Observation of tau neutrino interactions", Physics Letters B **504**, 218 – 224 (2001).

[6] S. Schael *et al.* (ALEPH, DELPHI, L3, OPAL, SLD, LEP Electroweak Working Group, SLD Electroweak Group, SLD Heavy Flavour Group), "Precision electroweak measurements on the Z resonance", Phys. Rept. **427**, 257–454 (2006).

[7] R. Davis, D. S. Harmer, K. C. Hoffman, "Search for Neutrinos from the Sun", Phys. Rev. Lett. **20**, 1205–1209 (1968).

[8] J. N. Abdurashitov *et al.* (SAGE Collaboration), "Solar neutrino flux measurements by the Soviet-American Gallium Experiment (SAGE) for half the 22 year solar cycle", J. Exp. Theor. Phys. **95**, 181–193 (2002).

[9] M. Cribier *et al.* (GALLEX Collaboration), "Results of the whole GALLEX experiment", Nuclear Physics B - Proceedings Supplements **70**, 284 – 291 (1999).

[10] Y. Fukuda *et al.*, "Erratum: Measurements of the Solar Neutrino Flux from Super-Kamiokande's First 300 Days [Phys. Rev. Lett. 81, 1158 (1998)]", Phys. Rev. Lett. **81**, 4279–4279 (1998).

[11] Q. R. Ahmad *et al.* (SNO Collaboration), "Direct Evidence for Neutrino Flavor Transformation from Neutral-Current Interactions in the Sudbury Neutrino Observatory", Phys. Rev. Lett. **89**, 011301 (2002).

[12] K. Eguchi *et al.* (KamLAND Collaboration), "First Results from KamLAND: Evidence for Reactor Antineutrino Disappearance", Phys. Rev. Lett. **90**, 021802 (2003).

[13] K. Abe *et al.* (T2K Collaboration), "Evidence of electron neutrino appearance in a muon neutrino beam", Phys. Rev. D **88**, 032002 (2013).

[14] B. Pontecorvo, "Neutrino Experiments and the Problem of Conservation of Leptonic Charge", Sov. Phys. JETP **26**, 984–988 (1968).

[15] Z. Maki, M. Nakagawa, S. Sakata, "Remarks on the Unified Model of Elementary Particles", Progress of Theoretical Physics **28**, 870–880 (1962).

[16] K. Abe *et al.* (Super-Kamiokande Collaboration), "Solar neutrino measurements in Super-Kamiokande-IV", Phys. Rev. D **94**, 052010 (2016).

[17] B. Aharmim *et al.* (SNO Collaboration), "Combined analysis of all three phases of solar neutrino data from the Sudbury Neutrino Observatory", Phys. Rev. C **88**, 025501 (2013).

[18] G. Bellini *et al.* (Borexino Collaboration), "Precision Measurement of the ^{7}Be Solar Neutrino Interaction Rate in Borexino", Phys. Rev. Lett. **107**, 141302 (2011).

[19] S. Abe *et al.* (The KamLAND Collaboration), "Precision Measurement of Neutrino Oscillation Parameters with KamLAND", Phys. Rev. Lett. **100**, 221803 (2008).

[20] K. Abe *et al.* (Super-Kamiokande Collaboration), "Atmospheric neutrino oscillation analysis with external constraints in Super-Kamiokande I-IV", Phys. Rev. D **97**, 072001 (2018).

[21] M. G. Aartsen *et al.* (IceCube Collaboration), "Measurement of Atmospheric Neutrino Oscillations at 6–56 GeV with IceCube DeepCore", Phys. Rev. Lett. **120**, 071801 (2018).

[22] M. H. Ahn *et al.* (K2K Collaboration), "Measurement of neutrino oscillation by the K2K experiment", Phys. Rev. D **74**, 072003 (2006).

[23] P. Adamson *et al.* (MINOS Collaboration), "Combined Analysis of ν_μ Disappearance and $\nu_\mu \to \nu_e$ Appearance in MINOS Using Accelerator and Atmospheric Neutrinos", Phys. Rev. Lett. **112**, 191801 (2014).

[24] K. Abe *et al.* (T2K Collaboration), "Search for CP Violation in Neutrino and Antineutrino Oscillations by the T2K Experiment with 2.2×10^{21} Protons on Target", Phys. Rev. Lett. **121**, 171802 (2018).

[25] M. A. Acero *et al.* (NOvA Collaboration), "New constraints on oscillation parameters from ν_e appearance and ν_μ disappearance in the NOvA experiment", Phys. Rev. D **98**, 032012 (2018).

[26] D. Adey *et al.* (The Daya Bay Collaboration), "Measurement of the Electron Antineutrino Oscillation with 1958 Days of Operation at Daya Bay", Phys. Rev. Lett. **121**, 241805 (2018).

[27] Y. Abe *et al.* (Double Chooz), "Measurement of θ_{13} in Double Chooz using neutron captures on hydrogen with novel background rejection techniques", JHEP **01**, 163 (2016).

[28] G. Bak *et al.* (RENO Collaboration), "Measurement of Reactor Antineutrino Oscillation Amplitude and Frequency at RENO", Phys. Rev. Lett. **121**, 201801 (2018).

[29] K. Abe *et al.* (The T2K Collaboration), "Measurement of neutrino and antineutrino oscillations by the T2K experiment including a new additional sample of ν_e interactions at the far detector", Phys. Rev. D **96**, 092006 (2017).

[30] M. Tanabashi *et al.* (Particle Data Group), "Review of Particle Physics", Phys. Rev. D **98**, 030001 (2018).

[31] K. Abe *et al.*, "Proposal for an Extended Run of T2K to 20×10^{21} POT".

[32] K. Abe *et al.*, "T2K ND280 Upgrade - Technical Design Report".

[33] T. Fukuda *et al.*, "First neutrino event detection with nuclear emulsion at J-PARC neutrino beamline", PTEP **2017**, 063C02 (2017).

[34] S. Bhadra *et al.* (nuPRISM), "Letter of Intent to Construct a nuPRISM Detector in the J-PARC Neutrino Beamline".

[35] C. L. Smith, "Neutrino reactions at accelerator energies", Physics Reports **3**, 261 – 379 (1972).

[36] R. G. Sachs, "High-Energy Behavior of Nucleon Electromagnetic Form Factors", Phys. Rev. **126**, 2256–2260 (1962).

[37] O. Gayou *et al.* (Jefferson Lab Hall A Collaboration), "Measurement of G_{E_p}/G_{M_p} in $\vec{e}\ p \rightarrow e\ \vec{p}$ to $Q^2 = 5.6\text{GeV}^{2}$", Phys. Rev. Lett. **88**, 092301 (2002).

[38] R. Bradford *et al.*, "A New Parameterization of the Nucleon Elastic Form Factors", Nuclear Physics B - Proceedings Supplements **159**, 127 – 132 (2006).

[39] V. Bernard, L. Elouadrhiri, U.-G. Meissner, "Axial structure of the nucleon: Topical Review", J. Phys. **G28**, R1–R35 (2002).

[40] D. Rein, L. M. Sehgal, "Neutrino-excitation of baryon resonances and single pion production", Annals of Physics **133**, 79 – 153 (1981).

[41] R. P. Feynman, M. Kislinger, F. Ravndal, "Current Matrix Elements from a Relativistic Quark Model", Phys. Rev. D **3**, 2706–2732 (1971).

[42] G. Breit, E. Wigner, "Capture of Slow Neutrons", Phys. Rev. **49**, 519–531 (1936).

[43] S. L. Adler, "Tests of the Conserved Vector Current and Partially Conserved Axial-Vector Current Hypotheses in High-Energy Neutrino Reactions", Phys. Rev. **135**, B963–B966 (1964).

[44] T. Sjöstrand, "High-energy-physics event generation with PYTHIA 5.7 and JETSET 7.4", Computer Physics Communications **82**, 74 – 89 (1994).

[45] J. Mousseau *et al.* (The MINERνA Collaboration), "Measurement of partonic nuclear effects in deep-inelastic neutrino scattering using MINERvA", Phys. Rev. D **93**, 071101 (2016).

[46] P. Adamson *et al.* (MINOS Collaboration), "Neutrino and antineutrino inclusive charged-current cross section measurements with the MINOS near detector", Phys. Rev. D **81**, 072002 (2010).

[47] A. M. Ankowski, O. Benhar, "Electroweak nuclear response at moderate momentum transfer", Phys. Rev. C **83**, 054616 (2011).

[48] R. Smith, E. Moniz, "Neutrino reactions on nuclear targets", Nuclear Physics B **43**, 605 – 622 (1972).

[49] J. Nieves, E. Oset, C. Garcia-Recio, "A theoretical approach to pionic atoms and the problem of anomalies", Nuclear Physics A **554**, 509 – 553 (1993).

[50] J. Nieves, I. R. Simo, M. J. V. Vacas, "Inclusive charged-current neutrino-nucleus reactions", Phys. Rev. C **83**, 045501 (2011).

[51] O. Benhar, A. Fabrocini, "Two-nucleon spectral function in infinite nuclear matter", Phys. Rev. C **62**, 034304 (2000).

[52] S. K. Singh, E. Oset, "Inclusive quasielastic neutrino reactions in ^{12}C and ^{16}O at intermediate energies", Phys. Rev. C **48**, 1246–1258 (1993).

[53] L. Pickering, "Examining nuclear effects in neutrino interactions with transverse kinematic imbalance", JPS Conf. Proc. **12**, 010032 (2016).

[54] M. Martini *et al.*, "Unified approach for nucleon knock-out and coherent and incoherent pion production in neutrino interactions with nuclei", Phys. Rev. C **80**, 065501 (2009).

[55] W. Alberico, M. Ericson, A. Molinari, "The role of two particle-two hole excitations in the spin-isospin nuclear response", Annals of Physics **154**, 356 – 395 (1984).

[56] I. R. Simo *et al.*, "Relativistic model of 2p-2h meson exchange currents in (anti)neutrino scattering", Journal of Physics G: Nuclear and Particle Physics **44**, 065105 (2017).

[57] J. Nieves, I. Ruiz Simo, M. J. Vicente Vacas, "Inclusive Charged–Current Neutrino–Nucleus Reactions", Phys. Rev. **C83**, 045501 (2011).

[58] L. Alvarez-Ruso, Y. Hayato, J. Nieves, "Progress and open questions in the physics of neutrino cross sections at intermediate energies", New Journal of Physics **16**, 075015 (2014).

[59] L. Salcedo *et al.*, "Computer simulation of inclusive pion nuclear reactions", Nuclear Physics A **484**, 557 – 592 (1988).

[60] P. de Perio, "NEUT pion FSI", AIP Conf. Proc. **1405**, 223–228 (2011).

[61] Y. Hayato, "A neutrino interaction simulation program library NEUT", Acta Phys. Polon. **B40**, 2477–2489 (2009).

[62] K. Abe *et al.* (T2K Collaboration), "Measurement of the inclusive ν_μ charged current cross section on iron and hydrocarbon in the T2K on-axis neutrino beam", Phys. Rev. D **90**, 052010 (2014).

[63] A. Higuera *et al.* (MINERvA Collaboration), "Measurement of Coherent Production of $\pi^{\pm}$ in Neutrino and Antineutrino Beams on Carbon from E_{ν} of 1.5 to 20 GeV", Phys. Rev. Lett. **113**, 261802 (2014).

[64] M. Glück, E. Reya, A. Vogt, "Dynamical parton distributions revisited", Eur. Phys. J. **C5**, 461–470 (1998).

[65] A. Bodek, U. K. Yang, "Modeling neutrino and electron scattering inelastic cross- sections in the few GeV region with effective LO PDFs TV Leading Order", Submitted to: Nucl. Phys. Proc. Suppl.

[66] C. Andreopoulos *et al.*, "The GENIE neutrino Monte Carlo generator", Nuclear Instruments and Methods in Physics Research Section A: Accelerators, Spectrometers, Detectors and Associated Equipment **614**, 87 – 104 (2010).

[67] D. Casper, "The nuance neutrino physics simulation, and the future", Nuclear Physics B - Proceedings Supplements **112**, 161 – 170 (2002).

[68] A. Gazizov, M. Kowalski, "ANIS: High energy neutrino generator for neutrino telescopes", Computer Physics Communications **172**, 203 – 213 (2005).

[69] O. Buss *et al.*, "Transport-theoretical description of nuclear reactions", Physics Reports **512**, 1 – 124 (2012).

[70] T. Golan, C. Juszczak, J. T. Sobczyk, "Effects of final-state interactions in neutrino-nucleus interactions", Phys. Rev. C **86**, 015505 (2012).

[71] T. G. *et al.*, "Effects of final-state interactions in neutrino-nucleus interactions", Physical Review C **86**, 15505– (2012).

[72] C. Andreopoulos *et al.*, "The GENIE Neutrino Monte Carlo Generator: Physics and User Manual".

[73] S. J. Barish *et al.*, "Study of neutrino interactions in hydrogen and deuterium: Description of the experiment and study of the reaction $\nu + d \rightarrow \mu^{-} + p + p_s$", Phys. Rev. D **16**, 3103–3121 (1977).

[74] D. Allasia *et al.*, "Investigation of exclusive channels in $\nu/\overline{\nu}$-deuteron charged current interactions", Nuclear Physics B **343**, 285 – 309 (1990).

[75] N. J. Baker *et al.*, "Quasielastic neutrino scattering: A measurement of the weak nucleon axial-vector form factor", Phys. Rev. D **23**, 2499–2505 (1981).

[76] G. Fanourakis *et al.*, "Study of low-energy antineutrino interactions on protons", Phys. Rev. D **21**, 562–568 (1980).

[77] T. Kitagaki *et al.*, "High-energy quasielastic $\nu_\mu n \to \mu^- p$ scattering in deuterium", Phys. Rev. D **28**, 436–442 (1983).

[78] A. A. Aguilar-Arevalo *et al.* (MiniBooNE Collaboration), "First measurement of the muon neutrino charged current quasielastic double differential cross section", Phys. Rev. D **81**, 092005 (2010).

[79] V. Lyubushkin (NOMAD), "A Study of Quasi-Elastic Muon (Anti)Neutrino Scattering in the NOMAD Experiment", AIP Conf. Proc. **1189**, 157–162 (2009).

[80] R. Gran *et al.* (K2K Collaboration), "Measurement of the quasielastic axial vector mass in neutrino interactions on oxygen", Phys. Rev. D **74**, 052002 (2006).

[81] K. Olive, P. D. Group, "Review of Particle Physics", Chinese Physics C **38**, 090001 (2014).

[82] A. A. Aguilar-Arevalo *et al.* (MiniBooNE Collaboration), "First measurement of the muon antineutrino double-differential charged-current quasielastic cross section", Phys. Rev. D **88**, 032001 (2013).

[83] D. Ruterbories *et al.* (MINERνA Collaboration), "Measurement of Quasielastic-Like Neutrino Scattering at $\langle E_\nu \rangle \sim 3.5$ GeV on a Hydrocarbon Target", arXiv, 1811.02774 [hep–ex] (2018).

[84] M. Betancourt *et al.* (MINERνA Collaboration), "Direct Measurement of Nuclear Dependence of Charged Current Quasielasticlike Neutrino Interactions Using MINERνA", Phys. Rev. Lett. **119**, 082001 (2017).

[85] K. Abe *et al.* (T2K Collaboration), "First measurement of the ν_μ charged-current cross section on a water target without pions in the final state", Phys. Rev. D **97**, 012001 (2018).

[86] K. Abe *et al.* (T2K Collaboration), "Measurement of double-differential muon neutrino charged-current interactions on C_8H_8 without pions in the final state using the T2K off-axis beam", Phys. Rev. D **93**, 112012 (2016).

[87] J. Nieves *et al.*, "Neutrino energy reconstruction and the shape of the charged current quasielastic-like total cross section", Phys. Rev. D **85**, 113008 (2012).

[88] M. Martini *et al.*, "Neutrino and antineutrino quasielastic interactions with nuclei", Phys. Rev. C **81**, 045502 (2010).

[89] K. Abe *et al.* (T2K Collaboration), "First measurement of the muon neutrino charged current single pion production cross section on water with the T2K near detector", Phys. Rev. D **95**, 012010 (2017).

[90] K. Abe *et al.* (The T2K Collaboration), "Measurement of $\overline{\nu}_\mu$ and ν_μ charged current inclusive cross sections and their ratio with the T2K off-axis near detector", Phys. Rev. D **96**, 052001 (2017).

[91] K. Abe *et al.*, "The T2K experiment", Nuclear Instruments and Methods in Physics Research Section A: Accelerators, Spectrometers, Detectors and Associated Equipment **659**, 106 – 135 (2011).

[92] S. B. *el. al.*, "Optical transition radiation monitor for the T2K experiment", Nuclear Instruments and Methods in Physics Research Section A: Accelerators, Spectrometers, Detectors and Associated Equipment **703**, 45 – 58 (2013).

[93] K. Matsuoka *et al.*, "Design and Performance of the Muon Monitor for the T2K Neutrino Oscillation Experiment", Nucl. Instrum. Meth. **A624**, 591–600 (2010).

[94] Y. Kudenko (T2K), "The Near neutrino detector for the T2K experiment", Nucl. Instrum. Meth. **A598**, 289–295 (2009).

[95] K. Abe *et al.* (T2K Collaboration), "T2K neutrino flux prediction", Phys. Rev. D **87**, 012001 (2013).

[96] A. Ferrari *et al.*, "FLUKA: A multi-particle transport code (Program version 2005)".

[97] G. Battistoni *et al.*, "The FLUKA code: Description and benchmarking", AIP Conf. Proc. **896**, 31–49 (2007).

[98] R. Brun *et al.*, "GEANT Detector Description and Simulation Tool".

[99] C. Zeitnitz, T. Gabriel, "The GEANT-CALOR interface and benchmark calculations of ZEUS test calorimeters", Nuclear Instruments and Methods in Physics Research Section A: Accelerators, Spectrometers, Detectors and Associated Equipment **349**, 106 – 111 (1994).

[100] N. Abgrall *et al.* (The NA61/SHINE Collaboration), "Measurements of cross sections and charged pion spectra in proton-carbon interactions at 31 GeV/c", Phys. Rev. C **84**, 034604 (2011).

[101] N. Abgrall *et al.* (NA61/SHINE Collaboration), "Measurement of production properties of positively charged kaons in proton-carbon interactions at 31 GeV/c", Phys. Rev. C **85**, 035210 (2012).

[102] T. Eichten *et al.*, "Particle production in proton interactions in nuclei at 24 GeV/c", Nuclear Physics B **44**, 333 – 343 (1972).

[103] J. V. Allaby *et al.*, "High-energy particle spectra from proton interactions at 19.2-GeV/c".

[104] I. Chemakin *et al.*, "Erratum: Pion production by protons on a thin beryllium target at 6.4, 12.3, and 17.5 GeV/c incident proton momenta [Phys. Rev. C 77, 015209 (2008)]", Phys. Rev. C **77**, 049903 (2008).

[105] D. Allan *et al.* (T2K UK), "The Electromagnetic Calorimeter for the T2K Near Detector ND280", JINST **8**, P10019 (2013).

[106] K. Hiraide, "The SciBar Detector at FNAL Booster Neutrino Experiment", Nuclear Physics B - Proceedings Supplements **159**, 85 – 90 (2006).

[107] T. Koga, "Measurement of neutrino interactions on water and search for electron anti-neutrino appearance in the T2K experiment", Ph.D. Thesis.

[108] P. A. A. *et. al.*, "The T2K fine-grained detectors", Nuclear Instruments and Methods in Physics Research Section A: Accelerators, Spectrometers, Detectors and Associated Equipment **696**, 1 – 31 (2012).

[109] K. Abe *et al.* (T2K Collaboration), "First measurement of the muon neutrino charged current single pion production cross section on water with the T2K near detector", Phys. Rev. **D95**, 012010 (2017).

[110] F. Hosomi, "Characterization of Multi-Pixel Photon Counters for a new neutrino detector", Master's Thesis.

[111] "Hamamatsu Photonics", https://www.hamamatsu.com.

[112] R. Tamura, "Construction and performance of a neutrino detector for neutrino-nucleus interaction cross-section measurements", Master's Thesis.

[113] N. Chikuma, "Research and development of magnetized muon range detector and readout electronics for a neutrino cross section experiment", Master's Thesis.

[114] Y. Hayato, "NEUT", Nucl.Phys.Proc.Suppl **112**, 171– (2002).

[115] G. D'Agostini, "A multidimensional unfolding method based on Bayes' theorem", Nuclear Instruments and Methods in Physics Research Section A: Accelerators, Spectrometers, Detectors and Associated Equipment **362**, 487 – 498 (1995).

[116] S. Wolfram, "Statistical mechanics of cellular automata", Rev. Mod. Phys. **55**, 601–644 (1983).

[117] T. Kikawa, "Measurement of Neutrino Interactions and Three Flavor Neutrino Oscillations in the T2K Experiment", Ph.D. Thesis.

[118] C. E. Patrick *et al.* (MINERνA Collaboration), "Measurement of the muon antineutrino double-differential cross section for quasielastic-like scattering on hydrocarbon at $E_\nu \sim 3.5$ GeV", Phys. Rev. D **97**, 052002 (2018).

[119] T. Vladisavljevic, "Constraining the T2K Neutrino Flux Prediction with 2009 NA61/SHINE Replica-Target Data".

[120] "Laboratoire Leprince-Ringuet", http://llr.in2p3.fr.

[121] Omega, http://omega.in2p3.fr.